3He in extreme conditions : from fundamental physics to applications in astrophysics

Johannes Elbs

THESE

pour obtenir le grade de

Docteur de l'Université Joseph Fourier
Grenoble I

Discipline : Physique

présentée et soutenue publiquement
par :

Johannes Elbs

le 12 Novembre 2007

---

^{3}He in extreme conditions : from fundamental physics to applications in astrophysics

---

Composition du jury :

C. Berthier (Président)
I. Moukharski (Rapporteur)
G. Pickett (Rapporteur)
C. Enss
Yu. M. Bunkov (Co-directeur)
H. Godfrin (Co-directeur)

Thèse préparée à l'Institut Néel
CNRS - GRENOBLE

Contents

1 Introduction **5**

I Dark matter detector prototype **13**

2 Quick reference to some important relations **15**

3 Liquid and Superfluid ^{3}He **19**
3.1 ^{3}He and ^{4}He 19
3.2 The Landau Fermi liquid theory 19
3.3 Superfluid ^{3}He 20
3.3.1 Cooper pairing and order parameter 20
3.3.2 Orientation of the order parameter 24
3.3.3 Thermodynamic properties of ^{3}He-B 29

4 Cosmology and Dark Matter **33**
4.1 The missing mass of the universe 33
4.2 The neutralino and possibilities of detection 37
4.2.1 Supersymmetry 38
4.3 Dark matter detection 40
4.3.1 Direct detection: expected signatures and experimental challenges . 42
4.3.2 ^{3}He as a sensitive medium 43

5 Experimental methods **47**
5.1 Cryogenic methods 47
5.1.1 ^{3}He/^{4}He dilution 47
5.1.2 Adiabatic nuclear demagnetisation 48
5.2 Vibrating Wire Thermometry in ^{3}He 49
5.2.1 Discussion of the choice of the thermometer 49
5.2.2 Resonance of a vibrating wire 51
5.2.3 The different operation modes of a VWR 53
5.2.4 Correlation between the friction and the temperature 56
5.3 ^{3}He Bolometry 59

5.3.1 The 3-cell ^{3}He Bolometer . . . 59
5.3.2 Detection of heating events . . . 62
5.3.3 Characteristic time constants . . . 62
5.3.4 Analytic form of a peak . . . 64
5.3.5 Calibration factor . . . 65
5.3.6 Calibration pulses . . . 66
5.4 Particle detection and energy deficit . . . 69
5.5 Scintillation and creation of metastable dimers . . . 71

6 Magnetic field dependence of the calibration factor 73
6.1 Experimental results . . . 74
6.2 Discussion . . . 77

7 A detailed analysis of the recovering time: A possible discrimination mechanism? 81
7.1 Statistical analysis of the recovering time . . . 82
7.1.1 Experimental distribution of the recovering time . . . 83
7.2 The effect of a delayed heat release . . . 86
7.2.1 Simulations of partly delayed energy deposition . . . 88
7.2.2 Expectations for other particles . . . 98
7.2.3 The time constant of metastable triplet dimers . . . 99
7.2.4 Conclusions and outlook . . . 102
7.3 Absolute value and temperature dependence of the recovering time . . . 103

II Application of the detector prototype to fundamental ^{3}He physics 105

8 Addendum specific heat of adsorbed ^{3}He 107
8.1 Comparison of heater pulses with and without solid ^{3}He . . . 108
8.2 Measuring the heat capacity of adsorbed layers of ^{3}He . . . 109
8.3 Specific heat of adsorbed layers of ^{3}He . . . 113
8.4 Conclusion . . . 114

9 Pressure dependence of neutron capture events 115
9.1 Kibble-Zurek mechanism . . . 115
9.2 New experimental results . . . 119
9.3 Discussion of the result . . . 123
9.3.1 Possible explanations for the discontinuity . . . 125
9.3.2 Can different textures change the energy deficit? . . . 127
9.3.3 Conclusion . . . 129

III ^{3}He confined in anisotropic aerogel 133

10 Continuous wave NMR measurements 137
10.1 The sample and the cell . . . 137
10.2 Continuous Wave NMR results . . . 138
10.2.1 Normal phase gradient measurements . . . 138
10.2.2 Normal, A-like and B-like phase . . . 140
10.2.3 Coexistence and strong pinning . . . 145
10.2.4 Signature of the polar phase? . . . 147

11 Pulsed NMR measurements 151
11.1 Expected resonance frequency . . . 151
11.2 Experimental results . . . 153
11.2.1 Experimental details . . . 153
11.2.2 B-phase pulses . . . 157
11.2.3 Temperature dependence . . . 157
11.2.4 Conclusion . . . 159

A Recovering time constant 161
A.1 "Flat" Hole . . . 161
A.2 Cylindrical hole . . . 163

B Magnetic field dependence of the heat capacity 165

C Detailed analysis of the neutron energy error bars 167
C.1 Experimental details . . . 167
C.2 Analysis of the statistical errors . . . 168
C.3 Systematic errors . . . 170

Chapter 1

Introduction

This thesis was done in the framework of a long term project of the Grenoble Ultra-Low Temperature group called ULTIMA (Ultra Low Temperature Instrumentation for Measurements in Astrophysics). The basic idea of this project is the use of superfluid ^{3}He as a target matter for a future dark matter detector, specially conceived to directly detect a hypothetical particle called neutralino, but which would also be sensitive to other dark matter candidates. The extremely low specific heat of ^{3}He at ultra low temperature makes it possible to measure the increase in temperature after a scattering particle deposits a small amount of energy. Several arguments can be listed in favour of using ^{3}He as a target matter, like the high neutron capture cross section and the low Compton cross section which provide a substantial inherent rejection factor of background events. ^{3}He having a nonzero spin makes it sensitive to the spin-dependent interaction and hence complementary to the most advanced existing detectors.

The idea to use superfluid ^{3}He as a sensitive medium for particle detection was first proposed about twenty years ago by the Lancaster group. Some years later, this group presented experimental data which demonstrated the measure of cosmic rays (mainly muons), as well as neutrons from a radioactive source. The Grenoble group started later the MACHe3 project (MAtrix of Cells of superfluid Helium-3), whose main goal was to demonstrate the feasibility to use superfluid ^{3}He as a dark matter detector and to collect the most information possible for an optimal design of a future large detector. This included on the one hand theoretical work, mainly done at the LPSC[1]. Expected event rates for neutralino and background events were calculated and the efficiency of background rejection by the use of a large matrix of bolometric cells was evaluated using simulations. On the other hand, our group did experimental work, first on a one cell-, then on a three cell prototype demonstrating several important points:

- A high precision thermometry is obtained using Vibrating Wire Resonators.
- An independent (i.e. not using an external source), precise energy calibration was achieved by introduction of a well known amount of heat using a second Vibrating

[1] Laboratoire de Physique Subatomique et de Cosmologie de Grenoble

Wire Resonator.

- Spectra for several particles (cosmic muons, neutrons coming from an AmBe source, electrons emitted by a ^{57}Co source) demonstrated a bolometric sensitivity of 1 keV. This sensitivity is enough to detect neutralinos which are expected to release 1-6 keV of heat.
- The use of a multicell detector allowed to experimentally verify the idea of a background rejection through the measurement of coincident events.

At the beginning of my thesis, this last, three-cell bolometer was still in place, and we decided to redo measurements using the same experimental setup. One goal was to gather more information for an application in a future dark matter detector. A first point which was studied, and which is presented in chapter 6 is the magnetic field dependence of the energy calibration. While this is not of a fundamental importance, it introduces a correction that increases the precision of the calibration for the detector. The most interesting effect regarding our long term project is the observation that the pulse shape found after a heating event depends on the nature of the event. To be precise, events caused by muons lead to a different pulse shape than events caused by neutrons and events simulated by heater pulses. Detailed measurements on this effect, resolving events down to 50 keV will be presented in chapter 7. If this observation can be confirmed in the future for low energy events down to 1 keV and for other particles like electrons and photons, this provides a powerful additional criterion for discrimination of background events. A model based on the assumption that metastable triplet dimers, created directly after an incidence, release their energy as heat on a timescale comparable to the response time of the bolometer will be presented.

Another reason why we continued to work using the same setup was that it could be used to do experiments on questions related to fundamental ^{3}He physics. In chapter 8 we will show that adsorbed layers of ^{3}He present a huge heat capacity. A method to determine its value has been developed. We show that this heat capacity can be eliminated by covering the cell walls with two monolayers of ^{4}He. This is also an important information for a future dark matter detector, as an increased heat capacity results in a loss of sensitivity.

In chapter 9 we finally present an experiment also related to astrophysics, but in a different way: in the standard cosmology model, it is thought that directly after the Big Bang, energy density was very high and the universe was inconceivably hot. The universe then underwent a period of extremely fast expansion, meaning that it cooled down. During this rapid cooling it is possible that a certain number of symmetry breaking second order phase transitions were passed rapidly. A theory by T.W.B. Kibble predicts that if such a phase transition is fast enough, different causally disconnected domains can cross the transition independently, leading to different values/orientations of the corresponding order parameters and ultimately to the production of topological defects. His idea can not be tested directly from astronomical observations, as these phase transitions happened

before the universe got transparent (before the recombination). W.H. Zurek recognised that causality is such a fundamental concept that some condensed matter systems can be used to test Kibble's idea. In our case, we locally heat superfluid ^{3}He above the transition temperature, using a neutron capture reaction. The subsequent cooling back to the superfluid phase verifies well the criterion of a fast second order phase transition. The number of vortices created can then be indirectly measured by doing bolometric measurements. To which extent the new measurements support the Kibble-Zurek scenario will be discussed.

In the third part of this thesis we treat a thematically very different subject: since several years, high porosity aerogel is used to study the influence of disorder on the otherwise 100 % pure superfluid ^{3}He. Several facts could already be established like the existence of superfluid phases that are similar to the phases observed in pure ^{3}He, a reduction of the superfluid transition temperature and the possibility of coexistence of two different superfluid phases. A very recent idea suggests that introducing a global anisotropy through compressing or stretching of the aerogel sample could on the one hand introduce a new preferred direction for the orbital part of the order parameter and on the other hand stabilise a new, up to now unobserved phase called *polar phase*. In chapter 10, continuous wave NMR measurements on a radially compressed aerogel sample, taken during very slow coolings and warmings through the superfluid transition will be presented. The data will then be compared to theoretical predictions about a stabilisation of the A-like phase and the appearance of the polar phase.

The orientation of the order parameter due to the aerogel anisotropy leads to a configuration which can not be achieved normally in bulk ^{3}He: the preferred direction of orbital momentum is perpendicular to the magnetic field. In such a configuration, a new precessing state in the nonlinear NMR regime of high deflection angles was predicted. In chapter 11, pulsed NMR measurements show that analysing the precession frequency during the free induction decay allows to identify experimentally for the first time this new precession mode. NMR pulses done at different field gradient values then demonstrate that in this state a coherent spin precession occurs.

Finally I would like to express my gratitude to some people who helped and supported me during the last three years, and without whom this work would not have been possible. First of all I want to thank my supervisors Yuriy Bunkov and Henri Godfrin, who provided me with constant support, advice and who were always willing to discuss my countless questions with me. A special thanks to Clemens Winkelmann for introducing me to ^{3}He bolometry, to Eddy Collin for all the little and big occasions he found to provide me with invaluable help, and to Valerie and Thomas, for not only being good coworkers but also good friends. Another "dankeschön" goes to my sister Katharina for proofreading this manuscript. Additionally I want to express my gratitude to the members of the jury, Claude Berthier, Iouri Moukharski, George Pickett and Christian Enss for investing much time in reading this work in detail and for travelling to Grenoble for my PhD defense. Many more people helped me directly and indirectly during these three years and I would like to cite at this place Jean-Louis Bret, Richard Haley, Bill Halperin, Jean-Louis Leviel,

Takao Mizusaki, Gerard Vermeulen and Grigori Volovik.

And last but not least there are those who know less about ^{3}He physics, but whose support is so much more valuable that words are not sufficient to express all my gratitude: xièxiè Yuyi and danke Mama und Papa.

Introduction (français)

Cette thèse s'inscrit dans le cadre du projet ULTIMA (Ultra Low Temperature Instrumentation for Measurements in Astrophysics). L'idée de base de ce projet est d'utiliser l'^{3}He superfluide comme matière sensible pour un détecteur de matière noire. Ce dernier est particulièrement conçu pour la détection directe d'une particule hypothétique dénommée neutralino. La chaleur spécifique extrêmement faible aux ultra basses températures permet de mesurer l'augmentation de température après qu'une particule ait interagit avec l'^{3}He. Plusieurs arguments inhérents à l'utilisation de l'^{3}He peuvent être cités en faveur d'un tel détecteur : la grande section efficace de capture de neutron et la faible section efficace Compton donnent un grand facteur de réjection des évènements ordinaires. L'^{3}He ayant un spin total non nul, il sera sensible à l'interaction dépendant du spin. Cela rend le détecteur ^{3}He complémentaire des détecteurs existants les plus avancés.

ULTIMA a été précédé par MACHe3 (MAtrix of Cells of superfluid Helium-3). Pendant ce projet, la faisabilité générale de cette idée a été démontré, et un grand nombre d'informations pour le design d'un grand détecteur futur ont été obtenues. Une équipe théorique du LPSC Grenoble[2] a calculé le taux d'évènement attendu. De plus une simulation a éé faite qui démontre que l'utilisation d'une grande matrix de cellules bolométriques permet de discriminer efficacement les évènements. Les travaux expérimentaux de notre équipe, d'abord sur un prototype à une cellule, puis à trois cellule, ont démontré que l'on obtenait une thermométrie à haute précision par l'utilisation de fils vibrants. Une calibration indépendante, c'est à dire sans l'utilisation d'une source extérieure, est obtenue en utilisant un deuxième fil vibrant. Des spectres d'énergie pour différentes particules (muons cosmique, neutrons provenant d'une source AmBe, électrons émis par une source ^{57}Co) démontrent la sensibilité bolométrique de l'ordre de 1 keV. L'utilisation d'un détecteur multicellulaire a permis de vérifier expérimentalement l'idée d'une discrimination par mesure de coïncidence entre cellules.

Au début de ma thèse, le dernier bolomètre à trois cellule était encore monté et nous avons décidé de recommencer des mesures avec le même dispositif expérimental. Un premier objectif était de compléter notre compréhension de ces bolomètres afin d'optimiser le design d'un détecteur de matière noire futur. Un premier point qui est étudié et qui est présenté dans le chapitre 6 est la dépendance en champs magnétique du facteur de calibration. Cette étude permet d'apporter une correction qui vise à améliorer la précision en énergie.

L'effet le plus intéressant concernant le projet ULTIMA est l'observation que la forme d'un pulse varie selon la nature de la particule incidente. Pour être précis, les évènements causés par un muon sont différents des évènements causé par des neutrons et des évènements simulés par un pulse de chauffage. Des mesures détaillées de cet effet sont présentées au chapitre 7. Si cette observation est confirmée dans le futur, en particulier pour des évènements de basse énergie et pour d'autres particules telles que les électrons et les photons, cela nous fournira un outil supplémentaire de discrimination des évène-

[2] Laboratoire de Physique Subatomique et de Cosmologie, Grenoble

ments. Nous présentons de plus un modèle basé sur l'hypothèse selon la quelle les dimères metastables, créés directement après une incidence, relâchent leur énergie tardivement.

Dans une deuxième partie nous utilisons le même dispositif pour étudier la physique fondamentale de l'^{3}He. Dans le chapitre 8 nous démontrons que les couches adsorbées d'^{3}He présentent une chaleur spécifique très importante. Une méthode pour mesurer sa valeur est présentée. Nous montrons que cette chaleur spécifique peut être éliminée en couvrant les parois des cellules de deux monocouches d'^{4}He. Ces observations sont également importantes pour un détecteur de matière noire car une chaleur spécifique supplémentaire réduit d'autant la sensibilité bolométrique.

Dans le chapitre 9 nous présentons finalement une expérience également liée à l'astrophysique mais d'une façon différente : dans le modèle standard de la cosmologie il est admis que la densité d'énergie, juste après le Big Bang, était très grande et que l'univers était très chaud. Ensuite l'univers passe par une phase d'expansion rapide qui engendre un refroidissement rapide. Pendant ce refroidissement il est possible que l'univers ait passé un certain nombre de transitions de phase de deuxième ordre, brisant des symétries (par exemple la baryogènese). Une théorie de T.W.B. Kibble prédit que si une telle transition de phase est assez rapide, différents domaines sans liens causal peuvent transiter indépendamment. Ceci mène à différentes valeurs/orientations du paramètre d'ordre et finalement à des défauts topologiques. Cette idée ne peut pas être validée directement par des observations astronomiques car ces transitions de phases auraient lieu avant que l'univers ne soit devenu transparent (avant la recombinaison). W.H. Zurek a observé que certaines système de la matière condensée ont des symétries similaires ce qui mène à l'idée de tester les prédictions de Kibble dans un laboratoire. Dans notre cas nous chauffons localement l'^{3}He au-dessus de la température de transition superfluide en utilisant une source de neutrons. Il s'ensuit un refroidissement vers la phase superfluide qui vérifie bien le critère d'une transition de phase de deuxième ordre rapide. Le nombre de vortex créé est alors obtenu indirectement par une mesure bolométrique.

Dans la troisième partie de cette thèse nous traitons un sujet très différent : depuis quelques années, les aérogels sont utilisés pour étudier l'influence du désordre sur l'^{3}He superfluide. Un certain nombre de faits sont déjà établis, comme l'existence de phases similaires aux phases observées dans l'^{3}He pur, la réduction de la température de transition et la possibilité de coexistence de différentes phases. Une nouvelle idée propose qu'une anisotropie globale, engendrée par une compression de l'échantillon peut d'une côté orienter le paramètre d'ordre, et d'un autre côté stabiliser une nouvelle phase dénommée *phase polaire*. Dans le chapitre 10, nous présentons des mesures de RMN continu, réalisées sur un échantillon d'aérogel comprimé radialement. Les données sont comparées à l'hypothèse de l'apparition de la phase polaire et de la stabilisation de la phase A près de la température de transition.

L'orientation du paramètre d'ordre nous permet de réaliser une configuration qui ne peut pas être obtenue normalement. En effet, le moment orbital est orienté perpendiculairement au champ magnétique. Dans cette configuration un nouvel état de précession

dans le régime non-linéaire de la RMN était prédit. Dans le chapitre 11 des mesures en RMN pulsé démontrent que nous avons pu mettre en évidence pour la première fois ce nouveau mode de précession. Des pulses RMN à différentes valeurs de gradient ont démontré qu'une précession cohérente peut être observée pour ce mode.

Part I

Dark matter detector prototype

Chapter 2

Quick reference to some important relations

In this short first chapter we introduce some relations which may be helpful when reading the subsequent chapters. We think that this might be helpful because the sensor used in these measurement is rather exotic. The relations presented here will be introduced in closer detail in later chapters, so readers who are not familiar with vibrating wire thermometry or with superfluid ^{3}He might choose to jump this first chapter. As we intend it to be a quick reference we will simplify some relations and only give the first order terms.

The sensor used in the main part of this thesis was a Vibrating Wire Resonator (VWR). This sensor gives through its interaction with the liquid ^{3}He information about the quasiparticle density in the ultra low temperature region $T/T_c < 0.3$, with T_c the superfluid transition temperature. In this region, the damping force on a VWR in the superfluid is linear in velocity $F_{vis} = \gamma v$, and the prefactor γ is proportional to the quasiparticle density $n \propto \gamma$.

Temperature dependence of the VWR resonance width

A frequency sweep of the VWR in this region delivers a resonance curve of Lorentzian shape. The Full Width Half Maximum W of this sweep is proportional to γ and hence to the quasiparticle density:

$$W \propto n \tag{2.1}$$

The quasiparticle density depends exponentially on the temperature so that the temperature dependence of the VWR resonance width is given by (eq. 5.20)

$$W(T) = W_{int} + \alpha \exp(-\Delta/k_B T), \tag{2.2}$$

with

- $\alpha = (1.81 \pm 0.1) \cdot 10^5\,\mathrm{Hz}$, $W_{int} \approx 0.055\,\mathrm{Hz}$ for the $4.5\,\mu$m thermometer wire and

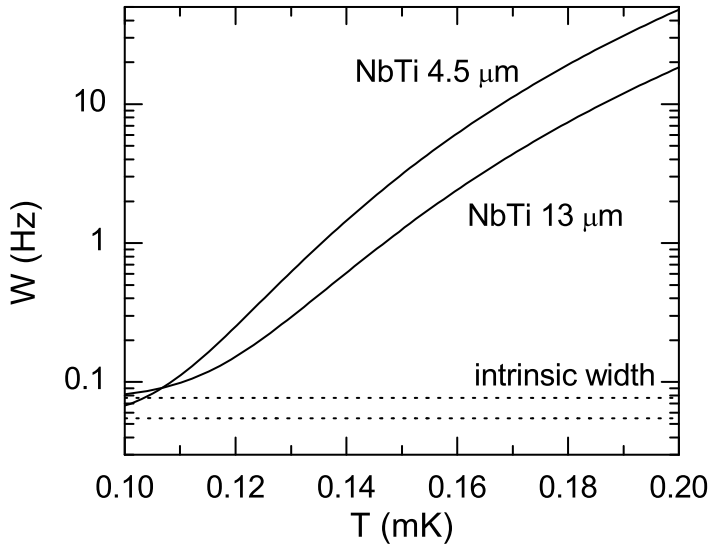

Figure 2.1: Temperature dependence of the 4.5 μm thermometer wire and the 13 μm heater wire.

- $\alpha = (0.69 \pm 0.05) \cdot 10^5$ Hz, $W_{int} \approx 0.077$ Hz for the 13 μm heater wire.

W_{int} corresponds to a constant term which is due to internal friction processes. Through this exponential temperature dependence VWR thermometers are very sensitive. A graph illustrating this relation is shown in fig. 2.1. This relation will be presented in detail in section 5.2.4.

Baseline resonance width W_{base}

In the chapters 6 to 9 we often have to deal with heating events which heat the superfluid ^{3}He slightly above the *baseline* temperature T_{base}. The corresponding resonance width $W(T_{base}) = W_{base}$ is called the baseline width. It is thus a measure for the baseline temperature. Because of relation 2.2 we express sometimes the temperature in units of a resonance width (Hz).

Limitations imposed by the thermometer on the working temperatures

The exponential temperature dependence of the VWR limits our working temperatures to a relatively narrow range. For $T/T_c > 0.2$, the resonance of the VWR thermometers used is very broad $W > 20$ Hz and thus the signal height very small which results in a loss of signal to noise ratio. For $T/T_c < 0.1$ the quasiparticle gas gets very dilute and the damping is dominated by internal friction processes $W_{int} \approx 0.077$ Hz. One remarkable feature is thus that while the temperature at which the VWR resonator works is limited to a very narrow range, the corresponding resonance width spans more than two decades.

Calibration Factor

In a bolometric experiment one determines the heat deposited by measuring the change in another parameter, related to the sensor physical properties. In our case the resonance width of the VWR is the key experimental parameter. The deposited energy is linearly related too the width change, for not to high energies:

$$\Delta W = \sigma E. \tag{2.3}$$

Because of this relation we will express sometimes a deposited energy in units of Hz.

The calibration factor can be expressed as follows:

$$\sigma = \frac{1}{C}\frac{dW}{dT}, \tag{2.4}$$

where C is the superfluid ^{3}He heat capacity. The calibration factor will be discussed in closer detail in section 5.3.5.

Definition of some time constants

τ_b Box time constant, thermalisation time or recovering time. The time constant of a bolometric cell to thermalise after a heating event.

τ_w VWR response time. The time a VWR needs to find a new equilibrium position after a sudden temperature change.

τ_m The metastable triplet dimer nonradiative life time. This time constant will be important in chapter 7 and describes the time scale on which metastable triplet dimers release their heat non radiatively.

Chapter 3

Liquid and Superfluid ^{3}He

3.1 ^{3}He and ^{4}He

^{3}He and ^{4}He are the only elements with an inter atomic interaction energy lower than the kinetic energy at the absolute zero, with the result that these two isotopes have the unique property to stay liquid even at the lowest temperatures (below a critical pressure). Since the non-zero kinetic energy at 0 K is a quantum mechanical effect the two Helium liquids are often called quantum fluids.

The chemical properties of these two elements are the same, so one could expect that they show rather the same behaviour. But when cooled to very low temperatures, there is one fundamental difference which will determine the physics of these two elements: ^{4}He is constituted of an even number (six) of spin $\frac{1}{2}$ particles giving a total spin which is an integral multiple of $\hbar$, characteristic of a boson. On the other hand ^{3}He has an odd number (five) of elementary particles, so that the intrinsic spin is a half-integral multiple of $\hbar$, characteristic of a fermion. Hence, ignoring the weak inter atomic forces, the ^{4}He atoms behave as a nearly ideal Bose gas, described by Bose-Einstein statistics, while the ^{3}He atoms behave as a nearly ideal Fermi gas described by Fermi-Dirac statistics.

3.2 The Landau Fermi liquid theory

Liquid below 3.2 K (at 1 bar), ^{3}He has a Fermi temperature T_F of about 1 K. For temperatures $T \ll T_F$, below typically 100 mK, this Fermi system is degenerated and can be described with high accuracy using the Fermi liquid theory presented by Landau. The main purpose of this theory is to replace the frequently colliding, strongly correlated ^{3}He atoms, by an equal number of nearly independent *quasiparticles*, and then describe the system as a degenerate, non interacting Fermi gas. Hence, the thermodynamic properties like specific heat, spin susceptibility, compressibility as well as the transport properties can be calculated using the same formula as derived for the non-interacting degenerate Fermi-gas, but with the corresponding parameters renormalised. The Fermi liquid interaction may be parametrised by a set of parameters F_l^j, with $j = s, a$ describing the difference between

spin-symmetric and spin-antisymmetric terms, and $l = 0, 1, ...$ indicating the order of the term. For most purposes, only the parameters with $l = 0$ and 1 play an important role.

The Landau theory being semi phenomenological, these parameters are obtained experimentally. It turns out that for example the effective quasiparticle mass m^*, which can be obtained by specific heat measurements, and which is linked to the parameter F_1^s via the equation

$$m^* = m(1 + \frac{1}{3}F_1^s), \tag{3.1}$$

has a pressure dependent value of 2.8 (s.v.p.) to 5.8 (melting pressure =34.4 bar) times that of the ^{3}He mass m. Another important Fermi liquid correction is the modification of the magnetic susceptibility

$$\chi_N = \frac{\chi_{n0}}{1 + F_0^a}, \tag{3.2}$$

where χ_{n0} is the susceptibility of ^{3}He with only effective mass correction. For a detailed description of this theory and the other properties of liquid ^{3}He in its normal phase, the books of Wilks [1] and Pines/Nozières [2] may be consulted.

3.3 Superfluid ^{3}He

At a critical Temperature T_c, varying between 0.93 and 2.49 mK as a function of pressure, ^{3}He passes a phase transition to its superfluid states, unique in their richness. These states show a lot of analogies to superconductors, but also some important differences which makes ^{3}He even more fascinating. The term *superfluidity* has its origin in the property that mass currents can occur without friction, but numerous other properties can be observed in these states.

This section has the purpose of giving a short introduction to the essential properties of superfluid ^{3}He which will be necessary for an understanding of the results presented in the subsequent chapters. For a complete discussion of superfluid ^{3}He, see Ref. [3]. For an easier understanding, the subsections will be marked to explain whether they are more important for the understanding of the bolometric or the NMR-measurements.

3.3.1 Cooper pairing and order parameter

The key to the theory of conventional superconductivity is the formation of *Cooper pairs*, i.e. pairs of electrons (or more precisely quasiparticles) with opposite momentum $\vec{k}$ and spin projection σ: $\left(\vec{k}\uparrow, -\vec{k}\downarrow\right)$ which form due to a small attractive interaction, mediated indirectly by an electron-phonon coupling. These pairs have a total spin of S=0 and total orbital momentum L=0, which corresponds to the so-called s-wave pairing. The macroscopic coherence of the system can be described by an isotropic, scalar order parameter

$\psi(\vec{k}) = \Delta e^{i\phi}$ and the dispersion relation for the elementary excitations (the Bogoliubov quasiparticles) gets

$$E = \sqrt{\xi^2 + \Delta^2}, \tag{3.3}$$

where Δ is the temperature dependent gap parameter and $\xi = \hbar^2(k^2 - k_F^2)/2m^*$ is the kinetic energy of the excitation. The striking feature of this dispersion relation is the fact that no excitations with $E < \Delta$ exist, hence the name *gap*.

The same BCS theory can be applied to ^{3}He. In this case the Cooper pairs consist of ^{3}He quasiparticles as mentioned in section 3.2, but there is an important difference: due to its finite radius and the strong repulsive short range interaction, a pair wave function with L=0 is energetically unfavourable and the ^{3}He atoms can not condense in the singlet state. Unlike Cooper pairs in conventional superconductors, the ^{3}He pairs hence form p wave states, with $L = 1$ and $S = 1$, similarly to some unconventional superconductors. This has the effect that the ^{3}He Cooper pairs have an internal structure corresponding to the different values for L_z and S_z. The pair wave function of such a triplet can be decomposed in its different S_z projections:

$$|\psi(\vec{k}) >= \psi_{\uparrow\uparrow}(\vec{k})|\uparrow\uparrow> + \psi_{\downarrow\downarrow}(\vec{k})|\downarrow\downarrow> + \sqrt{2}\psi_{\uparrow\downarrow}(\vec{k})|\uparrow\downarrow + \downarrow\uparrow> . \tag{3.4}$$

Each of the components $\psi_{\alpha\beta}\left(\vec{k}\right)$ depends on the parameters pressure, magnetic field and temperature and represents the amplitude of the corresponding sub states α, β. It is useful to represent the relation between the sub states by the vector $\vec{d}$, defined by the following equation:

$$\psi(\vec{k}) = \begin{pmatrix} \psi_{\uparrow\uparrow}(\vec{k}) & \psi_{\uparrow\downarrow}(\vec{k}) \\ \psi_{\downarrow\uparrow}(\vec{k}) & \psi_{\downarrow\downarrow}(\vec{k}) \end{pmatrix} = \begin{pmatrix} -d_x(\vec{k}) + id_y(\vec{k}) & d_z(\vec{k}) \\ d_z(\vec{k}) & d_x(\vec{k}) + id_y(\vec{k}) \end{pmatrix}. \tag{3.5}$$

As the Cooper pairs form a spin triplet, the vector $\vec{d}(\vec{k})$ is a linear combination of the L=1 angular-momentum eigenstates $Y_{1m}(\hat{k})$. Equivalently, it can be represented as a linear combination of the components $\hat{k}_j$ of the unit vector $\hat{k}$:

$$d_\mu(\vec{k}) = \sum_j d_{\mu j}\hat{k}_j \; or \; \vec{d}(\vec{k}) = \mathbf{d}\vec{k}. \tag{3.6}$$

The so defined tensor quantity $\mathbf{d}$ with elements $d_{\mu j}$ is the proper order parameter, describing the superfluid states. A physical interpretation of the $\vec{d}$ vector is that it is perpendicular to the quantisation axis of the spin operator $\mathbf{S}$.

In the zero field limit, there are two different sets of order parameters which minimise the free internal energy, depending on pressure and temperature. These two phases are referred to as A- and B-phase, shown in the phase diagram fig. 3.1.

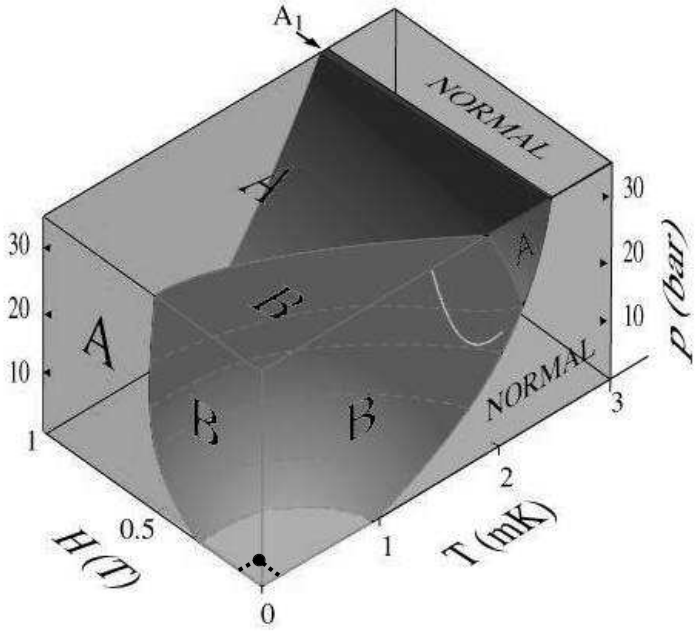

Figure 3.1: Phase Diagram of the superfluid phases of ^{3}He. At low magnetic fields, the B-phase occupies the largest part of the phase-diagram, with the A-phase only stable for high pressures and temperature close to T_c. Applying a magnetic field enlarges the zone in which the A-phase is stable. Additionally, in a small band close to T_c, the so-called A_1-phase appears.

B-phase

The B Phase which occupies at low magnetic fields the larger part of the phase diagram was first described by Balian and Werthamer in 1963 [4]. It turns out that this is the spherical symmetrical state which corresponds to a total angular momentum $\mathbf{J} = \mathbf{L} + \mathbf{S} = 0$, described by

$$d_{\mu j} = e^{i\phi}\Delta\delta_{\mu i}$$

such that the order parameter vector $\vec{d}$ gets

$$\vec{d}(\vec{k}) = e^{i\phi}\Delta\hat{k}.$$

This state has the feature that the gap is isotropic. Consequently it is in a lot of characteristics similar to superconductors with s-wave pairing, for example concerning the temperature dependence of the heat capacity.

The state is degenerate with the class of states formed by multiplying with a constant phase factor and by a relative rotation of spin and orbital space thus the general form of the B-phase order parameter has the elements

$$d_{\mu j} = \Delta e^{i\phi} R_{\mu j}, \tag{3.7}$$

where $R_{\mu j}$ are the elements of the rotation matrix around an axis $\hat{n}$ about an angle θ, implying $\vec{d}(\vec{k}) = \Delta e^{i\phi}\mathbf{R}\hat{k}$.

A-phase

For high pressures close to T_c, a second phase is stable, due to the higher order corrections of the strong coupling regime. The superfluid A-Phase, described by Anderson, Brinkmann and Morel (ABM) [5, 6] is a state of equal spin pairing (ESP), i.e. that the off diagonal elements of the matrix in eq. 3.5 and hence the amplitude of the $S_z = 0$ state gets 0. The order parameter of this axially anisotropic state is given by

$$d_{\mu j} = \Delta_{\mu j}\hat{d}_\mu(\hat{m}_j + i\hat{n}_j), \tag{3.8}$$

$$\vec{d}(\vec{k}) = \Delta_0\hat{d}(\hat{k}\hat{m} + i\hat{k}\hat{n}). \tag{3.9}$$

The tensor $d_{\mu j}$ is in this case of separable form in spin and orbital phase, with a single, i.e. $\vec{k}$ independent preferred direction $\hat{d}$ in spin space and $\hat{m}$, $\hat{n}$ in orbital space. The anisotropic gap parameter then has the form

$$\Delta(\hat{k}) = \Delta_0\sqrt{1 - (\hat{k}\cdot\hat{l})^2} = \Delta_0 * \sin(\theta), \tag{3.10}$$

where $\hat{l} = \hat{m} \times \hat{n}$ is a third preferred direction in orbital space. Note that the gap vanishes for $\theta = 0$, the gap thus has nodes in the direction of the $\hat{l}$ vector, a feature which manifests itself for example in the heat capacity calculations.

For completeness the A_1-phase should be mentioned. In non-zero magnetic field, the pairing energy for spin up and spin down pairs is slightly different. This means that there exists a small temperature range between the A- and the normal phase in which the condensation of only spin-up pairs occurs.

3.3.2 Orientation of the order parameter

Both phases presented in the previous section correspond to macroscopically ordered states, but they are still degenerate. We know for example that there exists a preferred axis $\hat{l}$ in the A-phase, but without considering further interactions, the system is degenerate with respect to a rotation of the total system. In this subsection we will see the most important contributions lifting (some of) the persisting symmetries. The corresponding interactions, either external like the magnetic field or internal like the dipole-dipole interaction are quite small compared to the gap and can thus be neglected for the pair forming mechanism itself. This section is thus mainly important for explaining the NMR measurements in Part III, but some unreproducible results between different demagnetisation runs for the bolometric measurements might have their origin in randomly created textures too.

Dipole interaction

The nuclear dipole interaction is in principle a quite weak interaction, and it came as a surprise when it proved to be a dominant part in the orientation of the order parameter. In the normal phase, the magnetic spins are oriented arbitrarily. Due to the different orientation, the interaction of one spin with its surrounding then sums up to zero, making it a negligible term. In the superfluid phases on the other hand, we have to deal with a quantum coherent state, which shows long range order. In this configuration, the interaction with the surroundings sums up and gives an important contribution to the free energy.

The nuclear dipole interaction is responsible for a coupling of the spin- and the orbital space as can be seen from the Hamiltonian:

$$H_D = \frac{1}{2}(\gamma\hbar)^2 \int d^3r \int d^3r' \left\{ \frac{\vec{\sigma}(\vec{r}) \cdot \vec{\sigma}(\vec{r'})}{|\vec{r} - \vec{r'}|^3} - 3\frac{[(\vec{r} - \vec{r'}) \cdot \vec{\sigma}(\vec{r})]\,[(\vec{r} - \vec{r'}) \cdot \vec{\sigma}(\vec{r'})]}{|\vec{r} - \vec{r'}|^5} \right\}. \tag{3.11}$$

The corresponding change in free energy can be calculated and amounts to

$$\Delta f_D^A = -\frac{3}{5} g_D(T)(\hat{d} \cdot \hat{l})^2 \tag{3.12}$$

for the A phase and

$$\Delta f_D^B = \frac{8}{5} g_D(T)(\cos\theta + \frac{1}{4})^2 \tag{3.13}$$

for the B phase. Here, $g_D(T) = \lambda_D N_F \Delta^2(T)$ is the temperature dependent dipole coupling constant, with $\lambda_D \approx 0.5 \cdot 10^{-6}$ the dipole coupling parameter and N_F the density of states. θ is the angle describing the rotation $\mathbf{R}(\hat{n}, \theta)$ (see eq. 3.7).

By minimising the free energy, it can be seen that the dipole interaction tends to align the $\hat{d}$ and the $\hat{l}$ vector in the A phase. In the B phase the free energy is minimised if the relative angle between spin and orbital space has a value of $\theta_L = \arccos(-1/4) \approx 104°$, where θ_L is called Leggett angle. Note that this result is independent of the orientation of $\hat{n}$, a result which is only valid in the zero field limit.

Magnetic field orientation

In general the magnetic energy density can be expressed as

$$\Delta f_H = -\frac{1}{2}\sum_{\mu\nu}\chi_{\mu\nu}H_\mu H_\nu \tag{3.14}$$

and therefore depends on the orientation of the susceptibility tensor $\chi_{\mu\nu}$ and hence on the order parameter itself. In the A-Phase the spin susceptibility is given by

$$\chi_{\mu\nu} = \chi_N\delta_{\mu\nu} - \Delta\chi\hat{d}_\mu\hat{d}_\nu \tag{3.15}$$

where $\Delta\chi$ is a temperature dependent anisotropy coefficient. The A-Phase free energy contribution writes

$$\Delta f_H^A = \frac{1}{2}\Delta\chi(\hat{d}\cdot\vec{H})^2 \tag{3.16}$$

and consequently leads to a preferred orientation of the $\hat{d}$-vector perpendicular to the field.

In the B-phase there is no orientation of the order parameter due to the magnetic field, because the magnetic susceptibility is isotropic in orbital space. Nevertheless there is a small orientational effect due to the dipole interaction, leading to the (temperature independent) free energy

$$\Delta f_H^B = -\frac{5}{12}\lambda_D N_F\left(\frac{\gamma\hbar}{1+F_0^a}\right)^2(\hat{n}\cdot\vec{H})^2 \tag{3.17}$$

which aligns the $\hat{n}$ vector with the magnetic field.

Surface energies

In a real experiment, the ^{3}He will always be in a cell of finite size, whose surfaces will interact with the ^{3}He. In general, the interaction of the atoms of a liquid with a surface (for example with a solid wall, a free surface or an interface between different phases) is a complicated subject, nevertheless the overall orientational effect is well established. Its basic effect is that the longitudinal component (i.e. parallel to the surface vector $\hat{s}$) of the order parameter $d_\mu^\perp = \sum_j \hat{s}_j d_{\mu j}$ falls off more rapidly than the transverse components as the surface is approached. This is intuitively plausible as close to a wall, the cooper pairs should tend to orbit in a plane parallel to the surface. Note that it is in principle also possible that the surfaces act directly on the spin part of the order parameter. This

is the case if the surface itself has magnetic properties and when spin-flip interactions are possible. In our experiments, we took care to cover the surfaces with ^{4}He, which is non-magnetic, so that we will not consider this interaction here.

As the surface potential changes on the order of a few inter particle distances, this interaction happens only on a microscopic scale. However, due to the rigidity of the order parameter, its influence on the order parameter will have an effect on a much larger scale, determined by the so called healing length ξ_h. In other words, the magnitude of the order parameter will recover its bulk value on a distance on the order of the coherence length $\xi(T)$, but the orientation of the order parameter will be influenced on a much larger scale ξ_h.

In the A phase, where the order parameter is anisotropic and has nodes, it is easy for the superfluid to avoid having a longitudinal component at the surface by simply orienting the vector $\hat{l}$ orthogonal to the surface. Orienting the $\hat{l}$ vector in this way might be unfavourable when considering other contributions like the dipole and the magnetic field orientation, but a calculation shows that the corresponding gain in energy is always much larger than the bending energy. At the surface, $\hat{l}$ is thus rigidly oriented.

In the pseudo-isotropic B-phase, the situation is a good deal more complex, but with a variational ansatz one gets the result, that the rotation angle θ stays at its bulk value $\theta_L = 104°$. On the other hand the orientation of the rotation axis $\hat{n}$ will be modified. By just looking at the surface dipole energy, one finds that the surface tends to align $\hat{n}$ parallel to $\hat{s}$. However, as the anisotropy introduced by the wall will effect the orientational energy of the magnetic field, this holds not true for external magnetic fields $H \gg H_s \approx 2.5\,\mathrm{mT}$. In this case two limiting cases can be considered: For $\vec{H} \| \hat{s}$ the surface still tends to align $\hat{n}$ and $\hat{s}$. For $\vec{H} \perp \hat{s}$, i.e. $\vec{H}$ in the plane, $\hat{n}$ is oriented such that a spin-orbit rotation by the Leggett angle θ_L about $\hat{n}$ takes $\hat{s}$ into $\hat{H}$. For $\hat{s} = (0,0,1)$ and $\hat{H} = (1,0,0)$ this is achieved when $\hat{n} = \pm(\frac{1}{5})^{1/2} \cdot (1, 3^{1/2}, \pm 1)$. This means that the vector $\hat{n}$ forms an angle of $\cos^{-1}(\frac{1}{5})^{1/2} = 63.4°$ with both, the $\hat{s}$ and the $\hat{H}$ vector.

This abstract result has a clear physical meaning if we consider the average orbital momentum $\bar{\mathbf{L}} = \mathbf{R}(\hat{n}, \theta)\bar{\mathbf{S}}$. By this parameter $\bar{\mathbf{L}}$ is exactly parallel to $\hat{s}$, meaning that the Cooper pairs prefer to rotate in the plain parallel to the surface.

Anisotropic aerogel

The last years, high porosity aerogel has been used to introduce disorder in the otherwise 100 % pure system of ^{3}He. An Aerogel is a "tangle" consisting of Si_2O strands, where the diameter of the strands is about 30 Å, i.e. much smaller than the coherence length, and where the distribution of the strands is random. The tangle thus forms a fractal, which, on a macroscopic scale, is isotropic. Consequently the system "Aerogel + liquid ^{3}He" is usually used to study the influence of "impurities" on superfluidity with non-trivial BCS-pairing. The novelty of the experiment presented in part III of this thesis is the squeezing of this aerogel in the radial direction, which hence introduces another preferred direction in orbital space. The exact nature of the superfluid phases appearing in the presence of aerogel is still disputed, but a large body of evidence points towards the conclusion that

they are principally the same as in the case of pure ^{3}He. The following explanation is based on a very recent theory proposed by Volovik [7, 8], and while it seems that it is a rather robust idea, it should be kept in mind that future development might impose some modifications.

Estimations show that for the A-phase, already a compression of about 0.1 % is sufficient to make the aerogel the dominant factor in the alignment of $\hat{l}$. In the radially compressed cell, this leads to the $\hat{l}$ vector being perpendicular to the cylinder axis.

While it is natural that the anisotropic A-phase is influenced by such a random and regular anisotropy of the aerogel strings, at first glance such an alignment is not expected for the B-phase. However, due to the spin orbit coupling, a magnetic field which tends to align the spin system will also influence the orbital part. The gap in the quasiparticle spectrum then becomes anisotropic, being smaller along the $\hat{l}$ axis, which is connected to the spin direction $\hat{s}$ by the order parameter matrix: $\hat{l}_i = R_{\alpha i}\hat{s}_\alpha$. The magnitude of the gap distortion is determined by the Larmor frequency and increases with increasing field: $\Delta_\perp^2 - \Delta_\parallel^2 \sim \omega_L^2$ (see Ref. [9] and references therein). Thus, in the applied magnetic field, the aerogel anisotropies do influence the orientation of the order parameter. However, the orientational effect is by a factor $\omega_L^2/\Delta_\perp^2$ weaker than in the gapless ^{3}He-A, where $\Delta_\parallel = 0$. Correspondingly, the Larkin-Imry-Ma (LIM) length at which the orientational order is destroyed by random anisotropy and which is about $1\,\mu$m in ^{3}He-A [7], is by a factor $\Delta_\perp^4/\omega_L^4$ larger in ^{3}He-B. In typical NMR experiments in ^{3}He-B with $\omega_L \sim 1\,$MHz, the LIM scale essentially exceeds the sample size, and thus the *random, local* anisotropy practically has no effect on the orientation of $\hat{l}$.

However the *regular, global* anisotropy produced by the deformation of aerogel may orient $\hat{l}$ globally. In a simple model, applicable for the description of the orientational effect of the aerogel on the order parameter in ^{3}He [7], aerogel is considered as a system of randomly oriented cylinders of diameter $\delta \sim 3\,$nm and length $\xi_a \sim 20\,$nm which corresponds to the diameter of and the distance between the silica strands. Applying the theory of Rainer and Vuorio [10] for a microscopic body with the size $\delta \ll \xi_0$, where ξ_0 is the superfluid coherence length, one obtains an estimate for the energy density of the interaction between $\hat{l}$ and the global uni-axial deformation along the axis $\hat{\nu}$ both, in ^{3}He-B in magnetic field and in ^{3}He-A:

$$\Delta f_{AN} = C\left(\hat{l}\cdot\hat{\nu}\right)^2 \ , \quad C \sim N_F\left(\Delta_\perp^2 - \Delta_\parallel^2\right)\frac{\Delta l}{l}\frac{\xi_0\delta}{\xi_a^2}. \tag{3.18}$$

Here $\Delta l/l$ is the relative change of the length of the aerogel sample, or otherwise said, the compression factor. For a typical sample of cylindrical shape, squeezing ($\Delta l < 0$) produces a preferred anisotropy axis for $\hat{l}$ parallel to the cylinder axis, as observed in Ref. [11] for ^{3}He-A. Stretching ($\Delta l > 0$) should give a preferred plane, perpendicular to the cylinder axis. In ^{3}He-B this energy is rather small, but it may compete with the dipole-dipole coupling between $\hat{l}$ and $\hat{s}$. The dipole interaction $E_d \sim N_F\Omega_L^2$ can be expressed in terms of the Leggett frequency Ω_L, which is linked to the NMR frequency shift from the Larmor value caused by this dipole interaction. The global anisotropy of aerogel is dominant if

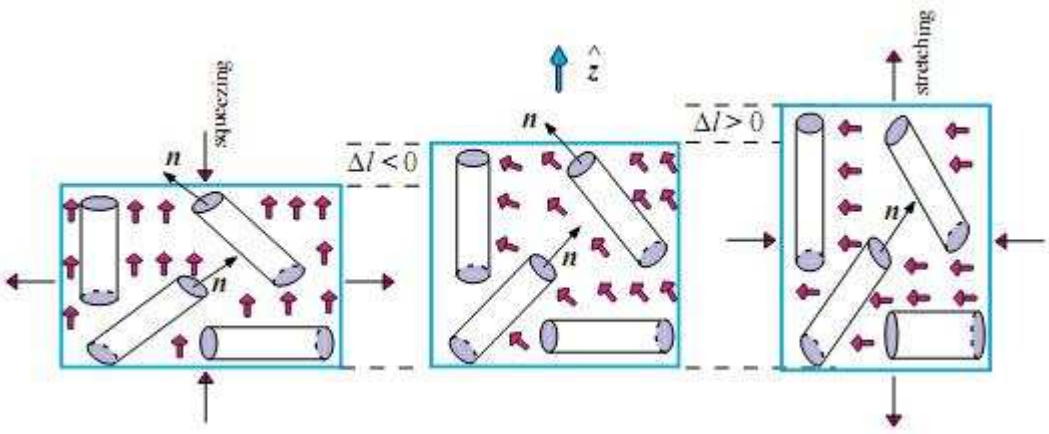

Figure 3.2: Illustration of uni-axial deformation of a sample of aerogel, using the randomly oriented cylinder model. Squeezing (stretching) of the aerogel cylinder along its axis $\hat{z}$ leads to global anisotropy for $\hat{l}$ with preferred axis along $\hat{z}$ (in the plane normal to $\hat{z}$). Figure from Volovik [7].

$$\frac{\Delta l}{l} > \frac{\xi_a^2}{\xi_0 \delta} \frac{\Omega_L^2}{\omega_L^2}. \tag{3.19}$$

With $\xi_0 \sim \xi_a$, $\delta \sim 0.1\,\xi_a$, $\omega_L \sim 1\,\mathrm{MHz}$ and $\Omega_L \sim 100\,\mathrm{kHz}$, this estimation states that squeezing or stretching the aerogel sample by about 10 % should lead to the global orientation of the order parameter, even in the B-phase.

To reformulate the above in more figurative terms, one can imagine that an aerogel consists of a lot of small "surfaces" and at each surface the orbital momentum prefers to be orthogonal to this surface. In the isotropic case, the different surface orientations are random, and no long range order is introduced. Deforming the sample will then lead to a mean orientation of these microscopic surfaces, introducing a new preferred direction in orbital space.

Counterflow

Even if it is not of importance for this thesis, let us mention for completeness another contribution to the free energy, the effect of superflow. A superflow will generally have an impact on the orbital part of the wave function. For the A-phase which has an intrinsic orbital anisotropy this leads to an alignment of $\hat{l}$ with the superfluid velocity $\vec{v}_s$. In the B-phase, the orientational effect depends on the presence of electric and magnetic fields, and has several concurrent terms, such that a general statement for the effect on the order parameter can not be given. Anyway, the corresponding energy is quite small, such that due to the gradient energy, the order parameter will only change on a long distance (order of mm). The counterflow influence is mainly studied in rotating cryostat experiments, where a circular counterflow can be induced by rotating the whole experiment.

The gradient free energy

We have seen contributions which will orient the order parameter, and we have seen that sometimes those contributions are in competition. For instance, let us consider a wall with a magnetic field perpendicular to this wall. In the A-Phase, the $\hat{l}$ vector wants to be perpendicular to the surface, but at the same time perpendicular to the magnetic field. The result is that close to the wall $\hat{l}$ will be perpendicular to the surface, as the surface energy is dominant, and then rotate smoothly until it gets to its bulk value at a certain distance. Such a bending of the order parameter is related to a free energy which is given by the following term:

$$f_{grad} = \frac{1}{2}(\frac{1}{5}N_F\xi_0^2)\sum_{jl\mu}(\nabla_j d_{\mu l})(\nabla_j d^*_{\mu l}) + (\nabla_j d_{\mu l})(\nabla_l d^*_{\mu j}) + (\nabla_j d_{\mu j})(\nabla_l d^*_{\mu l}). \tag{3.20}$$

The term $(\frac{1}{5}N_F\xi_0^2)$ represents the stiffness of the order parameter. The result of the gradient energy is, as already mentioned above, that it is energetically unfavourable for the order parameter to change on very small distances. Hence, in presence of different favourable conditions in different places in the cell, the order parameter will change (more or less) smoothly, and one gets a spatial *texture* for the order parameter.

3.3.3 Thermodynamic properties of ^{3}He-B

In this section we concentrate on the thermodynamic properties of ^{3}He -B, which are necessary to explain the observed phenomena in the bolometric measurements.

Superfluid gap

At zero magnetic field, ^{3}He-B has an isotropic gap, as obtained by the BCS-theory. It is temperature dependent, but at low temperatures $T < 0.4\,T_C$, it has a constant value of

$$\Delta_{BCS}(0) = 1.76\,k_B T_c. \tag{3.21}$$

While this value is well verified by experiments at low pressures, at high pressures a correction has to be applied. The hypothesis of weak coupling, which is necessary to obtain the equation above, is no longer verified at higher pressures. According to Rainer and Serene [12] the strong coupling terms appearing at high pressures can be taken into account by the introduction of the temperature independent strong coupling term κ

$$\Delta(p) = \kappa(p)^{-1/2}\Delta_{BCS}. \tag{3.22}$$

Experimentally it has been shown that κ^{-1} varies almost linearly between 1.03 and 1.3 between 0 bar and the melting pressure [13].

No analytic solution for the temperature dependence of the gap exists, but close to T_C it can be approximated by

$$\Delta(T \to T_c) \approx 1.74\,\Delta_0 \left(1 - \frac{T}{T_c}\right)^{1/2}. \tag{3.23}$$

Two fluid model

The superfluid phase transition is a second order phase transition, meaning that the order parameter is zero above T_c and then gradually reaches its low temperature value when temperature is decreasing. A model taking into account this gradual appearance and succeeding to explain a remarkably large number of phenomena is the two fluid model. In this model the fluid is described as a mixture of a *normal* fluid of density ρ_n, having the properties of the ^{3}He liquid above T_c, and a *superfluid* liquid of density $\rho_s = \rho - \rho_n$, having zero entropy.

For the superfluid B-phase, the temperature dependence of the normal fraction is given by [14]:

$$\frac{\rho_n}{\rho} = \frac{\left(1 + \frac{1}{3}F_1^s\right) Y_0(T)}{1 + \frac{1}{3}F_1^s Y_0(T)}, \tag{3.24}$$

where

$$Y_n\left(\frac{\Delta}{k_B T}\right) = \frac{1}{2}\int_0^\infty \left(\frac{x}{\xi}\right)^n \frac{dx}{\cosh^2\left(\frac{\xi}{2}\right)} \tag{3.25}$$

is the Yosida function of order n, with $\xi = \sqrt{x^2 + (\Delta/k_B T)^2}$. This two fluid model explains for example quite simply why the observed NMR-frequency shift has a temperature dependence, by claiming that the fraction of the liquid which is superfluid changes. Similarly, other thermodynamic and transport properties can be obtained using the two fluid model.

Heat capacity

Near T_c, one of the clearest signatures of the superfluid phase transition is the jump in the specific heat. For the normal-B phase transition, the BCS theory with strong coupling corrections predicts a jump of

$$\frac{\Delta C}{C_N} = 1.43\,\kappa^{-1}. \tag{3.26}$$

Measuring this jump thus allows measuring directly the value of the strong coupling constant κ, as the deviation of this jump from the weak coupling BCS value.

The temperature dependent value in ^{3}He-B is most easily calculated from the entropy equation, which leads to

$$C = -\frac{2}{T}\sum_k \frac{\partial n}{\partial E}\left(E^2 - \frac{1}{2}T\frac{\partial}{\partial T}\Delta^2\right), \tag{3.27}$$

where, in the zero field limit, E and Δ are linked through the dispersion relation eq. 3.3 and the summation over the spin substates is already done.

For the bolometric measurements, we are mainly interested in the low temperature limit of the heat capacity. In this region, the heat capacity is dominated by the Bogoliubov quasi-particle excitations. For $T \ll \Delta/k_B$, the Fermi-Dirac distribution n can be very well approximated by the Boltzmann statistic. Additionally, the second term in eq. 3.27 gets negligible as the gap is almost constant below $0.4\,T_c$. In the low temperature limit $T \to 0$, the heat capacity drops exponentially to zero because of the presence of an isotropic gap. The heat capacity thus gets

$$C = \sqrt{2\pi} N_F k_B \Delta \left(\frac{\Delta}{k_B T}\right)^{3/2} \exp\left(-\frac{\Delta}{k_B T}\right) \left[1 + \frac{21}{16}\frac{k_B T}{\Delta}\right], \tag{3.28}$$

where N_F represents the density of states at the Fermi surface. The corrective term of $(21/16)(k_B T/\Delta)$, does not vary much over the temperature range of interest ($0.13\,T_c < T < 0.18\,T_c$) and introduces thus an almost constant correction of about 10 %. At zero pressure and in the zero field limit, the specific heat approximates to

$$C \approx C_0 \left(\frac{T_c}{T}\right)^{\frac{3}{2}} \exp\left(-\frac{\Delta}{k_B T}\right), \tag{3.29}$$

with $C_0 = 2.07\,\mathrm{mJ\,K^{-1}cm^{-3}}$.

An interesting value is the total enthalpy as counted from the absolute zero. It can be obtained by integration of eq. 3.28 as

$$U = \sqrt{2\pi} N_F \Delta^2 \left(\frac{k_B T}{\Delta}\right)^{1/2} \exp\left(-\frac{\Delta}{k_B T}\right) \left[1 + \frac{13}{16}\frac{k_B T}{\Delta}\right], \tag{3.30}$$

which approximates at zero pressure to

$$U \approx U_0 \left(\frac{T}{T_c}\right)^{\frac{1}{2}} \exp\left(-\frac{\Delta}{k_B T}\right), \tag{3.31}$$

with $U_0 = 1.05\,\mu\mathrm{J\,cm^{-3}}$.

To get an idea for the order of magnitude: the box size of $0.13\,\mathrm{cm}^3$ used in the current experiment implies that at a typical working point of $130\,\mu$K the total enthalpy amounts to $U \approx 820\,\mathrm{keV}$, which is close to the energy deposited by a neutron capture event and only ten times more than a typical muon event.

Chapter 4

Cosmology and Dark Matter

This thesis inscribes itself in the ULTIMA project (Ultra Low Temperature Instrumentation for Measurements in Astrophysics), a project whose long term goal is to construct a particle detector based on superfluid ^{3}He bolometry, able to be used for direct dark matter search. The first tests of ^{3}He as a sensitive matter for elementary particle detection were done in Lancaster [15, 16] and Grenoble [17]. A detailed discussion of the principal advantages of using ^{3}He as a sensitive medium as well as its potential sensitivity to dark matter has already been presented a few years ago in the frame of the MACHe3 project (MAtrix of Cells of Helium3) [18, 19, 20], the predecessor of ULTIMA. The main focus of this theoretical work laid on the sensitivity to the so-called *neutralino*. This particle is predicted by the supersymmetric extension of the standard model, and is a promising candidate for dark matter. As supersymmetric calculations are a subject on their own, and the work done during this thesis concerns only the experimental aspects of a superfluid ^{3}He detector, this chapter will be limited to show briefly the general idea behind the search for dark matter and the main observational evidence for its existence, a short presentation of the supersymmetric theory, finally the predicted interaction between neutralinos and ^{3}He and the resulting requests for a future detector.

4.1 The missing mass of the universe

The results of observational cosmology seem to converge towards a Big Bang scenario with inflation. It describes the universe as a system which evolves, starting from a primordial singularity existing about $1.4 \cdot 10^{10}$ years ago. This model is based on the discovery of the Hubble law, the experiments on the diffuse cosmological radiation at 3 K (CMB, Cosmic Microwave Background) [21], the primordial nucleosynthesis (BBN, Big Bang Nucleosynthesis) [22] and the large scale structures of the present-day universe [23].

When Einstein presented his theory of general relativity in 1915 to give a framework for gravity compatible with the equations of the theory of special relativity, Friedmann, Lemaitre, Robertson and Walker proposed a solution which is still the standard model of cosmology. The assumption of a universe with completely isotropic distribution of matter

and radiation, added to the assumption of conserved energy lead to the Friedmann equation (see for example ref. [24]):

$$\left(\frac{\dot{R}}{R}\right)^2 = \frac{8\pi G\rho}{3} - \frac{Kc^2}{R^2} \tag{4.1}$$

where R is the parameter describing the spatial expansion of the universe, G the gravitational constant, c the speed of light and ρ the total energy density. The coefficient K is the curvature of the four-dimensional universe and can take the discrete values

$K = -1$: Open universe $K = 0$: Flat universe $K = 1$: Closed universe

The current measurements of the Hubble parameter $H(t) = \dot{R}(t)/R(t)$ show that a flat universe would be realised for a critical density $\rho_c = 5.1\,\mathrm{GeVm}^{-3}$ [23].

Without entering in the details of the effect on the evolution of the universe connected with the different values of the constants above, the crucial role of the average energy density appears clearly. This energy is in general composed of different contributions:

$$\rho = \rho_r + \rho_m + \rho_\Lambda$$

with

ρ_m: energy density of matter. This part includes the contribution from baryonic[1] (ordinary) matter ρ_B, whose value can be obtained from the primordial nucleosynthesis and the non baryonic matter, which can be estimated by comparing ρ_m and ρ_b.

ρ_r: energy density of radiation. This part can be obtained by the measurement of the diffuse background radiation. The measurements show that this term is much smaller than the energy density of matter and can thus be generally neglected.

ρ_Λ: this is a term which was originally added *ad hoc* by Einstein, in order to be able to introduce a cosmological constant $\Lambda = 8\pi G_N \rho_\Lambda$. Einstein used this term to "stabilise" the universe. After Hubble's discovery of the redshift of far away galaxies, leading to the conclusion that the universe is in expansion, Einstein considered this term as his biggest mistake. In the last years, this term saw a revival as it allows to describe the presence of a gravitational repulsive "dark energy" which could explain new measurements on supernovae that indicate that the expansion of the universe is accelerating.

[1] Baryons are hadronic fermions, like the neutron or the proton. So this part corresponds to the "normal" mass, like it is known from atoms.

The most recent measurements of the fluctuation of the Cosmic Microwave Background (CMB) made by the collaboration WMAP and the measurements of the spectral density of supernovae suggest that ρ is extremely close to ρ_c. In terms of the relative density $\Omega = \rho/\rho_c$ one obtains:

$$\Omega_r + \Omega_m + \Omega_\Lambda = 1.02 \pm 0.02$$

with $\Omega_m \approx 0.28$ and $\Omega_\Lambda \approx 0.74$. A flat universe would thus be compatible with the observations.

Up to now, no assumptions were made on the nature of the term Ω_m, and the natural idea would be to assume that it is simply "ordinary" baryonic matter. But a large body of observational evidence indicate that baryonic matter represents only a small part of total matter. Amongst the various evidences the following points can be listed:

- The most direct and compelling evidence comes from the rotational speed of galaxy clusters. Its radial distribution, observed experimentally can be compared to what one would expect by applying the virial theorem. Using this method for galaxies in the Coma cluster, Zwicky was the first to notice in 1933 that the measured rotation speed can only be explained when the total mass was much larger than what is observed for the luminous mass. Later, the same observation was made for the rotational speed of single spiral galaxies (fig. 4.1 [25]). Instead of showing a reduction of the velocity for stars far from the galaxy centre, as expected from Newton dynamics, the rotation curve is rather flat.

- The cosmic microwave background (CMB) is the light which was emitted after the so called recombination, happening some 400,000 years after the Big-Bang. Before this recombination, the universe was still hot enough so that electrons were ionised and photons could not propagate. After this phase transition, during which electrons combined with protons to form hydrogen atoms, the universe got transparent at a temperature of 3000 K. The corresponding (almost perfect) blackbody radiation can be observed today with a redshift due to expansion of about $z_* = 10^3$. To a high degree of about 10^{-5} this radiation is isotropic, but precise measurements, first by the COBE satellite and more recently by the WMAP collaboration succeeded to measure the anisotropy of this background radiation. A multipole development of these anisotropies shows several *acoustic peaks* which contain interesting physical signatures. The angular scale of the first peak determines the curvature of the Universe (but not the topology of the Universe). The second peak – truly the ratio of the odd peaks to the even peaks – determines the reduced baryon density. The third peak can be used to extract information about the dark matter density.

- One of the predictions of Albert Einstein's general relativity is the effect of *gravitational lensing.* This effect manifests itself when the light from a very distant, bright source (such as a quasar) is "bent" around a massive object (such as a massive galaxy) which is located between the source object and the observer. The magnitude of this bending is given by the mass of the lensing object. By measuring this effect for a

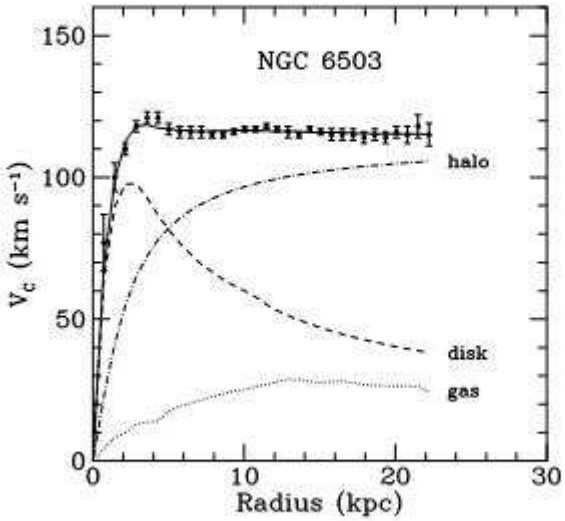

Figure 4.1: Rotation curve of galaxy NGC 6503. Especially for large distances from the rotation centre, the observed velocities can not be explained by only considering ordinary matter. From Ref. [25].

large number of distant galaxies and taking an average, the background distribution of dark matter can be reconstructed.

- The formation of structures like stars, galaxies and galaxy clusters from the almost homogeneous primordial universe is more easily explained when postulating the existence of dark matter: at the moment of structure formation, ordinary baryonic matter was still too hot, and thus had a too high pressure left over from the big-bang to collapse and form structures like stars. Adding something like cold dark matter, this scenario can be saved as the dark matter can act as a "compactor" of structures. Large computer simulations have been conducted, confirming that such a model could explain the present day galactic structures.

Combining these different observations, it can be concluded that Ω_m itself can be split up further: The total mass of baryons (estimated by the most favoured scenario of primordial nucleosynthesis) delivers a term $\Omega_b = 0.045 \pm 0.005$. This means that it can explain only 15% of the energy density of matter. So more than 80% of matter seems to consist of non-baryonic "dark-matter".

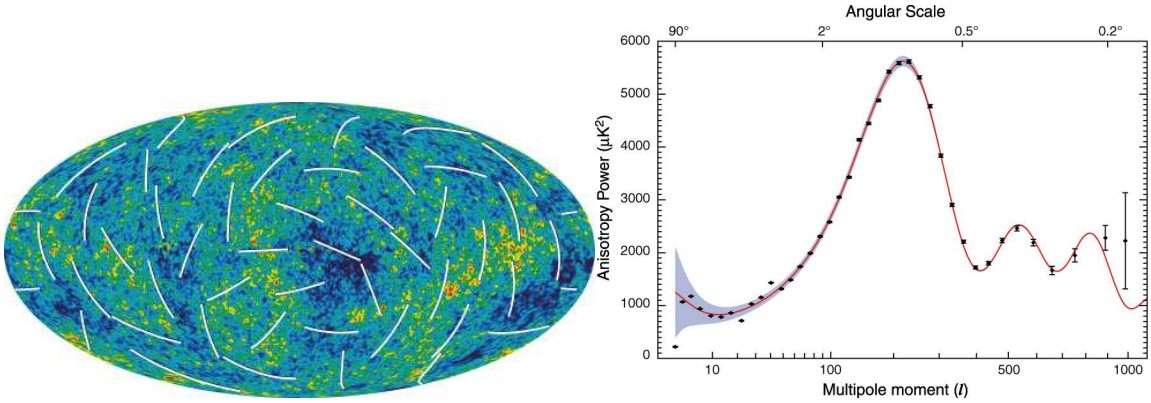

Figure 4.2: WMAP results a) Anisotropies of the microwave sky. Colours indicate warmer (red) and cooler (blue) spots. White lines indicate "polarisation" directions of the oldest light.
b) The multipole development of the anisotropy. A relatively simple model with only 6 parameters exists to explain the shape. By the fit, information on parameters like the curvature of the universe, the baryonic- and the dark matter density can be obtained. (From http://map.gsfc.nasa.gov/m_mm.html).

4.2 The neutralino and possibilities of detection

Particle physicists have many ideas about what dark matter could be made of. Some of the early candidates, like for example the *Massive astrophysical compact halo objects* (MACHO) and *neutrinos* have been proved to exist, but experimental evidence shows that they do not exist in sufficient abundance to represent a substantial fraction of dark matter. A very short list of the remaining favoured candidates include [26]:

- *Axions* [27] were introduced as a solution to the CP violation problem in particle physics. Laboratory experiments, the dynamics of supernova 1987A and stellar cooling show that axions would be very light ($<0.01\,\mathrm{eV}$). Exact calculations for its relic density are very uncertain, but a parameter space satisfying all present day measurements exists and make Axions a viable dark matter candidate.

- *Kaluza-Klein* (KK) particles [28], are excitations of Standard Model fields which appear when introducing additional universal dimensions. The initial idea of Kaluza in 1921 introducing extra dimensions was to unify electromagnetism with gravity by identifying the extra components of the metric tensor with the usual gauge fields. Later, it has been worked out that this model could be used to solve the hierarchy problem. The lightest Kaluza-Klein particle (LKP) is likely to be associated with the first KK excitation of the photon. Estimations considering that the LKP is responsible for the main part of dark matter give values for its mass in the range of 400 to 1200 GeV.

- *light bosonic particles* [29]: If only considering fermionic dark matter candidates with standard Fermi interactions, a lower bound of a few GeV can be found for such

particles. If however dark matter is made of another type of particle, this limit does not apply, and 1-100 MeV scalar candidates have been proposed. The motivation for such a particle lies in the possibility to explain a 511 keV gamma-ray line, observed by the INTEGRAL satellite. This radiation could be created by such light dark matter particles annihilating. As alternative explanation for this gamma line exist, further tests are needed.

- Weakly Interacting Massive Particle (*WIMP*) is the general term for particles which are massive and neutral in charge and in colour. This means that they do not interact by electromagnetism neither by the strong force. With the weak nuclear force and gravity being the only possibilities for interactions, the cross-sections with ordinary matter can be expected to be very small, explaining why no such particle has been found yet. Because of their large mass, their velocity can be expected to be relatively small and these particles should therefore be cold. With the assumption that there does not exist an additional "fifth" force, which would be important for those WIMPs, but which baryons would be insensitive to, interactions between WIMPs should be very rare too. Consequently, they are supposed to form a ballistic gas.
  In the Standard Model, there exists no particle which has all these properties. In order to find a viable WIMP, and hence a dark matter candidate, models beyond the Standard Model need thus to be considered. One of the most promising WIMP candidates is the so-called *neutralino*. The neutralino $\tilde{\chi}$ is a massive particle predicted by the supersymmetric extension of the standard model in particle physics (SUSY) [30]. To be precise, it is the Lightest Supersymmetric Particle (LSP), arising from the Minimal Supersymmetric Standard Model (MSSM). It would be a neutral fermion with a mass of about a hundred GeV. While the sensitivity of our detector would not be limited to neutralinos, this is the main candidate our development is aimed at.

The presented candidates are "favourite" models because they are motivated independently from the need for dark matter candidates and they arise from relatively simple, elegant ideas. Many other models, predicting more exotic particles would be compatible with the set of the present-day experimental observations. Note that in theory, nothing states that one sort of particles has to be responsible for all of dark matter, but in principle it is possible that dark matter is made of different constituents, which in turn would make it more difficult to detect either of them.

4.2.1 Supersymmetry

It would be impossible to review the theory of Supersymmetry (SUSY) in a few pages, especially as there exists not only one supersymmetric model, but a set of different models based on varying assumptions. Additionally, each model is described by a huge number of free parameters, mainly mixing angles and masses. In order to get a workable model, usable for phenomenological studies, theorists make (well motivated) guesses on most of

the parameters. Such a set of guessed parameters together with the corresponding model is then called a scenario.

The basic motivation for SUSY comes from the observation that in the Standard Model there is a fundamental difference between fermions and bosons: the former are mediators of interactions and the latter the constituents of matter. The question is then whether a symmetry exists which relates them and which could deliver a "unified" picture of matter and interaction. Otherwise formulated, the question is whether a Lie group exists which relates space-time (Lorentz) and internal (Isospin, *etc.*) symmetries.

Another major motivation arises from the *hierarchy problem*, which is linked to the enormous difference between the electroweak and the Planck energy scale, or otherwise said to the question why the Higgs boson is so much lighter than the Planck mass. One would expect that the large quantum contributions to the Higgs mass would inevitably result in a huge diverging mass, which would destroy the stability of the electroweak scale. Through the introduction of new particles proposed by SUSY models, the Higgs mass would be "protected" from the divergent part in the quantum corrections in an elegant way: to each virtual fermionic loop can now be associated a bosonic loop with same amplitude but opposite sign, cancelling out the divergence.

In supersymmetric theories, new generators Q are introduced which change fermions to bosons and vice versa, i.e.

$$Q|fermion>=|boson>; \qquad Q|boson>=|fermion> .$$

Because of their fermionic nature, the operators Q must carry a spin 1/2.

The Minimal Supersymmetric Standard Model (MSSM)

As already mentioned, different possibilities to implement a supersymmetric theory exist, and for simplicities sake only the *minimal* supersymmetric extension to the Standard model will be considered here. The MSSM is minimal in a sense that it contains the smallest possible field content necessary to give rise to all the fields of the Standard Model. In this model, one superpartner for every particle is introduced: Gauge fields like the gluons, $W^{\pm}$ and B bosons get fermionic superpartners called *gluinos* ($\tilde{g}$), *winos* ($\tilde{W}^i$) and *binos* ($\tilde{b}$) respectively, fermions, i.e. quarks and leptons are associated to scalar partners called *squarks* and *sleptons.*

Through the introduction of the so-called R-parity, Standard Model particles having R=1 can be separated from sparticles (i.e. supersymmetric particles) which have R=-1. As a consequence of the conservation of the R-parity, sparticles can only decay into an odd number of sparticles (plus Standard Model particles). In other words, when unstable sparticles decay, they necessarily create at least one new sparticle. This is where the interest of the supersymmetric theory for dark matter has its origin: Through this R-parity conservation, the lightest supersymmetric particle (LSP) is stable, and can only be destroyed by pair annihilation.

Experimentally, constraints on the nature of this LSP exist. It must be neutral in charge and in colour, otherwise it would strongly interact with baryonic matter and would

have condensed to produce heavy isotopes. SUSY presents various candidates having these properties, like the *sneutrino,* the *axino* and the *gravitino*, but for different reasons, the focus lies mainly on the lightest *neutralino* ($\tilde{\chi}$). The neutralino is a linear combination of four sparticles, one bino, one wino and two higgsinos. Generally, such a linear combination results in four different eigenstates $\tilde{\chi}^0_{1,2,3,4}$ with four masses, but usually, the realisation with the lightest mass is called *the* neutralino $\tilde{\chi}$. A lower bound for its mass[2] of $m_{\tilde{\chi}} > 50\,\mathrm{GeV}$ is obtained from collider experiments, especially from the absence of a signal at the Large Electron-Positron Collider (LEP) below 50 GeV and from the results of the WMAP data. However, scenarios exist where this limit does not apply, and neutralinos with masses $m_{\tilde{\chi}} < 50\,\mathrm{GeV}$ are possible. This is important to note, as for these "light" neutralinos, ^{3}He as a target matter would gain in sensitivity compared to heavier target nuclei. The Large Hadron Collider (LHC), which is scheduled to begin operation in May 2008, will be able to produce collisions between two 7 TeV protons, resulting in a 14 TeV collision. A large number of models can thus be tested. In addition to the Higgs boson, the LHC will be sensitive to most SUSY scenarios, so that in the near future, much better constraints on SUSY parameters could be obtained.

The MSSM, while being a relatively simple supersymmetric theory, has a huge number (>100) of free parameters, with the result that the precise properties of the $\tilde{\chi}$ can not be predicted. Nevertheless some general statements can be made about the possibility of its detection

4.3 Dark matter detection

Indirect detection

The search for WIMPs can be classified into two categories. The observation of the products of the annihilation process, where two supersymmetric particles react and create Standard Model particle, is the goal of the *indirect detection.* These annihilation products include neutrinos, positrons, anti-protons and gamma-rays. A short list of different collaboration searching for these indirect evidence include:

- Neutrino telescopes as AMANDA, ANTARES and IceCube. These detectors are installed in underground laboratories and measure the Cerenkov light, emitted by the "muon tracks", produced by highly energetic GeV-TeV neutrinos.

- Positron and Anti-Proton Experiments like the balloon-borne HEAT, BESS and CAPRICE and the space based AMS and PAMELA.

- Ground based gamma-rays telescopes like MAGIC, CANGAROO-III and HESS suffer from the fact that GeV to TeV photons interact with matter via e^+e^- pair production, meaning that they do not reach ground based telescopes. On the other hand,

[2] As a comparison, the proton mass is $m_p = 0.94\,\mathrm{GeV}$

the products of this interaction lead to a "Cherenkov light shower", which then is observable by those telescopes.

- Space based telescopes include EGRET and GLAST (scheduled for launch in January 2008). Being located in space, these telescopes can detect gamma rays directly and are complementary to the ground based telescopes.

Direct detection

The idea of direct detection is very simple: if a substantial part of the galaxy consists of WIMPs, a large number of them should constantly pass through the earth. While the interaction of WIMPs is expected to be very weak, it is thought to be non-zero. This in turn means that building a detector able to measure for example the recoil energy of such an event, dark matter scattering on ordinary matter could be recorded. The expected event rate R is approximately given by

$$R \approx \sum_i N_i n_\chi < \sigma_{i\chi} >, \tag{4.2}$$

with the index i discerning the different nuclei species, N_i the total number of a given species, n_χ the total WIMP density and $< \sigma_{i\chi} >$ the averaged cross section for the scattering of WIMPs off nuclei of species i. Commonly it is thought that the total cross section is the sum of two parts:

- The *Scalar* or *spin independent* interaction depends largely on the mass of the target nucleus. Due to the coherent summation of the diffusion amplitude of the different nucleons, the corresponding cross section is expected to depend strongly on the number of nucleons A in the nucleus

  $$\sigma^{SI}({}^A X) \propto \sigma^{SI}(N) \times A^4, \tag{4.3}$$

  with $\sigma^{SI}(N)$ the cross section for scattering on one nucleon. This means of course that the number of observed events should increase drastically for heavy elements. The most advanced dark matter detectors like Edelweiss and CDMS, using Si (A=28) and Ge (A=72) crystals, Cresst, using $CaWO_4$ crystals and Xenon10 using liquid Xe are mostly sensitive to the scalar interaction.

- The *axial* or *spin-dependent* interaction results from the coupling of a WIMP to the spin content of a nucleon. The summation of the diffusion amplitudes on the different nucleons then shows that the cross section is in first order proportional to J(J+1) and proportional to A^2. This means that using heavier atoms is much less beneficial than in the case of the spin independent interaction. Existing collaborations sensitive to the axial channel include DAMA (NaI), Zeplin (Xe) and Simple (F). A detector based on ^{3}He would add to this list, as due to its light mass but non-zero spin, the axial cross section is expected to be much larger than the scalar cross section.

It is important to note that due to the huge number of free parameters for MSSM models, it is quite possible that, for example, the scalar cross section is unmeasurably small while the axial interaction is important and vice versa.

4.3.1 Direct detection: expected signatures and experimental challenges

Background rejection

The problem in detecting WIMPs is their weak interaction with baryonic matter, meaning that the expected event rate is even for big detectors extremely small: in the most optimistic case, a few events per kg and per day can be expected, but in other scenarios this rate drops down to less than one event kg^{-1} year^{-1}. Detectors always are exposed to other radiations, like gamma rays, cosmic muons and neutrons, which can also interact in the detector. It is thus important to know what signature can be expected for neutralinos in order to be able to recognise a neutralino signal. The following characteristics can be mentioned:

- A $\tilde{\chi}$ will virtually never interact twice in the detector. This means that if one is able to measure multiple scattering events, these events can clearly be identified as not being $\tilde{\chi}$ events. To profit from this fact, the ULTIMA project plans to use in the future a large number of small detectors arranged in a three dimensional matrix. Operating simultaneously those different cells allows then to look for coincidences amongst them. A simulation based upon several assumptions shows that this technique alone already allows for a very good rejection factor [18].

- The $\tilde{\chi}$ is only interacting with the nucleus, producing a so-called nuclear recoil event. The importance of this remark lies in the fact that the ratio between ionisation and heat created is different for electronic and for nuclear recoils. If one succeeds to measure this difference, all events identified as electron recoil events can be rejected as not being $\tilde{\chi}$ events.
  An important part of this thesis deals with this effect: a difference in the heat signal for neutron and for muon events was observed, which is attributed to an indirect influence of the difference in ionisation. This means that potentially the measurement of the heat signal alone, followed by a thorough pulse shape analysis provides an efficient discrimination mechanism.
  Most of the existing collaborations are able to measure independently two different signals (for example heat and ionisation), and can separate, by comparing both signals, electronic and nuclear recoils. The possibility to install an ionisation probe in the bolometric cells is under consideration and will be tested in the future.

- One signature expected for the $\tilde{\chi}$ is an annual modulation of the event rate. In fact, the relative velocity between WIMPs and the detector is a parameter which plays a role in the event rate calculation. During summer, the earth's velocity adds

to the sun velocity through the halo, while during winter the earth moves in the opposite direction. This means that during summer, an increased event rate can be expected. When supposing that background events are constant with time, such a modulation would be a clear signature for WIMPs. The DAMA collaboration, using NaI detectors, reported such an annual modulation in 1996 [31], but their results are strongly contested by other collaborations as the obtained parameters are (in most scenarios) incompatible with experimental results from those groups.
While being a nice signature for $\tilde{\chi}$ identification, the ULTIMA project most probably can not profit from it: in order to observe an annual modulation of a signal, a significant number of events has to be measured each season. With the expected event rates for our detector, it is unlikely that we can rely on this effect.

Even if efficient methods for background discrimination exist, a good strategy consists in reducing the number of those background events in the first place. Most background events on the earth surface come from high energy cosmic muons, leading most collaborations to install their detector in an underground laboratory. In such an environment, the muon flux is largely reduced due to the shielding by the rock above. In the Canfranc laboratory where our experiment is supposed to do measurements in the next step, the muon flux is only about $170\,\mu\,\mathrm{m}^{-2}\mathrm{day}^{-1}$, compared to a muon flux at sea level of $11 \cdot 10^6\,\mu\,\mathrm{m}^{-2}\mathrm{day}^{-1}$. Additional methods for background reductions include shielding against ambient radioactivity, using lead against gamma rays and paraffin against neutrons, as well as a careful selection of materials used for the construction of the detector/cryostat, in order to prevent radioactive sources inside the shielding.

4.3.2 ^{3}He as a sensitive medium

While all these measures are generic for all dark matter detectors, ^{3}He as a sensitive medium presents some features which allows for an additional, intrinsic rejection factor:

- The deposited energy after a recoil event depends on the reduced mass. For a particle having a mass comparable to $\tilde{\chi}$, the possible energy spectrum thus varies from some keV to more than 100 keV and all signals in the corresponding range have to be considered. The $\tilde{\chi}$, expected to have a mass $m_{\tilde{\chi}} > 50\,\mathrm{GeV}$ is probably much heavier than ^{3}He atoms with a mass of 2.8 GeV. This means that the expected recoil energies are almost independent of the $\tilde{\chi}$ mass and limited to $E_{recoil} < 6\,\mathrm{keV}$. This allows for another discrimination mechanism as energies above this threshold can be rejected and it means that a ^{3}He detector can be optimised for measurements in a small energy range.

- In the energy range of the MeV, covering the principal sources of natural radioactivity, the photon cross section is inferior to 1 barn, dominated by the Compton scattering. In the energy range of interest ($\approx 10\,\mathrm{keV}$), the cross section for the photo electric effect is below 1 barn too[3], and dominated by a factor of 10 by the Compton scattering.

[3]For comparison, the photoelectric cross section of Ge is at the same energy $4.3 \cdot 10^3$ barn.

This means that ^{3}He is largely transparent to γ-rays, resulting in a reduced number of background events caused by photons.

- For the interaction of neutrons with ^{3}He, two main possibilities can be distinguished: additionally to the elastic scattering, which produces a nuclear recoil, ^{3}He has a large cross section for a so-called capture event (fig. 4.3). This capture reaction can be described by the equation:

$$n +^3 He \rightarrow p +^3 H + 764\,\mathrm{keV}.$$

The released energy is mainly dissipated as heat, resulting in a signal two orders of magnitude above the expected signal from a WIMP. The elastic scattering process is independent of the neutron energy and amounts to $\sigma_{el} \approx 2\,\mathrm{barn}$. The neutron capture reaction is roughly proportional to the "time the neutron stays near a nucleus", resulting in a v^{-1} and hence a $E^{-1/2}$ dependence. At about 100 keV, both cross sections are similar, but for lower energies, the neutron capture reaction gets more important. ^{3}He thus possesses the property to have an inherent (but not perfect) discrimination mechanism against neutron recoil events. As this type of event is considered to be the ultimate background, this presents one of the main arguments in favour of ^{3}He as a target material.

Prospects of ^{3}He bolometers

Due to the light mass of ^{3}He atoms, the neutralino scalar cross section is according to eq. 4.3 very unfavourable. On the other hand, the fact that ^{3}He has with 1 unpaired nucleon per 3 atomic masses an unequalled spin to mass ratio makes the axial cross section accessible. Unfortunately, calculations of the precise value of these cross sections depend on a large number of unknown parameters as well as on the exact SUSY model considered. Serious calculations delivering pertinent results are thus not easily obtained. Detailed simulations based on the DarkSUSY code [18, 19] conclude that the axial cross section is expected to be $\sigma_{SD} < 2 \cdot 10^{-2}\,\mathrm{pbarn}$, but as indicated above, other scenarios where larger cross sections can be obtained can not be excluded. Unfortunately scenarios with much lower cross sections can not be excluded either.

The expected event rate depends additionally on the WIMP density in our solar system and their mean velocity $\bar{v}$. Using the standard halo models with $\rho_c = 0.3\,\mathrm{Gev/cm^3}$ and $\bar{v} = 250\,\mathrm{km/s}$ Mayet [18] estimated an event rate of

$$R < 7 \cdot 10^{-2}\,\mathrm{kg^{-1}\,day^{-1}}.$$

It is this weak event rate which leads to the conclusion that the annual modulation can not be used for WIMP identification, as even for a 10 kg detector, a mass that would already be very difficult to obtain, not enough events can be expected (in this scenario) to see a statistically significant variation.

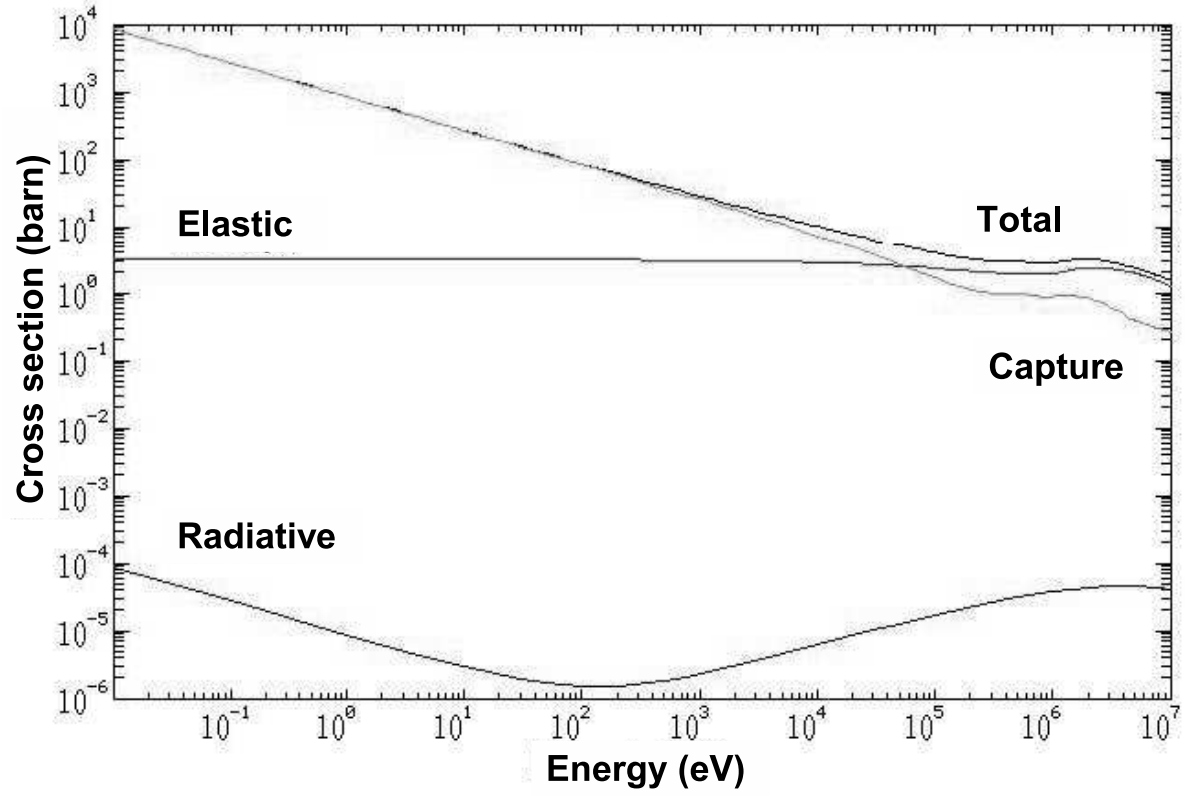

Figure 4.3: The cross section for scattering of neutrons on ^{3}He atoms is dominated for low kinetic energies $<$100 keV by the neutron capture reaction. The elastic cross section is almost constant and gets dominant for high energy neutrons. The inelastic (radiative) cross section is negligible on the whole energy range. The corresponding mean free path is obtained by the formula $\lambda = V_{mol}/N_A\sigma$. The molar volume V_{mol} of liquid ^{3}He varies between 36.82 cm^3(s.v.p.) and 25.32 cm^3 (melting pressure), which leads, for example, to an elastic mean free path of about 20 cm at 0 bar. From ref. [20]

New attempts to reconcile the positive result reported by the DAMA experiment with the negative results reported by other collaborations lead to the exploration of models in which the spin independent interaction is close to zero and the spin dependent interaction is important enough to show a higher cross section than the limit showed above. In such a case it can be shown that even a 100 g ^{3}He detector could be used to confirm the DAMA data [32].

The current experimental detector prototype has been used to show that some experimental requisites, necessary in any case, can be achieved using superfluid ^{3}He bolometers and that the points about the special features of ^{3}He, used in the simulations mentioned previously, can be verified experimentally. The results presented by Winkelmann [33] show:

- The energy threshold of 1 keV, and hence a sufficient sensitivity for dark matter research.
- Observation of coincident events caused by cosmic muons, meaning that discrimination by correlation is feasible.
- The demonstration of the transparency towards γ-rays.
- The possibility of a precise energy calibration, and clear identification of the cosmic muon spectrum, the electron spectrum from a ^{57}Co source and the neutron capture spectrum from a AmBe source.

The continuation of measurements with the same setup, while initially motivated by another idea, showed that even more conclusions can be drawn from this prototype which are important for a future dark matter detector. The main points which will be presented in this work are:

- The magnetic field dependence of the calibration (chapter 6).
- The possibility of event discrimination by a pulse shape analysis (chapter 7).
- The importance of covering the cell walls with one to two monolayers of ^{4}He (chapter 8).

Chapter 5

Experimental methods

5.1 Cryogenic methods

The work on superfluid ^{3}He bolometers imposes the quite challenging constraint that a macroscopic amount of ^{3}He has to be cooled down to temperatures of about 100 μK. To obtain these temperatures all the experiments described in this thesis were conducted on the nuclear demagnetisation cryostat (DN1) of the Grenoble Ultra Low Temperature group, constructed in 1995 by Yu. Bunkov and H. Godfrin. This cryostat has already been described in several previous PhD thesis [34, 35], and detailed information about cryogenic methods can be found in the reference works from Pobell [36] and Lounasmaa [37]. This chapter will hence only serve as a short summary.

To reach the working temperature, three stages are needed: In a first stage pumped liquid ^{4}He allows to descend to temperatures of about 1.3 K (the so-called 1 K pot). This is low enough to allow ^{3}He to condensate. The second stage is a ^{3}He /^{4}He dilution refrigerator which is used to pre-cool the third stage, called *nuclear stage* to about 7 mK. With this nuclear stage we can then reach in cycles of about one week temperatures in the desired range down to 100 μK by adiabatic demagnetisation of nuclear spins.

5.1.1 ^{3}He/^{4}He dilution

Below a critical temperature of about 800 mK (dependent on the ratio ^{3}He/^{4}He), the mixture ^{3}He/^{4}He is a liquid with two phases. A phase of pure ^{3}He floats on a phase where a small quantity of ^{3}He is diluted in the superfluid ^{4}He, with a concentration of about 6.4 % ^{3}He at very low temperatures and low pressures. This phase separation takes place in a cryostat in the so-called mixing chamber. The main principle of a dilution refrigerator is that by pumping ^{3}He out of the ^{4}He rich phase, one forces ^{3}He to diffuse from the ^{3}He phase to the ^{4}He rich phase. The diffusion can be seen similar as an evaporation from the ^{3}He liquid into the "renormalised vacuum" of superfluid ^{4}He. This "evaporation" is an endothermic process, and gives the dilution cryostat its cooling power. The mixing chamber is connected to the still. The ^{3}He in the ^{4}He phase diffuses to the still where the ^{3}He is pumped out. For doing this, the still is heated by a resistor to keep the temperature

at about 700 mK, a temperature which is a compromise between having a high flow rate of ^{3}He and a low flow rate of ^{4}He.

To allow an operation mode in a closed circuit, the pumped out ^{3}He is re-injected to the ^{3}He pure phase. Before entering the mixing chamber, it is condensed at the 1.3 K point, which is kept at this temperature by a thermal contact with the first stage. It is then cooled down further in several heat exchangers. These heat exchangers put the outgoing diluted phase (respectively gaseous ^{3}He) in thermal contact with the incoming ^{3}He, thus cooling down the incoming by the outgoing ^{3}He. This heat exchange is of a fundamental importance for the operation of the apparatus and often a limiting factor in obtaining lower temperatures.

In our cryostat we can descend with the dilution stage down to 5 mK when no nuclear stage is connected to the dilution stage, and down to 7 mK, when used to cool the nuclear stage.

5.1.2 Adiabatic nuclear demagnetisation

The dilution chamber is connected to the demagnetisation stage by a heat switch. This switch is a set of aluminium sheets placed inside a superconducting niobium coil. Below 1.17 K, in the absence of a current in the coil, the heat switch is superconductive, which means that it conducts heat very poorly at temperatures much lower than the transition temperature. The nuclear stage is thus thermally isolated from the rest of the cryostat. In contrast, by injecting a current to the coil one can suppress the superconductivity in the sheets. They thus get normal and are able to conduct heat, the nuclear stage is connected to the mixing chamber.

The nuclear stages used in this thesis consists of several ultra pure copper plates with a total mass of about 100 g for the Lancaster style cell and 1kg for the NMR experiment (see end of this section). These copper plates are in contact with the experimental cell filled with ^{3}He via sintered silver which is anchored on the copper surface. At ultra low temperatures the thermal resistance of liquid-solid interfaces (Kapitza resistance) gets very large. The sintered silver, which is in good thermal contact with the copper plate is needed to create the largest possible surface with the ^{3}He. The details of the nuclear stage can be found in Ref. [38].

So how does the nuclear stage work? Firstly, a very strong magnetic field (in our case 7 T) is applied upon the nuclear stage, while it is connected thermally to the dilution unit. The nuclear spins align with the external field at the temperature imposed by the dilution, so that the entropy will be reduced. After this pre-cooling under field[1], the heat switch is opened and the demagnetisation is started. This demagnetisation can be considered in good approximation adiabatic because it is slow and the system is isolated. The entropy (of the spins) S_{spin} depends only on the reduced variable $x = B/T$. As the demagnetisation is adiabatic $S_{spin}(x) = Cst$ and thus $x = Cst$. This leads to the relation:

[1]This pre-cooling takes, depending on the desired initial temperature, from 1 night (with $T_{initial} \approx 12$ mK) up to several days (with $T_{initial} \approx 7$ mK).

$$\frac{B_i}{T_i} = \frac{B_f}{T_f} \tag{5.1}$$

where the indexes i and f refer to the initial and the final state respectively. In other words, this means that the high magnetic field imposes that a part of the spins are aligned with the field, and hence that the occupation of the lowest Zeeman level is larger than the occupation of the higher ones. Due to the adiabaticity, the occupation of the levels stays the same during the demagnetisation, while the energy difference between the levels changes, thus leading to a different temperature. This formula shows that in theory the lower the final field, the lower the final temperature will be. However in practice there are some limitations, like interactions between the nuclear spins, corresponding to a weak internal magnetic field, and like an imperfect adiabaticity due to the weak coupling of the electrons to the nuclei. Finally, as one wants to cool down the whole nuclear stage, and not only the copper nuclei, one has to consider other parameters like the heat capacity and the coupling of the nuclei to the rest of the stage for an efficient operation. For detailed information on the principles of ultra low temperature cryostats see [36, 37].

Two different stages have been used during this thesis, with the main difference being the location at which the experimental cell is placed:

- For the bolometric measurements, used for the main part of this thesis, a stage of *Lancaster style* (fig. 5.1) allows to achieve final temperatures between 120 μK and 190 μK for a final field between 50 mT and 150 mT. The copper plates and the experimental cell are embedded in an outer cell containing copper powder. Both together are located inside the main coil, used for the demagnetisation. The outer cell serves mainly as a thermal screen at a temperature of order of mK. The working temperature can be kept after a demagnetisation for about 9 days.

- For NMR-measurements, the experimental ^{3}He cell is connected to a nuclear demagnetisation stage by long copper rods This allows to centre the cell inside another Nuclear Magnetic Resonance (NMR) grade solenoid, which can be operated independently of the demagnetisation coil. In this way the magnetic field for NMR has a high homogeneity and allows for very precise measurements.

5.2 Vibrating Wire Thermometry in ^{3}He

5.2.1 Discussion of the choice of the thermometer

The construction of a particle detector with superfluid ^{3}He as sensitive medium imposes some specifications on the thermometers used inside the bolometer cells:

- They have to be very accurate i.e. they must be able to measure the smallest temperature changes possible.

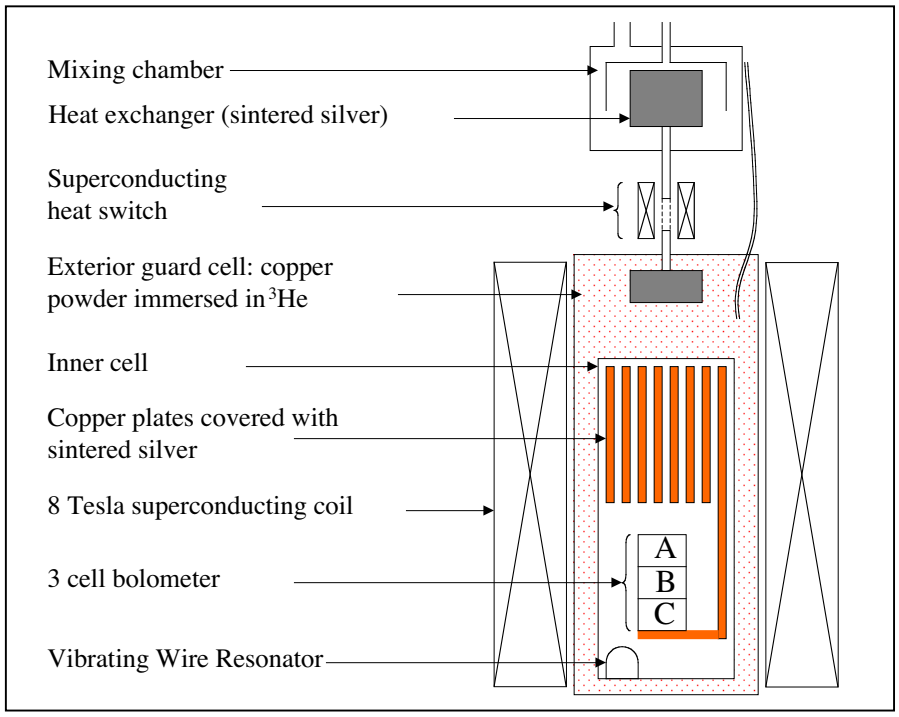

Figure 5.1: The Lancaster style cell used for the main part of this work, the bolometric measurements. The extremely low temperatures in the cell down to $\sim 100\,\mu$K are achieved because the guard cell acts as a thermal shield which limits the heat flux towards the experimental cell.

- They have to follow temperature changes of the sensitive medium rapidly, with maximal time constants on the order of a few seconds.
- They have to be usable in the temperature range from 130 μK to 190 μK.

There are several thermometers used in the mK region, like the measurement of the susceptibility of platinum or CMN, ^{3}He melting pressure thermometry, Coulomb Blockade Thermometry (CBT), resistance thermometry and others. These thermometers have all one common characteristic which makes them useless for our purpose: they have at least one liquid-solid interface to the sensitive medium ^{3}He. The thermal resistance of a liquid-solid interface rises at lower temperature (Kapitza resistance), and at the working temperature below 200 μK it is so large, that the thermalisation time of the thermometer is magnitudes above the imposed limit of a few seconds.

The use of a Vibrating Wire Resonator (VWR) has the advantage to give direct access to the properties of the liquid, without an intermediary liquid-solid boundary. It measures directly the density of quasiparticle excitations in superfluid ^{3}He. As the density of quasiparticles follows an exponential law, its measurement allows a precise determination of the temperature. The behaviour of VWRs in the ballistic regime has been widely studied by the Lancaster group, and is well understood [39, 40, 41].

A VWR was used in the bolometric experiment, and it was the main thermometer for the NMR experiment. In this experiment, the working temperatures were above $0.4\,T_c$, i.e. in the hydrodynamic regime and in the normal phase. The behaviour in this region is more complex than in the ballistic region, but a precise calibration has been done previously by Winkelmann *et al* [42].

5.2.2 Resonance of a vibrating wire

Mechanical Equations

The vibrating wire is a forced harmonic oscillator, consisting of a conducting, in our case superconducting, wire, fixed at both ends in the plane, and of an approximately semi-circular shape (see fig. 5.2). When deviated by small amplitudes, its restoring force is linear with the deviation. A detailed calculation [43], delivers the resonance frequency

$$f_0^{vacuum} = \frac{z_0^2}{4\pi \frac{a}{L^2}} \sqrt{\frac{Y}{\rho_{wire}}} \tag{5.2}$$

with Y the Young modulus, ρ_{wire} the mass density of the wire, a the radius of the wire, which is considered to have a cylindrical shape, L the diameter of the semi-circle and $z_0 \approx 4.730$ a numerical constant, which takes into account the non planar shape of the wire.

The wire is in a uniform, constant magnetic field $\vec{B}$[2]. This field is normally adjusted to values between $50 - 150\,\mathrm{mT}$, with a maximal field at higher pressures of 350 mT. Thus,

[2]For the Lancaster stage, this is the same field as the one used for the adiabatic demagnetisation. The VWR is placed in the main field in order to perform NMR experiments.

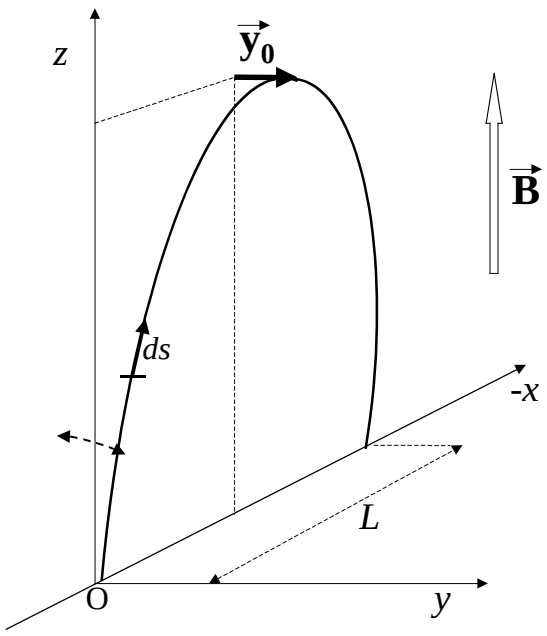

Figure 5.2: Sketch of a Vibrating Wire Resonator (VWR). The wire is excited by the Lorentz-force, induced by a current sent through the wire. The equation of motion is that of a forced harmonic oscillator. The damping is dominated by the interaction with the liquid, and contains information about the temperature of the liquid. The amplitude can be determined by measuring the voltage induced at the ends of the wire.

by sending an AC-current $I = I_0 e^{i\omega t}$ through the wire, one can apply an external force, which is determined by the laws of electromagnetism:

$$\vec{F}_{exc} = I_0 e^{i\omega t} \vec{e}_I \times \vec{B}, \tag{5.3}$$

where $\vec{e}_I$ corresponds to the unit vector indicating the direction of the current.

The detailed calculation of the mechanical motion is not trivial, as different parts of the wire have different amplitudes. Thus the restoring force $\vec{F}_{res}$, determined by the spring constant, as well as the viscous force $\vec{F}_{vis}$, dominated by the interaction with the liquid ^{3}He, are not constant along the wire. As the final result, apart from some corrective factor, is the same, we will present here only the simplified equation of motion:

$$\ddot{y} + \gamma \dot{y} + \omega_0^2 y = \frac{IlB_0}{m_{eff}}. \tag{5.4}$$

The effective mass m_{eff}, in this equation is smaller than the real mass of the oscillator, due to the previously mentioned fact that not the whole wire is oscillating at full amplitude. The interaction of the fluid with the wire can be splitted in a reactive and a dissipative part. In the ballistic limit, the reactive part is temperature independent. This term is in the above formula already incorporated into the term ω_0. The term γ contains the information of the dissipative, temperature dependent part of the interaction. The stationary solution to this equation has for the amplitude $y(\omega)$ the form of a Lorentzian:

$$y(\omega) = y_0 \frac{\omega_0^2 - \omega^2 - i\omega\gamma}{\left(\omega_0^2 - \omega^2\right)^2 + \gamma^2 \omega^2}. \tag{5.5}$$

Experimental measurement of the resonance

By measuring the amplitude of the oscillation for different frequencies, it is possible to determine the friction coefficient γ, because this coefficient is proportional to the full width at half maximum (FWHM).

Experimentally the amplitude is determined by measuring the voltage between the two ends of the wire, which is induced by the motion of the loop through the magnetic field. This AC voltage is proportional to the velocity of the oscillation and its amplitude is according to Faraday's law:

$$U(\omega) = i\omega \frac{BL}{2} y_0(\omega) \tag{5.6}$$

The electronic setup of the experiment can be seen in figure 5.3.

5.2.3 The different operation modes of a VWR

Frequency sweep

To get the Lorentz curves mentioned in section 5.2.2, a so-called frequency-sweep is done: For a constant drive, one measures the signal of the oscillation (In-phase and Quadrature)

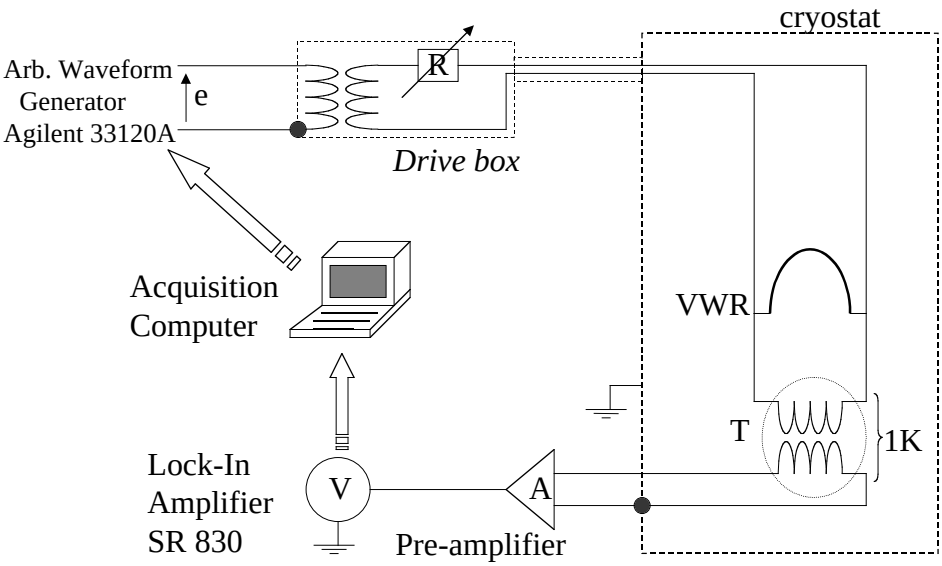

Figure 5.3: Electronic setup. The arbitrary waveform generator Agilent (HP) 33120A creates a sinusoidal signal of amplitude e. This voltage e is applied on a 1:1 transformer which allows to decouple the injection current form the ground at the input. A resistance $R_{inj} \gg |Z_{VWR}|, |Z_T|$ allows to impose a known AC current $I = e/R_{inj}$ on the wire. The oscillation of the wire induces a voltage V, which is amplified by a factor of 50 by a cold transformer, thermalised on the 1 K pot. At the top of the cryostat the signal is amplified by a "house-made" (service électronique CRTBT) low-noise preamplifier. The signal is measured by a SR830 lock-in amplifier and read out by a computer.

for different frequencies. A computer program is used, which sweeps automatically a desired frequency range. The step width, the drive and the sweep-rate can be chosen by the user. As the wire is out of equilibrium after changing the frequency, it is important to choose a low enough sweep-rate[3]. Normally a resonance sweep takes between 100 and 300 s. The chosen drive is a compromise between having a high signal, i.e. a high signal/noise ratio, and staying in the linear regime. A typical frequency sweep is shown in figure 5.4.

With a computer program the measured sweeps (the phase and the quadrature) can be fitted by a complex Lorentzian, which usually fits the curves very well. By the fit, the FWHM W_0 can be determined as well as the so-called "height-width-over-drive" $\mathcal{H} = \frac{VW_0}{I}$. At constant magnetic field B, $\mathcal{H}$ is a constant. With $\mathcal{H}$ known, one can determine the

[3] $\tau_{step} \approx 4\,\tau_{wire}$, with τ_{wire} the time constant for the relaxation of the wire to a new equilibrium, to allow the system to achieve the new stable amplitude

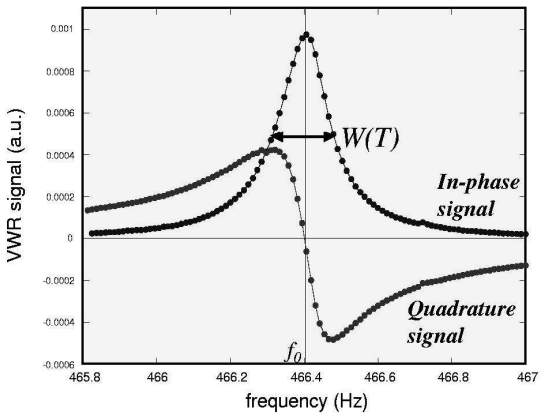

Figure 5.4: A typical frequency sweep. Simultaneous fitting of phase and quadrature yields a very good fit. All sweeps are of similar quality.

width W_0 by measuring the signal V at the resonance frequency:

$$W_0 = \mathcal{H}\frac{I}{V}. \tag{5.7}$$

Current sweep

In the current sweep mode, one varies the current, also called drive, at a fixed frequency, usually the resonance frequency. For low drives, the result is just a straight line as the amplitude is proportional to the excitation. For higher drives this is a good method to visualise the nonlinearities, which are mainly due to two effects. On the one hand the friction is only proportional to the velocity for small excitations. For higher excitations, the response gets non-linear with the remarkable feature that the first correction to linearity has a friction-reducing effect, leading to an apparently reduced W. On the other hand the friction of the vibrating wire produces heating of the ^{3}He, which increases as $P_{heating} \propto I^2$, resulting in a real increase of temperature and thus an increased W_0.

Monitoring

The frequency sweeps are not fast enough to follow temperature changes in the bolometer cells at an appropriate rate. Luckily, the FWHM W_0 is inversely proportional to the signal V at the resonance frequency, with a temperature independent constant $\mathcal{H}$. When $\mathcal{H}$, which can be determined by a frequency sweep, is known, it is sufficient to measure constantly V at the resonance frequency to get $W_0(t)$ and thus the time-resolved temperature $T(t)$ (cp. eq. 5.7). The conversion from resonance width $W_0(t)$ to temperature $T(t)$ is not trivial and will be explained in the next section.

It is important to notice that the response to a change in temperature is not instantaneous but that it takes some time for the VWR to relax to its new equilibrium position. The resolution in time is thus limited by the response time of the wire $\tau_{wire} = 1/\pi W$.

5.2.4 Correlation between the friction and the temperature

The main motivation for using VWR wires is that the width of the Lorentzian as well as the resonance frequency provide information about the real and the imaginary part of the viscosity in the hydrodynamic regime, and about the quasiparticle density in the ballistic regime. For the NMR measurements, a VWR was used as the main thermometer. In this work, we relied on a calibration done previously, and we refer for a detailed discussion of VWR thermometry in the hydrodynamic regime to Ref. [42].

The bolometric measurements were done well below the hydrodynamic regime, where the mean free path of quasiparticles largely exceeds the cell size, and it is no longer justified to talk in terms of viscosity. To calculate the interaction of the quasiparticle gas with the wire, the excitations can thus be described in terms of a ballistic gas.

Classic ballistic gas

For a first estimation of the interaction of the VWR with this dilute gas, a wall moving with velocity v in a dilute gas of number density n can be considered. For simplification we will stay for the moment in a one-dimensional picture, all collisions of the particles are considered elastic and they all move at a velocity v_g or $-v_g$. A simple balance of the momentum transfer leads, for velocities $v \ll v_g$ to the friction force

$$F = 2np_F v. \tag{5.8}$$

The prefactor on the right hand side term corresponds to the friction coefficient $\gamma = 2np_F$. One can see that if this prefactor is velocity independent, the friction term is linear in v. A comparison of the measured line width with this theoretical value (as well as the comparison with a more realistic 3 dimensional model) shows that the friction force is about 1000 times stronger than what the calculation using this model suggests. Thus the interaction of the quasiparticles with the wire is not the one of a classic dilute gas.

Ballistic gas of quasiparticles

The Lancaster group [40, 44] proposes an advanced model which succeeds in a satisfactory manner to explain the experimentally obtained results. The essential difference to the previous model is the presence of an order parameter associated to an energy gap in superfluid ^{3}He. The quasiparticles are living in the immobile fluid on a dispersion curve which is modified when one changes to the moving inertial frame of the wire. Let us have a look at the dispersion curve described in eq. 3.3 and represented in fig. 5.5. The states on the branches 1 and 4 are quasiparticles ($v_g \cdot p > 0$), the states on the branches 2 and 3 can be described as quasiholes ($v_g \cdot p < 0$). A particle of the branch 1 has to come from the right side to collide with the wire. After an elastic collision (i.e. at constant energy) with the wire, it can either be found on the branch 4, which corresponds to the classical case of inversion of velocity and momentum, or, in the case that it is transformed to a hole, it can be found on the branch 2. This second process is called Andreev reflection. It shows

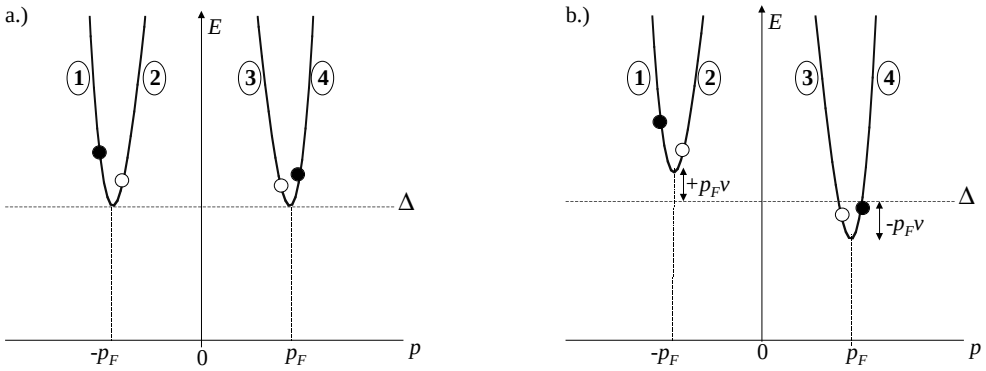

Figure 5.5: Dispersion relation of the quasiparticles in superfluid ^{3}He . a) in the laboratory inertial frame, b) in the inertial frame of the moving wire. v is the velocity of the moving wire.

an inversion of the group velocity but a momentum transfer which is negligible compared to p_F.

The force on a wall of height $2a$ exerted by all quasiparticles of branch 1 and 2 can be expressed by[4]

$$F_{1+2} = \int_{\Delta}^{\infty} n\left(E\right) \mathcal{P} \Delta p \, dE \tag{5.9}$$

where $n(E)\mathcal{P}$ is the number of quasiparticles which hit the wall by unit time. For $v \ll v_g$ it is independent of v and has a value of $n(E)\mathcal{P} = n(E)2av_g$. In our simple model Δp, the momentum transfer, is considered being $\Delta p = \pm 2p_F$ for a classical reflection and 0 for an Andreev reflection. Supposing a Boltzmann distribution, $n\left(E\right)$, the density of quasiparticles, can be written as the product of $g\left(E\right)$, the density of states, and the Boltzmann factor:

$$n\left(E\right) = g\left(E\right) \exp\left(-E/k_bT\right). \tag{5.10}$$

When the wire is not moving, $F_{1+2} + F_{3+4} = 0$, which corresponds to a friction force of 0 in its idle state, as it should be expected.

In the situation of a moving wire, the dispersion relation in the inertial frame of the wire is changed as shown in fig. 5.5b. The important consequence of this modulation is that the least energetic particles of the branches 3 and 4 can not find a state with equal energy in the branches 1 and 2. They are thus forced to undergo Andreev reflections and as the corresponding momentum transfer is negligible, they do not contribute anymore to the friction of the VWR. For a velocity v of the wire, it is now possible to write the forces as follows:

$$F_{1+2}\left(v\right) \;=\; \int_{\Delta+vp_F}^{\infty} n\left(E - vp_F\right) \mathcal{P}\left(E - vp_F\right) \Delta p \, dE \tag{5.11}$$

[4]All forces will be expressed by unit of wire length. To obtain the total force, it is necessary to integrate over the whole wire.

$$= -2p_F \int_{\Delta}^{\infty} n(E)\,\mathcal{P}(E)\; dE, \tag{5.12}$$

$$F_{3+4}(v) = \int_{\Delta+vp_F}^{\infty} n(E+vp_F)\,\mathcal{P}(E+vp_F)\,\Delta p\, dE \tag{5.13}$$

$$= +2p_F \int_{\Delta+2p_F}^{\infty} n(E)\,\mathcal{P}(E)\; dE. \tag{5.14}$$

The total force has finally the following equation:

$$F_{tot}(v) = -2p_F \int_{\Delta+vp_F}^{\infty} 2av_g g(E) \exp(-E/k_bT)\,\Delta p\, dE. \tag{5.15}$$

In the one-dimensional case the group velocity is given by

$$v_g = \frac{\partial E}{\partial p} = \frac{2}{h} g(E)^{-1} \tag{5.16}$$

which allows to simplify eq. 5.15 to:

$$F_{tot}(v) = \frac{16ap_Fk_BT}{h} \exp(-\Delta/k_BT)\left[1-\exp(-2vp_F/k_bT)\right] \tag{5.17}$$

$$\approx \frac{32ap_F^2}{h} \exp(-\Delta/k_BT) * \left(v - \frac{2p_F}{k_BT}v^2\right). \tag{5.18}$$

This quite simple model succeeds already to describe the exponential behaviour with temperature as well as the linear behaviour with v for low velocities $v \ll k_BT/2p_F$. Additionally, it describes the non linear behaviour for a higher velocity, with the first correction term decreasing the force compared to the linear behaviour. Contrarily, this model does not deliver quantitative correct results.

A more realistic 3-dimensional model [45] delivers an analytic result which agrees well with observations, and which has for low velocities a linear form:

$$F(v \to 0) = \frac{ap_F^4}{2\hbar^3} \exp(-\Delta/k_BT)\, v. \tag{5.19}$$

The line width (in Hz) of a vibrating wire is then given by

$$W_0(T) = \gamma \frac{p_F^4}{4\pi^2\hbar^3 a\rho_{wire}} \exp(-\Delta/k_BT) \tag{5.20}$$

$$= \alpha \exp(-\Delta/k_BT) \tag{5.21}$$

where γ is a geometrical factor. For the $4.5\,\mu$m NbTi VWR used in our cryostat, a total prefactor of $\alpha = (1.81 \pm 0.1) \cdot 10^5$ Hz has been found [33], which is in good agreement with calibrations made in Lancaster [46].

The deviation from the linear behaviour can be approximated in the 3-D model for velocities $v < 2k_BT/p_F$ similar to eq. 5.17:

$$F(T,v) = F_0(T)\left[1 - \exp\left(-v/v_0\right)\right] \tag{5.22}$$

with $v_0 = 1.36k_bT/p_F$.

Another deviation, which gains importance for the lowest temperatures, is the existence of an intrinsic line width W_{int} due to internal friction processes inside the VWR. It can be considered as independent of temperature and must be determined for each wire experimentally. The total line width can thus be written as

$$W(T) = W_{int} + W_0(T) \tag{5.23}$$

5.3 ^{3}He Bolometry

A bolometer is a device used to measure incident radiation or particles. It consists of an *absorber* or *sensitive medium*, which is connected to a heat sink (material of constant temperature) through a weak thermal link. The result is that any radiation or particle depositing energy in the sensitive medium raises the temperature of the bolometer above that of the heat sink, the higher the energy absorbed, the higher the temperature will be. A thermometer of some kind, attached to the absorber, is used to measure the temperature, from which the absorbed energy can be calculated.

In our case, a bolometer consists of a copper box filled with ^{3}He, which acts as the sensitive medium. A VWR inside the cell is used as the thermometer. The box has a tiny orifice at one of its sides which is used as the thermal link to the surrounding ^{3}He, representing the heat sink. Due to the Kapitza resistance, the ^{3}He is thermally decoupled from the cell walls, and the thermalisation only takes place through the orifice. The surrounding ^{3}He can of course also interact with particles, and stays thus strictly speaking not exactly at constant temperature. But firstly it is in good thermal contact with the sintered silver and thus with the cold reservoir of the copper nuclei, and secondly it has a much larger volume so that a single particle event leads to much less heating than inside the bolometric cell. Nevertheless it can be remembered that a part of the noise observed on the baseline of an acquisition file might be due to the ^{3}He bath really changing its temperature. A scheme of a single bolometer cell is shown in fig. 5.6.

5.3.1 The 3-cell ^{3}He Bolometer

The main purpose of the current experimental setup was to study whether superfluid ^{3}He could really be used as an efficient particle, and especially neutralino, detector. So several experimental points had to be checked:

- The sensitivity in the keV range. As the neutralinos are expected to deposit an energy of about 6 keV this is absolutely necessary.

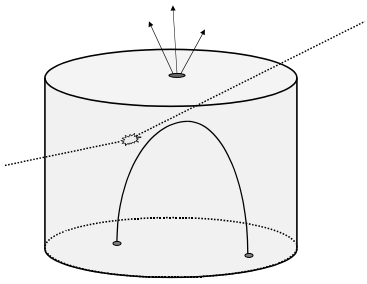

Figure 5.6: Sketch of a ^{3}He bolometer cell. An incident particle may have an interaction with the superfluid ^{3}He, heating up the cell. With a time constant τ_b the heat leaks out of the cell and the ^{3}He inside is thermalised to the surrounding temperature.

- The possibility of a precise calibration of deposited energies.
- The possibility to discriminate non-neutralino background events. This point is crucial, as the expected neutralino event rate is extremely low (see section 4.2).

The experimental device used to check these requisites is a bolometer consisting of three cells, labelled A, B and C, each of volume $V \approx 0.13\,\mathrm{cm}^3$ and each containing a NbTi vibrating wire thermometer of diameter $d = 4.5\,\mu\mathrm{m}$ (see fig. 5.7).

The use of three adjacent cells allows to study whether correlations between the cells can be used to discriminate events caused by particles which interact relatively strongly, like muons. Muons have a high cross-section with ^{3}He, leading to multiple scatterings with a mean free path of about $2\,\mu$m. A muon passing through 2 or all 3 cells will thus leave a simultaneous signature in all cells it crosses. A final detector ready to search for dark-matter will need a high granularity, in order to obtain an optimal rejection factor [19].

In the C-cell there is a second NbTi wire with three times larger diameter ($d = 13\,\mu\mathrm{m}$). This wire is used to do calibration pulses. By exciting this wire at the resonance frequency during short times, but with high AC currents, a well defined energy can be injected to the cell and particle events can thus be simulated.

Another feature of this setup is the presence of a gold sheet containing some radioactive ^{57}Co in the B-cell. The ^{57}Co atoms emit conversion electrons at well defined energies. The decay spectrum of ^{57}Co is not trivial, but the highest probabilities are found for conversion electrons having an energy $E^K_{CE} = 7.3\,\mathrm{keV}$, $E^L_{CE} = 13.6\,\mathrm{keV}$ and $E^M_{CE} = 14.4\,\mathrm{keV}$. These electrons are used to prove that a sensitivity of the order of 1 keV is possible with ^{3}He. In addition they can be used for calibration purposes, by comparing the experimentally observed statistical distributions of events with the expected electron spectrum [20, 47].

A large part of the characterisation of this setup has been done by C. Winkelmann during his PhD thesis and the current chapter is a brief summary of his findings necessary to understand the subsequent chapters. A more detailed description can be found in ref. [33, 48].

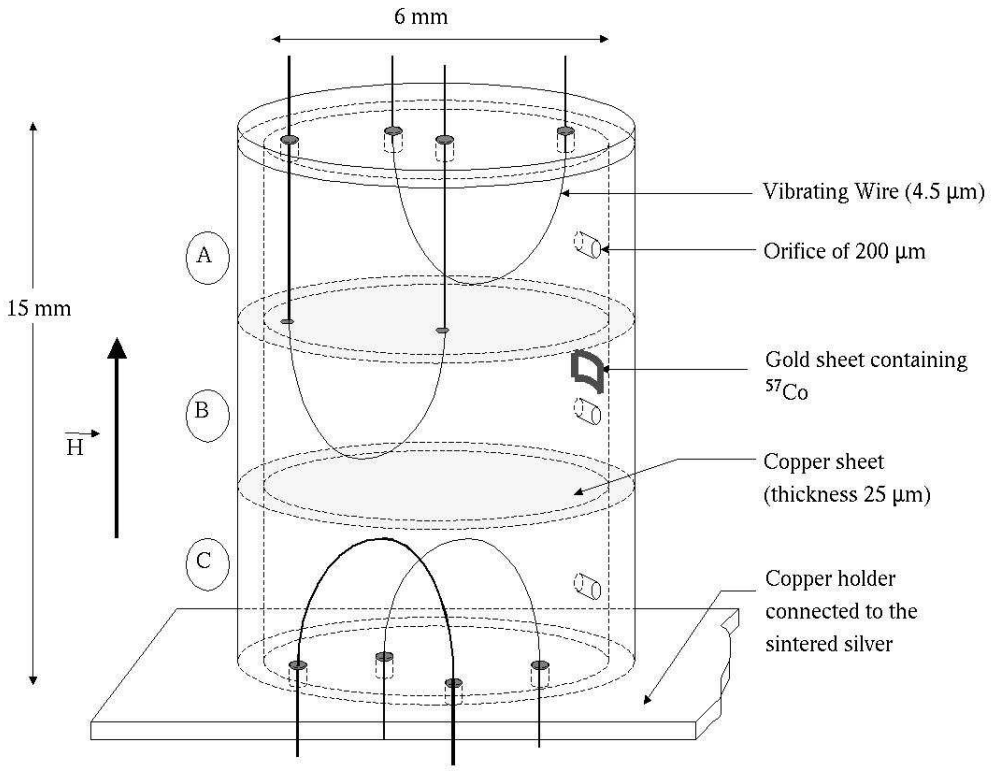

Figure 5.7: Scheme of the 3-cell ^{3}He bolometer. The cell consists of three separated cells, each containing a NbTi VWR thermometer of diameter $d = 4.5\,\mu$m. The B-cell contains in addition a radioactive ^{57}Co source, embedded in a gold sheet. This source delivers conversion electrons used for calibration purposes and for demonstrating that the 1 keV sensitivity has been achieved. A second VWR is mounted in the C-cell. This wire has a 3 times larger diameter ($d = 13\,\mu$m) and is used for calibration pulses.

The initial idea behind a continuation with the same setup was the plan to continue an older experiment on the pressure dependence of the released energy after neutron capture events, presented as a possible experimental proof for the Kibble-Zurek vortex creation scenario [17]. The details of this will be explained in chapter 9. However, during this work we recognised that other phenomena could be observed which are of interest both, for fundamental ^{3}He physics and for a better understanding of a future dark matter particle detector. These findings are the huge contribution of adsorbed layers of ^{3}He to the total heat capacity (chapter 8) at ultra low temperatures, the magnetic field dependence of the calibration factor (chapter 6) and a difference of the thermalisation time constant τ_b after an event, depending on the nature of the event (chapter 7). This last observation is especially important as it potentially delivers a discrimination mechanism based on a pulse shape analysis for a future dark matter detector.

5.3.2 Detection of heating events

For the detection of heating events, the VWR is used in the monitoring mode (see section 5.2.3). This mode allows to follow the time dependence of the full width half maximum $W(t)$ of the vibrating wire and thus the temperature in the cell. A typical acquisition file is shown in fig. 5.8.

At some instances, peaks appear in the three cells simultaneously. This corresponds to muons travelling through the cell vertically, and thus leaving some energy in each of the three cells. The B-cell shows a lot of small peaks with heights corresponding to about $\Delta W \approx 4\,\mathrm{mHz}$. Most of these correspond to conversion electrons from the ^{57}Co source and can be used to get a first rough estimation of the conversion factor $1\,\mathrm{mHz} \simeq 3\,\mathrm{keV}$.

In order to relate W to the actual temperature inside the cell and to model the observed peaks, one has to consider some important time constants.

5.3.3 Characteristic time constants

The first time constant of interest is the thermalisation time inside the cell. We are working in the ballistic regime, where the mean free path of quasiparticles is much larger than the size of the bolometric cells. The question of how the thermalisation happens is to our knowledge not known. Since two-body quasiparticle scattering should be very rare in the ballistic regime, we suppose that thermalisation takes place by non linear processes on the cell walls. It is thus thought that after the impact of a particle, internal equilibrium is achieved within a time given approximately by the time a quasi-particle needs to cross the cell. This time is of the order of $\tau_v \approx L/\bar{v}_g \approx 0.3\,\mathrm{ms}$, with $L \sim 6\,\mathrm{mm}$ the dimension of the cell and $\bar{v}_g \sim 20\,\mathrm{m/s}$ the mean group velocity. This time is much smaller than the other time constants presented later, and the internal equilibrium can therefore be considered as instantaneous. As we shall see in chapter 8 we have reasons to believe that this is not always correct, but for instance we will take it as a given.

Subsequent to a heating event, the deposited energy will escape the cell via the orifice. A first simple approach to calculate the form of the thermalisation is to consider the

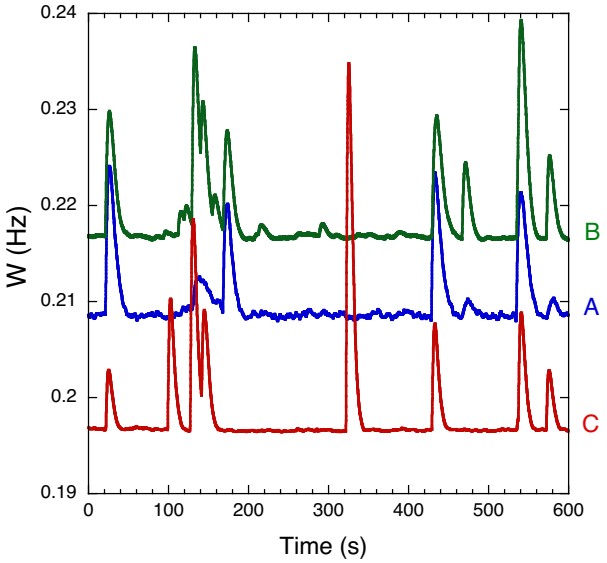

Figure 5.8: A typical acquisition file. Some events appear clearly simultaneous in the three cells, and can thus be characterised as muon events. The B-wire shows several events of small peak height, which come from the conversion electrons emitted by the radioactive ^{57}Co.

excitations as a ballistic gas of quasiparticles of the same energy $E \approx \Delta$. The outgoing heat flux is proportional to the number of quasiparticles leaving the cell by unit time. This outgoing stream can be considered as being proportional to the difference of quasiparticle densities inside (n_{cell}) and outside (n_{res}) the cell

$$\Delta n = 1/\tau_b \left(n_{cell} - n_{res}\right) \Delta t. \tag{5.24}$$

For one single event at t_0, creating an additional quasiparticle density of n_{event}, one finds an exponential law for the quasiparticle density :

$$n_{cell}\left(t\right) = n_{res} + \Theta\left(t - t_0\right) n_{event} \exp\left(\frac{t - t_0}{\tau_b}\right) \tag{5.25}$$

with $\Theta\left(t - t_0\right)$ the Heaviside step function.

The above consideration is an argument based on the fact that for $k_B T \ll \Delta$ all excited states have almost the same energy $E \approx \Delta$ and that it is thus sufficient to argue only in terms of quasiparticle density. A complete calculation of the heat flux, detailed in appendix A, delivers the result that the box time constant $\tau_b = RC$ is determined by the ratio of the volume V to the effective hole surface S_{eff} with a slight temperature dependence which is mainly given by the temperature dependence of the mean group velocity $\bar{v}_g$:

$$\tau_b(T) = 4\frac{V}{S_{eff}}\frac{1}{\bar{v}_g(T)}\left(1 - \frac{5}{16}\frac{k_B T}{\Delta}\right) \tag{5.26}$$

$$= 2\sqrt{2\pi}\frac{V}{S_{eff}}\frac{1}{v_F}\sqrt{\frac{\Delta}{k_B T}}\left(1 - \frac{5}{16}\frac{k_B T}{\Delta}\right). \tag{5.27}$$

Considering that the heat capacity depends exponentially on temperature one might have expected that the time constant has a strong temperature dependence too. The most interesting feature of this formula is thus that τ_b varies only slowly with temperature. In chapter 7 we will see how this theoretical result compares to our experimental data, and that experimentally we obtain values which are around 5 s.

Another important time constant is τ_w, the constant which describes the time the wire needs to find its new dynamical equilibrium after a fast temperature change. The response time of a harmonic oscillator is given by

$$\tau_w = \frac{1}{\pi W}. \tag{5.28}$$

As we work normally in the region between $W = 0.1 - 10$ Hz the values for τ_w are comprised between $0.03 - 3$ s. This means that for fast heating there is always a considerable delay between the real temperature W_{eq} and the indicated temperature W.

Finally there is the time constant of the electronics which is dominated by the time constant of the Lock-In amplifier, normally adjusted to $\tau_{LI} = 100$ ms. Its influence is quite marginal for low temperatures, but it has to be considered when looking at data taken at high temperature.

5.3.4 Analytic form of a peak

To derive an analytic formula of the measured line width after a heating event as a function of time one has to take into account that the wire can not immediately achieve its equilibrium position. One can start from the assumption that the change of the line width in a short time interval is proportional to the difference between the equilibrium and the actual line width

$$dW_{mes}(t) = [W_{eq}(t) - W_{mes}(t)] \frac{dt}{\tau_w} \tag{5.29}$$

where for a heat event at $t_0 = 0$ the equilibrium line width is (see eq. 5.25)

$$W_{eq}(t) = W_{base} + A \exp\left(-\frac{t}{\tau_b}\right) \Theta(t). \tag{5.30}$$

W_{base} is the baseline width. The amplitude A of the variation of W_{eq} is, for not too big energy events, directly proportional to the deposited energy. $\Theta(t)$ represents the Heavyside step function.

The parameter τ_w depends, as mentioned in the previous section, on the temperature. Anyhow, for small energies deposited ($A \ll W_{base}$) it can be considered as being constant $\tau_w = 1/(\pi W_{base})$. The solution of eq. 5.29 then becomes:

$$W_{mes}(t) = W_{base} + A\frac{\tau_b}{\tau_b - \tau_w}\left[\exp\left(-\frac{t}{\tau_b}\right) - \exp\left(-\frac{t}{\tau_w}\right)\right]\Theta(t). \tag{5.31}$$

This formula fits the measured peaks in general very well, but especially at the peak start the time constant introduced by the electronics becomes noticeable, especially at

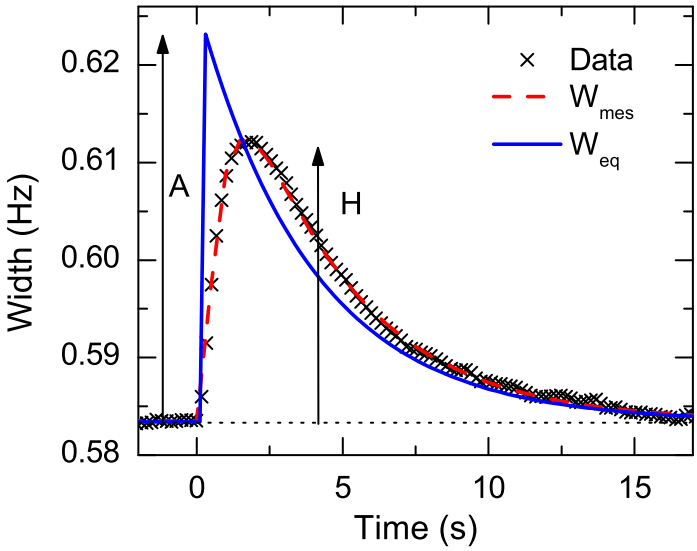

Figure 5.9: Data showing a typical event. The dashed line is a fit of the data using eq. 5.31, with $W_{base} = 0.5824\,\mathrm{Hz}$, $A = 0.0429\,\mathrm{Hz}$, $\tau_b = 3.93\,\mathrm{s}$. The solid line shows the corresponding equilibrium resonance width (eq. 5.30) using the parameters obtained from the fit. A and H illustrate the difference between the peak height which would be obtained by a thermometer with zero response time (eq. 5.30) and the really measured peak height.

high baseline widths, i.e. small τ_w. It is difficult to calculate an exact formula for this contribution, but it was found that by simply replacing the response time constant τ_w by $\tau_w^* = \tau_w + \tau_{LI}$, the above formula provides very good agreement with the experiment on the whole temperature range. A typical peak together with a fit using this formula is shown in fig. 5.9. As we are interested in the deposited energy A, it is interesting to have the relation between $H = |W_{mes} - W_{base}|_{max}$ and A :

$$G(W_{base}, \tau_b) = \frac{H}{A} = \left(\frac{\tau_w}{\tau_b}\right)^{\frac{\tau_w}{\tau_b - \tau_w}} \tag{5.32}$$

By analysing the height of the obtained peaks, this formula allows to extract information on the deposited energy of an event, under the condition that the relation between resonance width and energy is known.

5.3.5 Calibration factor

In order to be able to relate the variation of the VWR width A ($\ll W_{base}$) after an event to the corresponding heat release U, we define the calibration factor

$$\sigma_0 = \frac{A}{U} = \frac{1}{C(T)} \frac{dW(T)}{dT}. \tag{5.33}$$

Remembering the expressions for $W(T)$ (5.20) and $C(T)$ (3.28) we find in first approximation that again the exponential dependence drops out, and that we have only a weak dependence on temperature:

$$\sigma_0 = \frac{\alpha\Delta}{k_B C_0 V T_c^{3/2}} \frac{1}{\sqrt{T}}. \tag{5.34}$$

This calibration factor which uses the peak height of the equilibrium response A has to be corrected by the factor G defined in eq. 5.32 and one can then relate the measured peak height H to the heat released via

$$H = \sigma_0 G(W_{base}) U. \tag{5.35}$$

An additional correction factor $f(u, t')$ taking into account the non-linear behaviour of the VWR width with oscillation velocity v, has been considered in the data analysis presented in this thesis when it was necessary, but as it is a non trivial correction which adds nothing to the general comprehension, we refer to the publication by Winkelmann *et al.* [48].

Pressure dependence of the calibration factor

In eq. 5.34 several parameters are pressure dependent, namely α (through its pressure dependent term p_F, see eq. 5.20), Δ, C_0(through N_F and Δ, see eq. 3.28) and T_c. The pressure dependence of all these terms is tabulated[5], and overall the expected pressure dependence can be calculated numerically.

From fig. 5.10 it can be seen that the calibration factor strongly changes over the accessible pressure range, with the largest values at low pressures. This is one of the reasons why a working pressure of 0 bar is advisable for particle detection.

5.3.6 Calibration pulses

The calibration factor as defined in the previous section contains a geometrical factor, coming from the volume of the cell and from the shape of the VWR thermometer. This factor can be estimated to a good degree, but in order to have a higher accuracy on σ_0, an independent calibration is favourable. Due to the diverging Kapitza resistance, simulation of heating events by Joule heating is not feasible as the heat transfer from the resistance to the superfluid would take too much time. Bradley *et al.* [16] proposed a heating method based on the mechanical friction of a second VWR (called heater wire) present in the same cell. By driving it with an excitation current at its resonance frequency during a short time, a controllable amount of energy can be introduced into the system. The amount of energy introduced electrically to the wire can be easily calculated by the integral of the electric power $E_{electric} = \int UIdt$, where the current imposed and the voltage induced

[5] We used the values obtained from the Northwestern group website http://spindry.phys.northwestern.edu/he3.htm .

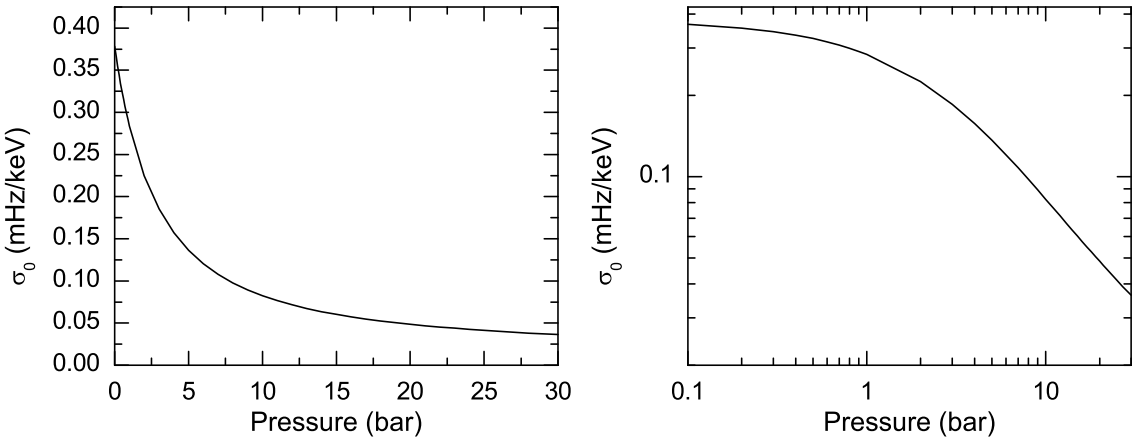

Figure 5.10: The expected pressure dependence of the calibration factor in linear and log-log scale. From this graph it can be seen that the peak height for a given heat deposition decreases drastically with pressure, making the bolometer more sensitive at lower pressures.

on the wire are both measured with Lock-In amplifiers. The electric power will first be transformed into kinetic/potential energy of the heater wire, and then be dissipated to the fluid via the velocity dependent frictional coupling. While the excitation of the heater wire can be chosen to be very short (in practice we use a pulse length of δt =80 ms), the typical timescale for the dissipation to the fluid is governed by the damping of the heater wire $\tau_h = 1/(\pi W_0^h)$ (see eq. 5.28), where W_0^h is the resonance width of the heater wire. The energy deposition is thus, contrarily to a particle event, not instantaneous. This means that eq. 5.31, while still a good approximation, does strictly speaking not apply. This delaying effect has a larger influence for lower temperatures as W_0^h decreases with temperature. The resulting difference on the pulse shape measured by the VWR thermometer has been simulated numerically [48]. The main finding of these simulations is that while the shape of the pulse, especially on the rising edge, is changed, the resulting peak height is the same within 1 % even for the lowest temperatures (see fig. 5.11). For higher base line resonance widths this gets almost completely negligible.

A second, more important correction has to be made due to intrinsic losses within the heater wire. The intrinsic damping can be well represented by a friction force linear in velocity, which therefore simply adds a temperature independent term W_{int}^h to the measured damping $W^h(T)$ (eq. 5.23). As this intrinsic damping only heats up the wire itself and, due to the Kapitza resistance, not the fluid, the energy transmitted to the fluid has to be corrected for this effect. The fraction of the total energy transmitted to the fluid is then

$$E_{pulse} = \frac{\left(W^h - W_{int}^h\right)}{W^h} E_{electric}. \tag{5.36}$$

According to eq. 5.35, the response to an energy deposition should be linear in energy. To reduce the error on the calibration factor, whose precise determination will play an essential role in chapter 9, between 10 and 25 pulses of different energies are usually made

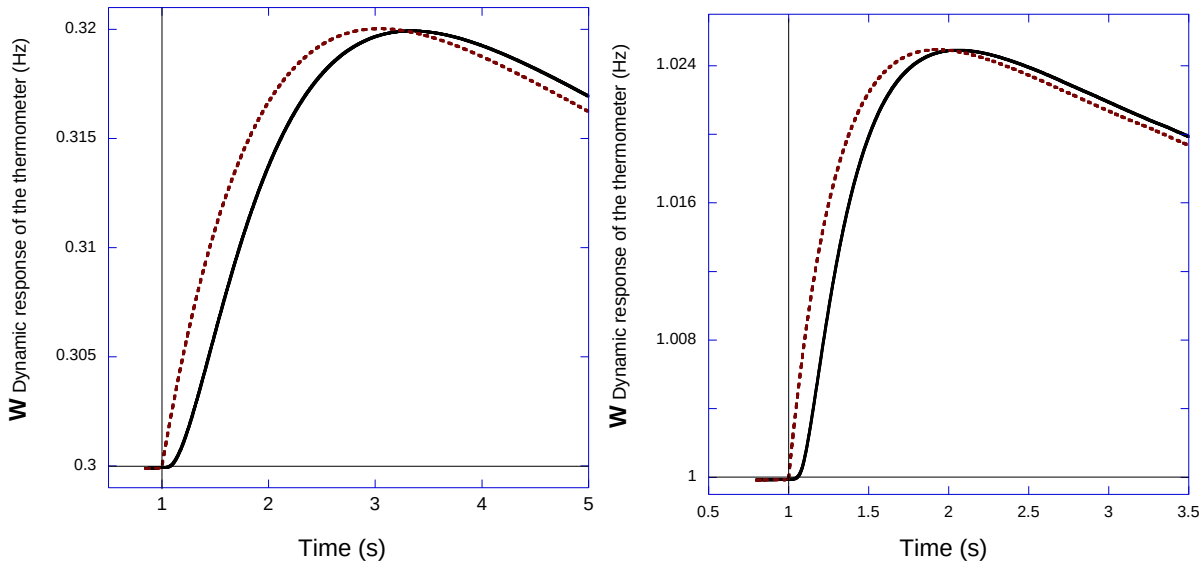

Figure 5.11: Numerical simulations of the response of the VWR thermometer to an instantaneous heat deposition at t=1 s (dotted line) and to a heat pulse by the heater wire (solid line) for two different baseline widths W_{base}, corresponding to the temperatures $\sim 120\,\mu$K ($W_{base} = 0.3\,$Hz) and $\sim 140\,\mu$K ($W_{base} = 1\,$Hz). Both pulses introduce the same total energy. The response to the instantaneous event is described by eq. 5.31. The simulations show that despite the difference in shape, the measured peak height H for a given energy is identical within 1 % even for the worst case of small temperatures. Nevertheless in chapter 7 where we are interested in the box time constant τ_b, the difference in shape was taken into account for the fits (from [33]).

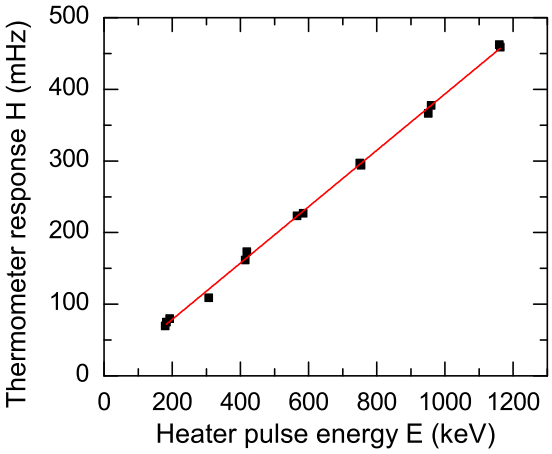

Figure 5.12: Example of a calibration curve obtained using 15 pulses made in about 10 min. The height H of the VWR thermometer is plotted as a function of the injected energy via mechanical friction by the VWR heater. The slope of the linear fit gives the experimental value for the calibration factor.

under a given condition (temperature, field) and the calibration factor is found as the slope of the resulting peak height/energy diagram (see fig. 5.12).

5.4 Particle detection and energy deficit

With the formalism developed above, all the tools are available to use the bolometers for particle detection: one simply has to cool down the cryostat to the working temperature, use the temperature wires in monitoring mode and wait. A typical acquisition file is presented in fig. 5.8.

The principal source for the events measured are muons, produced in the upper atmosphere by collisions of high energy cosmic particles with air particles. The flux density, energy distribution and interaction of muons are well known. A muon interacts quite strongly with ^{3}He and in first approximation the energy deposited can be calculated using the loss ratio

$$\frac{dE}{dx} = 1.92 \times \rho[\mathrm{g/cm^3}] \qquad \mathrm{MeV/cm},$$

in other words the deposited energy is proportional to the length of the track. As the muons can have different incident angles, the measured energies will show a rather large spectrum, with a peak at about 70 keV and a long tail up to about 200 keV. A more sophisticated modelling, using the simulation code GEANT4 has been made by a group from the LPSC, Grenoble and compared to the measured spectrum. The detection rate and the form of the spectrum are in good agreement, but the energies measured are 25 % below the calculated total deposited energy (fig. 5.13a).

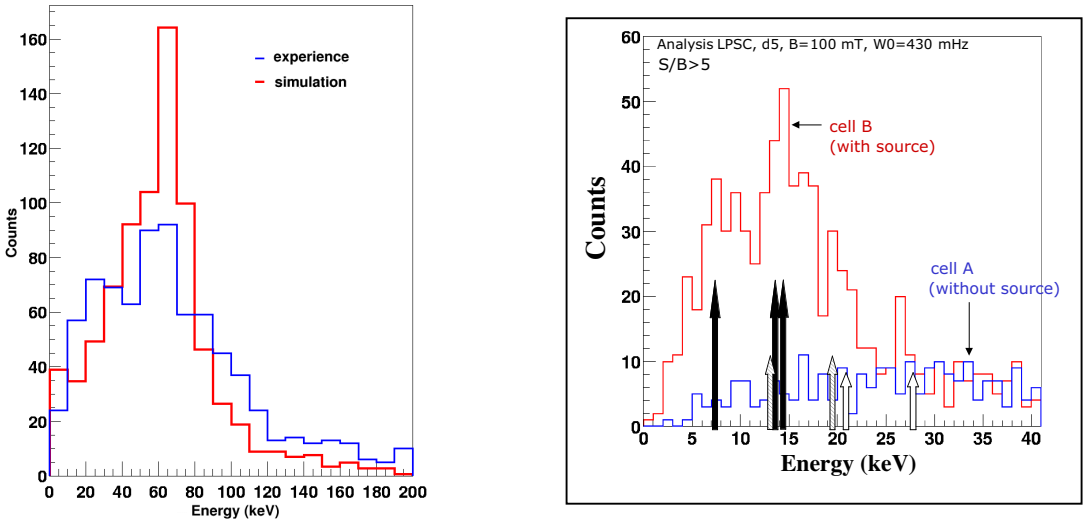

Figure 5.13: a) Muon spectrum as measured by the 3-cell prototype. The experimental data has been calibrated by comparison with the simulated spectrum.
b) Comparison of the low energy spectrum in the A- and the B-cell shows the effect of the ^{57}Co source present in the B-cell. The experimental data has been calibrated by the expected electron spectrum.
Using a calibration by heater pulses, the experimental data is shifted by 25 % to the left, indicating that not all of the deposited energy is released as heat. (both graphs: measurement by CRTBT, simulation and analysis by LPSC [20, 33]).

A comparison of the measured low energy spectrum in the B-cell with the beta emission spectrum of the ^{57}Co-source present in this cell provides the same result: the expected lines can be clearly identified but the measured spectrum is about 25% below the simulated spectrum (fig. 5.13b).

A third kind of particles detected with our bolometers are events caused by neutrons, where the neutrons come from an AmBe source placed outside the cryostat. These events are mainly neutron capture events, but neutron recoil events can be observed too. In the case of neutron capture events, the energy deficit is only about 15 % and we will see in chapter 9 that this deficit bears special interest.

The effect that not 100 % of deposited energy is dissipated as heat, also known as quenching, is well known in the dark matter detector community. In the case of the EDELWEISS collaboration for example, the total energy E_R goes to two channels: heat and ionisation ($E_R = E_H + E_I$). The quenching factor is defined as $Q = E_I/E_R$ [49]. The importance of this factor for dark matter search lies in the observation that it is different whether one observes an electronic or a nuclear recoil. As our dark matter candidate, the neutralino, is expected to only show nuclear recoil, this mechanism thus provides an important discrimination possibility if one measures ionisation and heat at the same time.

5.5 Scintillation and creation of metastable dimers

In the case of liquid Helium, it is thought that ionisation only survives a very short time when no electric field is applied to separate the charges. On the other hand, excited atomic states produced after a collision can deexcite radiatively, emitting UV-light, a phenomena called scintillation. As superfluid ^{3}He is transparent at the corresponding wavelengths, this light will only be absorbed in the copper walls and is hence "lost" for our heat detection. In order to understand the nature of this scintillation, it is necessary to study the processes from the incident particle until thermalisation. A lot of this knowledge is taken from scintillation measurements done on superfluid ^{4}He, which is investigated in detail for applications in neutrino detection [50], measurements of neutron lifetimes [51] and its electric dipole moment [52]. A good introduction as well as recent experimental results are proposed by McKinsey *et al.* [53, 54]. Following this introduction, we can explain the fast processes after an impact as follows:

As an ionising particle passes through liquid helium, most of its energy will be transferred to low-energy secondary electrons. These electrons in turn deposit their energy in a localised region of about 20 nm with high density of excited atoms. The spacing of these hot spots depends strongly on the mass and the charge of the ionising particle. As an estimation for this spacing, a simple division of the ionisation energy (=24.6 eV) by the loss ratio dE/dx yields for muons/electrons an average distance of about 1.5 μm/0.5 μm respectively. We have thus to do with spatially separated localised regions for light particles. For heavy particles, like ${}^4_2\mathrm{He}^{2+}$, ${}^1_1\mathrm{H}^+$ or ${}^3_1\mathrm{H}^+$ on the other hand, this estimation yields spacings of 1 to 3 nm, resulting in an overlap of the individual ionisation events and leading to a track of cylindrical shape.

In either case, following a quick thermalisation with the liquid helium, the electron forms after about 4 ps a bubble in the liquid, pushing away the surrounding helium atoms. The so-formed bubble has a mass of about 240 helium atom masses and moves slowly through the liquid. The He^+ ion forms after 100 ps to 500 ps together with a nearby neutral helium atom a He_2^+ dimer. After deexcitation of the vibrational excitations by inelastic scattering with the surrounding, the He_2^+ ion can react again to form a triatomic ion He_3^+, which quickly ($\approx$ 5 ps) represents the core of a "snowball" of about 40 helium masses.

Based on the initial separation of about 20 nm and the two effective masses, a typical recombination time of 0.3 ns is found, where the corresponding reaction can be described as follows:

$$(\mathrm{He}_3^+)_{snowball} + (\mathrm{e}^-)_{bubble} \rightarrow \mathrm{He}_2 + \mathrm{He}.$$

This reaction furnishes large quantities of He_2 dimers (excited states of He_2 molecules), which can be either in the singlet ($\mathrm{A}^1\Sigma_u^+$) or the triplet ($\mathrm{a}^3\Sigma_u^+$) state. The singlet states decay immediately (<10 ns) radiatively, emitting a 16 eV scintillation light (*prompt pulse).* After this quick elimination of the singlet dimers, the remaining electronic excitations are singlet atoms (2^1S), triplet atoms (2^3S) and triplet dimers. The excited atomic states can form together with a helium atom in its ground state new dimers, a process which

takes about 1.6 μs. If the so-formed dimer is in the singlet state, it will in turn radiate immediately (*afterglow*).

The triplet dimers on the other hand are metastable and have a radiative lifetime of about 13 s in liquid Helium. Note that this is the first time constant involved in the process which is not several orders of magnitudes faster than the response time of our VWR. Additionally to the radiative decay, two possibilities for non-radiative decay exist: Penning ionisation, which corresponds to a collision of two metastable dimers and which results in a partial repopulation of excited atomic states and in the release of heat, and non-radiative deexcitation after a collision with a wall.

Branching ratios

We will see that in chapter 7.2, the exact branching ratios, i.e. the weighting of the different processes involved, becomes an important parameter for explaining the different observations made.

Let us first have a look on the ratio singlet/triplet dimers. A basic estimation can be given by a simple number of states argument: if an electron is recombining with an arbitrary ion, all substates should have the same probability, which leads to a 25%/75% probability of forming singlet/triplet dimers. The measurements done by Adams *et al.* [55] on 364 keV electrons do not confirm these ratios, but suggest a ratio of 58%/42% (singlet/triplet), their explanation being that for the small ionisation densities caused by electrons, a relatively high probability exists for an electron to recombine with its parent ion, which favours the formation of singlet dimers. The processes involved are too complicated to be subject to calculations but as the initial energy density and the diffusion constant should intervene, it is doubtful to which extent measurements in ^{4}He are comparable to our conditions. We will see later that our measurements favour the ratio 1:3 given by the simple estimate.

For the questions of how much of the initial energy ends up in metastable dimers and scintillation, the same problem arises: as the processes are to complicated for a meaningful calculation we will limit ourself to some qualitative estimates and the presentation of results obtained in ^{4}He. For ^{4}He, Adams *et al.* [55, 56] found experimentally that about 35 % of the total energy produced by a 364 keV electron is scintillated by UV light in the prompt pulse. McKinsey *et al.* found that the energy scintillated in the afterglow shows half the value of the prompt pulse, which leads them together with the value of Adams *et al.* to the conclusion that the total amount of energy scintillated is about 50 % of the deposited energy, but the authors admit that this value is not very precise. For heavy particles, this ratio is measured with even less precision, but is estimated to be about half this value. The general tendency found from ^{4}He measurements is thus that for heavy particles, a significantly higher percentage goes directly to heat, and less dimers are produced.

Chapter 6

Magnetic field dependence of the calibration factor

In the bolometric experiments done in the framework of the ULTIMA project, the experimental cell is located in the same field as the one used for the nuclear demagnetisation. Due to this fact, the magnetic field can not be changed without changing temperature. Moreover, changing temperature by direct heating without varying the field is very time consuming. This is why when doing "normal" bolometric measurements, the strategy was to go to optimal temperature, and suppose that as the magnetic field is weak, the results do not depend on it too strongly.

Nevertheless, during our work on the pressure dependence of the heat release after a neutron capture reaction (chapter 9) we noticed a clear influence of the magnetic field on the calibration factor. T_c being higher at higher pressures, the largest field range can be scanned when working close to the melting pressure. In this chapter, systematic measurements done at 29.3 bar will be presented.

In order to study this effect, it would be nice to be able to regulate the temperature and the magnetic field independently, in order to scan the whole parameter space. Two problems make this difficult. The first problem is the thermometry: usually we obtain the temperature by measuring the baseline width W_{base} and applying the inverse function of eq. 5.20. However, this equation has been derived in the zero field limit. As we will see later, we consider the possibility that a magnetic field correction to this equation has to be applied. Unfortunately, the exact correction is not known, meaning that we possibly introduce an error in our conversion of the measured W_{base} to the temperature T. It should thus be kept in mind that tracing the field dependence at constant W_{base} does not necessarily correspond to an isothermal field dependence.

The second problem which prevents us from obtaining clear temperature/field dependencies is linked to the experimental setup: as the bolometric cell is in the magnetic field of the demagnetisation coil, changing the field means changing the temperature, preventing an easy isothermal measurement of the magnetic field dependence. The huge Kapitza resistance and the implied very long thermalisation after heating prevents temperature dependent measurements at constant field. The strategy used was thus to go first to a

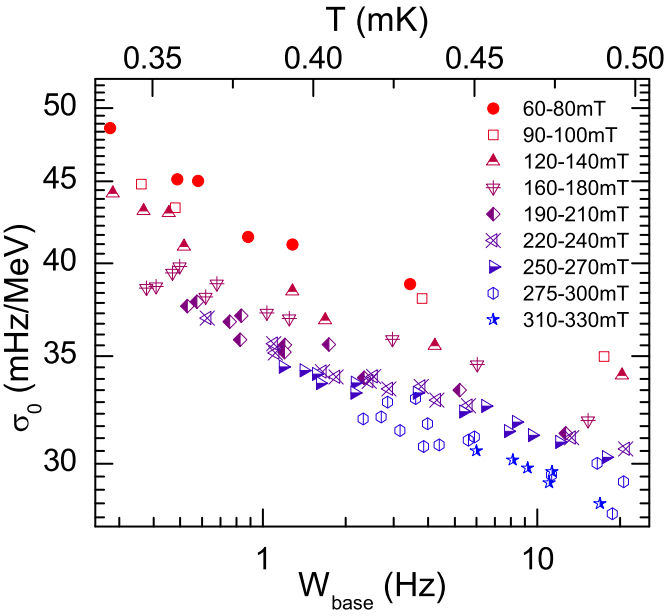

Figure 6.1: Calibration factor for different baseline width and magnetic fields (29.3 bar), all taken during one demagnetisation run. Different field strengths have been grouped together. The calibration factor is already corrected for the finite response time of the VWR, as expressed by the factor $G(W_{base})$ (see eq. 5.32). The temperature scale on the top has been obtained using eq. 5.20. As this equation does not take into account a magnetic field correction, this scale might be incorrect if the magnetic field has a noticeable effect on the VWR resonance width.

relatively small field, wait for thermalisation, do the measurement and increase the field in steps until the temperature is such that the VWR thermometer loses its sensitivity. Then go to an even lower field than before and repeat the procedure. Due to the inevitable heat leaks, when reaching by this method a second time a certain magnetic field, the temperature will then be higher. As a result, no clean temperature/magnetic field dependencies are obtained, but the total number of parameter pairs W_{base}, B measured is largely increased. It is then possible to take slices of almost constant baseline width/magnetic field.

6.1 Experimental results

In fig. 6.1, experimental results at 29.3 bar are plotted for field values between 60 and 330 mT as a function of the baseline width W_{base}. These points were all taken during one demagnetisation run. All points correspond to a series of 10 pulses with different energies injected. The energies E were taken between 200 keV and 8000 keV, depending on W_{base}, and care was taken to insure that the pulse responses H were in the linear regime, i.e. $H \propto E$. As usual, the calibration factor σ is obtained as the slope in the peak height-energy plot for one series of pulses (see section 5.3.6). All known corrections [48], especially the finite response time correction G (eq. 5.32), have been applied. The basic point of

this chapter is that systematically, higher magnetic fields correspond to smaller calibration factors.

As already explained, while we know that W_{base} contains the information about the temperature of the superfluid, we do not know the precise conversion. Unable to plot the calibration factor as a function of field for constant temperature, we instead chose to do this plot for constant W_{base}. Even if the magnetic field correction of the temperature conversion was weak, it is important to highlight that due to the exponential dependence of the heat capacity with temperature, this can have a noticeable effect.

In fig 6.2, the magnetic field dependence of σ^{-1} is shown for three different W_{base}. The reason why we preferred to plot σ^{-1} instead of σ is purely phenomenological: the inverse calibration factor seems to be linear with field on the whole field range 60 to 330 mT. Similar graphs at other baseline widths from 0.37 Hz to 10.9 Hz strengthen this observation. The experiment thus suggests that the effect of the magnetic field can be accounted for by correcting the zero field value of σ:

$$\sigma(W, B) = \sigma(W, 0) \cdot \frac{1}{1 + \gamma B}, \tag{6.1}$$

with γ being a phenomenological linear correction factor. Experimentally, γ is obtained by linear regression as presented in fig. 6.2. Two different methods have been used to obtain γ: firstly, fits can be made independently for all different W_{base}. The corresponding result is illustrated in fig. 6.3. It can be seen that while not varying a lot, the magnetic field correction seems to be more important at lower temperature. A second method is to suppose that γ is the same for all different W_{base}. In this case a correlated fit, with a common γ, but an independent $\sigma(W, 0)$ can be done. Fig. 6.2 demonstrates that this method provides very reasonable fits also, so that it can not be excluded that γ is unique on the whole temperature range of interest, with an average value of $\gamma = (1.25 \pm 0.09)\,\mathrm{T}^{-1}$.

Let us now look on the temperature dependence. In eq. 5.34 we found a theoretical temperature dependence of $\sigma(T) \propto T^{-1/2}$. Experimentally this has been already verified at low magnetic fields and at 0 bar [48]. In order to verify it in our conditions we are now confronted to the problem that we possibly do introduce an error by using for the conversion from baseline width W_{base} to temperature the formula derived in the zero field limit (eq. 5.20). Fig. 6.4a is basically the same graph as fig. 6.1, but with only three selected magnetic field ranges for a better readability. The dotted lines correspond to fits done using the equation

$$\sigma(T) = \beta T^{-1/2}, \tag{6.2}$$

with $\beta(B)$ the only fit parameter. The $T^{-1/2}$ dependence is very well confirmed, surprisingly even better for higher fields. We do not know the origin of the rather big deviation from this law at lower fields. One possibility is that the correction taking into account the intrinsic losses of the heater wire (eq. 5.36) introduces a systematic error as the internal friction is not exactly known (see section 5.3.6). This effect gets more important in the regime where the damping due to internal friction is no longer small compared to the interaction with

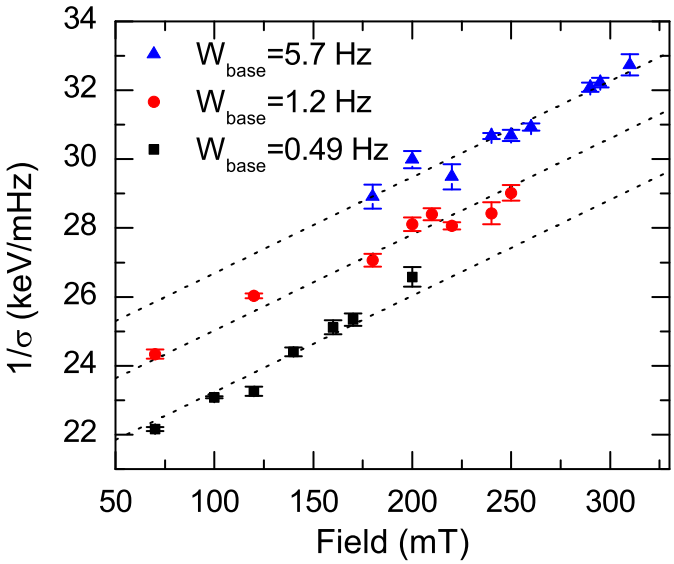

Figure 6.2: Taking slices of almost constant baseline width in fig. 6.1, σ^{-1} can be plotted as a function of the magnetic field. The dotted lines correspond to a simultaneous fit of the presented points, with a common slope $\gamma/\sigma(W_{base}, B = 0\,\mathrm{T})$, but independent offsets $1/\sigma(W_{base}, B = 0\,\mathrm{T})$. The error bars correspond to the values obtained by the linear regression in the pulse height energy plot. Fitting the data for different W_{base} independently yields slightly different slopes $\gamma/\sigma(W_{base}, B = 0\,\mathrm{T})$ (see fig. 6.3).

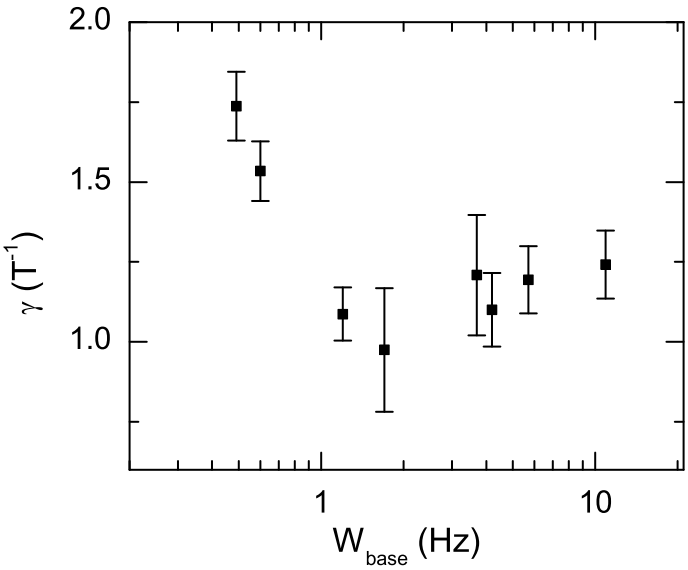

Figure 6.3: Result for the magnetic field correction factor γ for different W_{base}. The results are obtained by linear fits in the σ^{-1}/B plot. While not varying much, it still seems as if for lower temperatures, the correction increases. Nevertheless, as demonstrated in fig. 6.2, a constant γ does not seem unreasonable either, with a value of $\gamma = (1.25 \pm 0.09)\,\mathrm{T}^{-1}$.

the quasiparticle gas, i.e. at low temperature. Not considering the points for $T < 0.35\,\mathrm{mK}$, the $T^{-1/2}$ dependence is verified at low fields too.

Doing the fits presented in fig. 6.4a for all measured magnetic field ranges, we can now plot $\beta(B)^{-1}$ as a function of the magnetic field (fig. 6.4b). Another time, a linear relation with impressively small scatter can be observed. The linear fit with the equation

$$\frac{1}{\beta(B)} = \frac{1}{\beta_0}(1 + \gamma B) \tag{6.3}$$

gives us a third method to deduce the magnetic field correction value. With this method, a value of $\gamma = 1.33 \pm 0.07\,\mathrm{T}^{-1}$ and $\beta_0 = 0.89 \pm 0.01\,\mathrm{mHz\,keV^{-1}\,K^{1/2}}$ is found. We can now rewrite eq. 6.1, using β_0:

$$\sigma(W, B) = \frac{\beta_0}{T^{1/2} \cdot (1 + \gamma B)}. \tag{6.4}$$

It should be emphasised that while well describing the totality of the 29.3 bar data, this is a phenomenological formula. Nevertheless, it might be useful for future measurements as it provides a relatively easy mean for a first order correction.

The current measurements were done at 29.3 bar, but a future dark matter detector will certainly work at 0 bar. Our measurements at 0 bar indicate that a systematic effect can also be observed at 0 bar, but no dedicated measurements were done and the data from different demagnetisation runs suffer from small irreproducibilities. This means that it will certainly be necessary to confirm these observations in the final working conditions before applying the proposed correction systematically.

6.2 Discussion

Retaking eq. 5.33, one can see that a change in the value of σ should be either a result of a changing heat capacity or a change of the temperature derivative of the resonance width:

$$\sigma^{-1} = C\frac{1}{dW/dT}. \tag{6.5}$$

For both variables, obtaining the theoretical value includes an integral over the whole quasiparticle energy spectrum (for heat capacity, see [3] and appendix B, for vibrating wire width see [41]). In magnetic fields, a deformation of this quasiparticle spectrum occurs [57, 58], as the superfluid gap changes. Especially for quasiparticles with small angles between $\vec{k}$ and the magnetic field, a suppression of the gap is expected for spin up particles, while perpendicular to the magnetic field, the gap is increased. Due to this anisotropy, a change for both, the heat capacity and the wire resonance width with magnetic field can be expected. Especially the decrease of the gap parallel to the magnetic field leads to an increase in the total number of quasiparticles.

For the heat capacity, this clearly leads to an increase of its value. For the VWR resonance width it is at first not clear whether it increases or decreases its value: the

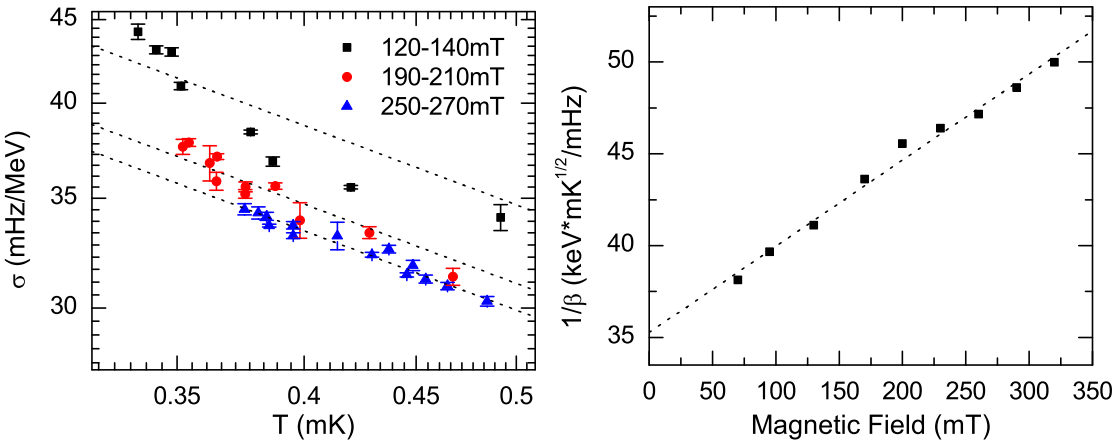

Figure 6.4: a) Using the W_{base} temperature conversion (eq. 5.20), the expected $T^{-1/2}$ temperature dependence of the calibration factor can be checked. This graph is basically the same as fig. 6.1, but for a better readability, only three field ranges are presented. Quite surprisingly, the fits, using the law $\sigma = \beta T^{-1/2}$, (dotted lines) work better for higher fields. b) Doing this temperature dependent fit for all available magnetic fields allows to show the mean effect of the magnetic field, averaged over the temperature range. Like for the plots at constant W_{base}, a linear effect is observed.

total number of quasiparticle increases, but the number of quasiparticles with the $\vec{k}$-vector parallel to the VWR velocity, which correspond to the quasiparticles transferring the largest momentum upon scattering, decreases. Anyway, the sheer number of quasiparticles with a small angle to the field outweighs the loss of quasiparticles parallel to the oscillation, leading finally to an increase of the damping. A full three dimensional calculation is a very complex subject, and must most probably include for high magnetic field values the influence of the textures on the trajectory of the quasiparticles. These textures are a priori unknown and quite complicated themselves too, and potentially even different for every demagnetisation. Nonetheless, with the arguments above, it can be stated that the influence of the magnetic field should be larger on the heat capacity than on the VWR-width. Calculating the heat capacity is much easier and a numerical application for the conditions presented in this chapter is presented in appendix B.

The calculation at 29.3 bar shows first of all that the correction due to the magnetic field is, as can be expected from symmetry arguments, quadratic in field. Secondly, the correction depends, unlike what has been observed experimentally, on temperature, with the magnetic field correction getting more important for lower temperatures. Even for the extreme cases of 0.35 mK, 180 mT, and 0.48 mK, 330 mT (see fig. 6.1), this correction is smaller than 3 % (fig. B.1), compared to an experimentally observed influence of the magnetic field of about 40 % (i.e. ten times stronger). As the corrections on the VWR-width are even smaller than these values, and tend to decrease the total effect due to the gap deformation, we conclude that the observed magnetic field dependence must have another origin than this deformation of the gap.

Another idea for a potential explanation was that possibly the rebaking process was not perfect (see chapter 8), and that parts of the cell surfaces were still covered with solid ^{3}He. Following chapter 8, this would lead to an addendum specific heat, linear in magnetic field, due to the heat capacity contribution of these layers. We refute such a possibility for two reasons: firstly, the corresponding deformation of the observed peaks, i.e. the appearance of a second time constant was not observed. A second and more import reason is that the observed temperature dependence in this chapter follows very well the expected $\sigma \propto T^{-1/2}$ law. The addendum specific heat was shown to depend nonexponentially on temperature, which would result in a significant deviation from this law for the calibration factor.

Chapter 7

A detailed analysis of the recovering time: A possible discrimination mechanism?

One of the most important features of any direct dark matter detector is the capability to discriminate "false events", i.e. heating events which are not due to an interaction with a dark matter particle. The principal sources of this background noise are cosmic muons or neutron-, electron- and γ-radiation from ambient radioactivity. In order to be able to reject background events, one has to study the differences between the corresponding interactions. The exact properties of dark matter are still unknown, but existing experiments like dark matter detectors, cosmic observations and accelerator experiments already put some constraints on its parameters. For all dark matter candidates our bolometer would be sensitive to, including the neutralino ($\tilde{\chi}$), the following essential characteristics are known:

1. Due to its very weak interaction the dark matter particle has at most one collision in the bolometer.

2. The dark matter particle only produces a nuclear recoil and has no interaction with the electrons.

3. The deposited energy is smaller than 6 keV[1].

The main discrimination mechanism intended for our detector is based on the first point: "normal" particles have a high probability to interact more than once in the ^{3}He. By an intelligent design of a bolometer matrix, it is possible to look for coincidences. As the probability for a $\tilde{\chi}$ to show coincident events is practically zero, this already provides a very strong discrimination mechanism. One main idea behind the current experimental setup was to prove that this concept works and as can be seen in fig. 5.8, it has indeed been

[1]This is strictly speaking only true when using the assumption that dark matter is in rest with our galaxy. This means that higher recoil energies are a priori not excluded completely.

shown that coincidences appear. Simulations done by Mayet *et. al.* [18, 19] show that an example matrix design of 10^3 cells provides already a very good background rejection.

The details of the calculation/simulation of the rejection coefficient are quite complex and depend on the nature and the energy of the incoming particle. For the worst case of a 10 keV neutron it was found that only one out of 75 events will be confounded with a dark matter particle. Making additional assumptions on the corresponding particle flux and energy distribution in an underground laboratory environment, a total false event rate after discrimination of about 0.1 events per day is predicted for a 10 kg detector containing 10^3 cells. A second discrimination is achieved by using the third point: especially neutrons, usually difficult to discriminate, have a high probability to undergo a neutron capture reaction with ^{3}He nuclei, a reaction which releases a well defined energy of 764 keV. This inherent discrimination mechanism constitutes one of the biggest advantages of using ^{3}He as a sensitive medium.

The second point is used in most existing dark matter detectors. As mentioned in section 5.4, the quenching factor for a nuclear recoil and an electron recoil is different. By a simultaneous measurement of heat release and scintillation/ionisation it is thus possible to discriminate muon-/electron events from neutron-/WIMP events. The possibility to use such a second channel for our system has been considered and especially the use of an ionisation detector might be feasible. But the constraints presented by the necessity to work at ultra low temperature certainly makes this a non-trivial task.

In this section we will show that the shape of the event peak, especially the thermalisation time constant τ_b (see section 5.3.3), seems to depend on the nature of the energy deposition, i.e. that the shape of the peak after a muon event is different than after a neutron event, at least in the studied region down to 50 keV. If this can be confirmed down to the interesting energy region of 1 keV, then a pulse shape analysis will provide us with an additional discrimination mechanism. The big advantage of this discrimination would be that it does not need an additional experimental implementation.

7.1 Statistical analysis of the recovering time

In order to study a possible influence of the interaction type on the peak shape, a statistical analysis of a relatively large dataset has been made. As we wanted to compare at least two different kind of interactions, the data was taken in the presence of an AmBe neutron source, placed outside the cryostat. This allows us to compare neutron capture-, neutron recoil-, muon- and heater events. Fig. 7.1a shows about one hour of a typical acquisition file in the presence of a neutron source and fig.7.1b shows a zoom on a single peak together with a fit using eq. 5.31. This figure illustrates well that the quality of the fit is very good, even for peaks of moderate amplitude.

For the purpose of analysing a large number of events, a semi-automatised program has been written, using the following algorithm:

- Search for peaks in the derivative of the width as a function of time to locate the

start of events. The criteria used is to have four consecutive points above a given threshold.

- Take about 30 points before the peak start and do a fit using a constant to determine W_{base} and hence $\tau_w = 1/(\pi W_{base})$.
- Take a slice of about 100 points ($\approx 13\,\mathrm{s}$) and fit with eq. 5.31

$$W_{mes}(t) = W_{base} + A\frac{\tau_b}{\tau_b - \tau_w}\left[\exp\left(-\frac{t-t_0}{\tau_b}\right) - \exp\left(-\frac{t-t_0}{\tau_w}\right)\right]\Theta(t-t_0) \quad (7.1)$$

  with the free fitting parameters being t_0, τ_b, A.
- Check by eye whether the fit looks reasonable. If yes, keep it otherwise dismiss this peak.
- Check by eye for coincidences with the neighbouring cell. If yes, mark the event with a flag.

Checking the fits by eye is necessary mainly due to the fact that the baseline is not always stable, especially if an event happens before the previous one is completely thermalised. A simple χ^2 test was not reliable enough to deal with small events happening on the tail of a previous event. Note that the analysis leading to the muon and electron spectrum shown in fig. 5.13, and resolving events down to 1 keV was done without fitting the peaks with their analytical form. In this way it was possible to determine the peak height distribution down to very small energies, but it did not provide results for the distribution of τ_b (see [47]).

Additionally to the fits done on particle events, the events simulated by heater pulses were evaluated. Due to the slightly changed shape at the start of the peak (see fig. 5.11), the usual peak form (eq. 5.31), while still providing a good fit, shows systematic deviation. No analytic form can be found for the differential equation describing the response to a heater pulse. The fit was thus made using as fit function a numerical integral of the differential equation.

7.1.1 Experimental distribution of the recovering time

In fig. 7.2a, the results for an acquisition during one experimental run in 48 h as well as the results of heater pulses taken in the same demagnetisation run are presented. The points have been distinguished as:

- Neutron capture events, identified by the peak height.
- Low energy ($<$600 keV) events showing coincidences.
- Low energy events without coincidences in the B-cell.
- Heater pulse events.

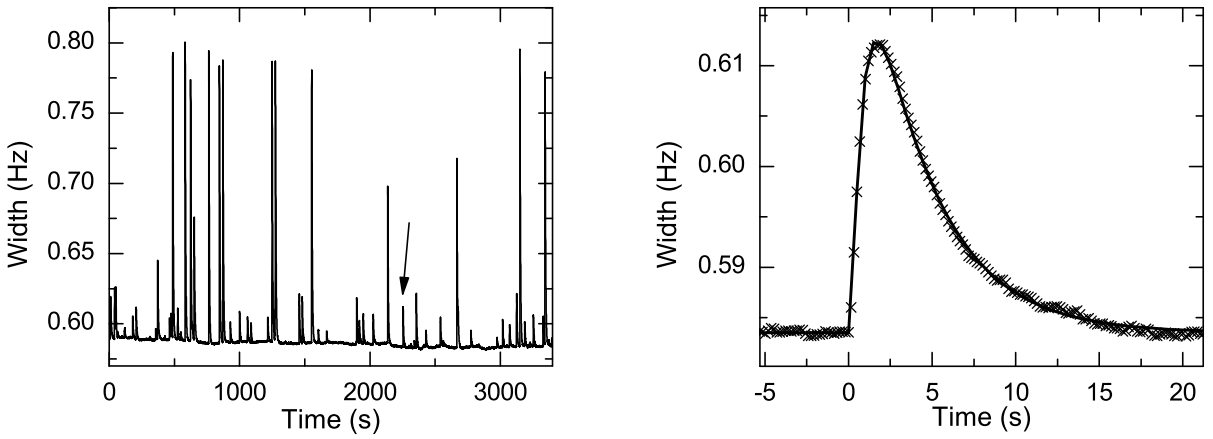

Figure 7.1: (a) About one hour of a typical acquisition file at 0 bar in the presence of a neutron source. The events of about 0.2 Hz peak height are neutron capture events, the events of smaller peak height are mostly caused by muons, but some might have their origin in neutron recoil events. (b) A zoom on the event marked by an arrow. The solid line is a fit using eq. 7.1. For this peak, most probably caused by a cosmic muon, the fit yields a value of $\tau_b = 3.79 \pm 0.03$ s.

The striking feature is the appearance of two distinct regions of τ_b values. All neutron capture and heater events are exclusively in the band of smaller τ_b values, with the heater events even slightly lower than the neutron capture events. All events showing coincidences are in the band of larger τ_b. Most events showing no coincidences are found in the upper band, but a noticeable part is found in the lower band.

The importance of looking for coincidences can be explained as follows: cosmic muons can come from the whole upper solid angle. This means that a part of the incoming muons travels through the B-cell before reaching the C-cell, leaving an energy in both cells. The rest enters the C-cell from the side-wall, leaving an energy only in the C-cell. The neutron source on the other hand is placed outside the cryostat at the same height as the cell. While it is still possible that a neutron scatters in the B-cell, then changes its direction and scatters again in the C-cell (or vice-versa), these events should be extremely rare, especially when considering the small cross section for an elastic neutron scattering (see fig. 4.3). In short, all events showing coincidences are caused by muons, the events showing no coincidences can be both, muon or neutron recoil events.

We thus conclude that the region $3.7\,\text{s} < \tau_b < 4.5\,\text{s}$ in fig. 7.2b where we find events with and without coincidences corresponds to muons, and the region $\tau_b < 3.6$ s where not a single coincidence has been found corresponds to neutron events.

To reinforce this point even more, a comparison can be made to an acquisition taken without the presence of a neutron source. Such a comparison is presented in fig. 7.3 in the form of a histogram of τ_b-values. Without the presence of a neutron source, it is expected that virtually all events are caused by muons. And indeed, it is found that the distributions for events with and without coincidences look the same, and both correspond very well

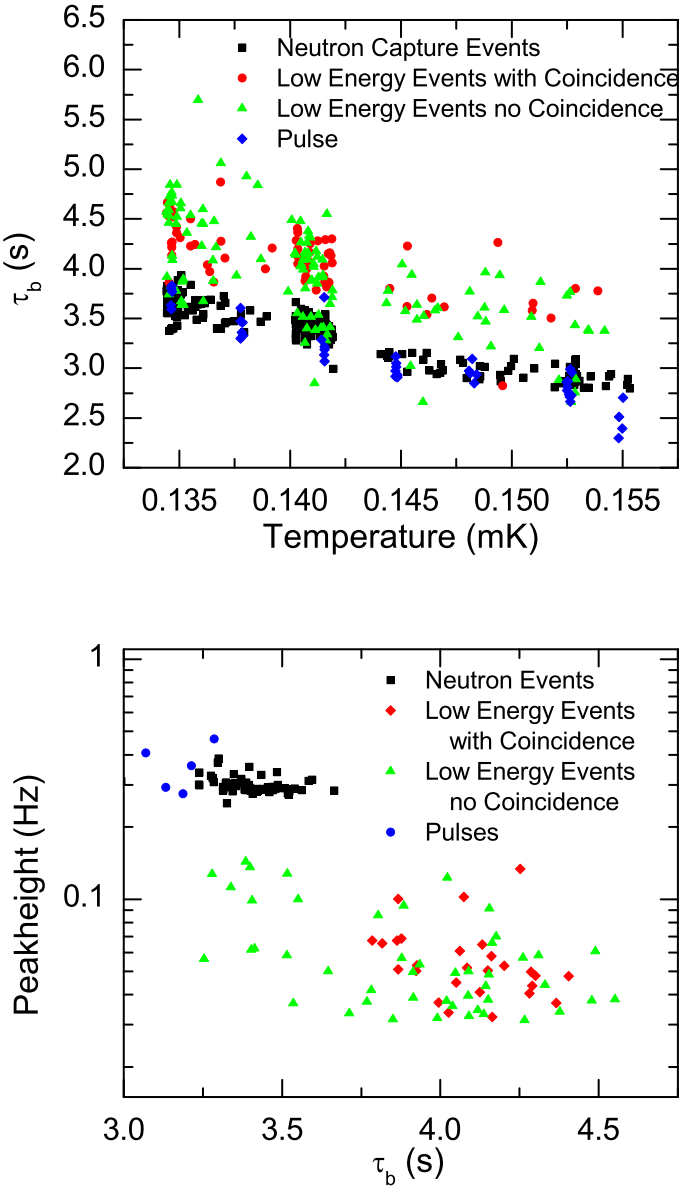

Figure 7.2: Values for τ_b obtained from the analysis of a total of 48 h of acquisition in the C-cell, all done during one demagnetisation run. Every point corresponds to the τ_b obtained from one fit. The results are separated in three categories: neutron capture events, identified by the peak height of about 300 mHz, low energy events with and without coincidences in cell B. Additionally the results obtained by heater pulses are presented. a) τ_b as a function of temperature. A clear gap can be seen between two distinct regions. All neutron events are in the lower band. Low energy events can be found in both, the higher and the lower band, but all low energy events appearing in the lower band show no coincidence with cell B. The gaps on temperature axis are due to experimental reasons, like warming during ^{4}He transfers. b) For a small slice of temperature around $0.140\,\mathrm{mK} < T < 0.143\,\mathrm{mK}$, the peak height as a function of τ_b. The separation of the two regions of different τ_b values is even clearer. We conclude that events produced by muons show longer thermalisation time constants than nuclear capture, nuclear recoil and heater events.

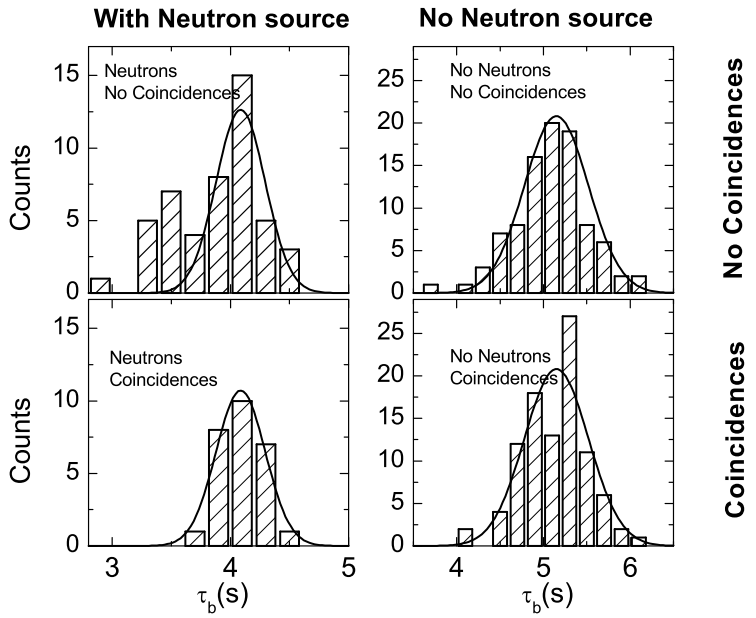

Figure 7.3: Histograms of the τ_b values distribution of low energy events (<500 keV) can be used to illustrate the differences observed between presence/absence (left/right column respectively) of a neutron source and separated in events showing/not showing coincidences (lower/upper row respectively). The solid lines correspond to a fit of the events with coincidences. This fit is then superimposed to the histogram without coincidences. It is obvious that in the case of the absence of a neutron source, this works very well, as expected if all events are due to muons. With a neutron source present, a second peak in the histogram of events without coincidences appears. This second peak is thus associated to events caused by elastic neutron scattering.
The absolute values of the τ_b obtained without a neutron source are higher because the corresponding temperature was lower, and the distribution is broader because the signal to noise ratio was less favourable.

to a Gaussian distribution. In the case of the presence of a neutron source, a Gaussian distribution is found when one only considers events with coincidences. For events without coincidences, a second peak with lower τ_b values appears. We attribute this second peak to neutron elastic scattering events.

7.2 The effect of a delayed heat release

Let us now look at a possible explanation of the data. According to our underlying assumptions, the fact that τ_b depends on the nature of the interacting particle should not be possible: until now it was thought that the energy deposition by a particle is quasi instantaneous and that subsequently the thermalisation inside the box is of the order of 1 ms. This estimation comes from the argument that as we are working in the ballistic limit, the only possibility for thermalisation is by inelastic scattering of QPs with the Helium close to/ adsorbed on the walls of the cell. The corresponding time constant should thus be the

time of flight of a QP towards the wall:

$$\tau_v \approx L/\bar{v}_g = \sqrt{\frac{\pi}{2}}\frac{L}{v_F}\sqrt{\frac{\Delta}{k_B T}} \approx 0.3\,\mathrm{ms} \tag{7.2}$$

The details of the inelastic scattering of non thermal QPs on the wall is to our knowledge not known, but even considering that about 100 collisions are necessary for thermalisation, this time is still faster than the acquisition rate and the response time of the wire. Once the cell is in inner equilibrium, all trace of the nature of the particle should be lost, and there should be no difference in τ_b.

In order to get an idea of possible mechanisms which explain this surprising result, let us first review the known differences for the particle's interaction (see section 5.4):

- Muons deposit their energy by elastic scattering with the atomic electrons. Each interaction leaves a relatively small energy of the order of 100 eV, but the cross section being large, a muon crossing the cell will scatter multiple times. We have thus to deal with several separate regions of relatively small energy density.

- Neutron capture events are due to a nuclear reaction of the incoming neutron with a ^{3}He nucleus: $n + {}^3_2He \rightarrow p + {}^3_1H$. In this reaction a total of 764 keV is released and distributed in the first place as kinetic energy to the proton (573 keV) and the tritium (191 keV), which after the reaction depart in opposite directions. Subsequently, the energy is transmitted through secondary processes to the superfluid, mainly via scattering with atomic electrons. The mean distance between the different scattering events of the products is small, leading to a highly energetic region of approximately cylindrical shape (see fig. 9.1 [59]).

- The cross section for neutron recoil events is almost independent of the neutrons kinetic energy and has a value of about $\sigma_{el} \approx 2$ barn, which corresponds for ^{3}He at 0 bar to a mean free path of $\lambda_{el} \approx 20$ cm (see fig. 4.3). This means that if such an event is observed, it most probably corresponds to one single recoil. The ^{3}He nucleus which has gained in this way some hundreds of keV, will afterwards lose its kinetic energy in secondary processes in a small volume. No simulation for this process exists, but as the mass, charge and kinetic energy are quite close to the tritium produced in the capture reaction, the numbers should be comparable to those found above.

- Our heater pulses were done with the heater wire not exceeding the pair breaking velocity. This means that all what the wire is doing is to accelerate existing quasiparticles, which subsequently thermalise via the cell walls. The introduction of heat is very different than in the former cases, as at no moment we have energy densities which allow ionisation of ^{3}He atoms or formation of vortices.

The main difference between muon and neutron events is thus that the energy density just after the event and around the location of the event is much higher in the case of neutrons. This difference in energy density leads to a difference in the subsequent processes leading to

varying ratios of scintillated light emitted, metastable triplet dimers created and metastable vortices created (see section 5.4 and 5.5).

If the calculations presented in appendix A are correct, then a change in τ_b can only be related to a change in the heat capacity or a changing mean heat flux. Based on the facts presented above, we could not find a consistent explanation for either, so the next logical step was to consider the possibility that one of the basic assumptions was wrong, or at least only partly correct.

7.2.1 Simulations of partly delayed energy deposition

Our best guess for such a "wrong" assumption was to question the hypothesis that the energy deposition is quasi instantaneous. Until now, we never doubted this hypothesis, mainly because eq. 5.31 which describes very well the shape of an event is based on it. Especially the sharp rise at the leading edge of an event is a strong indication of a quasi instantaneous rise of the quasiparticle density. In the following, we thus have to find a model which explains both, the sudden rise at the beginning, and the retarding effect for the tail of the pulse. Our idea, which as we will demonstrate has good success in explaining all the observations, was to imagine that the total deposited energy A_{tot} can be classified in three categories (fig. 7.4):

- A_h, the fraction of the energy which is released as heat immediately.

- A_m, the fraction of the energy which is stored in metastable states and released (completely or partially) as heat with a time constant τ_m, of same order of magnitude as τ_b.

- A_l, the fraction of the energy which is "lost", i.e. which does not contribute to the observed peak at all because it is either completely lost (like for example scintillated light), or which is stored in metastable states which have a time constant much longer than τ_b.

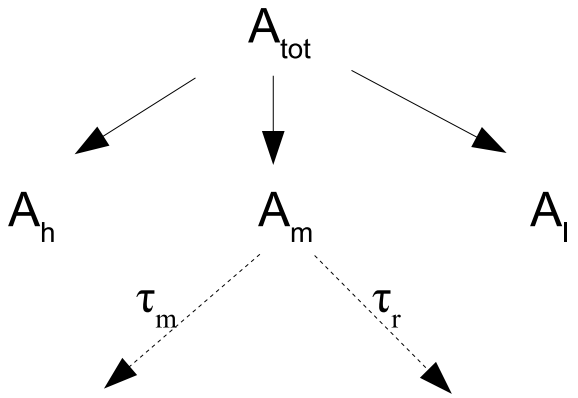

Figure 7.4: The total energy can go to three channels: energy dissipated as heat immediately A_h, energy "lost" A_l or energy stored in metastable states A_m. These metastable states can in the most general case either release heat with a time constant $\tau_m \sim \tau_b$, and influence the peak shape in a non trivial way, or lose their energy otherwise with a time constant τ_r.

The simplified case of $A_l = 0$

In a first step we want to demonstrate how assuming that there exists a fraction of the energy which is released not immediately as heat could explain an increase of the observed value of τ_b. The basic ansatz was to imagine that after an incidence, yielding a total energy A, only a fraction $A_h = (1-p) * A$ is transformed into heat immediately, and that the remaining fraction $A_m = p * A$ is stored in metastable states, releasing their energy as heat with a time constant τ_m.

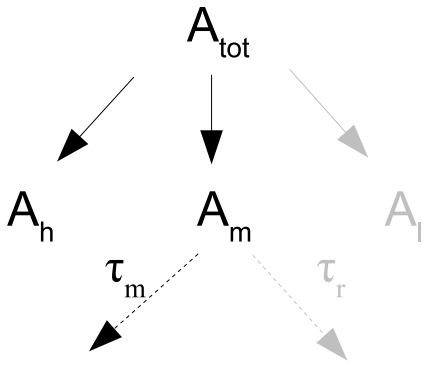

Figure 7.5: In a first step we show a simple model where we put $A_l = 0$ and we do not admit the possibility that the, still not specified, metastable states lose their energy in another way than through heat release.

As the principal candidate, we suspect the triplet dimer, which leads us, considering the measurements done on superfluid ^{4}He, to a first estimation of $p \approx 0.25$ for light particles, but obviously this analysis works assuming any metastable state storing a substantial part

of energy. As a priori we do not know the law according to which these metastable states decay, the natural assumption was to consider an exponential decay, giving a heating power of[2]

$$P_m(t) = \frac{A_m}{\tau_m}\exp(-t/\tau_m)\Theta(t). \tag{7.3}$$

The instantaneous heating can be expressed using Dirac's delta function,

$$P_i(t) = A_h\delta(t), \tag{7.4}$$

and the cooling power, corresponding to the thermalisation via the orifice, can be modelled considering it to be proportional to the difference of QP density inside and outside the box:

$$P_b = \frac{1}{\tau_b}(W(t) - W_{base}). \tag{7.5}$$

We consider the cell being in equilibrium with the bath before the impact (i.e. for $t < 0$: $W_{eq}(t) = W(t) = W_{base}$), where the index eq indicates the VWR equilibrium position while the indexless variable corresponds to the measured width. Due to the Dirac function we then have directly after the impact $W_{eq}(t = 0) = W_{base} + A_h$. For $t > 0$, the equilibrium width can be calculated using the following differential equation[3]:

$$\frac{dW_{eq}(t)}{dt} = -\frac{1}{\tau_b}(W_{eq}(t) - W_{base}) + \frac{A_m}{\tau_m}\exp(-t/\tau_m), \tag{7.6}$$

the solution of which is (for t>0)

$$W_{eq}(t) = W_{base} + A_h e^{-t/\tau_b} + A_m\frac{\tau_b}{\tau_b - \tau_m}\left(e^{-t/\tau_b} - e^{-t/\tau_m}\right). \tag{7.7}$$

The measured wire width is then obtained as a solution of the following differential equation, with the initial condition $W(t = 0) = W_{base}$:

$$\frac{dW(t)}{dt} = -\frac{1}{\tau_w}\left(W(t) - W_{eq}(t)\right), \tag{7.8}$$

which finally leads to

$$\begin{aligned} W(t) &= W_{base} + A_h\frac{\tau_b}{\tau_b - \tau_w}\left(e^{-t/\tau_b} - e^{-t/\tau_w}\right) + A_m\frac{\tau_b}{(\tau_b - \tau_w)(\tau_m - \tau_w)(\tau_b - \tau_m)} * \\ &\quad * \left(\tau_b(\tau_m - \tau_w)e^{-t/\tau_b} + \tau_w(\tau_b - \tau_m)e^{-t/\tau_w} - \tau_m(\tau_b - \tau_w)e^{-t/\tau_m}\right), \end{aligned} \tag{7.9}$$

[2] In order to simplify the equations, we consider the event to happen at $t_0 = 0$.

[3] It is good to remember at this point that for small enough events, talking in terms of enthalpy density, quasiparticle density and equilibrium VWR-width is equivalent. We hence express the deposited energy in units of Hz.

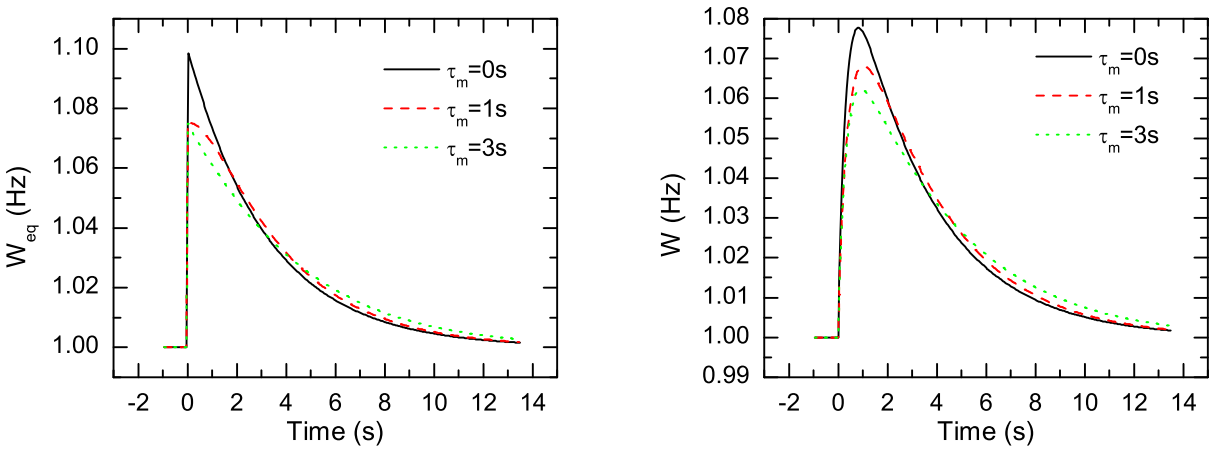

Figure 7.6: Simulation of a particle event with partly delayed energy deposition, using eq. 7.7 for the equilibrium wire width (left hand side) and eq. 7.9 for the response of the wire (right hand side). The parameters used are $W_{base} = 1\,\mathrm{Hz}$, $A = 0.1\,\mathrm{Hz}$, $p = 0.25$, $\tau_b = 3.25\,\mathrm{s}$. In addition to the value $\tau_m = 0\,\mathrm{s}$, which corresponds to the "normal" case of immediate energy deposition, two other values for τ_m are chosen to illustrate the delay, and peak height reduction effect. The obtained peak shapes look very similar not only by eye. Fig. 7.7 illustrates that a fit using the usual peak form is very reasonable.

with $\tau_w = (\pi W_{base})^{-1}$ being as usual the response time of the wire. It can be seen that the first two terms correspond to the usual peak form as presented in eq. 5.31, but with a reduced peak height $A_h = (1-p) * A$, and that we have a rather complicated additional term, which depends on the new time constant τ_m.

In order to get an idea about the influence of this term, simulations can be made using reasonable guesses for its parameters. Fig. 7.6 shows such simulations, using the following parameters[4]: $W_{base} = 1\,\mathrm{Hz}$, $A = 0.1\,\mathrm{Hz}$, $\tau_b = 3.25\,\mathrm{s}$, $p = 0.25$. It can be seen that in the limit $\tau_m \to 0$, the peak form is the usual one, but that for values $\tau_m \approx \tau_b$, the effective decay gets longer and the measured peak height is reduced, while the general shape does not change very much.

The important question is now whether such a modified peak can be mistaken for a peak of the usual form, and what the influence on the measured τ_b^* will be. To answer this question, a simulated dataset using the modified peak form, described by eq. 7.9, can be created, which is afterwards fitted using the peak form equation 5.31. In fig. 7.7, such a fit is illustrated using the same parameters as above and $\tau_m = 3\,s$. As can be seen, despite the fact that with $p = 0.25$ and $\tau_m \approx \tau_b$ parameters with relatively large influence on the shape have been chosen, the fit works rather well. The interesting point is that the obtained fit parameter for the thermalisation time constant is with a value of $\tau_b^* = 4.28\,\mathrm{s}$

[4]The first three values are typical values obtained experimentally (see fig. 7.2, $W_{base} = 1\,\mathrm{Hz}$ corresponds to $T \approx 0.142\,\mathrm{mK}$, and $A = 0.1\,\mathrm{Hz}$ corresponds to a relatively high energy muon event), the fourth value is an estimation using the typical fractions of dimers produced, as observed in ^{4}He scintillation measurements.

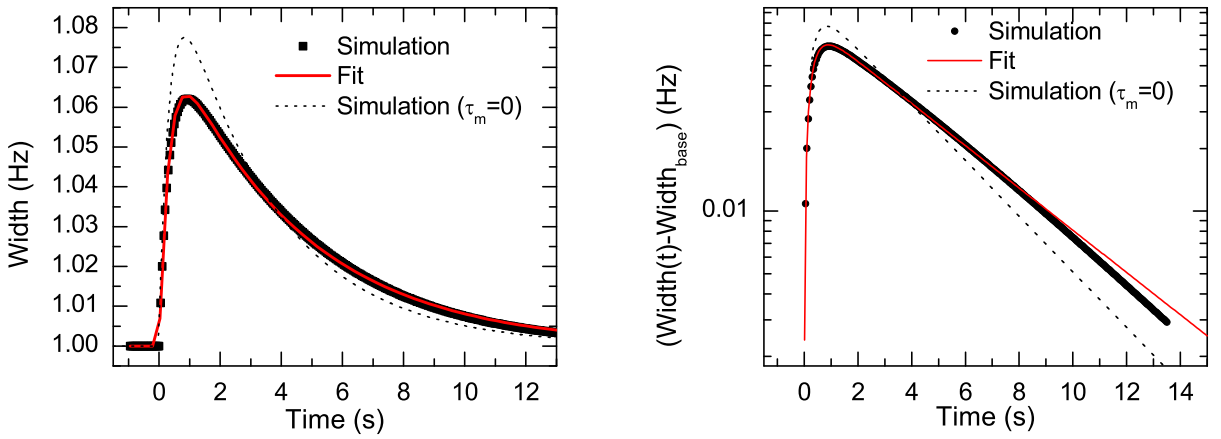

Figure 7.7: Using eq. 7.9, an event with partial delayed energy deposition is simulated (bold squares) with the following parameters: $W_{base} = 1\,\mathrm{Hz}$, $A = 0.1\,\mathrm{Hz}$, $p = 0.25$, $\tau_b = 3.25\,\mathrm{s}$, $\tau_m = 3\,\mathrm{s}$. Afterwards, the data is fitted (solid line) using the "normal" peak form equation (eq. 5.31) which is derived from the assumption of an immediate heat deposition. A peak of "normal" shape corresponding to a simulation with $\tau_m = 0$, but otherwise using the same parameters is plotted (dotted line) to illustrate the difference. The obtained fit parameters are in this case $A^* = 0.0777\,\mathrm{Hz}$, $\tau_b^* = 4.28\,\mathrm{s}$. The effect of this modified peak form is hence to simulate an event of "normal" peak form, but with an increased apparent box time constant τ_b^*, and a reduced peak height A^*.

largely enhanced compared to the box time constant $\tau_b = 3.25\,s$ used to create the dataset. Remembering that an exponential decay of the metastable states is only a first guess, that real measured data suffers from noise and that in the real case, the baseline is not 100% stable, it can be concluded that the presented mechanism could indeed explain the increased τ_b by "faking" an event of the usual shape. In order to test the new formula further, the most intuitive idea is to redo a new statistical analysis, this time using the modified equation for the fits. But unfortunately, introducing two additional parameters would lead to a total number of 5 fit parameters. As the newly introduced parameters p and τ_m have only a small influence on the shape of the peak, no significant fit results can be obtained, despite the good quality of the measured data.

An alternative strategy has thus been employed to look in detail at the implications of this hypothesis and to check which set of parameters p, τ_m would be compatible with the experimental results: A large number of simulations, similar to the one presented in fig. 7.7, has been made to sweep the whole parameter space. The procedure for these simulations is as already explained :

- Create a simulated dataset for a given set of parameters W_{base}, A, p, τ_b, τ_m using the modified peak form eq. 7.9.
- Fit this dataset using the "normal" peak form eq. 5.31, with W_{base} fixed, and A^*, τ_b^*,

t_0 as fitting parameters.

- Save results to a file and exploit them.

Plotting these results as a function of the different parameters allows us to verify to which extent this hypothesis is consistent with experimental results. Before looking at these figures, it is good to remember briefly the features that are required for muons from our experimental results presented above: Using the heater pulses as the reference, we get for the time constant the condition that $\tau_b^*/\tau_b \approx 1.25 \pm 0.05$, independent of W_{base} and A. From the observed energy deficit we know that[5] $0.77 \leq A^*/A$. Fig. 7.8 shows the result for such simulations as a function of τ_m, with the parameters $W_{base} = 1\,\mathrm{Hz}$, $\tau_b = 3.25\,\mathrm{s}$ and $A = 0.1\,\mathrm{Hz}$ fixed.

In Fig. 7.9 results for fixed τ_m but varying W_{base} are shown. The main message from this graph is that the dependence of τ_b^*/τ_b and A^*/A with W_{base} is very weak.

Adding the possibility of losses by radiative decay

From these graphs we can already see the scale on which this effect plays a role, but before going into detail, we have to consider some important modification: up to now we have not made any assumption on the nature of these metastable states. To our knowledge, the only two mechanisms which can store a significant amount of energy and are stable on the necessary timescale are vortices produced after the rapid expansion of a hot spot and the triplet dimers. For muons we know that more dimers are created than in the case of neutron events, and we expect that no vortices created. As the delaying effect is larger for muons than for neutrons, we strongly favour the hypothesis that it is the triplet dimers which are mainly responsible for this effect, in which case the above analysis must be slightly corrected: the triplet dimers do not necessarily decay non-radiatively but they can also decay through the radiative channel. The time constant $\tau_r = 13 \pm 2\,\mathrm{s}$ is known from scintillation measurements in ^{4}He. As scintillated light will be absorbed only in the walls, this means that the heating power due to triplet excimers is reduced compared to what we thought before.

[5] Considering that other processes like scintillation and vortex creation can explain the deficit, we only have a lower bound.

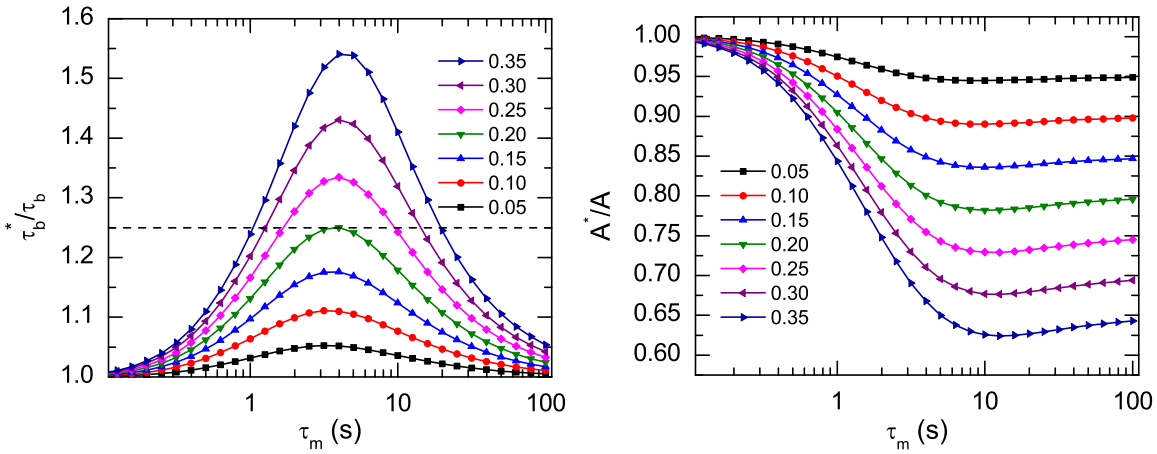

Figure 7.8: Results for τ_b^*/τ_b and A^*/A found on fitting with eq. 5.31 datasets created with eq. 7.9 using different parameters. These graphs do *not* consider the losses of energy through radiative decay of the metastable states. Fixed parameters : $W_{base} = 1\,\text{Hz}$, $A = 0.1\,\text{Hz}$, $\tau_b = 3.25\,\text{s}$. The different lines correspond to different values of the parameter p, chosen between 0.05 and 0.35.
a) Searching for the intersection of the dashed $\tau_b^*/\tau_b = 1.25$ line with the curves obtained by these simulations, gives the combinations of τ_m and p which are compatible with the experimentally observed increase of $\tau_b^* \approx 1.25 * \tau_b$. This graph thus shows that if this hypothesis is the correct explanation for the increased box time constant, τ_m necessarily has to be of the same order of magnitude as τ_b. A consistent couple of parameters would for example be $p = 0.25$ and $\tau_m = 1.5\,\text{s}$.
b) If a considerable fraction of the energy is dissipated as heat only after the peak has reached its maximum, the peak height necessarily is reduced compared to an immediate heat release. The exact reduction in peak height due to this effect can be seen on this graph as a function of the parameters p and τ_m. The two limiting cases are no peak height reduction if $\tau_m \ll \tau_b$, and a peak height reduction of p if $\tau_m \gg \tau_b$. The fact that a minimum is found at $\tau_m \approx 10\,\text{s}$ is a mathematical artifact which should have no physical meaning.

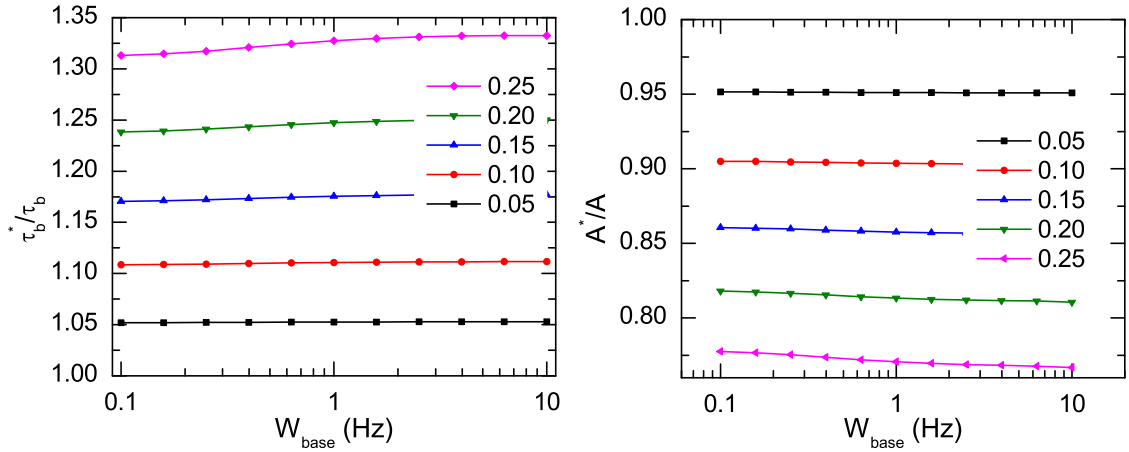

Figure 7.9: W_{base} dependence of τ_b^*/τ_b and A^*/A for fixed $\tau_m \approx \tau_b$. This graph shows that while a baseline dependence, especially for τ_b^*/τ_b exists it is rather small, and would thus be hard to be seen in an experiment. In the following we will thus limit our analysis to one fixed baseline $W_{base} = 1\,\mathrm{Hz}$. The different lines correspond to different values of p

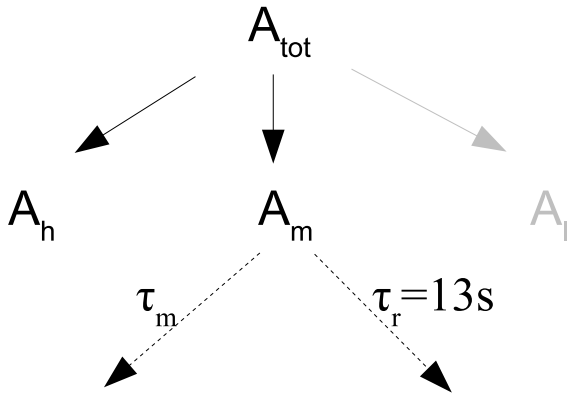

Figure 7.10: In this next step, we still keep $A_l = 0$, but we assume now that the previously unidentified metastable states are triplet dimers. For these triplet dimers it is known that they can decay radiatively with a time constant of $\tau_r = 13\,\mathrm{s}$. The corresponding energy will be lost for the heat measurement.

Mathematically it can be taken into account by multiplying the heating power (eq. 7.3) with the term $\exp(-t/\tau_r)$, which is equivalent to replacing the parameter $1/\tau_m$ in the exponential by $1/\tau_m + 1/\tau_r$:

$$P_m(t) = \frac{A_m}{\tau_m} \exp\left(-t * \left(\frac{1}{\tau_m} + \frac{1}{\tau_r}\right)\right). \tag{7.10}$$

The solutions of the differential equations basically remain the same, and especially eq. 7.9

still applies, with the partial substitution[6] $1/\tau_m \to 1/\tau_m + 1/\tau_r$. The analogous result to fig. 7.8 for the fixed parameters $W_{base} = 1\,\mathrm{Hz}$, $\tau_b = 3.25\,\mathrm{s}$ and $A = 0.1\,\mathrm{Hz}$ can be found in fig. 7.12. As can be seen, allowing the metastable states to deexcite by the radiative channel, reduces the delaying effect for the same set of parameters, which means that in order to be compatible with experiment, a higher percentage of energy has to go to the metastable states.

The next step is to create a curve for the combinations of p and τ_m which are compatible with the experimental results, i.e. the observed value of τ_b^*. This corresponds to finding the intersection of the horizontal lines with the different curves in fig. 7.12a. For all of these pairs of parameters p, τ_m, it is then possible to determine which reduction on peak height corresponds to these parameters. The results of these operations are presented in the figures 7.13a and b. Looking at the resulting peak height reduction is very important, as we have experimental information on what we called until now the energy deficit (see section 5.4). As we can see from figure 7.13b, triplet excimers already can account for a large fraction of the the observed energy deficit of 23% for muons.

Adding additional losses

In the beginning of this section we mentioned the possibility that part of the energy, A_l does not contribute to the peak at all, but in order to simplify the above analysis, we set $A_l = 0$.

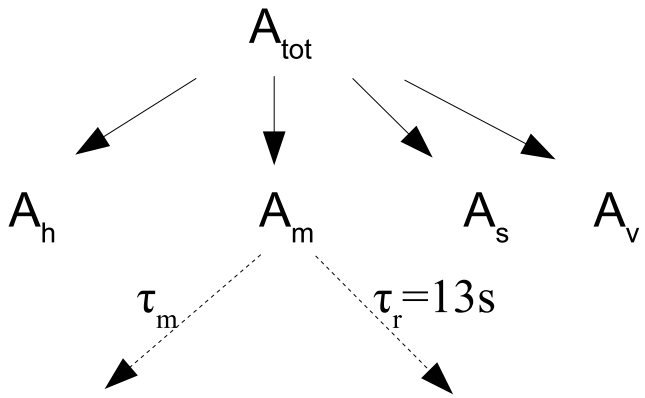

Figure 7.11: In this final step we add the possibility of energy being lost completely for the heat measurement. This means that it is either scintillated (A_s) or stored in other metastable states (A_v) with very long life times (with vortices being the only candidate we can think of).

The experiments done on scintillation of ^{3}He and ^{4}He tell us that if we create triplet excimers, we necessarily create singlet excimers too. For these singlet excimers we know that they will radiate UV-light quasi instantaneously, and that the corresponding energy

[6] As we substituted $1/\tau_m$ only in the exponential function, but not in the prefactor, one has to be very careful about the correct substitution in eq. 7.9.

A_s will be absorbed in the walls and hence lost for our measurements. Additionally, as presented in chapter 9, we think that for neutron capture events, metastable vortices with a decay constant $\tau_v \gg \tau_b$ are created, which will result in an energy A_v not contributing to the peak height.

Including these two terms, the total energy writes now

$$A_{tot} = A_h + A_m + A_s + A_v. \tag{7.11}$$

If A_s and A_v are not zero, the effect will be to reduce the observed peak height, but it will not influence the value of τ_b^*. The fraction p which was used until now, only corresponds to the fraction $p = A_m/(A_m + A_h)$.

We will now try to quantify the different terms for the different interacting particles, using all the available measurements and information, which are:

- the measured peak height reduction of $23 \pm 7\,\%$ for muons and $15 \pm 2\,\%$ for neutrons,
- the delaying effect of $\tau_b^*/\tau_b = 1.25$ for muons and $\tau_b^*/\tau_b = 1.06$ for neutrons,
- the well funded estimation that muons do not create a big number of vortices, which means $A_v^{muon} = 0$,
- the assumption based on a statistical argument that the singlet/triplet ratio is 1:3.

This last point is the weakest of the presented points, as experimentally another ratio has been found for light particle on measurements done on ^{4}He (see section 5.4). We nevertheless assume this ratio because i) assuming this measured ratio of 58:42, the peak height for muons would be reduced too much and ii), ^{3}He has a magnetic moment, meaning that various processes which lead to a loss of the coherence of the electrons during its separation from the parent ion are possible.

Fig. 7.13c is very similar to fig.7.13b, with the difference that now A_s is not zero but $A_s = \frac{1}{3}A_m$. As a result, we have to introduce a new fraction of energy stored in metastable states $p_m^{muon} = \frac{A_m}{A_{tot}} = \frac{3p}{p+3}$, where p is still $p = \frac{A_m}{A_h+A_m}$. While not in perfect agreement with the value of 23 %, it can be seen from fig. 7.13c that the peak height reduction A^*/A_{tot} in this theory is rather consistent within the error bars $23 \pm 7\,\%$. Our precision on the parameters is not very good, but we get the following values as the best guess: $p_m^{muon} = 0.27 \pm 0.05$, $p_s^{muon} = p_m^{muon}/3 = 0.09 \pm 0.02$, $p_h^{muon} = 0.64 \pm 0.05$, $p_v^{muon} = 0$, $\tau_m = 2 \pm 1\,\mathrm{s}$, with the energy deficit needed to be taken at about 27 %.

The ratio of 58:42 was rejected because by producing a similar graph with it, the peak height would be reduced much further, far below the observed value for the energy deficit.

Exactly the same procedure can be applied to neutron events and the results are depicted in fig. 7.14. We see no reason why the time constant τ_m should be different in the case of neutron events, so that we have to search for the energy deficit in the same regions of τ_m as found for muons. This leads us, not considering the vortices to the following values: $p_m^{neutron} = 0.075 \pm 0.04$, $p_s^{neutron} = p_m^{neutron}/3 = 0.025 \pm 0.013$, with a corresponding

	pulses	muons	neutron capture	electrons	neutron recoil
energy deficit	0	0.23 ± 0.07	0.15 ± 0.02	0.23 ± 0.06	< 0.15?
$\tau_b^*/\tau_b - 1$	0	0.25 ± 0.05	0.06 ± 0.02	~ 0.25?	0.06 ± 0.02
immediate heat A_h/A_{tot}	1	0.64 ± 0.05	0.82 ± 0.06		
triplet dimers A_t/A_{tot}	0	0.27 ± 0.05	0.075 ± 0.07		
singlet dimers A_s/A_{tot}	0	0.09 ± 0.02	0.025 ± 0.02		
vortices A_v/A_{tot}	0	0	0.08 ± 0.04	0	< 0.08?

Table 7.1: Summary for the ratios expected from the analysis presented in this chapter. The singlet dimer ratio is calculated using the assumption that the ratio singlet/triplet dimer is 1/3. For low energy electrons, an energy deficit of 0.23 ± 0.06 is observed and it is expected that the other values are identical to those found for muons too. For neutron recoil events, we only know the observed delaying effect. The other values should be similar to neutron capture events too, with the fraction going to vortices probably smaller. For neutralinos we expect that the delaying effect and the creation of dimers are very small.

peak height reduction of $7 \pm 4\,\%$. Contrarily to the result found for muon events, this value is not compatible with the energy deficit of $15 \pm 2\,\%$ determined experimentally. This whole analysis thus presents another strong evidence for the formation of metastable vortices, which should represent approximately $p_v^{neutron} = 0.08 \pm 0.04$. All of these results are presented in table 7.1.

7.2.2 Expectations for other particles

In the above analysis, τ_b^*/τ_b could be determined for 3 different particle interactions (neutron capture, neutron recoil and muon events), but as for neutron recoil events the energy deficit is not known, the determination of all ratios was only possible for neutron capture and muon events. On the other hand, for electrons, the signal was good enough to determine the energy spectrum by an analysis of peak heights, but not good enough to get meaningful values for τ_b.

For electrons, the spacings between the different impacts is $0.5\,\mu$m and thus much larger than the typical size of the hot spots and the energy deposition per scattering is relatively low. Because these two characteristics are basically the same as for muons, one expects that the branching ratios are relatively similar, and that no vortices are created either. Indeed, the observed energy deficit is practically the same as for muons. We have thus strong arguments to suppose that electrons show an increased time constant τ_b^* which is the same as for muons.

For neutron recoil events, it is supposed that in a first step, a neutron interacts exactly once with a ^{3}He nucleus. This energy is then transmitted to the fluid by secondary processes in which the now highly energetic ^{3}He ion ionises other ^{3}He atoms. This process should be very similar to the ionisation by the nuclear capture products tritium and proton. For high energies we thus suspect the ratios for dimer creation to be similar to the ones obtained for the neutron capture events. This idea is experimentally supported by the observation

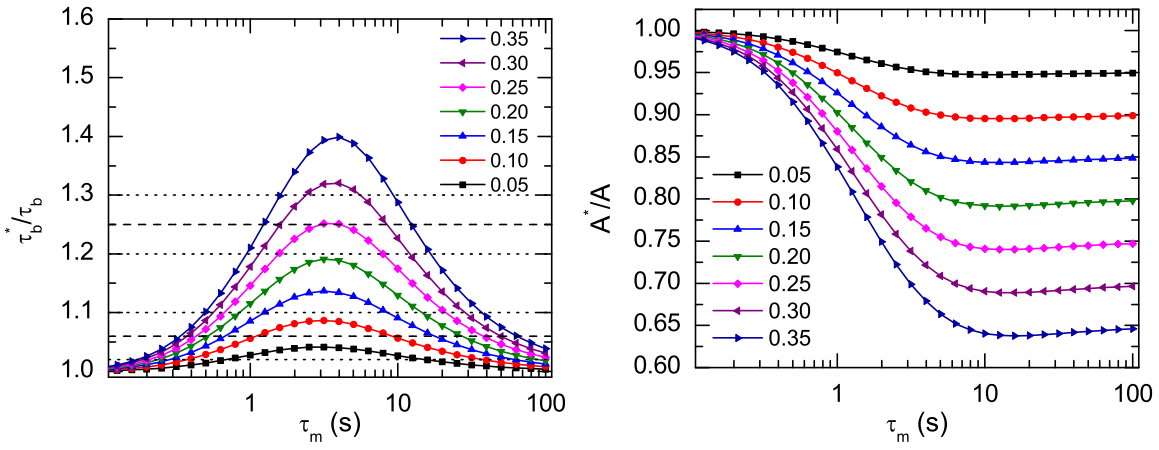

Figure 7.12: This figure is equivalent to fig. 7.8, with the difference that for the creation of the dataset, the losses by radiative decay of triplet excimers has been considered by replacing in eq. 7.9 $1/\tau_m \rightarrow 1/\tau_m + 1/\tau_r$, with $\tau_r = 13\,\mathrm{s}$. The result is that for the same values of p and τ_m, the delaying effect is reduced, which in turn means that the value of p compatible with observation increases.

that τ_b^* is already the same. For lower energies ($E < 100\,\mathrm{keV}$), the fraction going to dimers should decrease, as the Lindhard factor, describing the ratio of electronic to nuclear recoil, decreases.

For neutralinos it is thought that the energy transmission will be exactly the same as for neutron recoil events, which means that the increase of τ_b^* should be exactly the same as for low energy neutron recoil events.

7.2.3 The time constant of metastable triplet dimers

Up to now, we treated the time constant τ_m as a phenomenological parameter and obtained an idea of its value by comparing the simulations with the measured τ_b^*/τ_b. We want now to look briefly at the questions whether the found value of $\tau_m \approx 2\,\mathrm{s}$ is a reasonable number or not.

Two mechanisms for non radiative decay of triplet dimers in liquid Helium are known: Penning ionisation, in which two excimers meet, and interactions with the walls. The first mechanism can be excluded by the following argument:

The expansion time of the hot spot can be estimated to be of the order of $1\,\mu\mathrm{s}$ which means in turn that the diffusion constant diverges quickly, and the excimers should get ballistic in a time which is several orders of magnitude shorter than the measured τ_m. Considering a 100 keV event, which should produce according to the previously determined ratios $27\,\mathrm{keV}/16\,\mathrm{eV} \approx 1690$ metastable excimers (see table 7.1), the density is just too small for a significant number of dimers to meet each other.

So we will stick to the second mechanism, the interaction with the cell walls. Two parameters should determine the time constant which corresponds to this mechanism: the

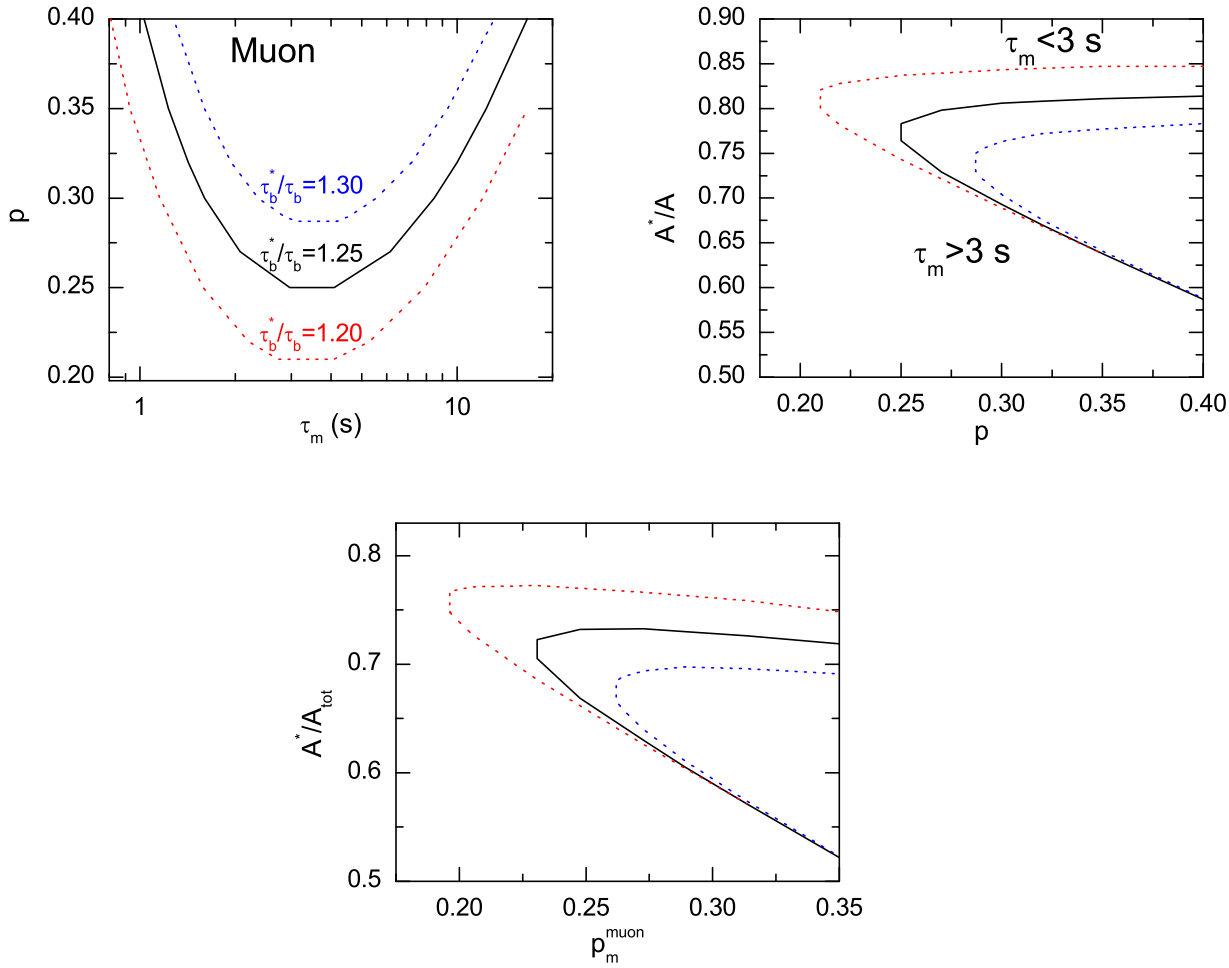

Figure 7.13: a) This graph presents the combinations of p and τ_m which are compatible with the observed $\tau_b^*/\tau_b = 1.25 \pm 0.05$ (for muons) and corresponds to the intersections of the horizontal lines with the different curves for constant p in graph 7.12a. The solid line corresponds to $\tau_b^*/\tau_b = 1.25$, and the dotted lines to the upper and lower bound.
b) For all these points, the corresponding reduction in peak height can be determined and is plotted as a function of p. Two solutions exist for each value of p. The lower half corresponds to $\tau_m > 3\,\mathrm{s}$ and the upper half to $\tau_m < 3\,\mathrm{s}$.
c) In graph b, other channels for energy are not considered yet, i.e. $A_l = 0$. Assuming a 1:3 ratio for singlet/triplet dimers, we set $A_l = A_s = \frac{1}{3}pA$. The total peak height reduction A^*/A_{tot} can now be plotted, where $A_{tot} = A + A_s = A\left(1 + \frac{p}{3}\right)$ and $A = A_h + A_m$. The experimentally determined energy deficit was $23 \pm 7\%$ (see graph 5.13), which corresponds to $A^*/A_{tot} = 0.77 \pm 0.07$. The model presented does thus explain relatively well all experimental observations (delaying effect and energy deficit) with $p = 0.25 \pm 0.05$ and $\tau_m = (2 \pm 1)\,\mathrm{s}$, if considering that the energy deficit for muons is taken at about 27 %.

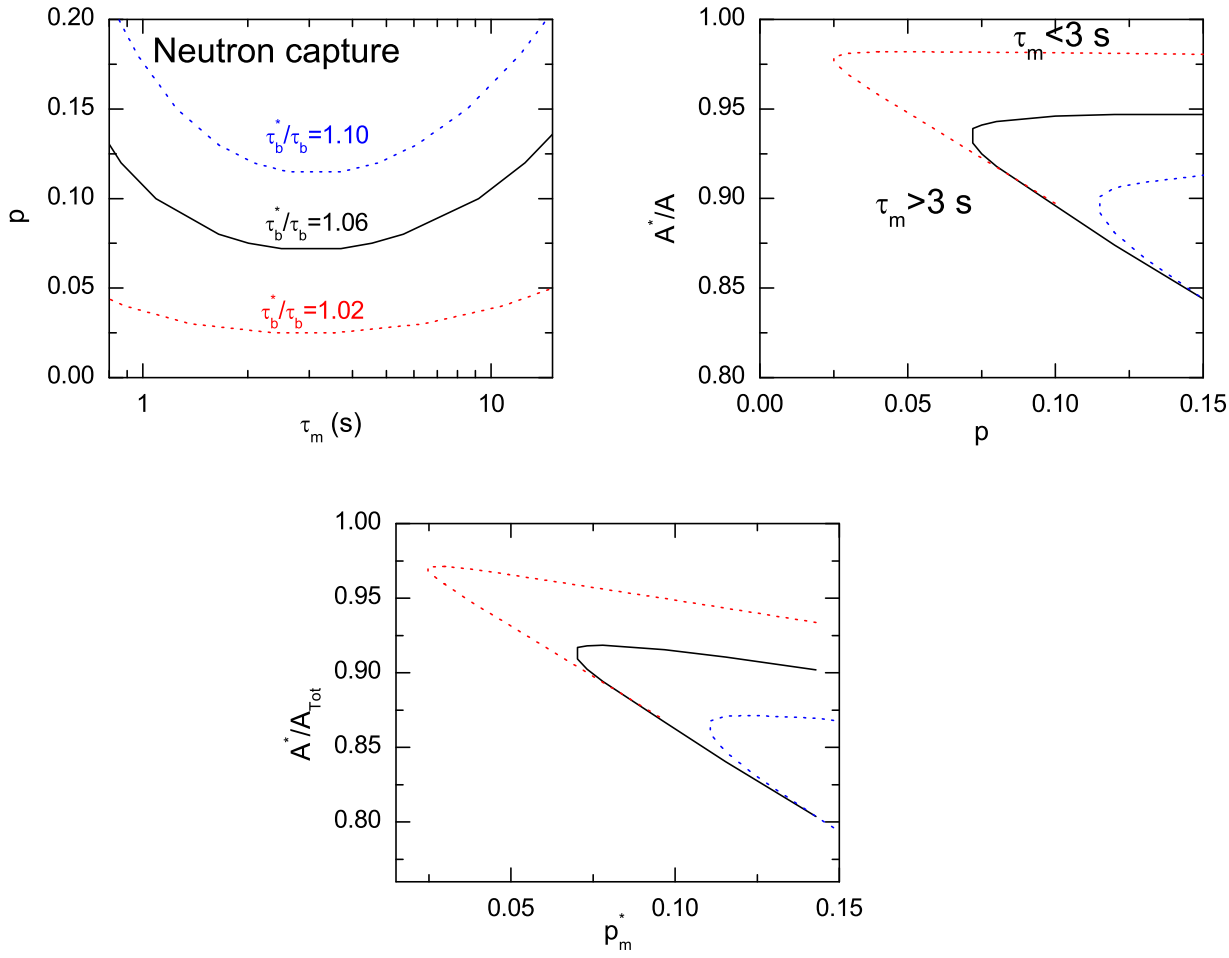

Figure 7.14: a) This graph presents the combinations of p and τ_m which are compatible with the observed $\tau_b^*/\tau_b = 1.06 \pm 0.04$ (for neutrons) and corresponds to the intersections of the horizontal lines with the different curves for constant p in graph 7.12a. The solid line corresponds to $\tau_b^*/\tau_b = 1.06$, and the dotted lines to the upper and lower bound.
b) For all of these points, the corresponding reduction in peak height can be determined and is plotted as a function of p. For each value of p two solutions exists The lower half corresponds to $\tau_m > 3\,\mathrm{s}$ and the upper half to $\tau_m < 3\,\mathrm{s}$.
c) In graph b, other channels for energy relaxation are not considered yet. When assuming a 1:3 ratio for singlet/triplet dimers, corresponding to an energy lost by scintillation of $A_s = \frac{1}{3}pA$, the total peak height reduction due to singlet and triplet excimers can be taken into account by taking the ratio A^*/A_{tot}, with $A_{tot} = A + A_s = A\left(1 + \frac{p}{3}\right)$. It can be seen that for neutron capture events, this can not explain all of the 15 % energy deficit. This new observation thus supports the hypothesis of creation of metastable vortices presented in a previous work(see ref. [17] and chapter 9).

typical time of flight τ_f for reaching a cell wall, and the probability p_d ($p_r = 1 - p_d$) of decay (rebound) upon hitting the wall. As we are in the ballistic regime for Bogoliubov quasiparticles, and we think that the same is true for dimers, the typical time of flight of the latter writes $\tau_f = \bar{v}/d$, with $\bar{v}$ the dimers mean velocity and $d \approx 0.5\,\mathrm{cm}$ the average dimension of the cell.

Unfortunately, very little is known about the details of this, neither the velocity $\bar{v}$, nor the ratio p_d/p_r. To get at least an order of magnitude, let us first estimate the time of flight if the dimers were moving at the Landau critical velocity (which we consider as an upper limit) $v_L = \Delta/p_F = 27.3\,\mathrm{mm\,s^{-1}}$: $\tau_f \approx 0.18\,\mathrm{s}$. This means that using this value on average 11 rebounds are necessary to get a value of $\sim 2\,\mathrm{s}$, and hence a value of $p_r \sim 0.94$.

One important piece of information about excimers in liquid Helium is that it forms bubbles of radius $r_B \approx 7\,\text{Å}$ due to a repulsive van-der-Waals potential [60]. This has two effects: firstly it should increase the effective mass significantly, meaning in turn a reduced velocity. Secondly it means that it will be more "difficult" to approach the wall closely, in other words, the container walls probably present an additional surface potential. As a spin flip is necessary for the triplet dimer to dissociate, the closest distance the dimer approaches the wall should play an important role. Considering additionally the fact that the walls are covered by solid ^{4}He, which can not participate in a spin flip interaction, we suppose that there should be a finite probability $p_r > 0$ for a dimer to backscatter upon hitting the wall.

More information on these numbers would be of great value, but we think that both effects induced by the repulsive potential plus the estimation of the time of flight taken together tell us that a time constant of $\tau_m \approx 2\,\mathrm{s}$ is not unreasonable.

7.2.4 Conclusions and outlook

An ultimate proof of the above picture is missing, and a certain number of hypothesis like the supposed branching ratio singlet/triplet have little experimental backing. Nevertheless, due to the lack of a competing theory and due to the fact that the numbers obtained seem to give a coherent description and are able to explain all of the experimental values, we think that it is a rather robust scenario.

As the delaying effect should depend on the ratio τ_b/τ_m, changing one of those two parameters, the ratio τ_b^*/τ_b should change too. The following experiments could thus test experimentally this theory:

- τ_b can be varied by producing similar cells, but with varying orifice diameters. As this should have no influence on τ_m, it should be the easiest method to test the general idea of metastable states being responsible for this effect.
- If the interaction with the cell walls is really the determining factor for τ_m, we can vary τ_m by using cells of different dimensions.
- Possibly the probability of rebounding on the wall depends on the exact configuration (material, rugosity...) of the wall, so that τ_m might depend on this coefficient too.

Unfortunately, all of these measurements are linked to a substantial time investment, so that a dedicated series of measurements is practically impossible.

An alternative way to test this theory is the parallel measurement of scintillated light. Until now it was believed that the whole of the energy deficit can be attributed to scintillation, while according to this new theory, only a fourth of it (in the case of light particles like muons) should be emitted as UV. If it is possible to make quantitative measurements on scintillation, this rather large difference should be possible to demonstrate. On the other hand this means that the idea of using scintillation as a supplementary discrimination mechanism might be harder than what was thought initially, as with this new observations we suppose to have four times less photons.

7.3 Absolute value and temperature dependence of the recovering time

After this detailed analysis of the difference in pulse shape for different events we want to discuss briefly an additional feature which can be observed in fig. 7.2 and in fig. 7.15: from these graphs it can be seen that the absolute value of τ_b depends on temperature, and has values between 2.5 and 5 s.

A theoretical calculation for the value of τ_b based on the assumption that the orifice is a flat hole gives the following equation:

$$\tau_b(T) = 4\frac{V}{S_{eff}}\frac{1}{\bar{v}_g(T)}\left(1-\frac{5}{16}\frac{k_BT}{\Delta}\right) \tag{7.12}$$

$$= \frac{V}{S}\frac{1}{v_F}\sqrt{8\pi\frac{\Delta}{k_BT}}\left(1-\frac{5}{16}\frac{k_BT}{\Delta}\right). \tag{7.13}$$

A detailed derivation of this equation is presented in appendix A. Using this equation the value at for example 0.140 mK amounts to $\tau = 0.64$ s, which is a factor of 5.5 smaller than what is measured for neutron capture events at this temperature. Additionally to this discrepancy in the absolute value, the expected $T^{-1/2}$ temperature dependence (in first order) can not be confirmed.

For high pressures (29.3 bar) on the other hand, the $T^{-1/2}$ law seems to be followed, but the absolute value is still about 4.2 times too large. For the difference in the absolute value, two arguments can be considered:

Firstly, the orifice is not, as assumed in the calculation a flat hole, but rather a cylinder whose length is in our case two times longer than the diameter. This means that only a small part of the outgoing quasiparticles (QP) will leave the cell directly, but a large part of the possible trajectories will imply multiple scattering on the cylinder wall. The possibility of Andreev reflections implies that a certain number of QPs are backscattered directly in the cell. Additionally, the "normal" (non-Andreev) scattering is probably not specular, but diffuse and inelastic, which leads to a further increase in the thermal resistance represented by the orifice.

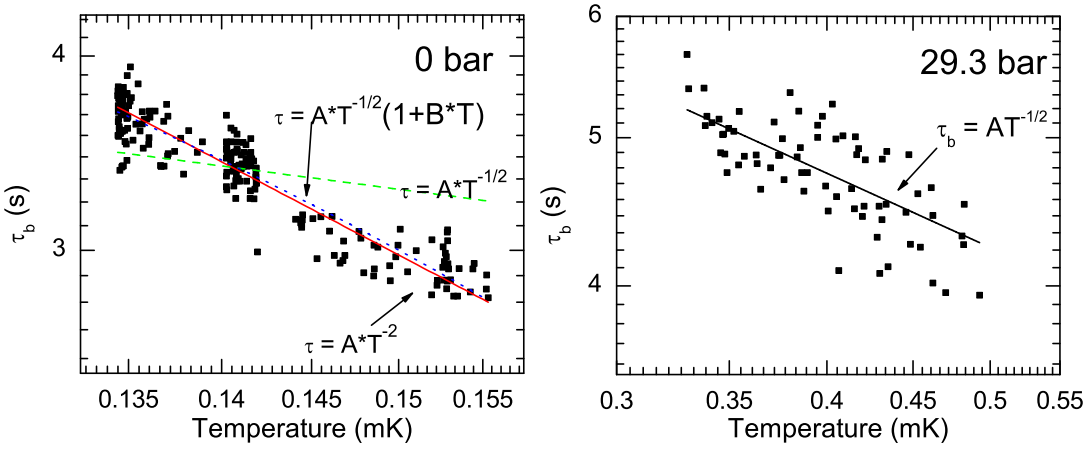

Figure 7.15: Temperature dependence of τ_b for neutron capture events at 0 and 29.3 bar. The temperature range is in both cases too small to give a definitive answer on the exact temperature dependence. While at 29.3 bar a $T^{-1/2}$ law fits the data reasonably well, this law does not work at 0 bar. A fit with the function $\tau_b = A * T^{-1/2}(1 + BT)$, which would correspond to taking into account a first order correction of $\bar{v}_g$ delivers a value of $B \approx 4\,\mathrm{mK}^{-1}$, much larger than the expected $\frac{5}{16}\frac{k_B}{\Delta} = 0.19\,\mathrm{mK}^{-1}$. Assuming a simple power law $\tau_b = A * T^{\gamma}$, a T^{-2} dependence would fit the data at 0 bar reasonably well.

A second argument is the possibility of Andreev reflections on "defects" of the order parameter. As the order parameter is bent in the proximity of walls, and this bending is probably non trivial for this small cylinder, it is possible that this has a major influence on the box time constant.

This second effect could explain a modified temperature dependence too: QPs of low energy in general have higher probabilities to be Andreev reflected. As the ratio of low- to high energy QPs gets larger for lower temperature, the relative number of quasiparticles backscattered due to Andreev reflections should increase at lower temperatures. A detailed calculation for this effect is still missing, so while providing a possible mechanism, we do not know whether this effect is strong enough to explain the magnitude of the observed discrepancies.

Part II

Application of the detector prototype to fundamental ^{3}He physics

Chapter 8

Addendum specific heat of adsorbed ^{3}He

During the first few demagnetisation runs on this dark matter detector prototype, the observed peak heights, both, for calibration pulses and for particle events were much lower than what was expected by applying eq. 5.35 (see fig. 8.1). Additionally, the calibration factor, instead of following the expected $1/\sqrt{T}$ dependence (see eq. 5.34), decreased much faster for lower temperatures. After, by coincidence, the whole nuclear stage heated to about 4 K, the response to a heating event in a subsequent demagnetisation run corresponded to the estimated value. In all following demagnetisation runs of the same series[1], between which the temperature never exceeded 20 mK, the calibration factor stayed normal. This behaviour was observed in all 3 cells simultaneously. After a second and a third initial cool down and hence condensation of ^{3}He, the same effect of a drastically reduced calibration factor was observed, and each time it could be destroyed by "rebaking", i.e. heating to about 4 K.

Since ^{3}He is a liquid of absolute purity at ultra low temperature, the only effect that such a rebaking can have is to change the structure of the adsorbed layers on the copper walls: the gaseous ^{3}He as coming from the tank is never 100 % pure, but is always contaminated with small amounts of ^{4}He (ppm level). On the way to the experimental cell, the gas is condensed on the heat exchangers and passes the guard cell. We filled the cell under cold conditions, i.e. the nuclear stage was already cooled by the dilution stage to the mK range. At these temperatures, a phase separation takes place[2], meaning that droplets of ^{4}He form and do not reach the cell, mainly trapped in the Ag sinters. The total result will be that even though the gaseous ^{3}He contains ^{4}He impurities, the liquid arriving at the experimental cell will be absolutely pure ^{3}He and the cell walls will be covered by adsorbed layers of ^{3}He.

During the rebake process the ^{3}He and ^{4}He are evaporated. On the subsequent cooling, ^{4}He will enter the cell, condense in the cell and will, due to its lower zero point energy, cover preferentially the cell walls. From the dimensions of the cell ($V = 0.13\,\mathrm{cm}^3$, $S = 0.94\,\mathrm{cm}^2$), considering a layer coverage of 15 atoms/nm^2 and an estimated roughness factor of five, we find that less than a 7 ppm concentration of ^{4}He is sufficient to cover the whole walls with

[1] We name a "series" a series of demagnetisation runs during which the cryostat is kept cold.

[2] The same effect which happens in the mixing chamber of the dilution stage.

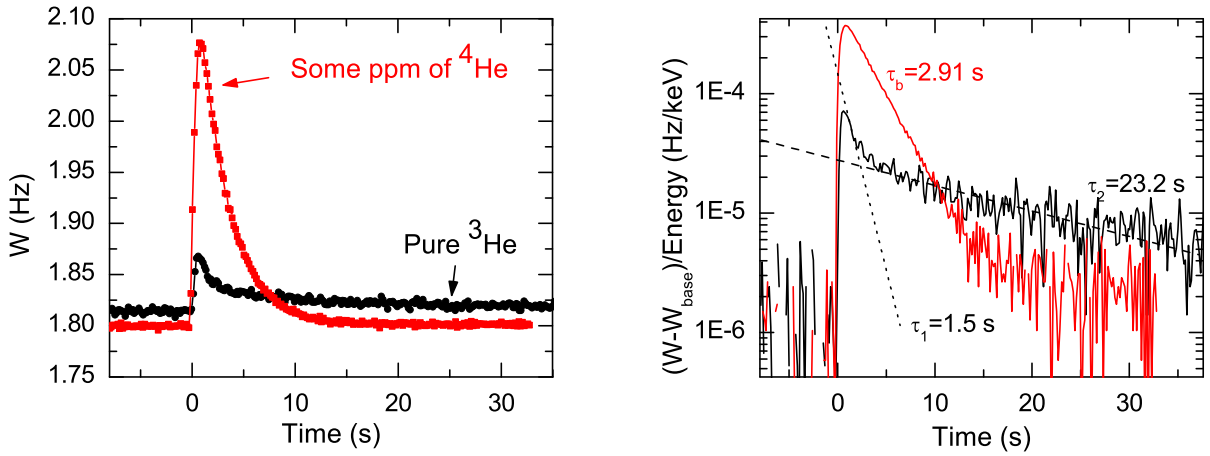

Figure 8.1: a) Two response peaks to a heater pulse of same energy (750 keV) and at almost the same baseline width W_{base}. The difference in the response is attributed to the addendum heat capacity due to the adsorbed layers of ^{3}Heon the walls. b) The same peaks in a logarithmic plot of normalised ΔW illustrates the existence of two timescales in the case of no ^{4}He present. A first, fast decay is followed by a slow decay. For this pulse the two corresponding time constants are $\tau_1 \approx (1.5 \pm 0.2)$ s and $\tau_2 \approx (23.2 \pm 1.3)$ s. In the case of the presence of ^{4}He only one time constant with a value of $\tau_b = (2.91 \pm 0.02)$ s is observed.

two monolayers of ^{4}He.

In the third demagnetisation series, where we put a special focus on studying this effect, and which provided the data presented in this chapter, special care was taken to do the initial condensation at very low temperatures and very slowly, to be sure that the above argument applies. On rebaking we added a small amount of ^{4}He to ensure that the necessary 7 ppm concentration in the cell is reached.

8.1 Comparison of heater pulses with and without solid ^{3}He

In order to study the differences between ^{4}He and ^{3}He coverages in detail, calibration pulses at different temperatures were made. Fig. 8.1 shows the difference of the response to a heater pulse of same energy at practically the same baseline width W_{base} in both cases. The striking feature of this graph is the much reduced peak height in the case of pure ^{3}He. But additionally it can be seen that the overall shape is different. While the shape of the peak after rebaking can be very well fitted using eq. 5.31, the peak with ^{3}He adsorbed on the cell walls seems to show (at least) two different time constants for the thermalisation.

In order to explain such a drastic difference a look at eq. 5.33 $\sigma(T) = \frac{1}{C(T)} \frac{dW(T)}{dT}$ shows that the reason should be either a changed interaction of the wire with the superfluid and hence a modified temperature dependence of the resonance width $W(T)$ or a difference in

the total heat capacity $C(T)$.

The former possibility is not only difficult to imagine but can be excluded with certainty. Firstly, as we will see later, the peak height is reduced by more than a factor of ten at low temperatures. This means that we would have to deal with a large change in $dW(T)/dT$, and thus with a largely changed $W(T)$. To rule this possibility out is a priori not easy, as we do not have an independent thermometer. Nevertheless such a big difference should be noticeable in the final demagnetisation field necessary to reach the working temperature, something which was not observed.

A more convincing argument is given by a lucky coincidence: in the third series of demagnetisation, the first rebaking was only partly successful. In the following demagnetisation run, the events in the A and the B-cell showed normal behaviour, i.e. the peak heights and thus the calibration factor were as expected. On the other hand the calibration factor in the C-cell was still significantly reduced. At the same time, the baseline width $W_{base}(T)$ was practically the same in all three cells. As the baseline temperature is necessarily the same in all three cells, this clearly is in contradiction to the assumption that the temperature dependence of the resonance width $W_{base}(T)$ is modified. We think that we just heated long enough to evaporate all Helium in the A and the B-cell, but not long enough to also empty the C-cell, with the result that the rebaking process did not work for this cell.

Another possibility we considered is that neither $C(T)$ nor $W(T)$ change, but that the adsorbed layers of ^{3}He just allow the transport of energy to the copper walls, for example by magnetic coupling. In this case, the total energy going to the quasiparticle gas would be reduced, which could easily explain the reduction in peak height. On the other hand copper is a good thermal conductor, meaning that heat transferred to the copper would diffuse through the whole copper and not return to the cell and create quasiparticles. But in this case, the significantly increased recovery time (see fig. 8.1) could not be explained.

We thus conclude that the reason for the reduced calibration factor is an addendum specific heat most probably given by adsorbed layers of ^{3}He.

8.2 Measuring the heat capacity of adsorbed layers of ^{3}He

After this initial analysis we will now see how this can be used to measure the heat capacity of the adsorbed layers $C_{surface}$. Fig. 8.2 shows the calibration factor as a function of temperature before and after annealing. The calibration factor in the "normal" case is obtained as explained in section 5.3.6. In the case of adsorbed layers of ^{3}He the peak height was obtained by extrapolation of the long tail. For this we fitted the tail with an exponential of the form $W(t) = W_{base} + W(t = t_0)\exp(-t/\tau)$. This allows to avoid counting the overshoot which probably indicates that the system is not yet at equilibrium (see fig. 8.1). The calibration factor is then obtained as usual as the slope in the peak height/energy plot. Every point corresponds to a series of at least 15 pulses. The points before rebaking were

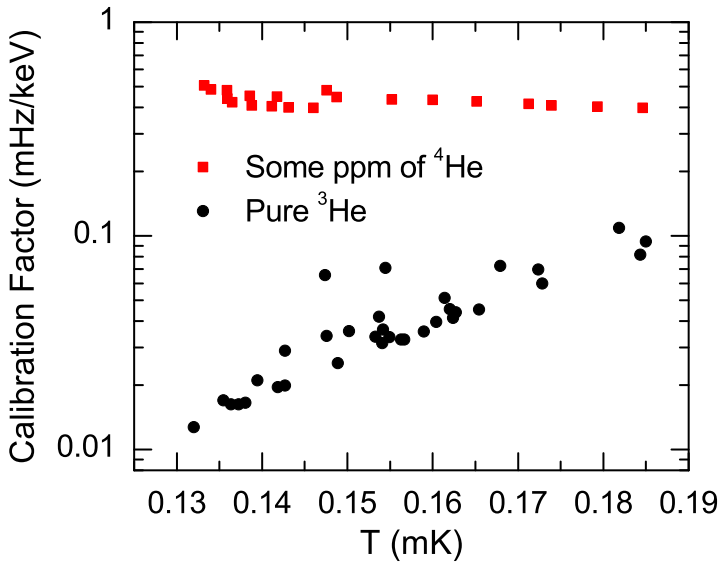

Figure 8.2: Calibration factor for different temperatures before and after rebaking. As the exponential dependencies drop out, the curve after rebaking (red squares) only slightly depends on temperature and agrees well with what is expected from eq. 5.34. In the pure ^{3}He case (black circles), the surfaces add a non-exponential dependence to the total heat capacity resulting in a strong reduction of the calibration coefficient. The scatter of the points is mainly due to the influence of the magnetic field, as results presented here are not corrected for its effect.

taken in a total of 6 different demagnetisation runs, the points after rebaking correspond to 2 demagnetisations.

One experimental difficulty is worth noting: in order to make temperature dependent measurements, it is normally necessary to be able to regulate the temperature. However, as already explained in chapter 6, thermalisation after heating by the Joule effect or by a VWR takes a long time due to the Kapitza resistance (typically 3 to 5 hours). In addition, using this method we can not aim for a given temperature.

A method which is more efficient is to go first to very low temperatures with a demagnetisation and then change the temperature by stepwise upmagnetisation. In this way it was possible to do the calibration at a rate of about two temperatures per hour. Unfortunately one problem persists: the temperature reached can not be regulated exactly. Additionally, as the sample is located in the same magnetic field used for the demag/upmag, this means that the corresponding measurements are not taken at constant magnetic field and that the study of field dependence at constant temperature and vice versa becomes quite complex. The strategy is thus not to try to regulate a specific temperature, but to do the measurement at whatever temperature it stabilises, increasing the number of measured points. We then use for the analysis slices of almost identical values.

Now let us have a look on the results presented in fig. 8.2. The results after rebaking show only a weak dependence on temperature. From eq. 5.34, this is exactly what one

would expect:

$$\sigma_0 = \frac{1}{C_{total}} \frac{dW}{dT}. \tag{8.1}$$

With

$$dW/dT \propto T^{-2} \exp -\Delta/k_B T \tag{8.2}$$

and

$$C_{after} = C_{bulk} \propto T^{-3/2} \exp -\Delta/k_B T \tag{8.3}$$

the exponential dependence drops out and we are left with $\sigma_0 \propto T^{-1/2}$. Taking into account the losses of the peak height due to the finite response time of the wire (expressed by the function $G(W_{base}, \tau_b)$, eq. 5.32), the results fit reasonably well the theory, with the only fitting parameter being a geometric factor.

In order to explain the results before rebaking we suppose that in addition to the bulk heat capacity, the adsorbed ^{3}He layers give a contribution which have a weaker temperature dependence: $C_{before} = C_{bulk} + C_{surface}$. In this case the heat capacity will be dominated at low temperatures by the surface term and the calibration factor will decrease due to the exponential decrease of dW/dT. In order to determine the corresponding heat capacity C_{bulk} it is now sufficient to divide the experimentally determined calibration factors:

$$\frac{\sigma_{after}}{\sigma_{before}} = \frac{C_{bulk} + C_{surface}}{C_{bulk}}. \tag{8.4}$$

The surface heat capacity then becomes

$$C_{surface} = C_{bulk} \left(\frac{\sigma_{after}}{\sigma_{before}} - 1 \right). \tag{8.5}$$

Using the BCS-formula for C_{bulk} (eq. 3.28) and the experimentally obtained values for the calibration factors, one finally finds the temperature dependent surface heat capacity as presented in fig. 8.3a.

The values for $C_{surface}$ presented in this graph were taken at different magnetic fields B. While a priori we do not know how the magnetic field could influence the heat capacity, we will assume for instance that the observed scatter in fig. 8.2 and fig. 8.3a is due to the magnetic field. In order to study the influence of the magnetic field at constant temperature we searched for slices of almost constant temperatures in which calibrations were made for different fields. The result is presented in fig. 8.4. As can be seen, this graph suggests that the heat capacity is proportional to B for the different temperatures studied. With this knowledge, the scatter due to the magnetic field dependence in fig. 8.3a can be eliminated by dividing by the magnetic field B. This leads to the normalised heat capacity 8.3b.

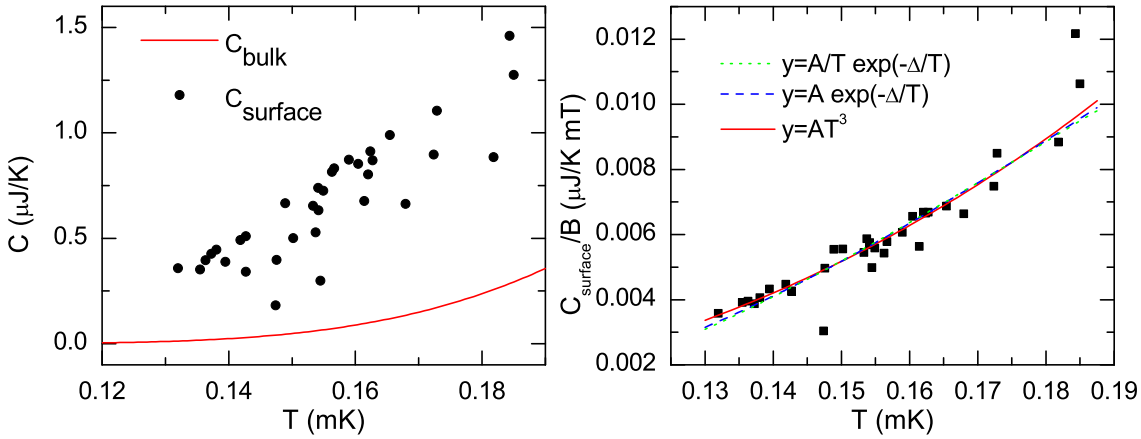

Figure 8.3: a) Surface heat capacity as a function of temperature, all magnetic field combined. The bulk heat capacity (solid line) has been calculated using the BCS formula (3.28), the surface heat capacity is determined from the experiment using eq. 8.5.
b) The surface heat capacity normalised by the magnetic field. Some plausible laws which fit the data reasonably well have been tried, but as the temperature range is quite limited, and mainly because we do not know the underlying mechanism of this addendum specific heat, no definite answer for the temperature dependence can be found.

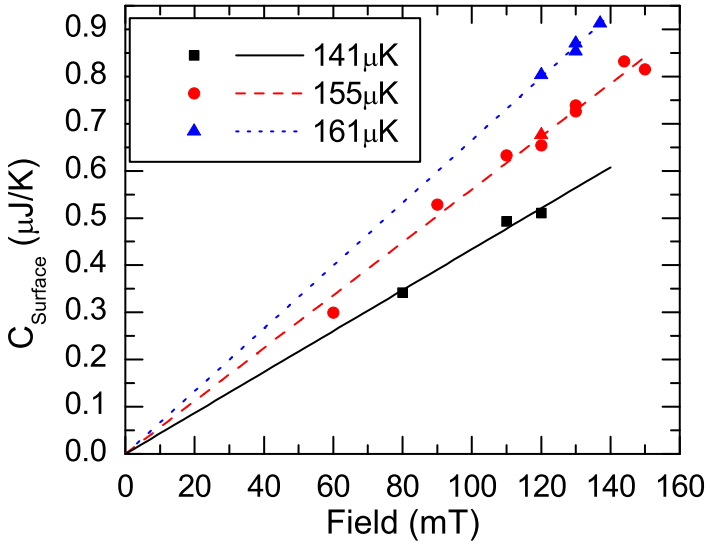

Figure 8.4: Field dependence of heat capacity of adsorbed layers at constant temperature. This graph suggests that the heat capacity is proportional to the magnetic field.

8.3 Specific heat of adsorbed layers of ^{3}He

A remarkable feature of this heat capacity is its magnitude. As this was not a dedicated experiment we do not know the precise effective surface of the cells, neither the density of the adsorbed layers. Nevertheless, doing some reasonable assumptions we can at least get an order of magnitude for the specific heat: the geometric surface area can be calculated as the surface of a cylinder $S_{geo} = 2\pi r(r+h) = 1.51\,\mathrm{cm}^2$. The total area is larger than this value due to the rugosity. The copper surface has not been specially prepared or polished, which leads us to an estimation of the rugosity ~ 5, leading to an effective surface $S_{tot} \sim 7.5\,\mathrm{cm}^2$. Together with an estimation of the surface density of two layers[3] of adsorbed ^{3}He $n_{at} \sim 15\,\mathrm{atoms/nm}^2$ we get a number for the total number of adsorbed ^{3}He atoms contributing to this addendum specific heat $N_{at} = S_{tot}/n_{at} \sim 1.9 \cdot 10^{-8}\,\mathrm{mol}$. The values of the heat capacity are $0.4\,\mu\mathrm{J/K}<C<1.3\,\mu\mathrm{J/K}$ (compare to fig. 8.3a). This corresponds to a specific heat of $21\,\mathrm{J\ K^{-1}mol^{-1}} < c < 68\,\mathrm{J\ K^{-1}mol^{-1}}$, or in terms of the universal gas constant $2.5\,\mathrm{R} < c < 8.2\,\mathrm{R}$. Assuming that all the analysis up to now was correct, we thus have to deal with an enormous specific heat, far beyond anything a paramagnetic heat capacity could explain.

We did not find the reason for this surprisingly big effect, but we want to present anyway a detailed discussion of it. First of all, lacking a theory delivering an expected temperature dependence, we tried to fit the data with several simple functions having few (one or two) parameters and which seemed reasonable to us. Unfortunately, the measured temperature range is far from being large enough to conclude on the real temperature dependence. Fig. 8.3b shows that a cubic law with only one parameter would represent the data very well. The other two fits of the form $y = A/T\,\exp(-\Delta/T)$ and $y = A\,\exp(-\Delta/T)$ have the interesting feature to comprise a gap parameter which yields a value of $\Delta = 0.64\,\mathrm{mK}$ and $\Delta = 0.49\,\mathrm{mK}$ respectively.

The linear magnetic field dependence as depicted in fig. 8.4 is quite intriguing too, as one would expect for symmetry reasons rather a quadratic than a linear dependence. Of course we are lacking points at low field values, meaning that possibly at low fields, the field dependence is quadratic and only at higher fields it approximates to a linear behaviour.

Comparison with existing measurements are difficult as measurements in comparable conditions are rare. A set of different measurements done on silver powder, porous Vycor and grafoil is presented by Golov and Pobell [52]. The measurements have been done for temperatures down to 0.4 mK in the case of silver powder and $\sim 7\,\mathrm{mK}$ for Vycor and grafoil, at zero magnetic field and without the presence of a liquid phase in contact with the adsorbed layers, making any comparison questionable. The heat capacity for the lowest temperatures ($\sim 0.4\,\mathrm{mK}$) on silver and high coverage factors seems to be temperature independent and is about $\sim 0.45\,\mathrm{J\ K^{-1}mol^{-1}} = 0.05\,\mathrm{R}$ and hence about 2 orders of magnitude smaller than in our case.

[3] It is hard to know the exact value of the number density to consider, as we do not know whether the second solid layer or even the liquid close to the solid layers contribute to this heat capacity, but in total this should give an uncertainty of no more than a factor 2.

Another comparison can be made with measurements done in Lancaster [61] using an aerogel sample as a substrate. The measurements were done like ours in the presence of a superfluid phase. The authors estimate the surface area to be $\sim 2\,\mathrm{m}^2$ and find at $198\,\mu$K a heat capacity which depends quadratically on the magnetic field for fields up to 27 mT. They describe their findings by the equation $C(B) = 4.4(5) \cdot 10^{-5} + 0.80(1)B^2\,\mathrm{J/K}$. Extrapolating these results to our typical fields of $\sim$100 mT, a specific heat of $\sim 4.0 \cdot 10^{-3}\,\mathrm{J/K\ m^2}$ is found, which corresponds, when using the same estimate for the coverage as before, to $c \sim 4.4\,\mathrm{J\ K^{-1}mol^{-1}} = 0.53\,\mathrm{R}$. While this is already closer to our result we still lack an order of magnitude. Additionally, the observed quadratic field dependence is not in agreement with our linear dependence.

8.4 Conclusion

In conclusion, we could not think of any model which can explain this surprisingly high heat capacity, and additional data from a dedicated experiment might be needed to establish such a model. The different experimentally established facts are:

- A significantly reduced peak height, indicating that either the total heat capacity has increased, or that part of the energy does leave the system without being transformed to quasiparticles.
- The observation of (at least) two time constants indicates that (at least) two thermal baths are in contact, with a coupling time constant of the order of τ_w and τ_b. The long tail shows that this second thermal bath transmits during a long time energy to the bulk, creating constantly quasiparticles.
- The effect is (within our precision) proportional to the magnetic field.

As in our conditions three characteristic energies, the thermal energy k_BT, the magnetic energy μB and the exchange energy J of the adsorbed layers are of comparable value, we think that a detailed study might provide some interesting physics.

Normally, the effects produced by the adsorbed layers are undesirable, as it complicates the system, and mainly because it reduces the calibration factor and hence the bolometer sensitivity. For this reason, all of the other measurements presented in this work were done after rebaking the surfaces, i.e. in a regime where no contributions of the surfaces could be observed. For a future dark matter detector it is of course equally important to avoid this effect.

Chapter 9

Pressure dependence of neutron capture events

An important reason to continue measurements after the end of C. Winkelmann's PhD thesis with the same experimental setup was to complete and clarify an older measurement published in 1996 [17]. In this experiment, the heat deposition after a neutron capture event was compared to the expected energy of 764 keV, which is released in total in superfluid ^{3}He. The bolometer used was similar to the ones used in the current experiment. Like in the current experiment, an energy deficit was observed, which amounted to about 14.5 % at 0 bar, but which increased to 15.5 % at 6 bar and to about 22 % at a pressure of 19.6 bar. Unfortunately, the cell exploded in this experiment while pressurising to 22 bar, so that the experimental data was limited to three points. During his work, C. Winkelmann found the same value at 0 bar, demonstrating the reproducibility of this energy deficit at low pressures. He succeeded to measure one additional point at 29.3 bar, which showed practically the same value as at 0 bar, hence introducing a jump from the 19.6 bar value.

The interest of these measurements lies mainly in the interpretation of a part of this energy deficit in terms of a vortex creation scenario, which shall be discussed in the next section.

9.1 Kibble-Zurek mechanism

A neutron capture reaction in liquid ^{3}He corresponds to the deposition of a high quantity of energy in a relatively small cylindrical region of about 1 μm diameter and 80 μm length, leading to an initial "hot spot" of about 60 μm^3 (see fig. 9.1, for a detailed numerical study see ref. [59]). This energy is sufficient to heat the corresponding region above the superfluid transition temperature. Subsequently, this region will rapidly cool down and pass the symmetry breaking second order phase transition to the superfluid phase. If this cooling is sufficiently fast, this transition takes place at different, causally disconnected regions at the same time. Thus, if the transition is fast enough, the spontaneous symmetry breaking will lead to a large number of small domains with different order parameter orientations and

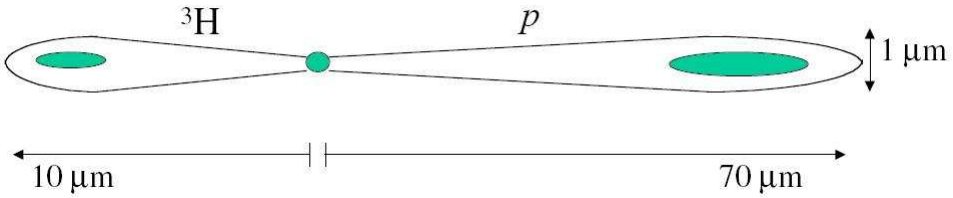

Figure 9.1: After a neutron capture event a proton and a tritium form and leave the place of scattering in opposite directions, with an energy of 573 and 191 keV respectively. Due to interactions with the surrounding ^{3}He, they lose their energy on a distance of about 70 and 10 μm respectively, and most of the energy is deposited at the end of the tracks. From ref. [59].

possibly even different superfluid phases. The size of these domains is smaller, when the transition is faster. As the system evolves, these inhomogeneities in the order parameter result in a tangle of topological defects.

This model of defect creation was initially proposed by Kibble [62] to explain the formation of cosmological structures: in the standard model of cosmology, the early universe underwent, as it cooled after the Big Bang, a series of spontaneous second order phase transitions (like for example the electroweak phase transition). Kibble suggested that during these fast phase transitions, the spontaneous symmetry breaking leads to inhomogeneities and thus topological defects. Unfortunately, astronomical observations are limited to after the recombination (about 380,000 years after the Big Bang), so that no unambiguous, direct checks of his predictions are possible. The idea of Zurek [63] was then that causality is such a fundamental principle, that it should be possible to apply Kibble's arguments to condensed matter physics, for which experiments could be performed. In some way, our experiment thus can be seen as a cosmological experiment, performed in a laboratory: we produce a "Big Bang" in superfluid ^{3}He and we observe the subsequent "inflation". A very interesting book by Volovik [64] shows many examples about other analogies between the ^{3}He condensed matter system and the universe.

How could the Kibble-Zurek scenario explain (at least a part of) the measured energy deficit? The idea is that the vortices created in this scenario store an energy, which will only be released as heat once the vortices are dissipated. Experimental evidence however shows that a vortex tangle can be metastable, with a time constant $>$10 s. In the case of our experiments the heat will be released only after the VWR resonance width has reached its maximum, and the corresponding vortex energy is "lost" for the bolometric measurement.

While providing a nice "qualitative" explanation for the observed energy deficit, an accurate quantitative model is extremely difficult to obtain due to the different rapid and complex processes involved. Nevertheless, a very rough estimation can be made.

The density of topological defects resulting from the phase transition is thought to depend on several intrinsic parameters: the zero temperature coherence length ξ_0, the time τ_0 which is the response time of the ordered phase at low temperatures and which can be estimated to $\tau_0 = \xi_0/v_F$ and the parameter τ_Q, which is a measure of the time scale for cooling through the phase transition (the quench time). For this scenario, Zurek then

derives a simple formula for an estimation of the average separation β between vortices as $\beta_{theo} = \xi_0(\tau_Q/\tau_0)^{1/4}$.

The next step is to estimate the volume in which those vortices form. For this, the easiest estimation can be obtained considering that the energy is deposited initially at one point, and that the heat propagates afterwards radially. In this case, the volume of the normal fluid sphere first increases, and then after reaching a maximal radius shrinks to zero, as the ^{3}He thermalises. The maximum radius of the normal fluid sphere is found to be $R \sim 0.4(E/CT_c)^{1/3}$ where C is the liquid heat capacity just above T_c. The cooling time constant can then be estimated to be about $\tau_Q \sim R^2/4D$ where D is the diffusion constant.

An estimation for the energy per unit length of a vortex is obtained from the energy of the circulating superflow: $E_L \sim (\rho/4\pi)(\hbar/2m_3)^2 ln(\beta/\xi_0)$ which corresponds to about 0.5 keV/mm at 0 bar. This enables one to convert the total vortex energy, which is the parameter obtained experimentally, into a total vortex length $L = E_{vortex}/E_L$. Assuming now that the total vortex length is evenly distributed over a volume corresponding to the maximum volume of the normal sphere, the experimentally obtained average vortex spacing β_{exp} can be estimated: $\beta_{exp} = \sqrt{V/L} = \sqrt{(4/3)\pi R^3/L}$. Despite the simplicity of the assumptions and approximations used β_{exp} was remarkably close to β_{theo}. It was thus taken as an experimental evidence in favour of the Kibble-Zurek mechanism [17].

Other experimental evidence

Other support for the Kibble-Zurek mechanism in ^{3}He comes from experiments done in Helsinki [65, 66]. In this experiment a rotating cryostat is used. Due to the rotation, counterflow is created and above a critical rotation velocity, the lowest energetic state is one where vortex lines stretch from the bottom to the top of the cell. These vortices decrease the total superflow and the corresponding free energy. The total number of rectilinear vortex lines can be measured by NMR methods. Using a good cell design, the rotation speed can be increased above the critical velocity, without creating vortices, thus creating a metastable state. After preparing such a vortex free state, an AmBe neutron source is brought close to the cryostat, and when plotting the number of vortices as a function of time, discontinuous steps occur. The most likely interpretation for these steps is that after a neutron capture event a random "vortex tangle", as predicted by the Kibble-Zurek mechanism, is created. Without the counterflow, this vortex tangle is metastable and will disappear sooner or later. Due to the rotation, vortex rings above a critical radius r_0 and with the good orientation, i.e. transverse to the counterflow, will be stable and eventually expand. They will finally form rectilinear vortex lines, bringing the system closer to the equilibrium state.

The critical radius r_0 decreases with increasing counterflow, i.e. rotation velocity Ω. This means that for larger Ω, smaller vortex rings succeed to end up as rectilinear vortex lines, leading to a higher number of vortex lines created per neutron event. Such a Ω dependence of the vortex creation rate is observed. While non-equilibrium phase transitions are an extremely delicate subject, and their interpretation difficult, the measurements done in Helsinki are in good semi-quantitative agreement with the Kibble-Zurek mechanism [66].

We thus have an independent confirmation of the general idea of the Kibble-Zurek mechanism in superfluid ^{3}He, but any interpretation of the energy deficit in bolometric measurements such as the ones done in our experiment must face an additional criticism: the vortex tangle created in this process only contributes to the energy deficit if its decay time constant τ_v is long enough to influence the observed peak height, i.e. $\tau_v \gg 1\,\mathrm{s}$. At temperatures not too far from T_c, the time scale of the processes leading to the vortex decay is dominated by the mutual friction damping between the superfluid and the normal components. At our working temperatures of $\sim 0.15\,T_c$, the density of thermal excitations is negligible and vortices can move with almost no dissipation. Theoretical estimations thus support the assumption of a large time constant. An experimental answer to the question of the vortex-tangle life time, in comparable working conditions to ours, comes from experiments done in Lancaster.

In a first experiment [67], a bolometric cell was irradiated with a high activity neutron source, heating the cell well above the baseline temperature, and the cooling after the removal of the source was compared with the decay after a comparable heating using a heater wire. The thermalisation after the neutron irradiation was, after a first initial cooling, found to be much slower in the case of heating by neutron events. When interpreting this result in terms of delayed energy release by previously created vortices, the authors found a strong dependence of the vortex decay time constant τ_v with temperature. At our temperatures their results would correspond to $\tau_v > 100\,\mathrm{s}$, satisfying well the previously formulated condition $\tau_v \gg 1\,\mathrm{s}$. However it must be stated that the authors are not convinced of an interpretation in terms of vortex decays, as other explanations like a delayed heat release from the walls, heated by the neutron irradiation could not be excluded.

A more recent experiment [68, 69] delivers more convincing results. In this case, vortices are not created by a neutron source, but by a grid operated similarly to VWRs. It is known that when driving such an object at sufficient velocity, vortex rings can form on imperfections on the surface and be emitted. The number of vortices created increases with the velocity of the grid. Operating a VWR at some distance (1-2 mm) from the grid, an influence of the vortex density on the resonance width is clearly measured. An interesting observation can be made when the vortex producing grid is stopped: when this grid was driven at low velocities, and the vortex density created was low, the influence on the resonance width of the sensor VWR almost immediately ($<$0.1 s) disappeared. On the other hand for high initial vortex densities the influence survived up to 10 s. This big change was explained by the formation of vortex tangles in the case of high vortex densities which are thought to be much more stable than isolated vortex rings.

For our measurement, the initial vortex density is much larger than in this Lancaster experiment but on the other hand the concerned region is much smaller. As today it is unknown whether the determining factor for the stability of a vortex tangle is the vortex density or the total volume, the comparability to our case is questionable. On the other hand it can be stated that this Lancaster experiment is only sensitive to the high density vortex tangle close to the VWR sensor, but that it does not say anything about the stability

of ballistic, independent vortex rings. Nonetheless these Lancaster experiments clearly indicate that a stability $\tau_v \gg 1\,\mathrm{s}$ seems not only to be reasonable but has experimental backing.

9.2 New experimental results

The current experiment was done as follows:

- After cooling to the working temperatures, frequency sweeps to determine the factor $\mathcal{H} = VW_0/I$ were done very accurately.
- The VWR thermometer was then driven in the monitoring mode.
- A first series of heater pulses was done to determine the calibration factor $\sigma = H/E$ at the lowest temperature. A typical pulse is shown in fig. 9.2, a typical linear fit of the results of a whole pulse series is shown in fig. 9.3.
- An AmBe neutron source, moderated by about 8 cm of paraffin was then placed close to the cryostat, and a long time ($>$12 h) was waited to acquire a large number of neutron capture events (~ 100). A typical acquisition file can be seen in fig. 9.4. The resulting histogram is shown in fig. 9.5.
- At least at the end of a run, but most of the time in the middle of a run, additional pulse series were done, in order to improve the calibration precision.
- The energy released as heat was determined by plotting the energy distribution in a histogram. The histogram was fitted with a Gaussian distribution, and the centre of this Gaussian was then taken as the energy released as heat (see fit in fig. 9.5).

The final result, together with results from the 1995 experiment [17], results from 2004 [33], and new results from 15 different demagnetisation runs, are shown in fig. 9.6. In this graph, we did not include the point at 19.6 bar from 1995 [17] since an analysis presented in a later publication [70] showed that a large uncertainty persisted about the calibration: calibrations were done at two different temperatures, and showed a discrepancy of about 14 %, with the calibration at "warm" temperature seemingly in line with the calibrations at lower pressures. The neutron measurements were done at low temperatures. So if the calibration factor used to calculate the neutron energy was the one taken at warm temperatures the discrepancy between the new neutron data and the 1995 data, which amounts to approximately 14 %, can be perfectly explained by such an error.

First of all it can be noted that we have an impressive accuracy at 0 bar, where measurements from four different demagnetisation runs, done on two different cells, show a dispersion which is smaller than one percent. This observation makes us confident that for a future application in a dark matter detector, the reproducibility of the energy calibration will be very good.

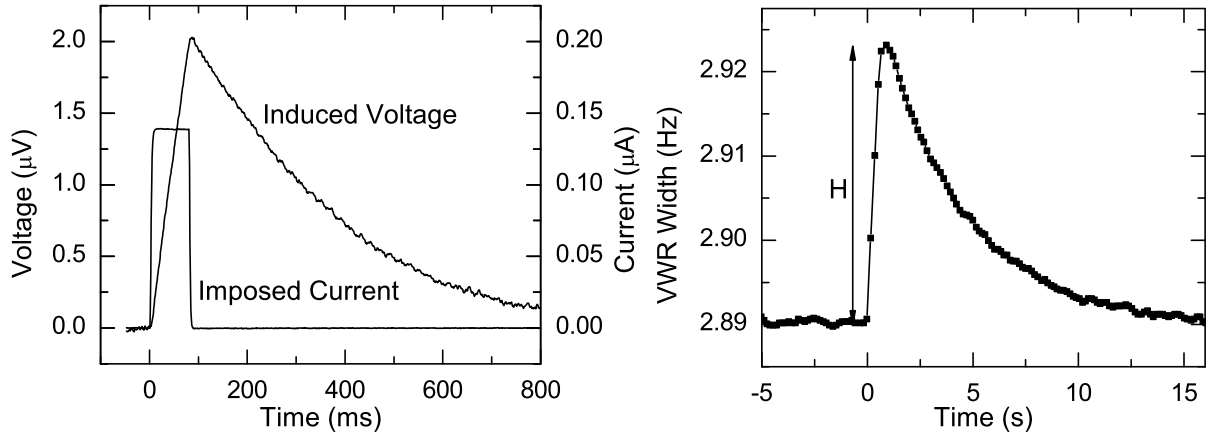

Figure 9.2: Example of a typical heating pulse, at $p = 15\,\mathrm{bar}$, $W_{base} = 2.89\,\mathrm{Hz}$. a) Heater wire measurement. The heater wire is excited during 80 ms at its resonance frequency with a constant drive. The acquisition rate is 1 point/ms. This graph illustrates well that the precision on the energy injection is very good. The injected energy is calculated as the time integral of the electrical power: $E_{electric} = \int UIdt$. An important correction to this energy due to intrinsic losses is explained in section 5.3.6, and systematically applied. This pulse corresponds to an energy injection of 671 keV. b) The response of the thermometer VWR to this pulse. The noise on the baseline W_{base} is estimated to be $\delta_{peak-peak}W \sim 1\,\mathrm{mHz}$, corresponding to $\delta_{1\sigma}W \sim 0.35\,\mathrm{mHz}$.

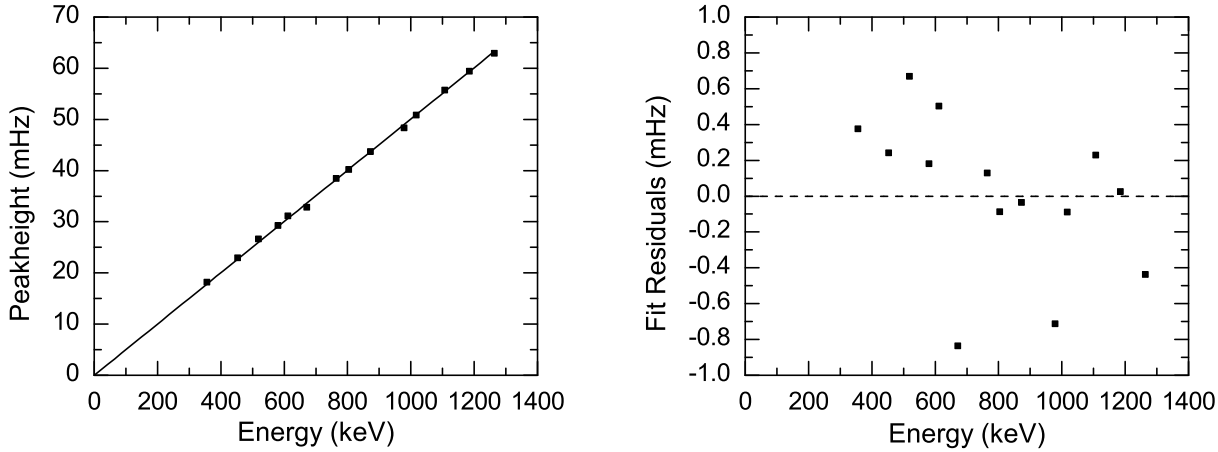

Figure 9.3: A typical result of a series of calibration pulses taken at the same temperature during a total time of about 12 minutes, at $p = 15\,\mathrm{bar}$, $W_{base} = 2.89\,\mathrm{Hz}$. The pulse shown in fig. 9.2 is one of the pulses of this series. The linear fit, using the model $H = \sigma E$ yields $\sigma = (50.08 \pm 0.14)\,\mathrm{mHz/MeV}$. The residual plot shows that the previously estimated precision of $\delta_{1\sigma}H \sim 0.35\,\mathrm{mHz}$ for a single peak has the correct order of magnitude.

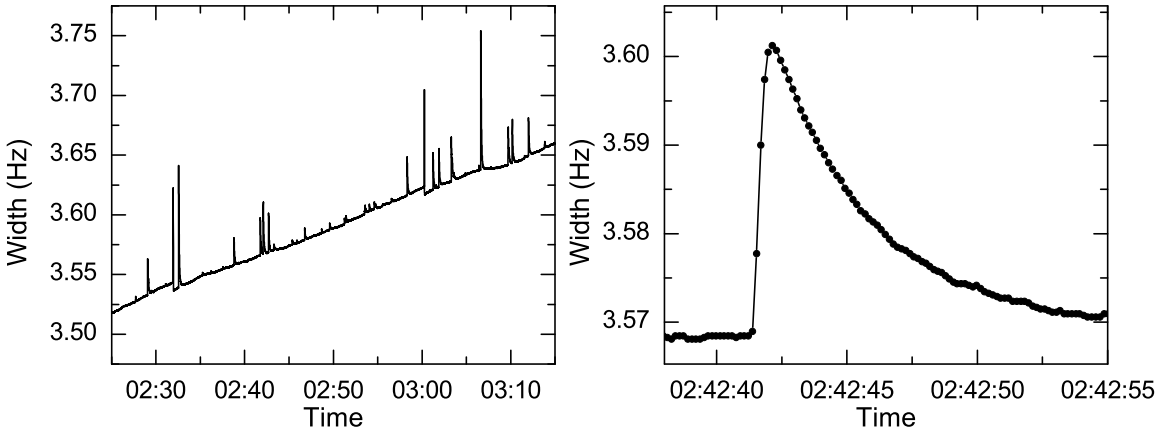

Figure 9.4: a) A typical neutron acquisition file (at 15 bar). The baseline resonance width is not globally stable, due to the cryostat's heat leaks. To work at constant velocity amplitude, the drive was adjusted automatically. The small jumps in the baseline at 2:32 and 3:00 are results of such adjustments. b) A zoom on a single neutron event. Even if the baseline is not perfectly stable, locally the slope is small enough to have a negligible influence on the measurement of the peak height.

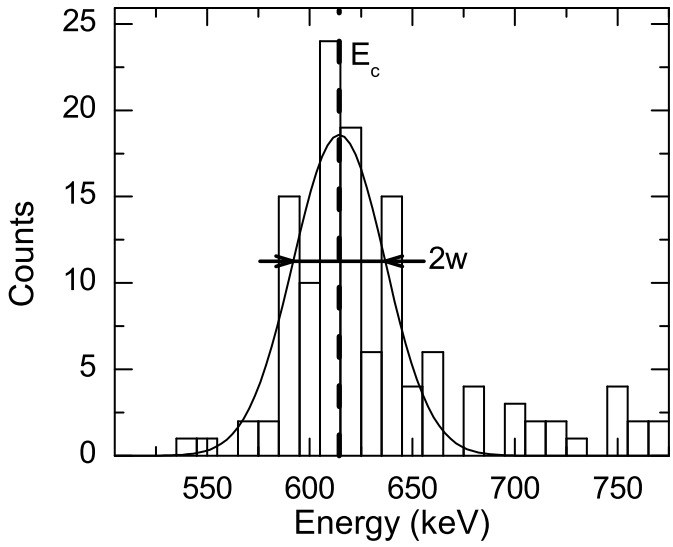

Figure 9.5: A Typical distribution of neutron events at 15 bar. The shape of the distribution is slightly asymmetric, due to the fact that the neutrons from the source are not completely moderated and capture events caused by neutrons with non negligible kinetic energies are possible. The Gaussian fit for this histogram (eq. C.1) yields the following values: $E_c = (614.3 \pm 2.3)$ keV (centre of the Gaussian), $w = (22.4 \pm 2.3)$ keV (one standard deviation), $A = 18.6 \pm 1.6$ (amplitude).

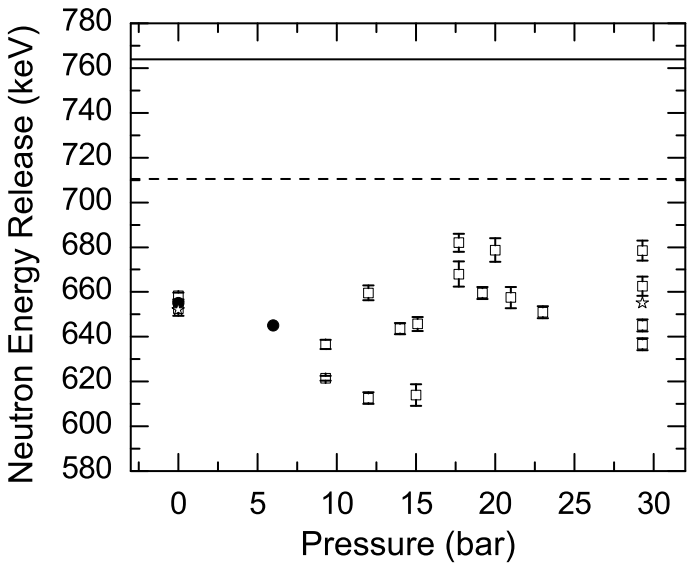

Figure 9.6: Final result for the pressure dependence of the heat release by a neutron absorption event. Full circles (0 and 6 bar) are results from 1995 [17]. Stars (0 and 29.3 bar) are results from 2004 [33], measured using the same setup as this work (squares with error bars). A point taken in 1995 at 19.6 bar has been removed due to large uncertainties in the calibration (see text). The solid line corresponds to the total energy of 764 keV deposited by a neutron capture event, the dashed line is the total energy minus the scintillated energy which is considered to be 7 % of the 764 keV released. Except for the values at 29.3 bar, all points correspond to measurements from a different demagnetisation run.
First of all it can be noted that at 0 bar, the scatter comprising results from four different demagnetisations done in two different cells is very small ($< 1\,\%$), giving us a high confidence that a precise calibration for a future dark matter detector operated at 0 bar can be obtained.
Values at non zero pressures show a much higher dispersion than what would be expected from an analysis of the statistical errors (indicated by the error bars).

At higher pressures, the measurements show a large scatter, much larger than what should be expected from the indicated error bars. This is why a detailed discussion of the possible inaccuracies is necessary before we try an interpretation of this pressure dependence. This discussion is quite lengthy and is presented in appendix C.

9.3 Discussion of the result

Assuming the error bars as obtained from the discussion in appendix C to be correct, we will now consider physical interpretations of the results. Unfortunately calculations on rapid phase transitions are notoriously complex and much beyond the scope of this thesis, so that the following discussion will remain very qualitative.

In fig. 9.6, two horizontal lines are drawn. The solid line at 764 keV shows the energy which is released by the neutron capture reaction. The first observation thus is simply that for all pressures measured, only 80-90 % of the total energy is released as heat at the moment of the peak, i.e. about 1 s after the primary event. As presented in section 5.4 and chapter 7, a part of the missing energy can be explained by the formation of ^{3}He-dimers, which either scintillate, and hence transport the energy to the cell walls, or which form metastable triplet dimers. The new measurements presented in section 7.2 show that the total peak height reduction due to dimers is about 7 % at 0 bar. This value is comparable to estimations which can be taken from scintillation measurements in ^{4}He. We consider this value to be pressure independent, but it should be kept in mind that due to the changed density and transport properties, a pressure dependence can not be excluded. The dashed line at 710 keV thus represents the total energy deposited minus the 7 % reduction due to scintillation and metastable triplet dimers. These assumptions lead us to the observation that a significant energy deficit persists, which supports the idea of a Kibble-Zurek vortex creation scenario.

Using the additional assumption that no other mechanism exists that contributes significantly to a reduction of the peak height, we can now present the energy stored in vortices as a function of pressure (fig. 9.7). A clear interpretation of this result is not easy due to the large scatter. Nevertheless some features can be observed:

- Between 15 and 17.7 bar, a substantial jump from ~ 80 keV to ~ 35 keV is observed.
- Below 15 bar, the vortex energy contribution increases with pressure.
- Above 17.7 bar, precision is not sufficient to conclude on a pressure dependence of the vortex energy contribution, but a slight increase seems possible.
- Especially in a wide range below 15 bar, the scatter is much larger than what is expected from the error analysis.

To explain these results in terms of a vortex creation scenario we remind that the energy deficit due to vortices is not only determined by the energy initially stored in vortices, but

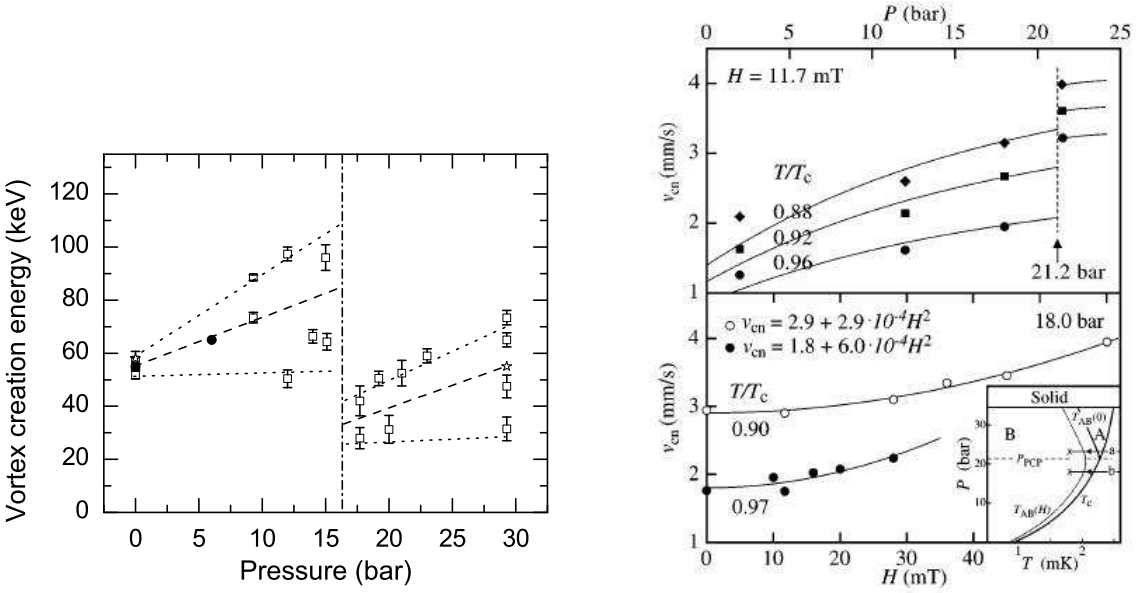

Figure 9.7: a) Considering the peak height reduction due to dimers to be 7 %, the energy stored in metastable vortices is obtained from experiments as 710 keV-$E_{neutron}$ (see fig. 9.6). Points from 1995 (bold circles), 2004 (stars) and new data (squares with error bars) are considered. The lines are guides to the eye. The scatter is relatively large, but a jump between the points at 15 bar and at 17.7 bar appears clearly. Below 15 bar and above 17.7 bar, the vortex energy seems to increase with pressure.
b) A comparison to pressure dependent data taken in Helsinki on a rotating cryostat shows that they observe a jump of the critical velocity at slightly higher pressures between 18 and 21.2 bar. As they work at a lower magnetic field, and observe an increase of critical velocity with magnetic field, both experiments seem to be in good agreement (from [65]).

also by the stability of these vortices. The created vortices contribute to the energy deficit only if they survive longer than the time of the maximal peak height $\tau_v \gg 1\,\mathrm{s}$. This leaves us thus with the possibility that the variations observed should be either the result of a change in the number of vortices created, or a change in their stability.

The most pronounced of the listed features is the discontinuity between 15 bar and 17.7 bar. Previous discussions brought the question whether not all of the observed energy deficit can be attributed to other channels like scintillation and dimer formation [71]. We do not know all the details of the fast processes leading to the dimer formation (see section 5.4). So while we think that a pressure dependence for these non-vortex contributions is unlikely, we admit the possibility that the pressure dependence for $p < 15\,\mathrm{bar}$ could be entirely due to dimers, for example through an enhanced dimer formation through the changed diffusion constant. But in this case it would be impossibly to explain the jump observed between 15 bar and 17.7 bar. We thus take the presented measurements as further evidence that the formation of dimers can only explain a fraction of the energy deficit, and we propose that all the pressure dependence can be attributed to vortices.

9.3.1 Possible explanations for the discontinuity

Baked Alaska* and *Aurore de Venise

When one cools down ^{3}He at pressures above the pressure of the polycritical point ($p > 21\,\mathrm{bar}$), ^{3}He undergoes first a phase transition to the A-phase before getting to the regime where the B-phase is the stable phase. Normally, the A-phase supercools a considerable amount, but after some time, of the order of a few minutes to an hour, the B-phase nucleates. The reason for this nucleation stayed during a long time a mystery, because thermal fluctuations alone are too small to overcome the energy barrier between both metastable states, and all obvious mechanisms provided nucleation rates magnitudes above the observed ones. Leggett [72] proposed in his *Baked Alaska* scenario that this nucleation is triggered by a cosmic particle, depositing enough energy to locally heat the liquid to the normal phase. If the subsequent cooling is then fast enough, there exists a finite probability that this region ends up as a "bubble" of B-phase. Leggett continues his argument that if this bubble grows above a critical radius of order $1\,\mu\mathrm{m}$, the surface energy σ_{AB} will not be enough to let it disappear again, and it can serve as a nucleation centre. Leggett advances the idea that a front of quasiparticles leaves ballistically (and not diffusively) the centre of the hot spot. This normal phase shell of temperature $T > T_c$ then acts as an isolation between the B- and the A-phase, and thus gives the B-phase bubble enough time to grow above the critical radius (for a good explanation see for example [73]).

An alternative model, baptised *Aurore de Venise,* is proposed by Bunkov and Timofeevskaya (BT) [74, 75]. While Leggett considers that only one phase nucleates at the place of the incidence, and the energy is distributed amongst few quasiparticles which then leave the centre ballistically, this scenario proposes a more hydrodynamic picture, in which a whole region is heated above T_c. The rapid cooling then gives place to a number of

different causally disconnected phases. The point of the BT-model is that arbitrarily, both phases, A and B, can nucleate at different places. The probability to nucleate in either is in the BT-model not determined by the difference in free energies of the two states as one might intuitively suggest. Bunkov and Timofeevskaya calculate instead the 18-dimensional energy profile and claim that the probability is determined by the asymmetry of the profile near the high symmetry state. In other words, even if one state has a lower energy (and would thus be the ground state), if more trajectories lead from the high symmetry state to another metastable state, this second one has higher probability to form. The numerical calculations presented in ref. [75] show that in this Aurore de Venise scenario, the probability of the superfluid A state nucleation can be above 50 % even below the polycritical pressure down to pressures of about 12 bar.

What does our measurement tell about these two models? The Baked-Alaska scenario does not predict the production of a noticeable amount of vortices. Until these new measurements, it could be argued that uncertainties about the exact amount of energy going to scintillation are large enough to account for all of the energy deficit observed. This in turn would leave no place for energy stored in vortices and save the baked Alaska scenario. But the fact that a jump for the energy deficit is observed, that the Helsinki experiment succeeds to show directly the production of vortices and the observations presented in chapter 7 makes the Baked Alaska scenario seem to be unlikely.

For the Aurore de Venise scenario it has to be mentioned first that it has been developed using the Ginzburg-Landau theory. It is thus questionable to which extent the BT-model is of relevance for our measurements which are done at a base temperature far below T_c. Nonetheless it can be stated that Aurore de Venise does allow for a pressure dependence, and it predicts that differences can be observed at low and at high pressures: as can be seen from the phase diagram, the A phase is stable, and thus lower in free energy for high pressures and close to T_c. On the other hand, the thermodynamically stable phase at the working temperatures far below T_c is the B-phase. This means that at high pressures, a high number of A-phase domains should nucleate at first, but disappear quickly in a few milliseconds. It is known from experiments done in Helsinki that vortices can not cross the A-B phase boundaries, which finally results in the prediction for the BT model that above a certain pressure, the number of vortices created is much reduced compared to the low pressure value. On the other hand we expected the transition of this regime to be closer to $p_{PCP} = 21$ bar, and we naively expected a smoother transition instead of having a jump. In any case, more theoretical work is certainly needed to show whether these results are supporting the Aurore de Venise model.

The different kinds of stable vortices

An alternative, albeit only qualitative idea to explain the observed jump delivers a phase diagram which includes the regions in which different kinds of vortices are stable (see fig. 9.8). Most of the knowledge about vortices in ^{3}He comes from measurements done on a rotating cryostat in Helsinki, where counterflow stabilises vortices and allows to do systematic NMR studies on this kind of topological defects [76, 77, 78]. A review about

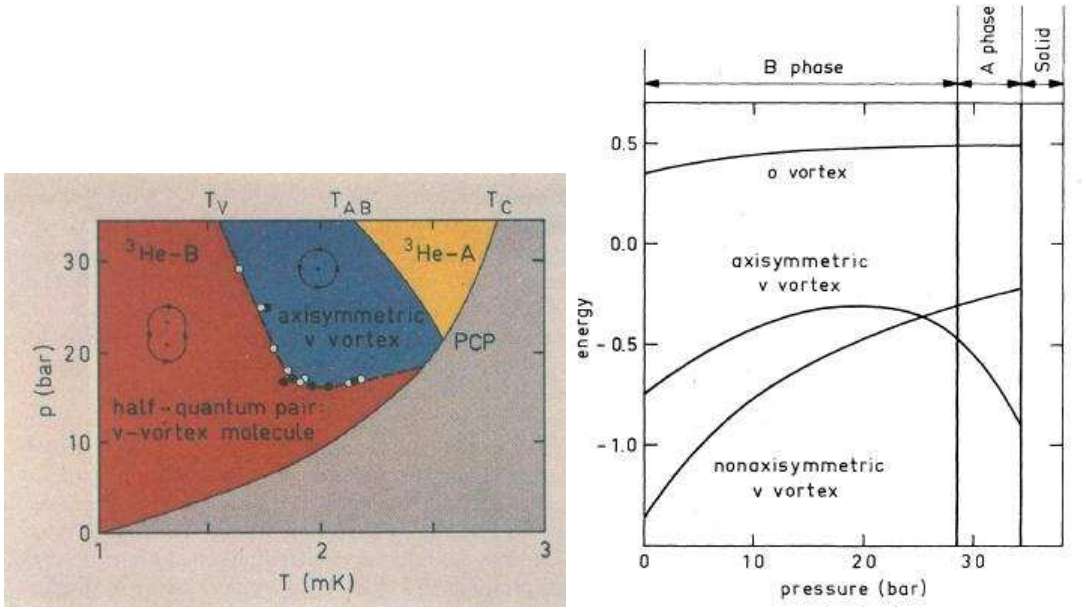

Figure 9.8: a) Phase diagram of ^{3}He (from [79]). NMR studies in a rotating cryostat show that close to T_c, different kinds of vortices are stable at different pressures in the B-phase. b) Calculation of the vortex energy for different kind of vortices at different pressures near T_c, in a Ginzburg-Landau region where all parameters are known (from [82]).

the main findings from these experiments is presented by Salomaa and Volovik [79]. One very interesting point of their findings is the observation that in the B-phase two distinct regions exist where different kind of vortices have the lowest free energy. The so-called nonaxisymmetric v-vortex is observed below 16.5 bar and at temperatures $T < T_V$ for $p > 16.5$ bar. On the other hand the so-called axisymmetric v-vortex minimises the free energy in a region at pressures between 16.5 bar and above T_V (see fig. 9.8). For simplicity we will call the former type I vortex and the latter type II vortex. The intriguing point is that this critical pressure of 16.5 bar lies exactly between the two pressures where our jump in vortex creation energy is observed.

The idea is thus that the observed jump is due to these two phases: below 16.5 bar, mainly type I vortices form. Above 16.5 bar, at the working temperatures of $\sim 0.15\,T_c$, the stable vortices are still type I vortices, but during the quench after an event, the hot spot region crosses on its way back to the working temperatures the type II-vortex phase. The type II vortices are known to live a very long time even below T_V. On the other hand it is well possible that the dynamics of the vortex tangle is very different for the two types of vortices [80, 81].

9.3.2 Can different textures change the energy deficit?

Especially for $p < 16$ bar, the observed scatter is larger than what is expected from the error analysis, and even for constant pressure very different values for the energy deficit

are found for different demagnetisations. As upon cooling through T_c the order parameter spontaneously "chooses" an orientation, the possibility exists that the texture is different for different demagnetisation runs. But can textures have a significant influence on the observed energy deficit? As the production of vortices happens very locally on a small volume around the incidence, we see no reason why the texture should play any role in the vortex creation mechanism and should thus not influence the number of vortices created. The only possibility to explain the observed difference in energy deficit in terms of vortices is thus to suppose that textures could influence the stability of vortices: if the vortices decay on a time scale faster than the response time of the wire, they do not contribute to the energy deficit.

For ordinary textures we know that they should not destabilise vortices, mainly because the topological charge of the vortices is a conserved quantity. On the other hand there exists experimental evidence that two dimensional topological defects ("branes") can form and that they can be metastable [83, 84]. This formation can happen spontaneously after a demagnetisation [84]. In the case of the Lancaster experiment [83] they can be created by first creating an A-phase layer between two layers of B-phase using a magnetic field. After reducing the magnetic field, the A-phase disappears, but topological defects persist. Topological defects, as opposed to ordinary textures, have the possibility to destroy vortices, as they have the possibility to take the topological charge.

A possible mechanism to explain the non-reproducibilities would thus be to assume that an arbitrary number of topological defects is created during the demagnetisation. Depending on the number of these defects, the stability of the created vortices largely varies, leading to a different energy deficit.

Unfortunately considering the random nature of this defect formation it is very difficult and time consuming to study this idea systematically. The only try that was made is a series of measurements at 29.3 bar.

The 29.3 bar measurements

All points presented in fig. 9.6 were made at different demagnetisation runs, except the four points taken at 29.3 bar. In fact, for pressures between 0 and 29.3 bar, every transfer of liquid ^{4}He to the bath leads to a cooling of the ^{3}He filling line, which in turn leads to a decreased pressure in the cell. Due to this change of pressure, liquid ^{3}He starts to move which finally leads to a heating of the liquid ^{3}He by viscous friction. While this is not an enormous effect, it is sufficient to heat the liquid above the working temperatures. This mechanism does not work at 0 bar because the pressure can not decrease further. When working at 29.3 bar, we apply from outside a higher pressure than 29.3 bar, but as we pass the minimum of the melting curve, a "plug" of solid ^{3}He forms and the pressure inside the cell will be fixed at 29.3 bar, independently of the pressure changes above the plug.

In short, at 29.3 bar, due to a longer time of one demagnetisation, we had the possibility to make measurements in four different conditions during one demagnetisation run. The chronology of the four acquisitions was as follows:

1. We stopped the initial demagnetisation at 280 mT, and made a first neutron acquisition in the obtained conditions.

2. Then we demagnetised to 40 mT and magnetised back to 280 mT, doing a second neutron acquisition. In a previous experiment we had observed that topological defects, blocking a VWR could be "annealed" by this method [84], so the idea was to observe whether such an annealing would have an effect on the energy deficit.

3. After a ^{4}He transfer, we demagnetised to 250 mT doing a third neutron acquisition.

4. Finally we heated the cell with the heater VWR above T_c. After the cell recovered, we had to demagnetise further to 210 mT to be back at the working temperature and the fourth neutron acquisition could be done.

The results of these measurements are presented in fig. 9.9. Two features can be observed in this figure: the centre of the distribution is moving to lower energies, corresponding to a higher energy deficit and the width of the distribution becomes smaller. This second observation might contain some information as the observed noise, and hence the expected precision on the baseline was practically the same in the four cases.

Only looking on the result of this 29.3 bar experiment, the most obvious observation is that there seems to be a magnetic field dependence, the lower the field the higher the energy deficit. However, for the other pressures, which were done at different magnetic fields, such a systematic is not at all observed. The magnetic field thus might be influencing the energy deficit, but it definitely is not the dominant factor.

We can thus say that we found a positive effect of the systematic annealing: as expected, the energy deficit increased which is a signature that the lifetime of vortices has increased. An increased vortex lifetime points to a decreased number of stationary topological defects. We were surprised that the main annealing effect happened during transfer as we supposed that demagnetising to 40 mT or heating above T_c should have a larger effect. One possible explanation could be an influence of the mechanical vibrations which happen during transfer on the stationary topological defect.

9.3.3 Conclusion

We presented detailed measurements of the pressure dependence of the energy released as heat after a neutron capture event in superfluid ^{3}He. We have found a systematic increase of the energy deficit, but with a large scatter. A thorough error analysis showed that the known experimental uncertainties can not explain the observed scatter, meaning that physical explanations must be considered. We suppose it is due to two-dimensional stationary topological defects which form randomly on the initial cool down. In addition we found a jump at a pressure between 15 and 17.7 bar. This jump occurs at the pressure at which the vortex phase diagram changes from one type of stable vortex to another, which possibly is the reason behind this jump. We think that such a jump is incompatible with a Baked Alaska scenario. The Aurore de Venise scenario should be sensitive to the

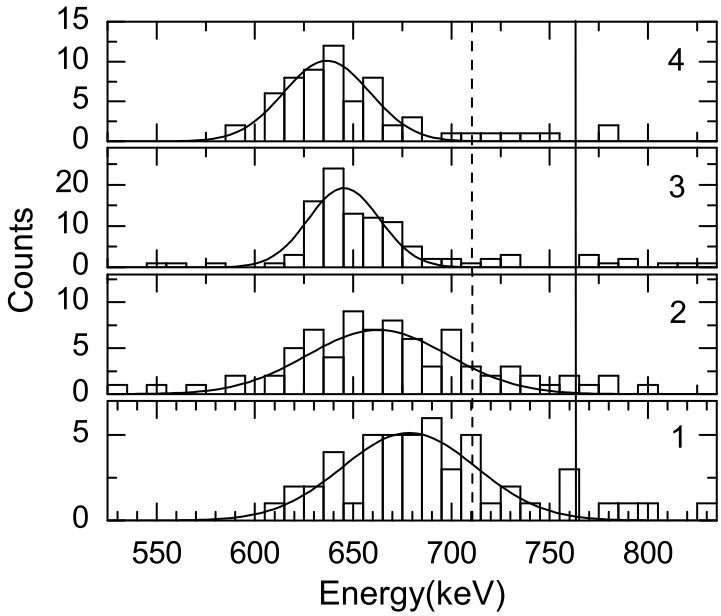

Figure 9.9: Neutron histogram for the four different neutron acquisitions at 29.3 bar taken during one demagnetisation run. Series 1 was taken immediately after the initial cool down at 280 mT, series 2 after a demagnetisation to low field and subsequent upmagnetisation to the working field of 280 mT, series 3 after a ^{4}He transfer and a subsequent demagnetisation to 250 mT and series 4 after a heating above T_c using a VWR and a subsequent demagnetisation to 210 mT. The two observable features are a decrease of the width of the distribution and a shift of the peak towards lower energies. The solid and the dashed lines correspond again to the energy released by a neutron capture event and this energy minus the expected dimer energy respectively.

pressure at the region of the tricritical point ($p_{PCP} = 21\,\mathrm{bar}$). In a naive approximation we expected to see a smooth change around 21 bar instead of observing a jump. The further development of the Aurore de Venise scenario needs to compare with this new experimental data.

Part III

^{3}He confined in anisotropic aerogel

Introduction

This third part treats a very different subject than the first two parts. New measurements studying the effect of anisotropic aerogel on superfluid ^{3}He are presented. Many experiments were done on liquid ^{3}He impregnated in high porosity aerogel since the observation that superfluidity can occur in such a configuration [85, 86]. As the strands of aerogel are only of about 3 nm in diameter, and hence much smaller than the superfluid ^{3}He coherence length, aerogel can be used to study the influence of impurities on the otherwise 100 % pure ^{3}He. Several facts are now well established: the superfluid transition temperature is reduced, and the effect of pair breaking is enhanced, especially at low pressures. This leads to the fact that below a critical pressure p_c, whose value depends on the details of the aerogel sample, no superfluidity occurs. Three phases have commonly been identified, labelled A-like, B-like and A_1-like phase [85, 87, 88]. The B-like and the A_1-like phase are observed to be very similar to the B and the A_1 phase of pure bulk superfluid. Some discussion has arisen over the nature of the A-like phase. Experimental evidence, especially from NMR magnetisation measurements indicate that it is an equal spin pairing state like the pure A phase. Several interpretations of this A-like phase have been proposed [89, 90, 91]. For an overview of the current experimental and theoretical knowledge about ^{3}He in aerogel, the review article of Halperin and Sauls may be consulted [92].

The initial idea behind the current experiment was driven by the recent observation of Kunimatsu *et al.* [11] that using a compressed aerogel sample, the orbital momentum $\mathbf{L}$ of the cooper pairs tends to align in the direction of squeezing. In other words, using anisotropic aerogel allows to orient the order parameter. Contrarily to this experiment by Kunimatsu *et al.*, we compressed the cylindrical shaped sample in the radial rather than in the axial direction. This allowed us to simulate a stretch in the axial direction, with the result that $\mathbf{L}$ preferred to be orthogonal to the cylinder axis. As the cylinder axis was parallel to the magnetic field $\mathbf{B}$, this corresponded to an orientation of $\mathbf{L}\perp\mathbf{B}$. While for the A-phase the orbital momentum in the bulk is usually orthogonal to the magnetic field, in the B-phase we obtained a texture which can not be realised in pure bulk ^{3}He (see section 3.3.2).

Recent theoretical calculations by Aoyama and Ikeda [93, 94], predict that such a radial compression would

1. stabilise the A-phase with respect to the B-phase in a significant region of the phase diagram,

2. stabilise a new, so-called polar phase in a small temperature region between the A-phase and the normal phase (see fig. 10.12).

The continuous wave NMR (cw-NMR) measurements presented in the following sections will show to which extent our experiment supports these predictions.

The pulsed NMR measurements presented in chapter 11 were then used to study the spin dynamics in the B-phase in the non linear regime, i.e. for high deflection angles. In the pure bulk ^{3}He case, where $\mathbf{L} \parallel \mathbf{B}$, this leads to the formation of homogeneous

precessing domains (HPD) for deflection angles $> 104°$ (see review article [95]). In our new configuration with $\mathbf{L} \perp \mathbf{B}$, the formation of another, up to day unobserved precession mode, called HPD2, was predicted for spin deflection angles $> 90°$ [96]. Our measurements presented in chapter 11 correspond very well to these predictions, and we will show the characteristics of this new precession mode.

The tool of choice to study the influence of anisotropic aerogel is the use of nuclear magnetic resonance (NMR). NMR is a widely used technique and a lot of literature exists on the matter. For its application in condensed matter physics the reference work of Abragam may be recommended [97]. The spectrometers used for continuous wave and for pulsed NMR were already installed and are explained elsewhere (see [35, 98]).

Chapter 10

Continuous wave NMR measurements

10.1 The sample and the cell

The aerogel cell and the RF coil used in this experiment have been prepared by Yu. M. Bunkov, the aerogel sample used is a 98 % porosity sample, produced by N. Mulders (Delaware university). Its dimensions are diameter $d = 5.2\,\mathrm{mm}$ and length $L = 15\,\mathrm{mm}$. The sample was put in an inner cylinder, with inner diameter $d_{i,1} = 5.2\,\mathrm{mm}$ and outer diameter $d_{i,2} = 7\,\mathrm{mm}$. Six 1 mm thick longitudinal slots have been cut every 60°. This allowed to put this cylinder into an outer cylinder of inner diameter $d_{o,1} = 6\,\mathrm{mm}$. In total the inner cylinder is thus compressed by $d_{i,2} - d_{o,1} = 1\,\mathrm{mm}$, corresponding to a compression of the aerogel of about 20 %. Assuming that the length of the aerogel sample is not affected by this compression, the volume shrinks by about 35 %, leading to an effective aerogel porosity of 97 %. The cylinder is closed on the bottom, but in direct contact with bulk ^{3}He at the top of the cell, where it is connected to the NMR demagnetisation stage. The cylinder axis is oriented vertically and hence parallel to the magnetic field. This stage contains several resistor thermometers for higher temperatures, and a Tantalum 125 μm VWR thermometer for low temperatures $T < 50\,\mathrm{mK}$. This VWR thermometer has been calibrated in detail previously [42], allowing for an accurate thermometry down to the lowest temperatures used during this work.

The RF-coil was made using a 70 μm copper wire. It was wound on Stycast impregnated paper in the form of a double saddle coil, with 50 turns on each side. Each side is about 13 mm long and 11 mm wide. The resonance frequency of the RF circuit was measured to be 1.1774 MHz with a quality factor of 61.6.

Before condensation of the ^{3}He, about 100 ccSTP[1] of ^{4}He have been added to the cell, in order to cover all surfaces with up to three monolayers of ^{4}He. This avoids magnetisation contributions of paramagnetic adsorbed ^{3}He and it prevents the possibility of a spin flip scattering of quasiparticles with the aerogel strands. In this way, it is assured that aerogel only acts on the orbital, and not on the spin part of the order parameter. During

[1] Measure of a number of atoms, corresponding to $1\,\mathrm{cm}^3$ of gas in standard conditions, i.e. 0 °C and atmospheric pressure 1.01325 bar.

the experiment, no 1/T component, as expected for a paramagnet, was observed in the magnetisation, indicating that we succeeded in preventing the formation of solid ^{3}He on the surfaces.

Accuracy of the thermometry

The VWR thermometer has been used in the frequency sweep mode permanently, with every sweep taking 100 s. The quality of the obtained Lorentz curves is excellent, leading together with the previous calibration to a temperature precision of better than 1 μK. As an illustration of the statistical error of the temperature precision, fig. 10.2 shows the temperature as a function of time, taken in very stable temperature conditions. While this does of course not indicate whether the absolute value of the temperature is correct, it shows that the scatter between different points is very small.

10.2 Continuous Wave NMR results

The first method used to study the orientational effect expected is the use of continuous wave NMR (cw-NMR). The excitation frequency has been fixed at the resonance frequency of the RF-circuit, and the sweeps have been done scanning the magnetic field around the Larmor value of $B_0 = 35.5\,\mathrm{mT}$. The data can then be converted to obtain the corresponding sweep in the frequency domain using the gyromagnetic factor $\gamma = 32.433\,\mathrm{MHz/T}$. Our cryostat is equipped with a double core coil, where the main coil is used to impose a fixed field, adjusted close to B_0, and a second, smaller coil is used for the scans around this value. This allows us to do very precise sweeps with a field resolution better than 0.2 μT, corresponding to a frequency resolution of 6.5 Hz.

All cw-NMR measurements presented in this work have been done in the linear regime, i.e. for low RF excitations. This means that the deflection from the equilibrium magnetisation is very small, and that the spin deflection angle is close to zero.

Measurements at four different pressures, 0 bar, 19.5 bar, 25.0 bar and 29.3 bar have been done. At 0 bar, no superfluid transition has been found, as expected from previous aerogel experiments. For the other three pressures, the observed temperature dependent features where qualitatively the same, with pressure dependent transition temperatures.

10.2.1 Normal phase gradient measurements

In our setup, a gradient coil allows to modify the magnetic field gradient in the $\hat{z}$ direction. The relation between the current imposed on the gradient coil and the corresponding gradient field is known.

Although our main and modulation coils are of good quality, and the field from the demagnetisation solenoid is compensated by a compensation coil, a broadening of the NMR-line due to the magnetic field inhomogeneity can be observed when no current is imposed on the gradient coil. Due to the motional narrowing, the natural line width is,

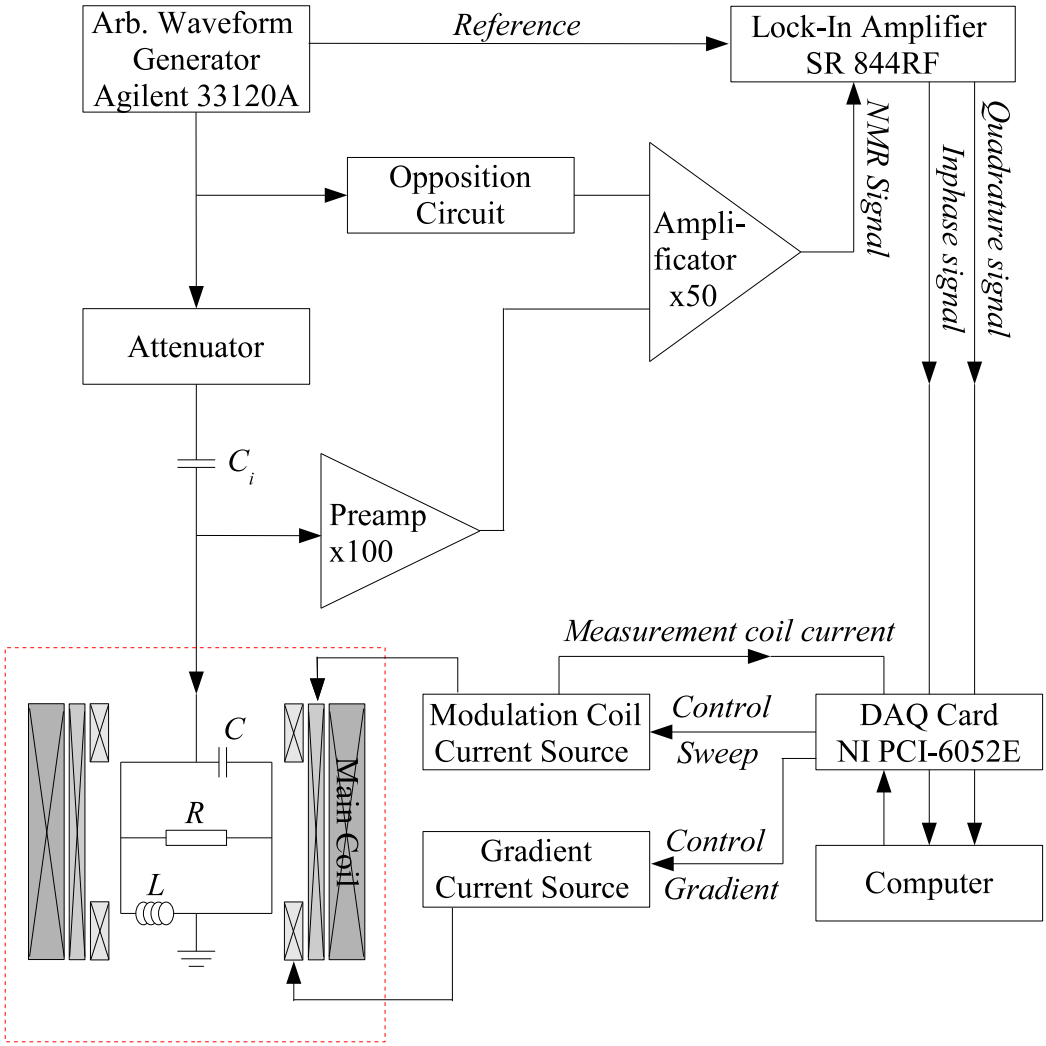

Figure 10.1: Illustration of the electronic circuit for cw-NMR. The excitation energy of the RF coil is fixed with the arbitrary waveform generator at the resonance frequency of the RCL circuit. A current is put on the main coil such that it produces a static field close to the Larmor field. This value is kept constant by shunting the superconducting main coil. The gradient coil is usually put on a value to compensate as much as possible the inhomogeneities of the magnetic field. The sweep around the Larmor field is done by the modulation coil.

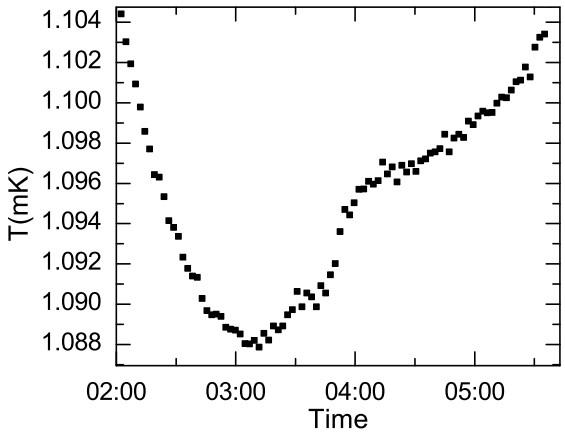

Figure 10.2: This graph shows the temperature as a function of time as measured by the thermometer wire. It is a zoom on an arbitrary piece of data, when the temperature was very stable. It shows that the sensitivity is better than $1\,\mu$K.

at the temperatures we are working at, very small. This means that even for small field inhomogeneities the line shape in normal phase ^{3}He is dominated by these inhomogeneities. Before starting with the main measurements, we thus did several cw-NMR sweeps at different gradients, to determine at which gradient field the line width is minimal (see fig. 10.3). Afterwards, we defined this to be our optimal gradient, and all other gradients are calculated starting from this value. When not stated otherwise, we worked at the optimal gradient. A remarkable feature of this setup is the quality of the obtained lines: at the optimal gradient, a line width of $2.6\,\mu$T (84 Hz) at $B_0 = 35.5\,$mT ($f_0 = 1.1774\,$MHz) was found. The settings were stable all along the experiment.

10.2.2 Normal, A-like and B-like phase

Fig. 10.4 and fig. 10.5 show a series of cw-NMR sweeps, measured during cool down at 25 bar. Fig. 10.6 shows lines from the same cool down, compared to lines from the subsequent warming up. The cooling rate was almost constant at about $4.2\,\mu$K/min. Every line was swept with a step width of $0.2\,\mu$T (6.5 Hz) and a sweep rate of $2\,\mu$T/s (65 Hz/s). The temperature during the sweeps was not stable, but due to the slow cooling rate, the temperature drift during one sweep is very small. The indicated temperature corresponds to the temperature measured at the maximum of the cw-NMR line. Fig. 10.7 shows a summary of the presented run, plotting the frequency shift of the line maximum $\Delta f = f_{max} - f_0$, the height of the highest peak and the sliding average (average over five sweeps) of the magnetisation as a function of temperature.

Several features can be observed in these graphs:

- Above about 1.6 mK, the lines are practically temperature independent. This is what

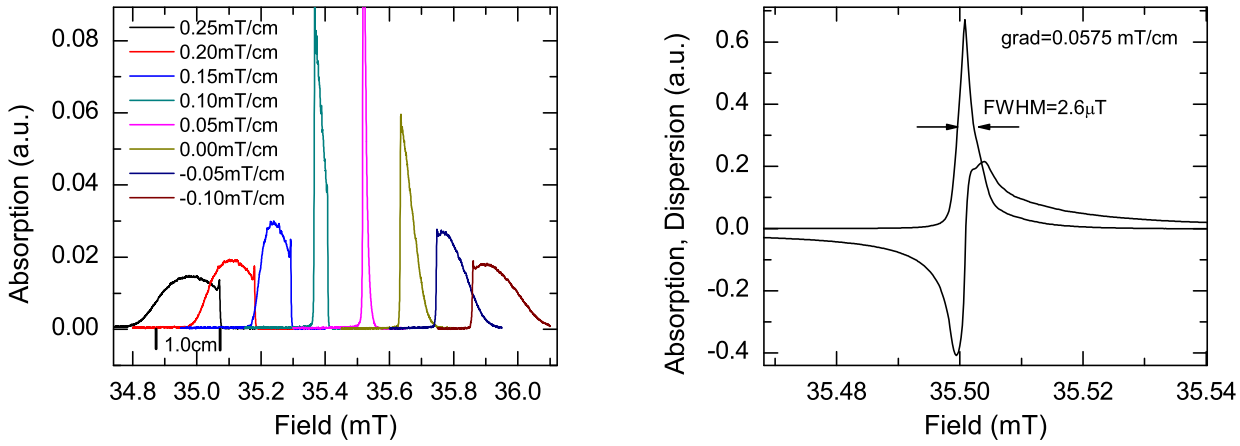

Figure 10.3: a) several cw-NMR lines at different gradient field values in the normal phase. The very steep edge observed for high gradients (e.g. right edge for the 0.25 mT/cm line) corresponds to the bottom of the cell. The smoother edge on the other side of the line corresponds to the loss of sensitivity of the RF-coil at the top of the cell. The sweeps at the different gradients are not centred around the same field value because the gradient coil does not only introduce a gradient term, but also a constant field term. The values shown on the field axis are dismissing this term. The indicated length-scale is calculated using a gradient of (0.25-0.0575) mT/cm, and thus only valid for the black line. It shows that the coil dimension corresponds well to the observed line width.
b) The smallest line width was found for a gradient of 0.0575 mT/cm. For this value the full width at half maximum of the absorption was only 2.6 μT (84 Hz). The asymmetric shape of the line indicates that even at this optimal gradient, the line shape in the normal phase is dominated by the field inhomogeneities.

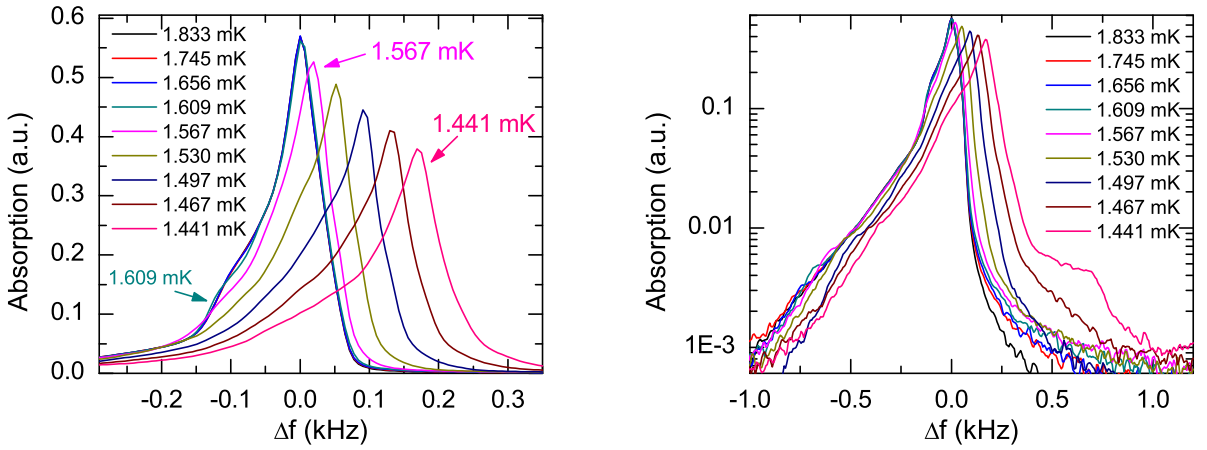

Figure 10.4: cw-NMR lines measured on cooling (25 bar), showing the transition from the normal to the A-like phase. The first four lines (1.833 mK - 1.609 mK) are practically identical, as expected for a Fermi liquid in the low temperature limit. A very small, but significant, negative shift at Δf ∼-0.13 kHz is observed comparing the 1.609 mK line with the higher temperature lines (for a more detailed presentation of this shift see section 10.2.4). Starting from the fifth line (1.567 mK) a positive shift is observed with a reduction of the peak height. Down to ∼ 1.45 mK, the shift gets larger, but the magnetisation, calculated from the integral over the whole line, is constant. This corresponds to what is commonly identified as the A-like phase. For the last line (1.441 mK), the first appearance of the B-like phase can be seen in the logarithmic plot.

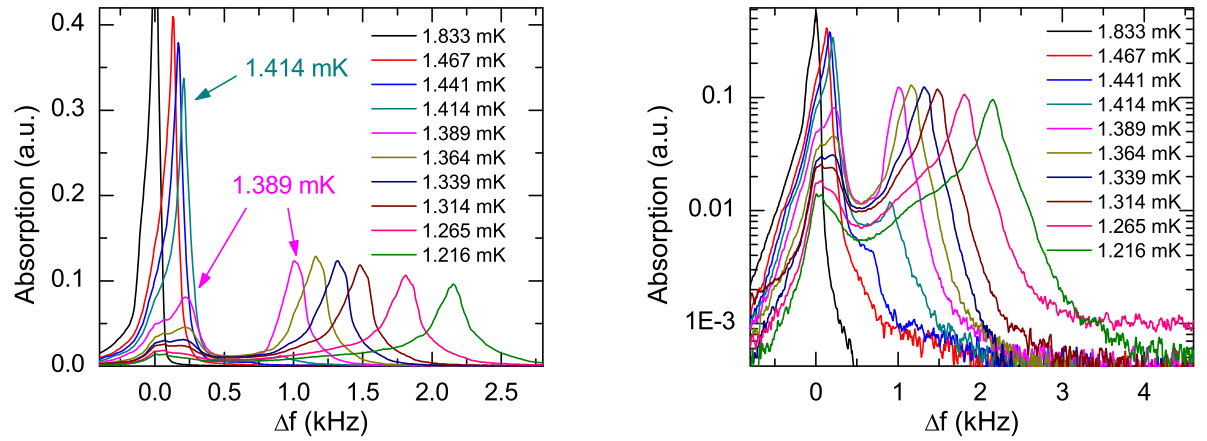

Figure 10.5: Continuation of the cool down presented in fig. 10.4, showing the transition from the A-like to the B-like phase. The most drastic change in line shape happens between 1.41 mK and 1.39 mK. In the logarithmic scale, it can be clearly seen, that the first precursor of the B-like phase appears at the 1.441 mK line and that down to the line 1.216 mK an A-like signal persists, indicating a coexistence of both phases. The transition temperature of T_{AB} ∼1.45 mK corresponds well to what is observed from the magnetisation (see fig. 10.7c).

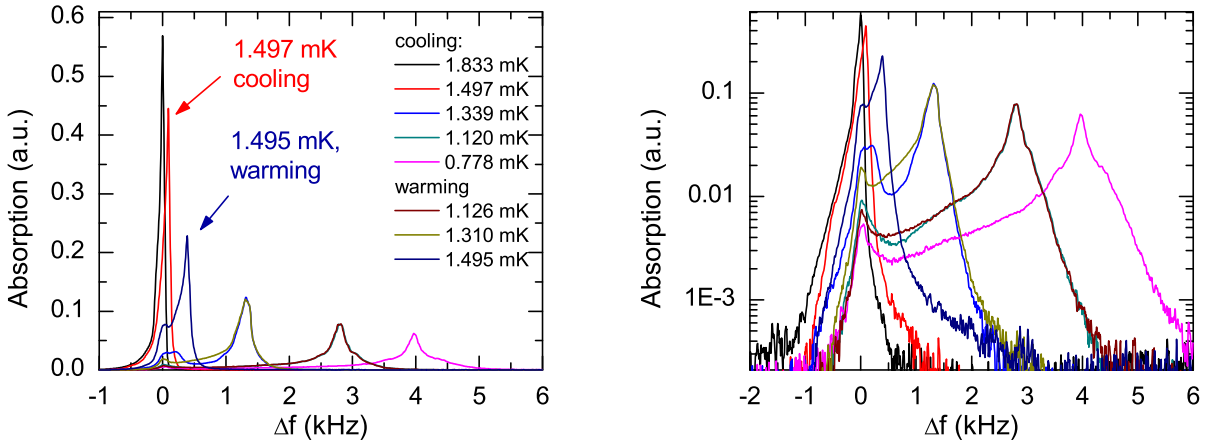

Figure 10.6: cw-NMR lines from the same cool down as shown in fig. 10.4 and fig. 10.5, extended to lower temperatures, with lines from subsequent warming added. The first line (1.833 mK) corresponds to the normal phase, the second line (1.497 mK) to the A-like phase. The third line (1.339 mK) is already mainly B-like phase. At 1.12 mK and at 1.32 mK, the B-like peak ($\Delta f > 1$ kHz) is virtually identical for cooling and warming. Contrarily, for small shifts <1 kHz, a small difference is observed (visible in the logarithmic plot). At $\sim$1.5 mK, the two lines for cooling and warming are completely different, an indication for either the supercooling of the A-like phase or superheating of the B-like phase.

is expected for a Fermi liquid in the low temperature limit and indicates that effects from solid ^{3}He layers are negligible.

- At 1.61 mK, a small, but visible negative shift can be observed. A more detailed measurement on this effect and a discussion on a possible interpretation in terms of a new phase will be presented in section 10.2.4.

- On cooling, at about 1.6 mK, the line starts to shift to higher frequencies, the peak height gets lower, but the magnetisation stays constant. The constant magnetisation indicates that we have to deal with an equal spin pairing phase, the positive shift is typical for an A-phase configuration with the orbital momentum axis $\hat{l}$ orthogonal to the magnetic field. We thus identify this phase as the A-like phase.

- Below about 1.45 mK, the magnetisation starts to drop and a second peak with much larger positive shift appears, which gets at about 1.40 mK higher than the first peak. The first peak nevertheless stays visible down to lower temperatures. This indicates the coexistence of the A-like and the B-like phase, something observed previously and explained in terms of strong pinning [99, 100].

- Below 1.40 mK, in the so-called B-like phase, the largest part of the line shows a high frequency shift. This is quite different from previous aerogel experiments, and we take

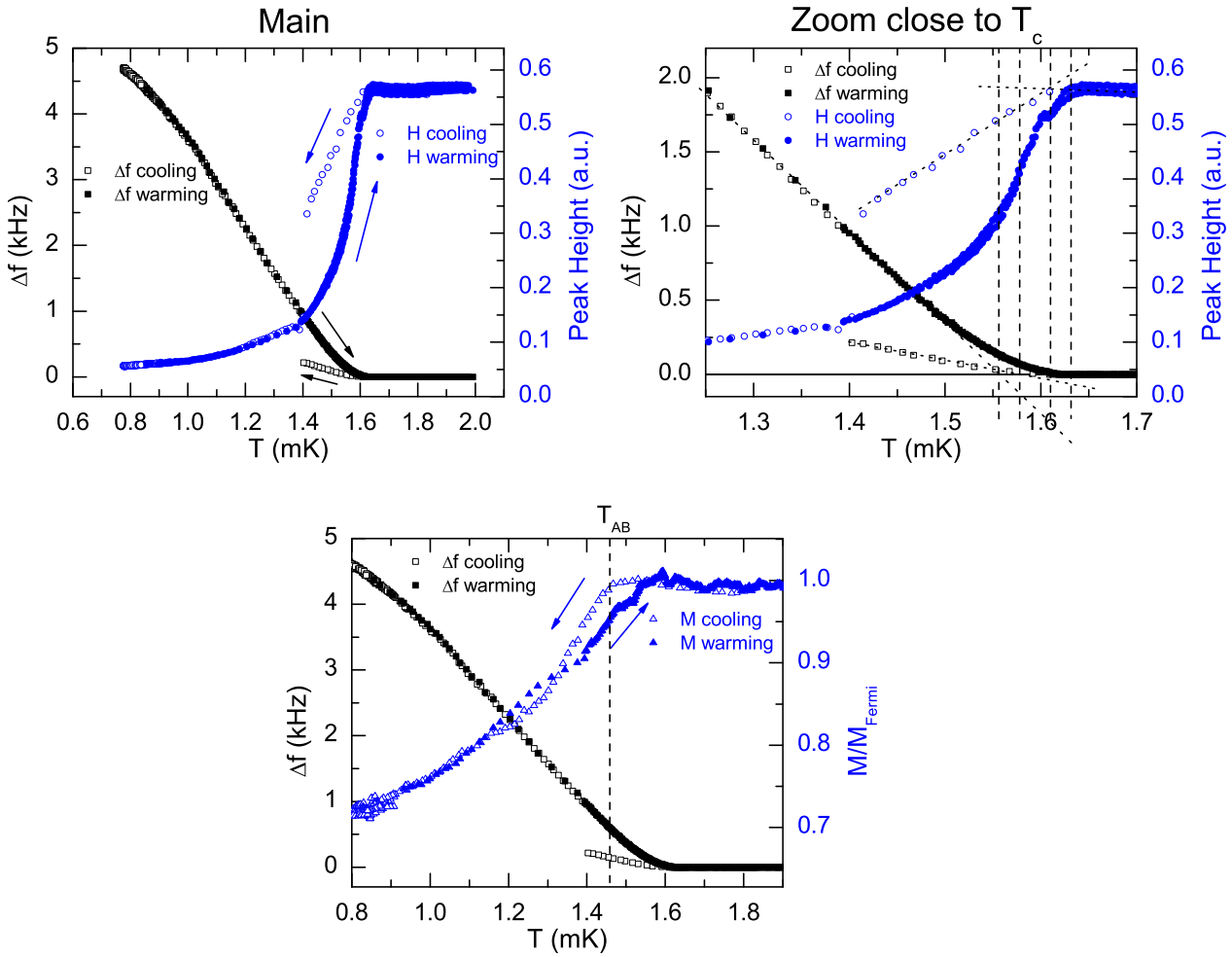

Figure 10.7: a) Summary of a single cool down and warm up. The frequency shift and the height of the absorption line are shown. The hysteresis between 1.4 mK and 1.6 mK is due to the metastability of the supercooled A-like phase or the superheated B-like phase.
b) A zoom on the transition temperature shows that the superfluid transition seems to be smeared out, and depending on the chosen criterion, T_c varies between 1.56 mK and 1.63 mK (see text).
c) The same graph but with the magnetisation plotted instead of the peak height. Each point corresponds to the sliding average of 5 sweeps. The onset of the decrease of the magnetisation upon cooling occurs at $T_{AB} \sim 1.45$ mK, which corresponds well to what is observed in fig. 10.4.

it as evidence that the orientation of the orbital momentum is indeed orthogonal to the magnetic field, due to the aerogel compression.

- The frequency shift in both, the A-like and B-like phase increases with decreasing temperature, which is simply a sign that the superfluid fraction increases.
- On warming, the features typical of the B-like phase are completely reproducible. The features of the A-like phase on the other hand do not reappear. Such a hysteresis has also been observed in previous aerogel experiments.

Leggett frequency

In pure bulk ^{3}He, a formula exists to describe the expected frequency shift in the B-phase as a function of temperature and the angle β between the order parameter $\hat{n}$-vector and the magnetic field. In a simplified version [101], it is

$$f = f_0 + \frac{f_L^2}{2f_0}\sin^2\beta, \tag{10.1}$$

where f_0 is the Larmor frequency and f_L the temperature dependent Leggett frequency. f_L as a function of T/T_c and pressure has been tabulated by Hakonen *et al.* [101], which allows us to compare our observed frequency shifts with the pure bulk case. In the simplified local oscillator picture, one expects that every part of the sample resonates at a frequency determined by the local value of β. The total shape of the line is then a direct picture of the distribution of the order parameter orientation. Plotting the absorption as a function of $2f_0(f-f_0)/f_L^2$ should then give a shape which is independent of temperature (disregarding the stretch in y-direction), and show values between 0 and 1. Fig. 10.8 shows the corresponding plot, using the pure bulk Leggett frequency. When we assume that the maximal shift we observe corresponds to $\beta = 90$, we can see that f_L^2 is reduced by a factor of 5. This reduction is similar to what has been seen by Dmitriev *et al.* [102].

10.2.3 Coexistence and strong pinning

The coexistence of the B-like and the A-like phase has already been mentioned and shown in the previous section. In this section we present data taken at 29.3 bar, which even more clearly show to which extent the A-like and the B-like phase can coexist. The data presented in fig. 10.9-10.11 was taken during a total of 31 hours. The peak shift, peak height and magnetisation as a function of temperature are summed up in fig. 10.11. The average cooling rate was about 1.1 μK/min, the average warming rate was about 0.34 μK/min. The cooling stopped in the middle of the A-B transition, which lead to the coexistence of both phases. It is difficult to tell the exact proportion of the A/B phase, as we do not know whether the whole of the B-like phase shifts to higher frequencies, and whether all of the signal with small shift belongs to the A-phase. However a rough estimation based on the surface of both peaks delivers a ratio of 65 % B- and 35 % A-phase. The temperature stayed within $\sim 2\,\mu$K constant at the lowest temperature of 1.401 mK for about 80 min, during

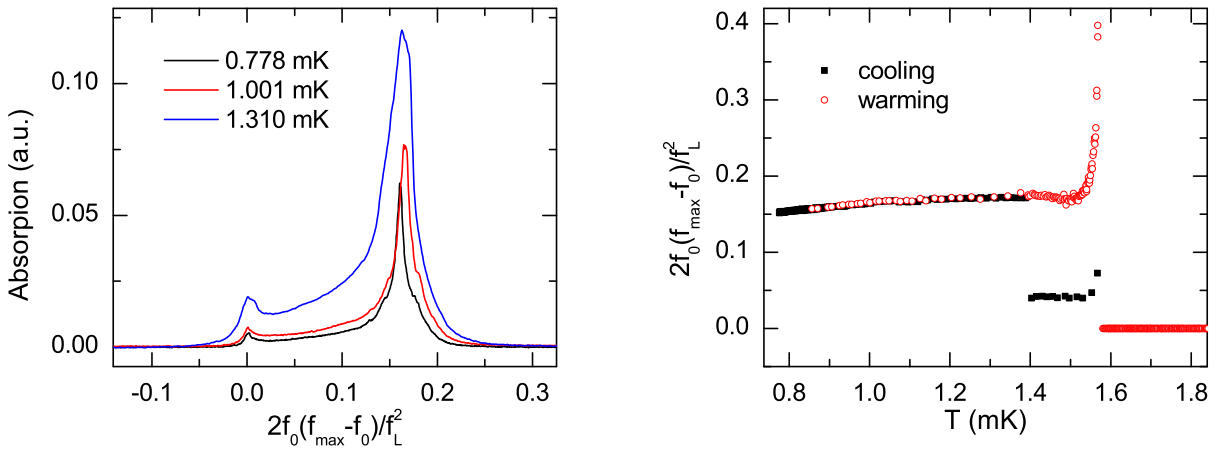

Figure 10.8: a) Normalising the frequency shift by the Leggett frequency, the temperature dependence of the shift can be eliminated. Using the values tabulated in ref. [101], we see that such a normalisation does work, even when using the values found in the pure bulk case. When we consider that the maximal shift corresponds to an angle of $\beta = 90$ we see that the magnitude of f_L^2 is reduced by a factor of 5.
b) Plotting the position of the maximum of the absorption line shows that the temperature dependence can be almost completely eliminated. The divergence close to T_c results from f_L going to zero for $T \to T_c$ and the difficulty to determine T_c precisely.

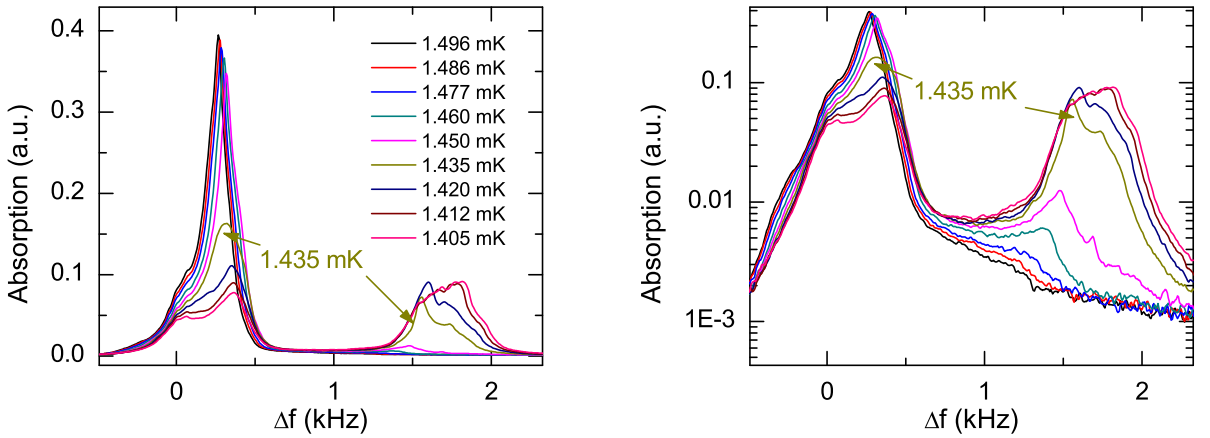

Figure 10.9: The A-B transition in high temperature resolution at 29.3 bar ($T_c \approx 1.80\,\mathrm{mK}$). These graphs were taken on a very slow cooling of about $1.1\,\mu\mathrm{K/min}$, in a total of 90 minutes. They clearly show the coexistence of both phases. The change in the structure of the B-like peak between the lines at 1.420 mK and 1.412 mK is possibly due to a small change in orbital momentum of the B-like order parameter.

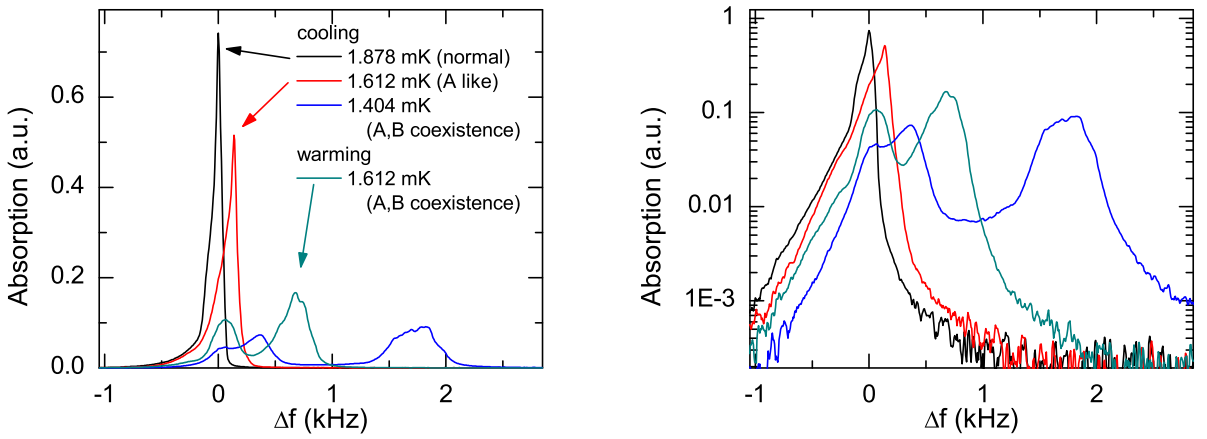

Figure 10.10: Lines from the same series as shown in fig. 10.9 (29.3 bar). The first three lines are taken on cooling. The cooling was stopped in the middle of the A-B transition (at 1.404 mK). The fourth line was taken on the subsequent very slow warming at a rate of about 0.34 μK/min. During the whole warming process, the A-like and the B-like part of the line grew proportionally, hence no transition from B to A was seen.

which no change in line shape (including 26 sweeps) was observed. During warming, which was extremely slow (0.34 μK/min) we did not see any sign that some of the B-phase had a transition to the A-phase (see for example the magnetisation curve). While it can not be excluded that we just have to deal with a very robust, superheated B-phase, we think that this measurement contradicts the predictions of Aoyama and Ikeda [93, 94] that the aerogel anisotropy stabilises the A-like phase.

In conclusion, the principal features which can be observed, like the supercooling of the A-phase, the coexistence and the reduction of the transition temperatures were all already known. But due to our high field homogeneity, and due to the fact that the orientation of the order parameter leads to a neat separation of the A-like and the B-like peak, in our measurement these features can be seen much more clearly, thus providing experimental support to the interpretation of earlier work.

10.2.4 Signature of the polar phase?

One main purpose of this experiment was the search for the polar phase predicted by Aoyama and Ikeda. Their calculations lead them to the phase diagram presented in fig. 10.12. This phase diagram is calculated for a 98 % porosity sample stretched in the axial direction by 7 %. In these conditions, a stability of the polar phase on a temperature region of about 50 μK is predicted. As our compression of 20 % corresponds to a much larger stretch, an enhancement of this region can be expected in our conditions.

According to Ikeda [103] the signature of the polar phase in our conditions, i.e. with the preferred axis parallel to the magnetic field and for small tipping angles, should be a

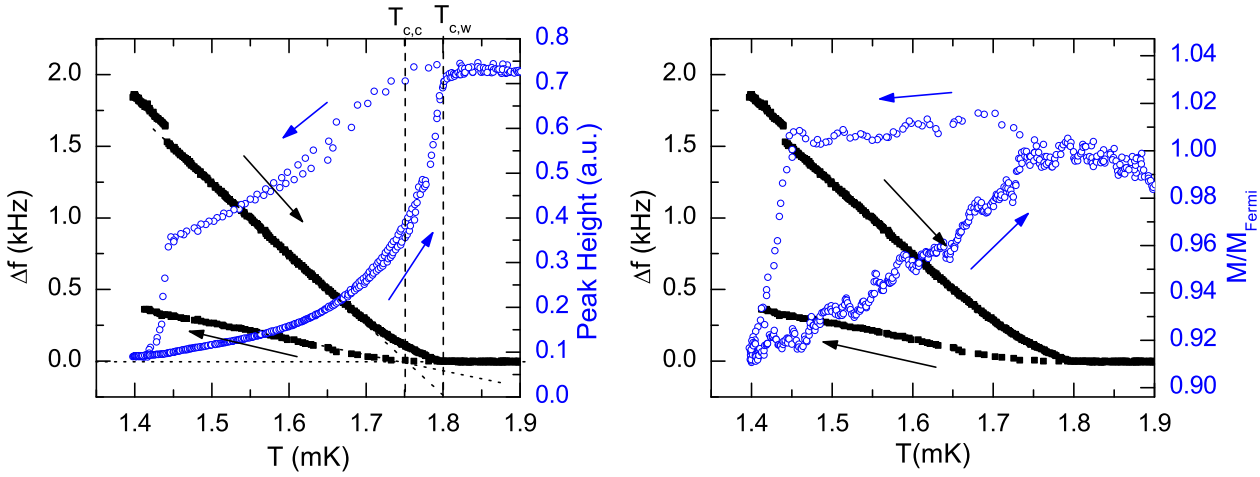

Figure 10.11: A summary of the lines presented in fig. 10.9 and fig. 10.10. The position and the peak height of the main peak, as well as the magnetisation (sliding average over 5 sweeps) as a function of temperature at 29.3 bar are shown. The arrows indicate the direction of warming/cooling. Depending on the criterion, a T_c between 1.75 mK and 1.80 mK is found. The onset of the B-phase formation on cooling is $T_{AB} = 1.45$ mK. The warming from 1.4 mK to 1.8 mK took 20 hours.
We think that the small magnetisation increase of about 1.6 % just below T_c is not significant, but linked to the difficulty to determine the baseline precisely.

positive frequency shift, four times stronger than the A-phase shift. This means that we should on cooling at first observe a positive shift, increasing with decreasing temperature. On further cooling, once the superfluid ^{3}He transits to the A-phase, a reduction by a factor of 4 for the frequency shift is expected. An additional characteristic comes from the fact that the polar phase is like the A-phase an equal spin pairing state. This means that no reduction in magnetisation is expected.

Fig. 10.13 shows lines from the same cool down at 29.3 bars as presented in the previous section (fig. 10.9-10.10), but this time with the focus on the cool down close to T_c. It shall be reminded that according to fig. 10.11 no single T_c can be determined, but that at 29.3 bar, T_c is between $T_{c,c}$ =1.75 mK and $T_{c,w}$=1.80 mK. The first obvious observation is that the lines show a positive frequency shift starting between 1.76 mK and 1.73 mK, a shift that we attribute to the formation of the A-like phase. But looking more carefully on the region presented in fig. 10.13b, a small, but clear negative frequency shift can be observed, starting already with the 1.792 mK line and getting more pronounced down to the 1.711 mK line. This shift appears in a narrow temperature region, and has the opposite sign compared to the A-phase shift. While other explanations may be possible, we interpret this result as the manifestation of a new phase, clearly distinguishable from previously known phases through its unusual NMR properties. In order to identify this phase theoretical calculations will be necessary, but it can be stated that the observed shift does not correspond to the predictions for the polar phase from Ikeda [103].

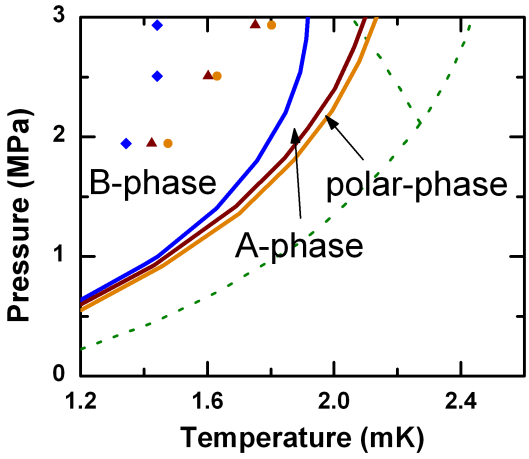

Figure 10.12: The phase diagram predicted by Aoyama and Ikeda [93], based on calculations considering a 98% porosity aerogel sample stretched in the axial direction by 7%. The different transition temperatures observed in this work are added to the graph. The crosses correspond to the appearance of the A-phase on cooling ($T_{c,c}$), the diamonds indicate the start of the A-B phase transition (T_{AB}). The squares correspond to the transition temperature on warming ($T_{c,w}$), which is the same temperature at which the small negative shift starts to appear on cooling (see fig. 10.11).
As we use a radial, cylindrical symmetric compression of 20%, we expected the region where the polar phase is stable, if it exists, to get larger. The compression decreased the porosity to 97% and as expected, the transition temperatures are reduced.

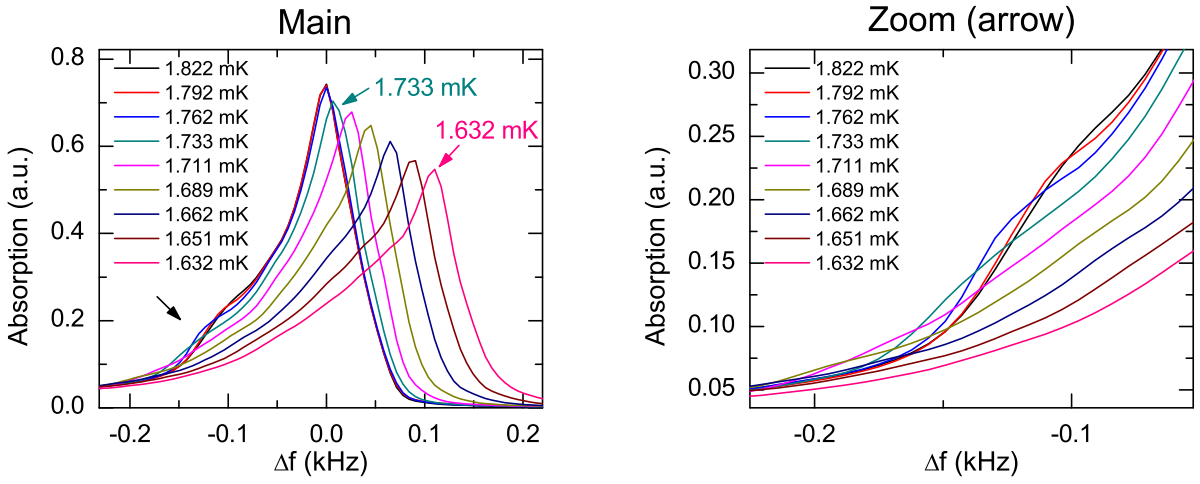

Figure 10.13: A detailed view close to T_c at 29.3 bar on cooling. A small but significant negative frequency shift is observed, starting from the 1.792 mK line. At this temperature, the right shift of the main peak has not started yet, as can be seen from the left graph. This negative shift gets more pronounced at lower temperatures and stays clearly visible down to 1.689 mK.

Chapter 11

Pulsed NMR measurements

In cw-NMR, we are limited to small RF-powers as otherwise the sample would heat up, and no measurements could be done in the superfluid regime. This means that cw-NMR is limited to the linear regime of small deflection angles. While in a lot of applications, it is advantageous to work in the linear regime, in superfluid ^{3}He interesting non-linear effects can be observed for higher deflection angles. In superfluid ^{3}He the spin dynamics is well described by the Leggett-Takagi equations (see for example ref. [3]), which consider that additionally to the torque due to the external magnetic field, the spin motion is influenced by the dipole torque. This in turn means that the orientation of the orbital momentum $\mathbf{L}$ relative to the spin part $\mathbf{S}$ plays an important role in the spin dynamics and hence in the observed NMR spectrum.

11.1 Expected resonance frequency

Following Bunkov and Volovik [104] an analytic description of spin precession in ^{3}He-B with arbitrary orientations of $\mathbf{S}$ and $\mathbf{L}$ can be determined when neglecting magnetic relaxation and the interaction with the excitation field. While in zero-order perturbation theory the precession is given by the Larmor frequency $f_0 = \gamma H$, a first order correction shows that a frequency shift can be observed which should be given by the derivative of the dipole energy F_D, averaged over the period of the precession:

$$f - f_0 = -\partial F_D / \partial S_z. \tag{11.1}$$

Considering only the case when the precessing spin has its equilibrium magnitude $S = \chi_B H/\gamma$, the time averaged dipole energy F_D can be written as

$$\begin{aligned} F_D &= \frac{2}{15}\frac{\chi}{\gamma^2} f_B^2 \left\{ \left[s_z l_z - \frac{1}{2} + \frac{1}{2}\cos\Phi\,(1+s_z)\,(1+l_z) \right]^2 + \right. \\ &\left. + \frac{1}{8}\,(1-s_z)^2\,(1-l_z)^2 + (1-s_z)^2\,(1-l_z)^2\,(1+\cos\Phi) \right\}. \end{aligned} \tag{11.2}$$

Here, $s_z = S_z/|\mathbf{S}| = \cos\beta$ is the projection of the spin on the $\hat{z}$ axis and can be calculated from the tipping angle β, and l_z is the projection of the orbital momentum $\hat{l}$ on the direction of the magnetic field $\mathbf{H}$. The angle Φ is a soft variable related to the ^{3}He-B order parameter. One constraint is given by the condition that the energy F_D needs to be stationary with respect to $\Phi : \partial F_D/\partial\Phi{=}0$.

Using this dipole energy, the variation with respect to the spin S_z (which can be seen as an analog of the global charge) delivers now the different precessing modes as a function of the frequency shift and of the other global charge L_z. Because of orbital viscosity, L_z is considered to be fixed. Omitting the limiting cases $\beta = 0$ and $\beta = \pi$, three different solutions are found [96]: solution 1

$$\cos\Phi = -\frac{(1-2l_z)(1-2s_z)}{(1+s_z)(1+l_z)}, \quad s_z = \frac{3-18l_z+15l_z^2+4w}{15(1-l_z)^2}, \tag{11.3}$$

solution 2

$$\cos\Phi = 1, \quad s_z = -\frac{-1+4l_z+5l_z^2+4w}{-13+10l_z+35l_z^2}, \tag{11.4}$$

and solution 3

$$\cos\Phi = -1, \quad s_z = -\frac{3(1-l_z^2)+4w}{3(1-l_z)^2}, \tag{11.5}$$

with w the dimensionless frequency shift[1]:

$$w = \frac{15f_0(f-f_0)}{2f_B^2}. \tag{11.6}$$

The free energy for these three solutions can be calculated as a function of l_z and s_z. This leads to the phase diagram shown in fig. 11.1a. In bulk ^{3}He the orbital momentum aligns with the magnetic field, meaning that states with $l_z = 1$ are realised. For $l_z = 1$, the Brinkman-Smith (BS) mode for $\beta < 104°$ and the Osheroff-Corruccini (CO) mode for $\beta > 104°$ can be observed experimentally [105].

The novelty of our experiment is that we succeeded to align the orbital momentum perpendicular to the magnetic field, meaning that l_z is fixed at $l_z = 0$. Using pulsed NMR we can control the parameter s_z and doing $\beta > 90°$ pulses we thus have the possibility to do measurements in the region where solution 3 is realised. In such a configuration the following frequency shifts are expected:

$$f - f_0 = \frac{f_B^2}{2f_0}\left(\cos\beta - \frac{1}{5}\right), \quad s_z > 0 \tag{11.7}$$

$$f - f_0 = -\frac{f_B^2}{10f_0}\left(1+\cos\beta\right), \quad s_z < 0. \tag{11.8}$$

[1] note that we use a different notation than in Ref. [96]: f_0 is the Larmor frequency, and f_B the B-phase Leggett frequency.

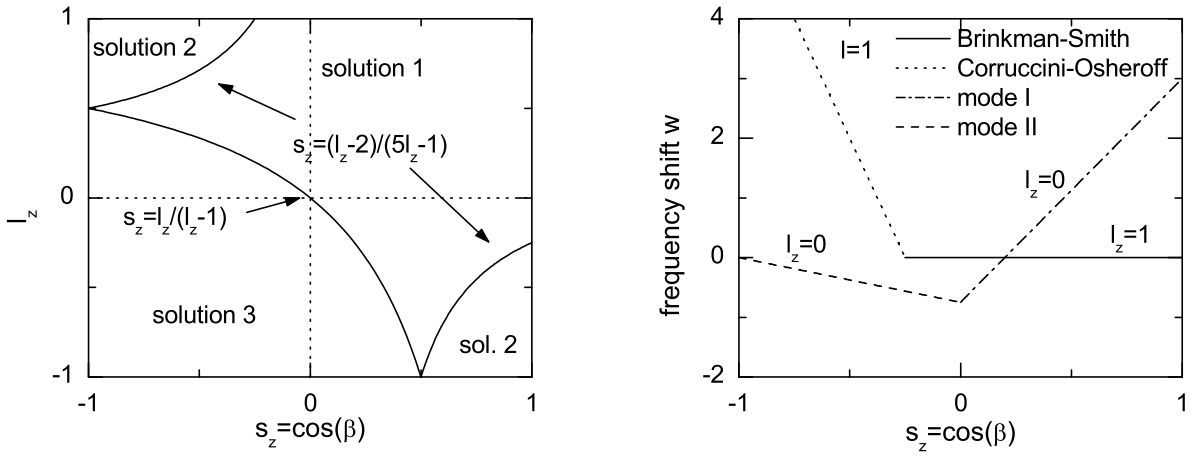

Figure 11.1: a) Different solutions have minimal free energy for different values of l_z and s_z. Usually the $\hat{l}$ vector tends to align with the magnetic field, and in pure bulk ^{3}He a state with $l_z = 1$ is realised. In this work we present for the first time measurements done for $l_z = 0$. Using pulsed NMR we can deflect β by more than 90°, which allows us to do for the first time measurements in the region of the phase diagram where solution 3 should be realised.
b) The equations 11.3-11.5 allow to predict the frequency shift for fixed l_z as a function of the tipping angle β. In the "usual" case of $l_z = 1$ this corresponds to the Brinkman-Smith mode for $\beta < 104°$ and to the Corruccini-Osheroff mode for $\beta > 104°$. The mode for $l_z = 0$, $\beta < 90°$ has already been put in evidence using cw-NMR measurements on a rotating cryostat [96] (mode I on the right graph). A new mode of precession for $\beta > 90°$ is expected (mode II on the right graph).

These shifts together with the shifts which are calculated for $l_z = 1$ are shown in fig. 11.1b.

11.2 Experimental results

11.2.1 Experimental details

The pulsed NMR measurements have been done using a spectrometer designed about 9 years ago by J.L. Bret of the service électronique of the former CRTBT. A scheme of the electronic setup can be seen in fig. 11.2. The electronics allows us to do only pulse lengths which are integral multiples of the exciting frequency, which was fixed by the waveform generator 1 at the Larmor frequency $f_1 = f_0$. In order to relate the different cycle lengths CL to a deflection angle β, calibration pulses in the normal phase at optimal gradient were made (see fig. 11.3). The expected amplitude of the free induction decay is proportional to the magnetisation perpendicular to the $\hat{z}$ axis, and should thus be of the form $A = A_0 |\sin \beta|$. Considering the tipping angle to be proportional to the pulse length, we then got experimentally the conversion $\beta = CL \cdot 12°$.

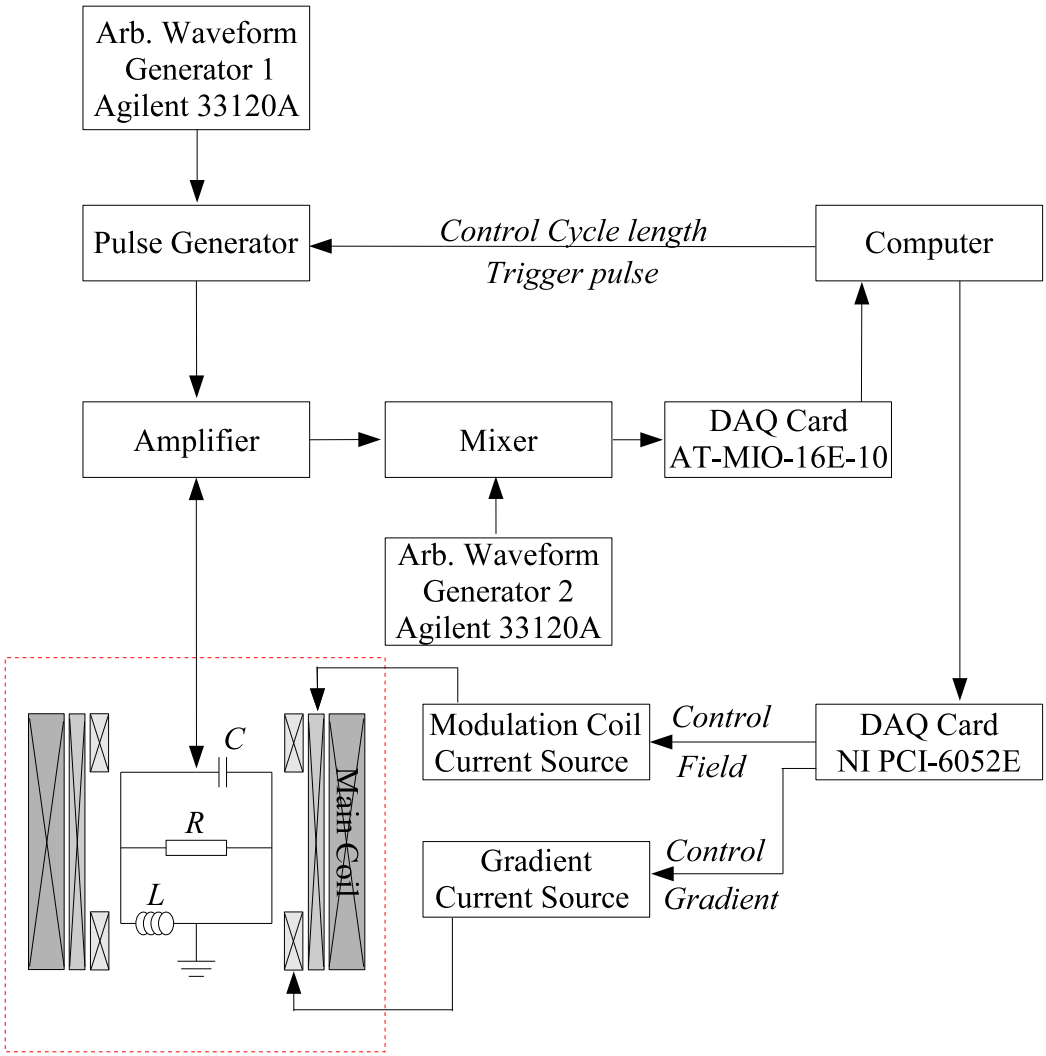

Figure 11.2: Simplified scheme of the used pulsed NMR spectrometer. As the acquisition card acquisition rate is not fast enough to resolve signals in the MHz regime, the induced NMR signal is multiplied with a sinusoidal function of frequency $f_2 = f_0 + 15.5\,\mathrm{kHz}$ created by the arbitrary waveform generator 2. The DAQ card then records the beating signal.

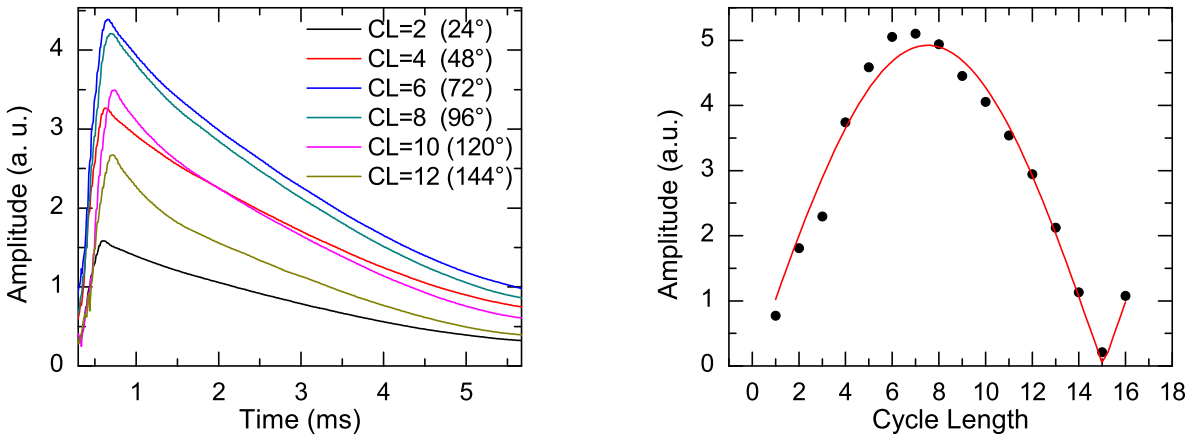

Figure 11.3: Calibration pulses done in the normal phase for optimal gradient. Pulses for different cycle lengths CL were done, and the amplitude as a function of this cycle length is plotted. The fit uses the formula $A = A_0 \,|\sin\beta|$ and delivers the conversion $\beta = CL{\cdot}12°$. The pulse of 15 cycles, which corresponds almost exactly to a 180° pulse, has a very low amplitude, which indicates that we have a very good RF-field homogeneity.

Determination of amplitude and frequency.

The electronic setup includes a mixer which multiplies the free induction decay signal of frequency f with a sinusoidal reference signal of frequency $f_2 = f_0 + \delta f$. The signal measured is then the beating signal with a frequency $f_m = f - f_2$. The reference frequency f_2 was chosen such that $7\,\text{kHz} < f_m < 22\text{kHz}$, corresponding to $\delta f = 15.5\,\text{kHz}$. The data acquisition worked at a rate of 89 kHz, meaning that for one period, relatively few points were recorded.

What we were interested in was the amplitude and the frequency as a function of time. The method used to obtain these parameters was to take a slice of 20 points, fit it by a sinusoidal, shift the slice by one point and repeat until the whole file is fitted. Two different models have been used. Model 1 considered that the amplitude does not change during one slice, leading to the fit formula $y(t) = y_0 \sin(\omega t + \varphi) + y_{off}$. A small DC offset y_{off}, which did not exceed 1 % of the pulse height was necessary to fit the data. The second model considered that during the short time of one slice, the amplitude changes linearly with time $y(t) = y_0(1 + s \cdot t)\sin(\omega t + \varphi) + y_{off}$. Both models provided virtually the same fit parameters for the amplitude and the frequency.

The Larmor frequency $f_{m,0}$ was determined experimentally by pulses done in the normal phase, and all frequency shifts presented are calculated as $f_m - f_{m,0}$.

Directly after a pulse, the electronics is “dazzled”, due to the very intense initial excitation. This is why for $t < 0.6\,\text{ms}$ the signal is increasing and no good fit can be found. For evaluation of the free induction decay we thus only considered the signal after the maximum.

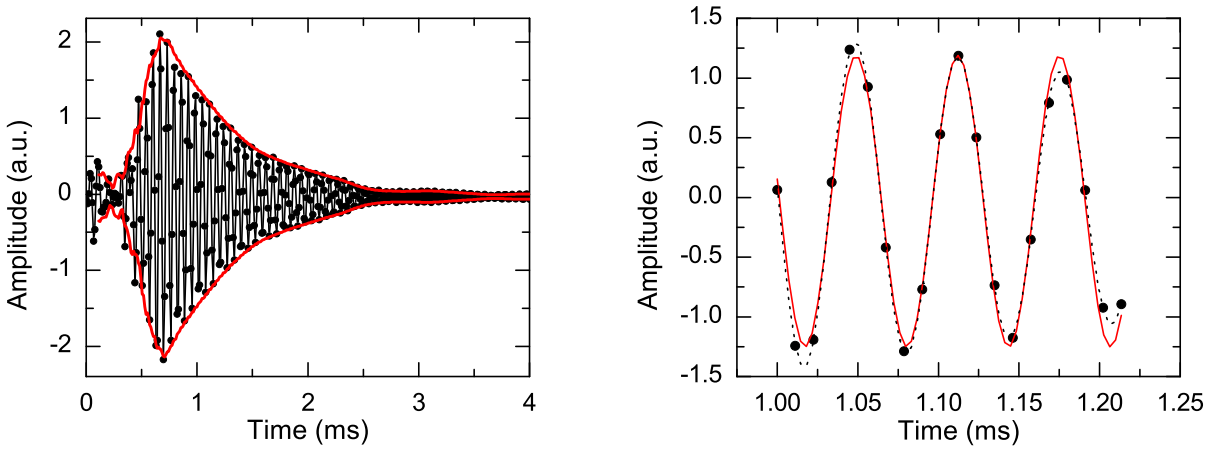

Figure 11.4: A typical pulse as recorded by the data acquisition card.
a) The full circles are the points acquired, the points are linked by a solid line to demonstrate the oscillation.
b) A zoom on the signal around 1.1 s. A slice of 20 points was taken and fitted by a sinusoid. The red, solid line corresponds to a fit considering the amplitude to be constant over a few oscillations: $y(t) = y_0 \sin(\omega t + \varphi) + y_{off}$, the dotted line uses a fit with a slope on the amplitude $y(t) = y_0(1 + s \cdot t) \sin(\omega t + \varphi) + y_{off}$. Doing such fits for all possible slices, the frequency and the amplitude as a function of time was obtained. Next to no difference was found for both models used. The red, solid line in the left graph corresponds to the amplitude as a function of time obtained by such a sliding fit.

11.2.2 B-phase pulses

To test the solutions calculated by Dmitriev *et al.* [96] and the prediction of HPD2 made by Bunkov and Volovik [104] (see section 11.1), pulses with different deflection angles were made at three different temperatures in the B-phase. The results for some of the pulses done at 0.91 mK are shown in fig. 11.5a, and the dependence of the resonance frequency on the tipping angle is presented in fig. 11.5b. From this graph it can be seen that for $\beta < 90°$, the agreement with the predicted frequency shift corresponding to solution 1 (eq. 11.7) is very good. This is another strong indication, additionally to the cw-NMR lines, that we successfully oriented the orbital momentum perpendicular to the magnetic field. We will name the corresponding precession mode mode I. This mode has already been observed by Dmitriev *et al.* [96].

For $\beta > 90°$ the phase diagram presented in fig 11.1 suggests that a mode described by solution 3 should be the stable mode, labelled mode II. The lines drawn in fig. 11.5b show that agreement between the observed and the predicted frequency shift (eq. 11.8) is very good except for the region close to $\beta = 180°$. We thus claim that we indeed observed a new mode of precession. A similar behaviour is found for measurements in bulk ^{3}He-B [105] where close to $\beta = 180\,°$ the measurements deviate from the analytic solution. This problem has been discussed by Golo and Leman [106].

Another information comes from the amplitudes observed. In the normal phase, the amplitude of a pulse is proportional to $|\sin(\beta)|$ (see fig. 11.3). From fig. 11.5a it is obvious that this is not the case in the B-phase with $\mathbf{L} \perp \mathbf{H}$. Firstly it can be seen that the amplitude for the 48° pulse is higher than the one for a 72° pulse, a feature that is not understood. Additionally it can be seen that the 120° pulse has a higher signal, and a slower decay than the 96° pulse. The same is true for the 144° pulse which lives longer than the 48° and the 72° pulse. All this indicates that mode II is more robust against dephasing than mode I. Such a robustness was explained in the case of the CO mode by the fact that for superfluids, thanks to the possibility of formation of spin supercurrents, the precession is homogeneous, and thus "protected" against dephasing. The observed decay time constants are much less enhanced than in the case of the CO mode (see for example Ref. [95]). Nevertheless, measurements done at different field gradient indicate that we have clear evidence that we have to deal with a coherent precessing state.

11.2.3 Temperature dependence

In order to check whether the temperature dependence of f_B corresponds to what has been observed in ^{3}He-bulk, we did a lot of pulses at a deflection angle of 48° for different temperatures on cooling and on warming. The normalised results are presented in fig. 11.6. The agreement in the A-phase is very good. In the B-phase a difference can be observed and extrapolating the tendency to $\Delta f = 0$, a $T_c \approx 1.53\,\mathrm{mK}$ much below the $T_c \approx 1.80\,\mathrm{mK}$ would be found. The reason for this difference is unclear.

A very interesting fact from fig. 11.6 is that for pulsed NMR, no hysteresis is observed, i.e. on warming, it seems as if there is a transition to the A-like phase. This is different

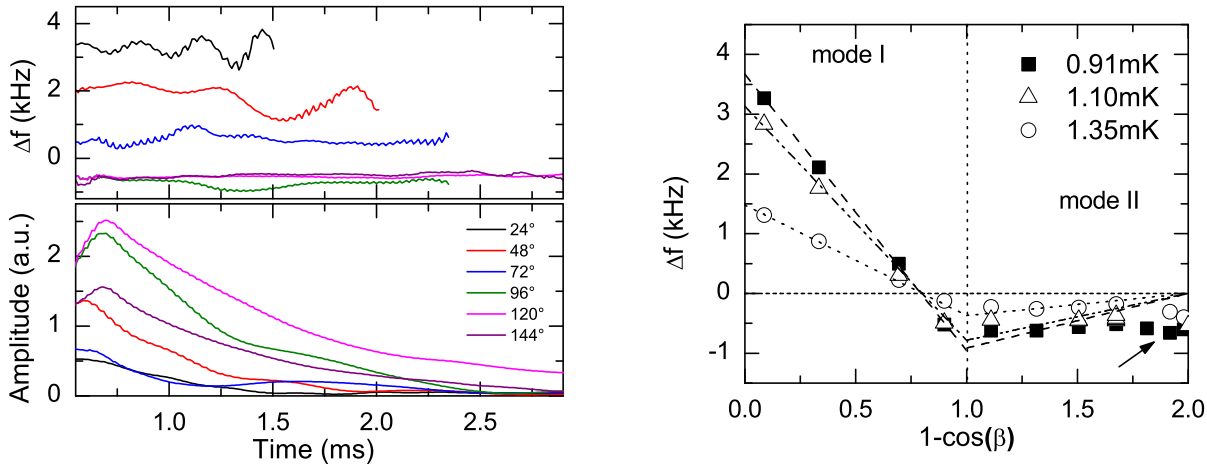

Figure 11.5: a) This graph shows the free induction decay signal for different tipping angles β at $T = 0.91\,\mathrm{mK} \approx 0.5\,T_c$. It can be seen that for small β a positive shift can be observed, and for $\beta > \arccos(1/5)$ the shift is negative. One remarkable feature of the amplitude plot is the observation that the highest signal is obtained for the 120° pulse, and not for the 96° pulse. Additionally it can be seen that the 72° pulse shows a lower amplitude than the 48° pulse, a feature that is not yet understood.
b) The resonance frequency shortly after the maximum of amplitude as a function of the tipping angle for three different temperatures. For $\beta < 90°$ (corresponding to the BS-state) agreement with the prediction presented in section 11.1 is perfect. The corresponding lines are fits using eq. 11.7, with f_B the only free fitting parameter. The lines for $\beta > 90°$ are plotted using eq. 11.8 with the value of f_B obtained from the previous fit for $\beta < 90°$. While the agreement with theory is less good than in the case of $\beta < 90°$ especially for large tipping angles (arrow), we think that we clearly observed a new mode of precession which corresponds to solution 3 (eq. 11.5).

from the other measurements done in aerogel. It has to be noted that for this graph, the warming has been done by the pulses themselves. This means we waited very little time (about 2 minutes) between two pulses, which left the system not enough time to cool back to the base temperature as it would be given by the cold reservoir. It has to be remembered that the VWR-thermometer is placed outside the aerogel sample. This means that one possible explanation why we saw no hysteresis is because locally, in the aerogel sample, we heated above T_c, and the measured points are thus in reality not taken on warming but on cooling. We refute this explanation for the following reasons:

The RF pulse heats directly the ^{3}He in the aerogel by changing the magnetisation. However the corresponding energy is easily calculated and it can be shown that it is several magnitudes below what would be necessary to heat the superfluid ^{3}He above T_c. Neither the cell walls nor the aerogel are electric conductors so that there is no possibility that Foucault currents heat the parts which are in direct contact with the ^{3}He in the aerogel. We thus think the main heating effect due to pulses is the indirect heating coming from the RF coil, heating all of the ^{3}He. In such a case, there is no reason to believe that the ^{3}He in the aerogel is at any moment significantly warmer than the bulk ^{3}He where the temperature is measured, and we think especially that between two pulses the heating was not enough to cross T_c.

With these measurements from pulsed NMR we can now interpret the results from the cw-NMR measurements concerning the A-phase stability slightly differently. Possibly, the A-phase is, at least in a stressed aerogel, the really stable phase above 1.45 mK, and the B-phase is metastable, as predicted by Aoyama and Ikeda [93]. Using pulses we can then overcome the metastability and induce the transition from the B-like to the A-like phase.

11.2.4 Conclusion

In conclusion, thanks to our configuration in which we succeeded to orient the orbital momentum perpendicular to the magnetic field, we identified a new precession mode for large tipping angles $\beta > 90°$. The observed frequency as a function of the tipping angle corresponds well to what has been predicted earlier. For these conditions, the appearance of a phenomena comparable to the homogeneously precessing domains HPD was predicted. Analysis especially for pulsed NMR measurements done in a field gradient will show to which extent we can confirm the formation of such a HPD2 state [107].

Very recent work by Bunkov and Volovik [108, 109] shows that previously observed coherent precessing states can be interpreted in terms of a Bose-Einstein condensation of magnons (spin waves). The possibility to use the same interpretation for this newly observed HPD2 state is under consideration [107].

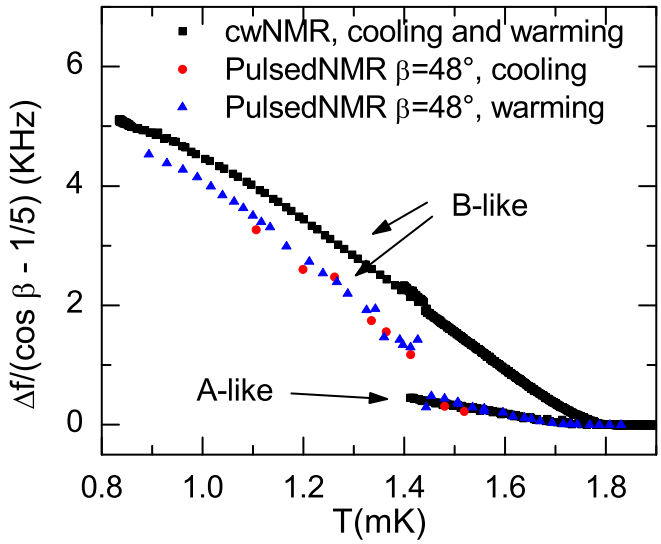

Figure 11.6: Comparison of the frequency shifts obtained using cw-NMR and pulsed NMR. For easier comparison the shift has been divided by $(\cos\beta - 1/5)$ (see eq. 11.7). In the A-phase the agreement is very good. In the B-phase, the agreement is rather poor and the extrapolation of the frequency shift towards zero seems to point to another T_c.

Appendix A

Recovering time constant

A.1 "Flat" Hole

In order to calculate the characteristic time constant for the thermalisation of the bolometer, we start by calculating the heat flux given by quasiparticles (QP) leaving the cell:

$$\Phi_{QP,out}(T) = \sum_{QP} E(\xi) P(\xi, \hat{p}) f(T, \xi) \tag{A.1}$$

The first term represents the energy of a QP, given by the dispersion relation 3.3, the second term is the probability per unity of time for this QP to leave the cell, and the third term the probability for this QP to exist, hence the Fermi-Dirac distribution. $\xi = v_F |\vec{p}|$ is the excitation energy of the quasiparticle. These terms are given by the following relations:

$$E(\xi) = \left(\xi^2 + \Delta^2\right)^{1/2} \tag{A.2}$$

$$P(\xi, \hat{p}) = \frac{S}{V} \vec{v}_G(\xi, \hat{p}) \hat{p} \cdot \hat{s} \tag{A.3}$$

$$f(T, \xi) = \frac{1}{1 + \exp\left(\frac{E(\xi)}{k_B T}\right)} \tag{A.4}$$

with $\hat{s}$ the unity vector normal to the hole of surface area S, V the volume of the box and $\vec{v}_G$, the QP group velocity given by

$$\vec{v}_G(\xi, \hat{p}) = \frac{\partial E}{\partial \vec{p}} = v_F \frac{\xi}{E(\xi)} \hat{p}. \tag{A.5}$$

Replacing the sum in A.1 by an integral we find

$$\Phi_{QP,out} = \frac{1}{4\pi} \frac{N_F}{V} S v_F \int_0^\infty \mathrm{d}\xi \int_0^{\pi/2} \mathrm{d}\theta \int_0^{2\pi} \mathrm{d}\phi \, E(\xi) \frac{\xi}{E(\xi)} \cos\theta \frac{1}{1 + \exp\left(\frac{E(\xi)}{k_B T}\right)} \sin\theta. \tag{A.6}$$

The integration over the polar angle θ has been taken from 0 to $\pi/2$, in order to take into account that only QPs travelling towards the hole will leave the cell. The summation over the spin states is already included in the density of states on the Fermi surface N_F. As we are working in the low temperature limit i.e. $k_BT \ll \Delta$, the Fermi-Dirac distribution can be approximated by the Boltzmann distribution and the solution to the integral becomes analytic:

$$\Phi_{QP,out} = \frac{1}{4}\frac{N_F}{V} S v_F \int_0^\infty \mathrm{d}\xi \xi \exp\left(-\frac{\sqrt{(\xi^2+\Delta^2)}}{k_BT}\right) \tag{A.7}$$

$$= \frac{1}{4}\frac{N_F}{V} S v_F (k_BT + \Delta) k_BT. \tag{A.8}$$

For now, we have calculated the heat flux due to quasiparticles leaving the cell. Energy is not only transported by quasiparticles, but also by quasiholes. As the dispersion relation is symmetric close to the minimum, the same calculation applies, and we only get an additional factor of two for the total heat flux out.

We are dealing with small temperature differences between the inside and the outside of the box which means that the heat flux coming from outside into the box, which is given by the same equation, can not be neglected. Considering a temperature T outside and $T + \Delta T$ inside the box we thus get for the total heat flux

$$\Phi_{tot}(T, \Delta T) = \Phi_{out}(T + \Delta T) - \Phi_{in}(T) \tag{A.9}$$

and we get for the linear response of the heat flux to a temperature gradient ΔT

$$\frac{d\Phi}{dT} = \frac{1}{4}\frac{N_F}{V} S v_F \frac{\Delta^2}{T}\left(1 + \frac{2k_BT}{\Delta} + \frac{2k_B^2T^2}{\Delta^2}\right) e^{-\frac{\Delta}{k_BT}} \equiv \frac{1}{R}. \tag{A.10}$$

This last equation allows us to find the thermal resistance of the hole and together with the heat capacity given by 3.28, we finally find in first order the characteristic time constant τ_b

$$\tau_b = RC = \frac{V}{S}\frac{1}{v_F}\sqrt{8\pi\frac{\Delta}{k_BT}}\frac{1 + \frac{21}{16}\frac{k_BT}{\Delta}}{1 + 2\frac{k_BT}{\Delta}} \tag{A.11}$$

$$\approx \frac{V}{S}\frac{1}{v_F}\sqrt{8\pi\frac{\Delta}{k_BT}}\left(1 - \frac{5}{16}\frac{k_BT}{\Delta}\right). \tag{A.12}$$

It is instructive to express τ_b as a function of the mean group velocity

$$\bar{v}_g = \frac{\int_0^\infty v_g(\xi) f(T,\xi)\mathrm{d}\xi}{\int_0^\infty f(T,\xi)\mathrm{d}\xi} \tag{A.13}$$

$$\approx \sqrt{\frac{2}{\pi}} v_F \sqrt{\frac{k_BT}{\Delta}} \tag{A.14}$$

where the approximation can be achieved by replacing the Fermi-Dirac distribution in the numerator by the Boltzmann distribution and by additionally expanding the square root of the dispersion relation in the denominator. Comparing this result with numbers found by numerical integration one finds that the introduced error is smaller than 4% for $T < 0.2\,T_C$.

We finally find

$$\tau_b = 4\frac{V}{S}\frac{1}{\bar{v}_g}\left(1 - \frac{5}{16}\frac{k_B T}{\Delta}\right) \tag{A.15}$$

A.2 Cylindrical hole

The previous result has been derived under the assumption that we have to deal with a "flat" hole, i.e. that all particles hitting the surface area S will leave the cell. In reality this is most probably not true, as our hole is better described by a cylinder of radius $r = 100\,\mu$m and length $L = 400\,\mu$m. A relatively large number of particles, namely those with large values for the polar angle θ, will hit the cylinder wall at least once on their way to the outside. This fact can influence τ_b by two mechanisms. Firstly, the scattering is not necessarily specular, implying the possibility for particles to be backscattered to the cell. This mechanism should be especially important for θ close to $\pi/2$. Secondly, one important difference to classical particles has to be considered, the possibility for Andreev scattering. As explained in section 5.2.4, an Andreev scattered particle has an inversed group velocity providing a second mechanism for a backscattering towards the cell. Unfortunately the important parameters of the probability for an Andreev scattering and for the degree of specularity of the surface are not known. Additionally, the texture which might be different for every demagnetisation run in the vicinity of the hole probably has a noticeable influence on the Andreev reflection rate, especially for low energetic quasiparticles. Any calculation thus remains speculative, but considering that for any particle with incident angle $\theta > \arctan 1/4 = 14°$ at least one scattering on the wall becomes likely, and for particles with $\theta > \arctan 1/2 = 26°$ it becomes sure, it can be seen that a considerable increase due to backscattering becomes likely.

To get at least an order of magnitude of this effect, we will present here what factor is obtained considering the simplest model possible. If we assume that *all* particles which hit at least one time the cell walls will be backscattered, and that the effective surface is not reduced by effects due to textures, we can calculate the fraction of the quasiparticles entering the cylinder will leave the cell. In this case numerically calculations show that only 5.6 % have trajectories that do not hit the cylinder wall which corresponds to an enhancement of τ_b of a factor 18. When assuming that the influence of textures are negligible this presents an upper limit, and it illustrates that the observed enhancement of a factor of 5 is not unreasonable.

Appendix B

Magnetic field dependence of the heat capacity

The B-phase specific heat can be calculated from the entropy. Following Vollhardt and Wölfle [3] we can start from the equation

$$C_V = -\frac{1}{T}\sum_{k\sigma}\frac{\partial f_{\rm k}}{\partial E_{k\sigma}}\left[E_{k\sigma}^2 - \frac{1}{2}T\frac{\partial}{\partial T}(\Delta_k^+\Delta_k)_{\sigma\sigma}\right], \tag{B.1}$$

where f_k is the Fermi-Dirac distribution and $E_{k\sigma}$ the quasiparticle excitation energy. In the low temperature limit ($T < 0.4\,T_C$), the gap is almost constant in temperature and the second term can be neglected. Additionally, the Fermi Dirac statistics approximates very well with a Boltzmann distribution

$$-\frac{\partial f_{\rm k}}{\partial E_k} \approx \frac{1}{k_B T}\exp\left(-\frac{E_k}{k_B T}\right). \tag{B.2}$$

Transforming the sum to an integral, we obtain

$$C_V = \frac{1}{2}\frac{N(0)}{k_B T^2}\sum_\sigma \int_0^\pi \sin(\theta)d\theta \int_0^\infty d\epsilon_k E_{k\sigma}^2 \exp\left(-\frac{E_k}{k_B T}\right), \tag{B.3}$$

with $N(0)$ the density of states at the Fermi energy.

In a magnetic field in $\hat{z}$ direction, the excitation energy $E_{k\sigma}^2$ can be written as [58]

$$E_{k\sigma}^2 = \Delta_1^2(\hat{k}_x^2 + \hat{k}_y^2) + (E_z - \frac{1}{2}\sigma\Omega_0)^2, \tag{B.4}$$

where

$$E_z^2 = \epsilon_k^2 + \Delta_2^2\hat{k}_z^2, \tag{B.5}$$

and $\sigma = \pm 1$ has two discrete values. Ω_0 the effective Larmor frequency is

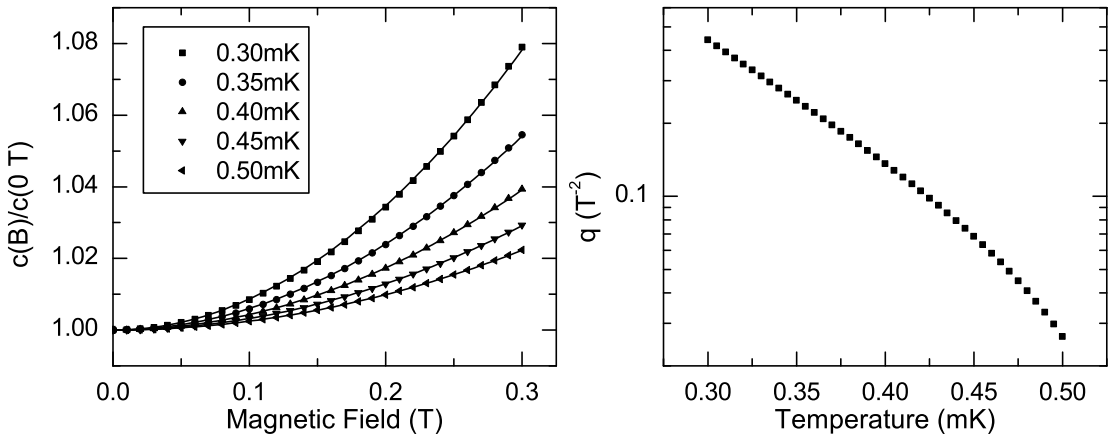

Figure B.1: a) A numerical calculation of the field dependence of the specific heat shows that at 29.3 bar, a quadratic correction to the zero field value can be expected in the whole temperature and magnetic field range of interest. The lines are fits through the points, using the formula $y = 1 + qB^2$. b) The prefactor q of this quadratic correction decreases with temperature.

$$\Omega_0 = \gamma B - 4 f_0^a S_z, \tag{B.6}$$

with S_z the total spin polarisation due to B along $\hat{z}$ and $N(0) f_0^a = F_0^a$. As the spin polarisation is small, we will neglect this term.

Δ_1 is the transverse gap for the $S_z = \pm 1$ pairs and Δ_2 the longitudinal gap for the $S_z = 0$ pairs. With Δ_{00} the zero field zero temperature gap, and Ω a renormalised Larmor frequency these gaps are expressed as [57]

$$\Delta_1^2 = \Delta_{00}^2 + \frac{1}{4}\hbar^2\Omega^2; \quad \Delta_1^2 = \Delta_{00}^2 - \frac{1}{2}\hbar^2\Omega^2 \tag{B.7}$$

with Ω given by

$$\Omega = \gamma B \left[1 + \frac{F_0^a \chi_{BW}(\Omega)}{\chi_N} \right]^{-1}. \tag{B.8}$$

The ratio $\frac{\chi_{BW}(\Omega)}{\chi_N}$ depends almost not on Ω and temperature in the zero field, zero temperature limit and has a value of $\frac{\chi_{BW}(\Omega)}{\chi_N} \approx 0.33$.

With the magnetic field dependence of the excitation energy known, the integral of eq. B.3 can be solved numerically.

In fig. B.1a) the field dependent heat capacity normalised by its zero field value at 29.3 bar is shown for different temperatures, in the temperature range which is relevant for chapter 6. Fitting the calculated points with the formula $y = 1 + qB^2$ shows that the field correction to the specific heat is quadratic in field. This correction gets more important at lower temperatures, but even for the "worst case" of 180 mT and 0.35 mK (see fig. 6.1), the expected effect is smaller than 3 %.

Appendix C

Detailed analysis of the neutron energy error bars

As presented in chapter 9, the pressure dependence of the observed neutron energy showed a relatively big scatter. A detailed analysis of the expected uncertainty tells us whether a physical interpretation of this result has to be considered or not.

C.1 Experimental details

Before going into the details of the error analysis, we want to present a certain number of points for which special care was taken. To our knowledge, some of these points should have no effect on the neutron calibration and hence should not influence the precision.

- After the end of the initial demagnetisation, a long time (>1 h) was waited before starting the neutron measurements in order to do the measurements on an almost flat baseline, i.e. at constant temperature. Due to "natural" heating, temperature was in general not globally stable. But locally, especially in the short time scale of one pulse, temperature drifts were very small. Additionally, within our working precision, we did not notice that the slope of the baseline dW_{base}/dt had any systematic effect on the peak height.

- Frequency sweeps driven with the same current as used later for monitoring were done regularly for the thermometer wire to determine accurately the factor $H = \frac{VW_0}{I}$. This factor does cancel out, as it intervenes in the same manner for neutron peaks and for calibration pulses, and should hence play no role for the overall accuracy. Nevertheless, it is a good way to control whether "something" is wrong.

- The thermometer wire was driven to oscillate with a velocity well below the critical velocity, with $0.6\,\mathrm{mm/s} < v_{RMS} < 0.9\,\mathrm{mm/s}$. Any effects/corrections depending on this parameter are the same for neutrons and for heating pulses, and should thus drop out for the calibrated neutron energies.

- The calibrations by heating pulses were done at least at the beginning and the end of a demagnetisation run, and most of the time in the middle of a neutron acquisition too. The settings for the thermometer VWR during these calibration pulses were exactly the same as during the neutron irradiation. In this way, the various corrections to the calibration factor linked to the behaviour of the thermometer VWR, introduced by Winkelmann *et al.* [48], drop out when calculating the energy of the neutron events, decreasing the number of possible systematic errors.

- The calibrations were done using a series of at least 10 pulses with different energies, covering the energy region from low energies to above 1000 keV, i.e. well above the neutron-capture energy. The calibration factor was obtained as the slope using a linear fit $H = \sigma E$. For all pulse series the energy - peak height curve was clearly linear.

- From chapter 8 we know that solid layers of ^{3}He can drastically decrease the calibration factor. Of course we took care to completely replace those solid layers by ^{4}He in order to keep the pulse heights as high as possible.

- It would have been good to do all measurements at the same magnetic fields and the same baseline resonance widths W_0, to prevent systematic errors linked to a variation of these parameters, but experimental limitations, coming mainly from the fact that we can not change temperature without changing the magnetic field and vice versa, did not allow us to do so.

C.2 Analysis of the statistical errors

In order to obtain the energy dissipated as heat after a neutron event and hence the energy deficit, two measurements are necessary: the calibration pulses, delivering the calibration factor σ and the measurement of peak heights after neutron events $H_{neutron}$.

The uncertainty of the calibration due to one single pulse can be decomposed as the error due to the measurement of the energy injected by the heater wire E and the uncertainties on the thermometer VWR response $H_{pulse}(E)$. A typical pulse can be seen in fig. 9.2. The quality of the acquisition of the heater VWR is found to be excellent for all data taken and statistical errors on the energy injected can be neglected. We thus can concentrate on the error coming from uncertainties of $H_{pulse}(E)$. For an accurate determination of the peak height, it was first tried to fit the pulse response, using the formula derived in section 5.3.4 (eq. 5.31). It was found that this method produced a larger scatter than a method where the baseline W_0 was determined by a fit of the points before a pulse, and the peak height is then determined as $H = \max(W) - W_0$. The uncertainty of the measured peak height can then be estimated by looking at the stability of the baseline. This stability varied for different demagnetisation runs, and even for different magnetic fields during one run, but typical values of the baseline noise were $\delta_{peak-peak}W \sim 1\,\mathrm{mHz}$, corresponding to an estimated value for 1σ of the peak height $\delta_{1\sigma}H \sim 0.35\,\mathrm{mHz}$. Pulses were typically made

for energies between 400 keV and 1600 keV, leading to peak heights of 15 mHz to 60 mHz in the "worst case" of 29.3 bar. This leads to an estimation of the relative error of 0.5 %-2% for a single pulse. As the calibration factor increases (see fig. 5.10), the signal to noise ratio increases for lower pressure. But between 10 bar and 30 bar, this only represents a small factor of 2, so that this error estimate is valid for all but the 0 bar measurements[1].

As already mentioned, the calibration factor was not determined by a single pulse, but always using a series of at least 10 pulses, reducing the statistical error further. As an example, a typical calibration curve consisting of 14 pulses is presented in fig. 9.3. The pulse example shown in fig. 9.2 corresponds to one of these pulses. As can be seen, the linear fit of form $H = \sigma E$ is excellent, yielding in this case a calibration factor of $\sigma = (50.08 \pm 0.14)\,\mathrm{mHz/MeV}$. This corresponds to a relative error of $\delta\sigma/\sigma = 0.28\,\%$, well in line with what is expected from the relative error of a single pulse:$\sim 1\,\%/\sqrt{13} = 0.28\,\%$. In the following, we thus take as the statistical error of the calibrations the error given by the fit algorithm

The statistical uncertainties of single neutron peak heights are obtained with the same arguments as above from the stability of the baseline, amounting to roughly $\delta_{1\sigma}H \sim 0.35\,\mathrm{mHz}$. As the neutron peak height changes with pressure and the baseline stability was not the same in all experimental runs, it is another time impossible to give a single value for the relative error, but in the "worst case" of 29.3 bar, with typical peak heights of $\sim 19\,\mathrm{mHz}$, the uncertainty should be of order of 1.8 %, corresponding to roughly 12 keV. To increase precision, the cell has been exposed a long time to neutron irradiation, typically 10-15 hours, a time during which approximately 100 neutron events can be observed. A typical acquisition file together with a zoom on a single event is shown in fig. 9.4. As can be seen, the baseline resonance width W_0 is not stable on a timescale of one hour, but the slope is small enough not to limit the precision of the peak height measurement. Analysing a large number of such events then leads to a histogram as shown in fig. 9.5. In this graph, the peak heights have already been converted to energy using the simple function $E_{neutron} = H_{neutron}/\sigma$. The obtained distributions were then fitted using a Gaussian law to obtain the centre E_c, and hence the most likely "real" value for the neutron energy:

$$n(E) = Ae^{-\frac{1}{2}\left(\frac{E-E_c}{w}\right)^2} \tag{C.1}$$

In the depicted graph, this fit yielded the parameters $E_c = (614.3 \pm 2.3)\,\mathrm{keV}$, $w = (22.4 \pm 2.3)\,\mathrm{keV}$, $A = 18.6 \pm 1.6$. Comparing $w/E_c = 3.6\,\%$ with the error estimations for a single peak shows that the half width half maximum is almost twice than what one could have expected from the uncertainty of a single peak. The reason of this can be either found in systematic errors, which will be discussed later, or it could be due to a "real" broadening due to the energy deficit being different for each event. Nevertheless, as we consider a high number of events, the centre of the distribution can be determined with high precision $\delta E_c/E_c = 0.37\,\%$.

The total statistical error as shown by the error bars in fig. 9.6 and fig. 9.7 is a combination of the calibration errors and the error given by the Gaussian fit:

[1] For the pressure dependence of the calibration factor, compare to fig. 5.10.

$$\frac{\delta E}{E} = \sqrt{\left(\frac{\delta E_c}{E_c}\right)^2 + \left(\frac{\delta \sigma}{\sigma}\right)^2}.$$

C.3 Systematic errors

The above discussion showed that considering only statistical errors, very precise values can be expected. But comparing the error bars with the observed scatter, especially the occurring dispersion for fixed pressure values, it becomes clear that either something physical is happening between several demagnetisation runs or that some important systematic errors have not been considered yet.

As already mentioned, we rule out the possibility of the introduction of systematic errors linked to the measurement of the peak height. If any such error would occur, it would equally show up for calibration pulses and for neutrons, and hence drop out when calculating the calibrated energy $E_{neutron} = H_{neutron}/\sigma = \frac{H_{neutron}}{H_{pulse}} E_{pulse}$.

This means that we are left with possible errors due to an inaccurate measurement of the energy injected E_{pulse}. Because of the corrections due to intrinsic losses, this factor can be decomposed in two parts (eq. 5.36): $E_{pulse} = E_{electric} \frac{\left(W^{heater} - W_{int}^{heater}\right)}{W^{heater}}$. We rule out variations of systematic errors of the electric energy injected which exceed the statistical errors presented earlier. The last possible source of errors is then an inaccuracy of the correction factor.

Demagnetising at high pressures to low fields, values of T/T_c were reached at which the quasiparticle gas was so dilute that the resonance width of the heater wire was purely determined by its intrinsic width. Using this method a value of $W_{int}^{heater} = 77 \pm 6\,\mathrm{mHz}$ was found. This value was used for all calibrations throughout the experiment. Unfortunately we have no independent way to verify this value but while we think that it is unlikely let us consider that this value changes over time or might even show a magnetic field dependence. Assuming such a case let us estimate the expected error: $\frac{\delta E_{pulse}}{E_{pulse}} = \frac{\delta W_{int}^{heater}}{W^{heater} - W_{int}^{heater}}$. Except two demagnetisations, all have been made above a baseline of $W_0^c > 2\,\mathrm{Hz}$, which corresponds to a value for the heater wire $W^{heater} > 0.85\,\mathrm{Hz}$. In this "worst case", a relative change of the intrinsic width of the heater wire of $\frac{\delta E_{pulse}}{E_{pulse}} = 0.1 \cdot \frac{\delta W_{int}^{heater}}{W_{int}^{heater}}$ means that a variability of 10 % would make this the dominant error source, and that a variability of about 50 % would be needed to explain all the observed scatter. The measurements were interrupted only once by a warming to room temperature, meaning that the temperature between demagnetisation runs did not exceed 100 mK. It is thus hard to imagine that internal friction due to defects, which we consider to be the dominant term, changes over time. Another possibility that this term introduces an error is that its value is constant but the 77 mHz value we used is not correct. In this case, a systematic error depending on the temperature should be seen. Some neutron measurements during a single demagnetisation run extended actually over a large temperature region, and such an effect was not observed.

A final source for systematic error comes from the fact that the series of calibration pulses were only taken at some specific value for baseline values W_0. Normally, the temperature slightly and continuously increased during the acquisition of the neutron peaks, meaning that neutron peaks were observed at all baseline values (and hence temperatures) between the initial and the final calibration series. An interpolation between the different series, using eq. 5.34 allows to have a good calibration for all different temperatures. Errors introduced by imperfections of this extrapolation should however show up in the histogram, so that it is not necessary to discuss it further as it is already taken into account by the results of the Gaussian fit.

In conclusion, no source of error, neither statistical nor systematic was found which could account for the observed scatter of up to 10 %, and we think it is justified to search for physical explanations of the observed values.

Bibliography

[1] J. Wilks, *The properties of liquid and solid Helium* (Clarendon Press Oxford, 1967).

[2] D. Pines and P. Nozières, *The Theory of Quantum Liquids* (W.A. Benjamin, Inc., Advanced, Advanced Book Classics, 1966).

[3] D. Vollhardt and P. Wölfle, *The Superfluid Phases of Helium 3* (Taylor & Francis, 1990).

[4] R. Balian and N. R. Werthamer, Phys. Rev. **131**(4), 1553, 1963.

[5] P. W. Anderson and P. Morel, Phys. Rev. **123**(6), 1911, 1961.

[6] P. W. Anderson and W. F. Brinkman, Phys. Rev. Lett. **30**(22), 1108, 1973.

[7] G. E. Volovik, *On Larkin-Imry-Ma State of 3He-A in Aerogel*, 2007, 0704.2484, http://arxiv.org/abs/0704.2484.

[8] J. Elbs, C. Winkelmann, Y. Bunkov, E. Collin, and H. Godfrin, Journal of Low Temperature Physics **148**(5), 749, 2007.

[9] D. J. Cousins, M. P. Enrico, S. N. Fisher, S. L. Phillipson, G. R. Pickett, N. S. Shaw, and P. J. Y. Thibault, Phys. Rev. Lett. **77**(26), 5245, 1996.

[10] D. Rainer and M. Vuorio, Journal of Physics C: Solid State Physics **10**(16), 3093, 1977.

[11] T. Kunimatsu, T. Sato, K. Izumina, A. Matsubara, Y. Sasaki, M. Kubota, O. Ishikawa, i. T. Mizusak, and Y. M. Bunkov, *NMR of superfluid ^{3}He in anisotropic aerogel*, 2007, cond-mat/0612007, http://arxiv.org/abs/cond-mat/0612007.

[12] D. Rainer and J. W. Serene, Phys. Rev. B **13**(11), 4745, 1976.

[13] D. S. Greywall, Phys. Rev. B **33**(11), 7520, 1986.

[14] A. J. Leggett, Phys. Rev. **140**(6A), A1869, 1965.

[15] G. R. Pickett, in *Proceedings of the Second European Workshop on Low Temperature Devices for the Detection of Low Energy Neutrinos and Dark Matter*, 1988.

[16] D. I. Bradley, Y. M. Bunkov, D. J. Cousins, M. P. Enrico, S. N. Fisher, M. R. Follows, A. M. Guénault, W. M. Hayes, G. R. Pickett, and T. Sloan, Phys. Rev. Lett. **75**(10), 1887, 1995.

[17] C. Bäuerle, Y. M. Bunkov, S. N. Fisher, H. Godfrin, and G. R. Pickett, Nature **382**(6589), 332, 1996.

[18] F. Mayet, *Détection directe et indirecte de Matière Sombre Supersymétrique*, Ph.D. thesis, Université Joseph Fourier, Grenoble, 2001.

[19] F. Mayet, D. Santos, Y. M. Bunkov, E. Collin, and H. Godfrin, Physics Letters B **538**, 257, 2002.

[20] E. Moulin, *Détection Directe de Matière Sombre non-baryonique avec l'Hélium 3*, Ph.D. thesis, Université Joseph Fourier, Grenoble, 2005.

[21] A. Penzias and R. Wilson, Astrophys. J. **142**, 419, 1965.

[22] D. Tytler, J. M. O'Meara, N. Suzuki, and D. Lubin, Physica Scripta **T85**, 12, 2000.

[23] S. Eidelman, K. G. Hayes, K. A. Olive, M. Aguilar-Benitez, C. Amsler, D. Asner, K. S. Babu, R. M. Barnett, J. Beringer, P. R. Burchat, *et al.*, Physics Letters B **592**(1-4), 1, 2004.

[24] P. Peebeles, *Principles of Physical Cosmology* (Princeton University Press, 1993).

[25] K. Begeman, A. Broeils, and R. Sanders, MNRAS **249**, 523, 1991.

[26] G. Bertone, D. Hopper, and J. Silk, Physics Reports **405**, 279, 2005.

[27] R. D. Peccei and H. R. Quinn, Phys. Rev. D **16**(6), 1791, 1977.

[28] K. Agashe and G. Servant, Journal of Cosmology and Astroparticle Physics **2005**(02), 002, 2005.

[29] C. Boehm and P. Fayet, Nuclear Physics B **683**, 219, 2004.

[30] P. Fayet and S. Ferrara, Physics Reports **32**, 249, 1977.

[31] R. Bernabei, P. Belli, R. Cerulli, F. Montecchia, M. Amato, G. Ignesti, A. Incicchitti, D. Prosperi, C. J. Dai, H. L. He, *et al.*, Physics Letters B **480**(1-2), 23, 2000.

[32] K. Belotsky, Y. Bunkov, H. Godfrin, M. Khlopov, and R. Konoplich, *^{3}He experimentum crucis for Dark Matter puzzles*, 2007, astro-ph/0606350.

[33] C. Winkelmann, *MACHe3: Protoype d'un détecteur bolomètrique de Matière Sombre non-baryonique à base d' ^{3}He superfluide*, Ph.D. thesis, Université Joseph Fourier, Grenoble, 2004.

[34] C. Bäuerle, *L'^{3}He adsorbé sur du graphite : Un système modèle pour la physique des Fermions en interactions à deux dimensions*, Ph.D. thesis, Université Joseph Fourier, Grenoble, 1996.

[35] E. Collin, *Effets du désordre sur l'^{3}He à ultra-basses températures*, Ph.D. thesis, Université Joseph Fourier, Grenoble, 2002.

[36] F. Pobell, *Matter and Methods at Low Temperatures* (Springer, 1996).

[37] O. V. Lounasmaa, *Experimental Principles and Methods Below 1 K* (Academic Press, 1974).

[38] C. Bäuerle, J. Bossy, Y. M. Bunkov, S. N. Fisher, C. Gianèse, and H. Godfrin, Czechoslovak Journal of Physics **46**(0), 2791, 1996.

[39] A. M. Guénault, V. Keith, C. J. Kennedy, S. G. Mussett, and G. R. Pickett, Journal of Low Temperature Physics **62**(5 - 6), 511, 1986.

[40] S. N. Fisher, A. M. Guénault, C. J. Kennedy, and G. R. Pickett, Phys. Rev. Lett. **63**(23), 2566, 1989.

[41] S. N. Fisher, G. R. Pickett, and R. J. Watts-Tobin, Journal of Low Temperature Physics **83**(3), 225, 1991.

[42] C. B. Winkelmann, E. Collin, Y. M. Bunkov, and H. Godfrin, Journal of Low Temperature Physics **135**(1 - 2), 3, 2004.

[43] D. C. Carless, H. E. Hall, and J. R. Hook, Journal of Low Temperature Physics **50**(5), 583, 1983.

[44] J. P. Carney, A. M. Guénault, G. R. Pickett, and G. F. Spencer, Phys. Rev. Lett. **62**(26), 3042, 1989.

[45] S. N. Fisher, A. M. Guénault, C. J. Kennedy, and G. R. Pickett, Physica B **165&166**, 651, 1990.

[46] S. N. Fisher, A. M. Guénault, C. J. Kennedy, and G. R. Pickett, Phys. Rev. Lett. **69**(7), 1073, 1992.

[47] E. Moulin, C. Winkelmann, J. Macias-Perez, Y. Bunkov, H. Godfrin, and D. Santos, Nuclear Instruments and Methods in Physics Research Section A: Accelerators, Spectrometers, Detectors and Associated Equipment **548**(3), 411, 2005.

[48] C. Winkelmann, J. Elbs, Y. M. Bunkov, E. Collin, H. Godfrin, and M. Krusius, Nuclear Instruments and Methods in Physics Research Section A: Accelerators, Spectrometers, Detectors and Associated Equipment **574**(2), 264, 2007.

[49] O. Martineau, A. Benoit, L. Berge, A. Broniatowski, L. Chabert, B. Chambon, M. Chapellier, G. Chardin, P. Charvin, M. De Jesus, *et al.*, Nuclear Instruments and Methods in Physics Research Section A: Accelerators, Spectrometers, Detectors and Associated Equipment **530**(3), 426, 2004.

[50] S. R. Bandler, S. M. Brouër, C. Enss, R. E. Lanou, H. J. Maris, T. More, F. S. Porter, and G. M. Seidel, Phys. Rev. Lett. **74**(16), 3169, 1995.

[51] J. M. Doyle and S. K. Lamoreaux, Europhys. Lett. **26**, 253, 1994.

[52] A. Golov and F. Pobell, Phys. Rev. B **53**(19), 12647, 1996.

[53] D. N. McKinsey, *Detection of Magnetically Trapped Neutrons: Liquid Helium as a Scintillator*, Ph.D. thesis, Harvard University, 2002, http://www.doylegroup.harvard.edu/neutron/publications/Theses/Danthesis.pdf.

[54] D. N. McKinsey, C. R. Brome, S. N. Dzhosyuk, R. Golub, K. Habicht, P. R. Huffman, E. Korobkina, S. K. Lamoreaux, C. E. H. Mattoni, A. K. Thompson, *et al.*, Phys. Rev. A **67**(6), 062716, 2003.

[55] J. Adams, Y. Kim, R. Lanou, H. Maris, and G. Seidel, Journal of Low Temperature Physics **V113**(5), 1121, 1998.

[56] G. M. Seidel, R. E. Lanou, and W. Yao, Nuclear Instruments and Methods in Physics Research Section A: Accelerators, Spectrometers, Detectors and Associated Equipment **489**, 189, 2002.

[57] L. Tewordt and N. Schopohl, Journal of Low Temperature Physics **37**(3), 421, 1979.

[58] M. Ashida and K. Nagai, Prog. Theor. Phys. **74**, 949, 1985.

[59] J. S. Meyer and T. Sloan, Journal of Low Temperature Physics **V108**(3), 345, 1997.

[60] S. Kafanov, A. Parshin, and I. Todoshchenko, Journal of Experimental and Theoretical Physics **91**(5), 991, 2000.

[61] D. Bradley, S. Fisher, A. Guénault, R. Haley, N. Mulders, G. Pickett, P. Skyba, and R. Whitehead, Journal of Low Temperature Physics **V138**(1), 129, 2005.

[62] T. Kibble, Journal of Physics A: Mathematical and General **9**(8), 1387, 1976.

[63] W. H. Zurek, Physics Reports **276**(4), 177, 1996.

[64] G. Volovik, *The Universe in a Helium Droplet*, vol. 117 of *International Series of Monographs on Physics* (Clarendon Press; Oxford University Press, Oxford, U.K.; New York, U.S.A., 2003).

[65] V. M. Ruutu, V. B. Eltsov, M. Krusius, Y. G. Makhlin, B. Plaçais, and G. E. Volovik, Phys. Rev. Lett. **80**(7), 1465, 1998.

[66] A. P. Finne, S. Boldarev, V. B. Eltsov, and M. Krusius, Journal of Low Temperature Physics **135**(5), 479, 2004.

[67] D. Bradley, S. Fisher, and W. Hayes, Journal of Low Temperature Physics **113**(5), 687, 1998.

[68] D. I. Bradley, D. O. Clubb, S. N. Fisher, A. M. Guénault, R. P. Haley, C. J. Matthews, G. R. Pickett, V. Tsepelin, and K. Zaki, Phys. Rev. Lett. **95**(3), 035302, 2005.

[69] D. I. Bradley, D. O. Clubb, S. N. Fisher, A. M. Guénault, R. P. Haley, C. J. Matthews, G. R. Pickett, V. Tsepelin, and K. Zaki, Phys. Rev. Lett. **96**(3), 035301, 2006.

[70] C. Bäuerle, Y. M. Bunkov, S. N. Fisher, and H. Godfrin, Phys. Rev. B **57**(22), 14381, 1998.

[71] A. J. Leggett, Journal of Low Temperature Physics **126**(3), 775, 2002.

[72] A. J. Leggett, Phys. Rev. Lett. **53**(11), 1096, 1984.

[73] P. Schiffer and D. D. Osheroff, Rev. Mod. Phys. **67**(2), 491, 1995.

[74] Y. M. Bunkov and O. D. Timofeevskaya, Phys. Rev. Lett. **80**(22), 4927, 1998.

[75] Y. M. Bunkov, *Topological Defects and the Non-Equilibrium Dynamics of Symmetry Breaking Phase Transitions* (Kluwer, Dordrecht, 2000).

[76] P. J. Hakonen, M. Krusius, M. M. Salomaa, J. T. Simola, Y. M. Bunkov, V. P. Mineev, and G. E. Volovik, Phys. Rev. Lett. **51**(15), 1362, 1983.

[77] J. P. Pekola, J. T. Simola, P. J. Hakonen, M. Krusius, O. V. Lounasmaa, K. K. Nummila, G. Mamniashvili, R. E. Packard, and G. E. Volovik, Phys. Rev. Lett. **53**(6), 584, 1984.

[78] Y. Kondo, J. S. Korhonen, M. Krusius, V. V. Dmitriev, Y. M. Mukharsky, E. B. Sonin, and G. E. Volovik, Phys. Rev. Lett. **67**(1), 81, 1991.

[79] M. M. Salomaa and G. E. Volovik, Rev. Mod. Phys. **59**(3), 533, 1987.

[80] V. Eltsov, private communication, 2007.

[81] G. E. Volovik, private communication, 2007.

[82] E. V. Thuneberg, Phys. Rev. Lett. **56**(4), 359, 1986.

[83] D. Bradley, S. Fisher, A. Guénault, R. Haley, J. Kopu, H. Martin, G. Pickett, J. Roberts, and V. Tsepelin, Journal of Low Temperature Physics **148**(5), 465, 2007.

[84] C. B. Winkelmann, J. Elbs, Y. M. Bunkov, and H. Godfrin, Phys. Rev. Lett. **96**(20), 205301, 2006.

[85] D. T. Sprague, T. M. Haard, J. B. Kycia, M. R. Rand, Y. Lee, P. J. Hamot, and W. P. Halperin, Phys. Rev. Lett. **75**(4), 661, 1995.

[86] J. V. Porto and J. M. Parpia, Phys. Rev. Lett. **74**(23), 4667, 1995.

[87] H. Alles, J. J. Kaplinsky, P. S. Wootton, J. D. Reppy, J. H. Naish, and J. R. Hook, Phys. Rev. Lett. **83**(7), 1367, 1999.

[88] B. I. Barker, Y. Lee, L. Polukhina, D. D. Osheroff, L. W. Hrubesh, and J. F. Poco, Phys. Rev. Lett. **85**(10), 2148, 2000.

[89] G. Volovik, JETP Letters **63**(4), 301, 1996.

[90] I. A. Fomin, Journal of Low Temperature Physics **134**(1), 769, 2004.

[91] C. L. Vicente, H. C. Choi, J. S. Xia, W. P. Halperin, N. Mulders, and Y. Lee, Phys. Rev. B **72**(9), 094519, 2005.

[92] W. P. Halperin and J. A. Sauls, *Helium-Three in Aerogel*, 2007, cond-mat/0408593, http://arxiv.org/abs/cond-mat/0408593.

[93] K. Aoyama and R. Ikeda, Phys. Rev. B **73**(6), 060504, 2006.

[94] K. Aoyama and R. Ikeda, *Strong Coupling Correction in Superfluid ^{3}He in Aerogel*, 2007, a0707.0954, http://arxiv.org/abs/0707.0954.

[95] Y. M. Bunkov, Journal of Low Temperature Physics **135**(5), 337, 2004.

[96] V. V. Dmitriev, V. B. Eltsov, M. Krusius, J. J. Ruohio, and G. E. Volovik, Phys. Rev. B **59**(1), 165, 1999.

[97] A. Abragam, *Les principes du magnétisme nucléaire* (Presses Universitaires de France, 1961).

[98] A. S. Chen, *Propriétés Magnétiques Nucléaries de l'^{3}He Superfluide à Ultra-basse Température*, Ph.D. thesis, Université Joseph Fourier, Grenoble, 1999.

[99] V. V. Dmitriev, I. V. Kosarev, N. Mulders, V. V. Zavjalov, and D. Y. Zmeev, Physica B: Condensed Matter **329-333**(Part 1), 320, 2003.

[100] J. E. Baumgardner, Y. Lee, D. D. Osheroff, L. W. Hrubesh, and J. F. Poco, Phys. Rev. Lett. **93**(5), 055301, 2004.

[101] P. J. Hakonen, M. Krusius, M. M. Salomaa, R. H. Salmelin, J. T. Simola, A. D. Gongadze, G. E. Vachnadze, and G. A. Kharadze, Journal of Low Temperature Physics **76**(3), 225, 1989.

[102] V. V. Dmitriev, private communication, 2007.

[103] R. Ikeda, private communication, 2007.

[104] Y. Bunkov and G. Volovik, Zh. Éksp. Teor. Fiz. **103**, 1619, 1993.

[105] L. R. Corruccini and D. D. Osheroff, Phys. Rev. B **17**(1), 126, 1978.

[106] V. Golo and A. Leman, *Helium Three* (Elsevier Science Publisher B.V., 1990), chap. 12, pp. 727–756.

[107] J. Elbs, E. Collin, Y. M. Bunkov, H. Godfrin, and G. E. Volovik, *Ordering of the orbital momentum in superfluid 3He-B in the deformed aerogel and new modes of coherent precession of spins*, 2007, 0707.3544, http://arxiv.org/abs/0707.3544.

[108] Y. M. Bunkov and G. E. Volovik, Phys. Rev. Lett. **98**(26), 265302, 2007.

[109] G. E. Volovik, *Twenty years of magnon Bose condensation and spin current superfluidity in 3He-B*, 2007, cond-mat/0701180, http://arxiv.org/abs/cond-mat/0701180.